Next-Generation Multi-Junction Photovoltaic Design Paradigms and Adaptive Optics Techniques for Telecommunications Applications and the Global Energy Transition

by

Robert Francis Holub Hunter

A thesis submitted to the University of Ottawa
in fulfillment of the thesis requirement for the degree of
Doctor of Philosophy in Electrical Engineering

Ottawa, Ontario, Canada, 2025

There is power in the light.

Abstract

Multi-junction photovoltaic devices offer the best performance in both solar and laser-based photovoltaic applications but have greater complexity and higher cost than their single-junction counterparts. In this thesis I demonstrate several pathways to improve the applicability and competitiveness of multi-junction photovoltaic devices. First, I investigate multi-junction solar cells and their application to the global energy transition and niche high performance domains. I start by studying silicon-germanium-tin as a potential material to extend the indium gallium phosphide/indium gallium arsenide/germanium lattice-matched multi-junction solar cell material system. That project aims to leverage the maturity of the three-junction design while boosting device efficiency by improving current-matching through introduction of the silicon-germanium-tin subcell. Next, I examine subcell segmentation, a nascent multi-junction solar cell design paradigm. I elucidate how subcell segmentation eases the simultaneous lattice and current matching requirements for multi-junction solar cells, greatly increases the number of bandgap combinations which can achieve high performance, reduces junction growth constraints, and unlocks the potential for operation at the most extreme solar concentration factors. I then shift focus to multi-junction photonic power converters and laser-based applications. I introduce machine learning enhanced design of ten-junction photonic power converters operating at a telecommunications wavelength of 1550 nm. I show that the novel machine learning enhanced approach greatly increases the number and variety of optimal designs, reduces computational expense, and simultaneously offers a new pathway to discover and understand fundamental physics in the design space. Finally, I detail development of a cost-effective, infrared-capable adaptive optics technique. I demonstrate how a single-pixel camera with compressive sensing could be used as input to adaptive optics to overcome fast signal fading in free-space telecommunications and power-by-light systems.

Acknowledgments

I am grateful for this opportunity. To all people, causes, and effects which have led me to this point. It is on the wonderful weight of accumulated history that we fly. To the all that came before, the all that will follow, and the All that is all around through all time and space. It is to our flourishing which I dedicate my work.

I am grateful to my self. To my indomitable spirit, to all those times I felt defeated, that there was no point, and yet I persevered. To the spark which kept me going. To the parts which tired and doubted thank you for never giving up. To all the pain, frustration, passion, and satisfaction I have alchemized to bring me here.

I am grateful for those around me, my friends and family, without you I would not be here. At all. Your support has been immeasurable. This accomplishment is all of ours. Thank you, from the depths of my heart.

I am grateful to all those wonderful people who supported, guided, and taught me. To Profs. Karin Hinzer and Alex Walker, for your supervision, understanding, motivation, and grace, your bright lights shining have gilded my path. To Drs. Chris Valdivia, Oliver Pitts, Costel Fleuraru, Gavin Forcade, and to Prof. Yuri Grinberg, for your close and considerable tutelage. To the colleagues at uOttawa and abroad that I had the privilege of working with, your contributions are integral to this achievement. To the colleagues at the SUNLAB which I did not have the privilege of directly working with but whose friendly, helpful presence spurred me forward and kept me grounded.

Cursum perficio.

. . .

This thesis was written on the unceded ancestral territory of the Anishinaabe Algonquin Nation.

Statement of Originality

I hereby declare that I am the sole author of this thesis. Chapters 1, 2, and 7 provide an introduction, background information for contextualizing my thesis research, and a summary. Chapters 3 through 6 present research projects which I contributed to over the course of this thesis. Most of the research in this thesis has been presented and/or published at international conferences or submitted to peer-reviewed scientific journals, as is indicated within. Unless otherwise stated all simulations and the corresponding data analysis were conducted by myself. Further details on the contributions of co-authors to publications are provided proceeding their placement in the thesis.

Contributions

The research presented in this thesis has led to the following publications and presentations.

Journal Articles

1. **R.F.H. Hunter**, G.P. Forcade, Y. Grinberg, D.P. Wilson, M.N. Beattie, C.E. Valdivia, M. de Lafontaine, LP. St-Arnaud, H. Helmers, O. Höhn, D. Lackner, C. Pellegrino, J.J. Krich, A.W. Walker, K. Hinzer, "Machine learning enhanced design optimization and knowledge discovery for multi-junction photonic power converters," *Scientific Reports*. In peer-review. July 2025.

2. M. de Lafontaine, C. Succar, **R.F.H. Hunter**, G.P. Forcade, J.P.D. Cook, J. Patel, B. Ellis, H. Fritzsche, J.J. Krich, K. Hinzer, "Figures of merit to quantify carrier collection in betavoltaics: Gain and gain efficiency," *Cell Reports Physical Science*. In print. July 2025.

3. G.P. Forcade, D.P. Wilson, M.N Beattie, H. Helmers, **R.F.H. Hunter**, O. Hohn, LP. St-Arnaud, C.E. Valdivia, D. Lackner, A.W. Walker, J.J. Krich, and K. Hinzer, "Multi-junction laser power converters exceeding 50% efficiency in the short wavelength infrared", *Cell Reports Physical Science*, 6(6):102610. May 2025. https://doi.org/10.1016/j.xcrp.2025.102610

Conference Proceedings

1. **R.F.H. Hunter**, M. Pashazanoosi, S. Hranilovic, C. Flueraru, A. Orth, O.J. Pitts, "Experimental point spread function imaging of turbulent wavefronts using compressive sensing," *2023 IEEE Sensors Applications Symposium (SAS)*, (July 18-20, 2023). https://doi.org/10.1109/SAS58821.2023.10254074

2. **R.F.H. Hunter**, C.E. Valdivia, L.S. Baribeau, K. Hinzer, "Unlocking the potential for extreme solar concentration via subcell segmentation," *17th International Conference on Concentrator Photovoltaic Systems (CPV-17)*, (April 12-14, 2022). https://doi.org/10.1063/5.0099470

3. **R.F.H. Hunter**, C.E. Valdivia, L.S. Baribeau, K. Hinzer, "Subcell segmentation for the optimization of a four-subcell multijunction solar cell design," *OSA Advanced Photonics Congress*, (July 13-16, 2020). https://doi.org/10.1364/PVLED.2020.PvM2G.6

Conference Presentations & Seminars

Presenter (does not include those with proceeding)

1. **R.F.H. Hunter**, G.P. Forcade, Y. Grinberg, M.N. Beattie, D.P. Wilson, C.E. Valdivia, M. de Lafontaine, L-P. St-Arnaud, H. Helmers, O. Hohn, D. Lackner, C. Pellegrino, J.J. Krich, A.W. Walker, K. Hinzer, "Using machine learning to optimize multi-junction photonic power converters," *Photonics West*, San Fransisco, USA, (2024). [Oral]

2. L.S. Baribeau, **R.F.H. Hunter**, C.E. Valdivia, and K. Hinzer, "Drift-diffusion modelling of four-junction InGaP/InGaAs/SiGeSn/Ge solar cells," *2022 IEEE 49th Photovoltaic Specialists Conference (PVSC)*, Philadelphia, PA, (June 5-10, 2022). [Oral]

Co-author

1. P. Wilson, G.P. Forcade, **R.F.H. Hunter**, A.W. Walker, Y. Grinberg, J.J. Krich, and K. Hinzer, "Impact of Luminescent Coupling on Multijunction InGaAs Photonic Power Converters under Current Mismatched Conditions in the C-Band", *Photonics North 2025*, Ottawa, Canada, (2025). [Oral]

2. M. de Lafontaine, **R.F.H. Hunter**, G.P. Forcade, J.P.D. Cook, J. Patel, B. Ellis, H. Fritzsche, K. Hinzer, "Optimizing Tritium Powered GaAs p-i-n and p-n Betavoltaic Cells", *14th International Conference on Tritium Science and Technology*, Ottawa, Canada, (2025). [Oral]

3. Y. Grinberg, D.-X. Xu, M.Al-Digeil, D. Melati, **R.F.H. Hunter**, A.W. Walker, G.P. Forcade, J.J. Krich, K.Hinzer, M.M. Masnad, O. Liboiron-Ladoceur, P. Cheben, J. H. Schid, and S.Janz, "Dimensionality Reduction in Photonics Design – New Methods and Applications," *Photonics North 2024*, Vancouver, Canada, (2024). [Invited talk]

4. K. Hinzer, **R.F.H. Hunter**, D.P. Wilson, G.P. Forcade, M.N. Beattie, C.E. Valdivia, O.Hohn, L-P.St-Arnaud, D. Lackner, Y. Grinberg, M. de Lafontaine, C. Pellegrino, J.J. Krich, A.W. Walker, H. Helmers, "C-band Multi-Junction Photonic Power Converters: AI Techniques for Optimized Designs and Role of Luminescent Coupling," *6th Optical Wireless and Fiber Power Transmission Conference (OWPT)*, Japan, (2024). [Invited talk]

5. K. Hinzer, **R.F.H. Hunter**, D.P. Wilson, G.P. Forcade, M.N. Beattie, C.E. Valdivia, O. Hohn, L-P. St-Arnaud, C. Pellegrino, D. Lackner, Y. Grinberg, J.J. Krich, A.W. Walker, H. Helmers, "Multi-junction photonic power converters: AI enhanced design optimization," *52nd IEEE Photovoltaic Specialists Conference (PVSC)*, Seattle, USA, (2024). [Poster]

6. P. Wilson, G.P. Forcade, **R.F.H. Hunter**, M.N. Beattie, A.W. Walker, Y. Grinberg, H. Helmers, O. Hohn, D. Lackner, J.J. Krich, K. Hinzer, "Quantifying the luminescent coupling process in C-band multi-junction photonic power converters," *Photonics West*, San Francisco, USA, (2024). [Oral]

7. M. de Lafontaine, **R.F.H. Hunter**, G.P. Forcade, J.P.D. Cook, D. Drouin, J.J. Krich, K. Hinzer, "p-i-n Betavoltaic Cells under 63Ni Irradiation: Quantifying Carrier Collection and Power Output," *52nd IEEE Photovoltaic Specialists Conference (PVSC)*, Seattle, USA, (2024). [Oral]

8. G.P. Forcade, M.N. Beattie, C.E. Valdivia, H. Helmers, O. Hohn, P. Wilson, L-P. St-Arnaud, **R.F.H. Hunter**, D. Lackner, J.J. Krich, A.W. Walker, and K. Hinzer, "High-Performance Multi-Junction C-Band Photonic Power Converters: Calibrated Optoelectronic Model for Next Generation Designs," *50th IEEE Photovoltaic Specialists Conference (PVSC)*, San Juan, Puerto Rico, (2023). [Oral]

Table of Contents

List of Figures

List of Abbreviations

AI artificial intelligence 47, 75, 76, 79, 80

AlGaAs aluminum gallium arsenide 32

AM0 air mass 0 - standard extraterrestrial solar spectrum 21

AM1.5D air mass 1.5 direct - standard direct solar spectrum xii, xiv, 2, 20, 30, 32, 35, 52, 59, 60, 66, 67

AM1.5G air mass 1.5 global - standard global solar spectrum xii, 21, 22, 29, 43

AO adaptive optics xiii, 8, 39–41, 106, 115, 118

ARC anti-reflection coating 4, 24, 25, 27, 49, 80

CPV concentrator photovoltaics xiii, 1, 6, 34–36, 44, 49, 60, 67, 68, 116

DBL detailed balance limit 6, 58

DMD digital micro-mirror device xiv, 41, 42

EQE external quantum efficiency 25, 26, 49

GaAs gallium arsenide 29, 33, 117

GaInAsP gallium indium arsenic phosphide 32

Ge germanium xii–xiv, 2, 3, 5, 6, 29–32, 44, 48, 49, 51, 52, 57, 58, 60, 64, 66, 115–117

InGaAs indium gallium arsenide xii–xiv, 2, 3, 5, 6, 29–32, 40, 44, 48–52, 57, 58, 60, 64, 66, 67, 115–117

InGaAsP indium gallium arsenic phosphide xii, 23, 24, 40, 117

InGaP indium gallium phosphide xii–xiv, 2, 3, 5, 6, 29–32, 44, 48–52, 57, 58, 60, 64, 66, 67, 115–117

InP indium phosphide xii, 23, 24, 117

IQE internal quantum efficiency 25, 49

J -junction xii, xiv, 2–5, 29, 30, 32–34, 48–52, 60, 64, 66, 75, 79, 80, 104, 115–117

JV current density - voltage xv, 13, 14, 16, 20, 28, 35, 43, 65, 66

LC luminescent coupling 28

LM lattice-matched xii, 5, 23, 24, 32, 58, 117

mDBL modified detailed balance limit xiv, 6, 43, 57, 59, 60, 67, 68, 116

MJ multi-junction xii–xiv, 1, 4–7, 9, 25–29, 31–35, 37, 38, 43–45, 47, 48, 52, 57–60, 75, 78–80, 104, 105, 115–118

ML machine learning xv, 3, 4, 7, 47, 75, 77–80, 104, 105, 115, 117, 118

MPP maximum power point 14, 35

PPC photonic power converter xii, xiii, 1, 2, 4, 6–8, 10, 20, 22–24, 26–28, 30, 33, 34, 36–38, 43–45, 47, 75, 76, 78–81, 104, 105, 117, 118

PV photovoltaic 1, 6, 7, 9, 10, 16, 19, 20, 22–28, 33, 34, 43–45, 49, 104, 115, 117, 118

RCWA rigorous coupled wave analysis xiv, 45, 46

SiGeSn silicon germanium tin xiii, xiv, 2, 3, 5, 6, 31, 32, 44, 48, 49, 51, 52, 57, 64–67, 115–117

SWIR short-wave infrared (approx. 700 nm to 2500 nm) 40

TCAD technology computer-aided design xiv, 5–7, 43–46, 48, 51, 57, 64, 66, 77–80, 104, 117

TMM transfer matrix method 45

Chapter 1

Introduction

Quantum mechanics tells us that there is power in light [1–3]. In this thesis, I explore modern approaches to the design of photovoltaic (PV) devices, which convert light energy into electricity, and applications of photonic power to remote technologies, telecommunications, and the global energy transition. The PV devices explored herein fall into two categories depending upon the light source they are optimized for: solar cells, which are designed for sunlight, and photonic power converters (PPCs), which are designed for laser light. The applications explored are distinguished along the same lines; conversion of sunlight for small-scale niche application power generation or utility-scale power generation using concentrator PV (CPV) systems, and conversion of laser signals for wireless and fibre-based remote power and data transfer (power-by-light systems, free-space optical communications, photonic data transmission, etc.).

This thesis focuses on PV devices which employ multi-junction (MJ) architectures of III-V and group IV semiconductor materials. MJ PV devices offer the best performance in both solar and laser applications but are more expensive than their single-junction counterparts [4–7]. Most of the projects in this thesis aim to improve the performance of MJ PV devices by introducing new materials or new design paradigms (Chapter 3 to Chapter 5). This increased performance translates to lower operational costs improving the competitiveness of MJ designs [5]. The final project (Chapter 6) addresses technical issues in the application space of wireless photonic power transmission (where a PPC would be used as receiver), directly improving it's applicability.

The remainder of this chapter collects the innovations achieved in this thesis into a single list. It then provides brief introductions to the research topics investigated and outlines the motivations for the variety of projects which were completed. In Chapter 2 I provide context and basic theory. Then Chapter 3 to Chapter 6 detail the research topics themselves. The focus is on solar power and the global energy transition in Chapter 3 and Chapter 4 and then

shifts to PPCs and laser-based photonic applications in Chapter 5 and Chapter 6. Finally, in Chapter 7, I summarize and provide directions for further study.

The innovations that were achieved over the course of this doctoral thesis are listed below. These have been copied from the sections in the body of the thesis where each project is detailed and collected into a single list here. They are presented in the order that they appear in the thesis.

- Determination of a potential current and lattice matching composition for the emerging silicon-germanium-tin material: $Si_{0.14}Ge_{0.824}Sn_{0.036}$ (SiGeSn) with an indirect bandgap of 0.77 eV, direct bandgap of 1.05-1.08 eV, and germanium lattice match. Modeling of the SiGeSn composition within the Sentaurus environment using literature data creating a material parameter database which is now being used in other SUNLAB projects. Incorporation of this material into established Sentaurus projects for the indium gallium phosphide/indium gallium arsenide/germanium (InGaP/InGaAs/Ge) three-junction (3J) material stack.

- Determination of potential efficiency gains for the 4J device over the 3J when considering reasonable material quality (1.3% absolute gain in power conversion efficiency at 1000 suns concentration of the air mass 1.5 direct (AM1.5D) spectrum for SiGeSn with a trap-assisted recombination lifetime of 1 µs and 10^3 cm/s surface recombination velocities in the device). Establishment of limits on the material quality for the 4J to retain higher efficiency than the 3J (trap-assisted recombination lifetimes of 100 ns or greater, with surface recombination velocities of 5×10^4 cm/s).

- Elucidation and discussion on the loss mechanisms and design challenges in the 4J device. Presentation of possible approaches to curb these losses such as thinning the upper junctions or introducing strain to the SiGeSn layer. Identification of current underproduction in the bottom subcell as one of the material system's limiting factors.

- First study of subcell segmentation for a $\sim$1.0 eV third subcell extension to the InGaP/InGaAs/Ge system. Extension of the Segments modified detailed balance code.

  - Subcell segmentation greatly loosens the bandgap requirement of novel 3J extension materials; segmented designs from across 36% of the 0.75-1.25 eV bandgap space exceed the peak standard efficiency (with up to 10 segments per subcell at 800 suns AM1.5D).
  - Subcell segmentation allows 4J devices to achieve extreme solar concentration operation.

- Direct comparison of simulated optoelectronic performance for 4-subcell InGaP/InGaAs/SiGeSn/Ge solar cell without and with realistic subcell segmentation (the top two or three subcells segmented into two junctions apiece), including a comparison to a 3J InGaP/InGaAs/SiGeSn device and the 3J InGaP/InGaAs/Ge baseline.
- Determination that the 3J InGaP/InGaAs/SiGeSn could potentially perform as well as or slightly better than the industry standard InGaP/InGaAs/Ge solar cell stack but without the use of the thick and expensive germanium substrate. The efficiency gain when adding the active substrate is 1% absolute.
- Demonstration that segmented designs (2:2:1:1 or 2:2:2:1 top to bottom segment multiplicities) have significantly boosted (+70% or greater) open-circuit voltages and greatly reduced (-40% or greater) SiGeSn junction growth requirements compared to the unsegmented 4J variant.
- Presentation of the potential for high-efficiency one- and two-subcell solar cell operation at extreme concentrations in the high hundreds, thousands, and even tens of thousands of suns. This potential is demonstrated for;
  - The per-concentration optimized and standard InGaP (1.7 eV)/InGaAs (1.1 eV) bandgap values.
  - As a function of maximum segments per subcell; here, the efficiency peak shifts from the high hundreds of suns solar concentration at segment multiplicities of $\leq$5 to tens of thousands at segment multiplicities of $\leq$15 (total junctions; $\leq$30). Efficiency gains of a few percent absolute are obtained as the peak shifts to thousands of suns illumination.
  - One-subcell optimized bandgap designs.
- Demonstration of an expansion in the high-efficiency bandgap space across all concentrations. This evolution is tracked and it is shown that, even at the unsegmented peak concentration factor of 200 suns, the number of high-efficiency ($\geq$45%) designs doubles with segmentation. This advantage only grows at higher concentrations, at 2000 suns, 60% of the 2-subcell bandgap space can achieve theoretical efficiencies of 45% or higher with 15% of that achieving 50% efficiency or higher. At 2000 suns, unsegmented two-subcell solar cells have begun to succumb to series resistance losses, the peak efficiency is 40% and dropping.
- First-ever application of dimensionality reduction to the design of active III-V optoelectronic devices. Development of a novel simulation environment, aiirmap, with an integrated calibrated device model and machine learning (ML) capabilities.

- Demonstration that the ML-enhanced method accelerates the design optimization of the MJ PPCs. It produces a much greater number of designs which attain the highest optical performance, which have greater layer thickness variability, and which have a lower computational cost than those found using classical optimization algorithms alone.
- Demonstration of the potential for knowledge discovery inherent in the ML-enhanced method by showing that the reduced dimensional subspace construction encodes fundamental physics in the design space.
- Determination that the conventional design approach to MJ PPC design (Beer-Lambert law absorber thicknesses with optimized anti-reflection coatings (ARCs)) is sufficient for the on-substrate 10J 1550 nm PPCs in this work. It achieves comparable optoelectronic performance to the top designs from the ML and classical optimizations.
- Development of a fully functional, well-calibrated test bench with the capability to simulate and capture the phase-distortion caused by atmospheric turbulence using a Shack-Hartmann wavefront sensor in the pupil plane and both single pixel and multi-pixel cameras at the focal plane. Collection of single pixel images with a 64x64 Hadamard basis. Exemplification of clear visual congruence between single pixel, multi-pixel, and simulated focal plane wavefront speckle patterns.
- Provision of evidence that speckle spot-based adaptive optics algorithms should perform just as well with single pixel images as standard multi-pixel images and that single pixel images with compressive sensing fractions as low as 15% may perform almost as well. Walsh down-sampling of the single pixel camera basis outperforms random across essentially all down-sampling rates between 45% and 15%. The metrics show that Walsh down-sampled images are better at retaining general (as indicated by higher structural similarity index measures) and speckle spot related information (as indicated by lower intensity-weighted average pairwise distances and relative intensity errors).

1.1 Silicon-germanium-tin

MJ solar cells combine junctions of different bandgap semiconductors into a monolithic device. This multi-material structure allows them to collect greater portions of the solar spectrum with greatly reduced thermalization losses and leads to the highest attainable solar to electrical power conversion efficiencies [8, 9]. However, these ultra-high efficiencies are only possible if all junctions produce the same current (current-matched) and if all materials have similar lattice constant (lattice-matched), otherwise recombination of charge carriers in the device will limit its

performance. MJ solar cell material systems are developed to fulfill these two requirements and lead to the classical approach to improving MJ solar cell performance; extension of an existing material system to include more materials and junctions (so-called "bandgap engineering") [8–13]. In Chapter 3, I begin my studies with this conventional approach.

Chapter 3 investigates the novel material silicon-germanium-tin (SiGeSn) as a potential third junction extension to the germanium lattice-matched (Ge-LM) indium gallium phosphide/indium gallium arsenide/germanium (InGaP/InGaAs/Ge) 3J solar cell. Historically, this 3J design has been one of the most popular MJ material systems due to its high-quality LM nature [14, 15]. However, it is not current-matched; it has a significant over-production of current in the germanium. Extension of the InGaP/InGaAs/Ge material system to include a lattice-matched, ∼1.0 eV bandgap third subcell has long been studied as a way to increase efficiency while taking advantage of the mature manufacturing capabilities of the existing 3J material system. SiGeSn is a recent candidate for this role with a ternary nature that allows it to fulfill both lattice-matching and current-matching requirements [16–23].

In Chapter 3, I outline experimental measurements of solar cells composed of the top two junctions of the InGaP/InGaAs/SiGeSn/Ge 4J solar cell design [24]. I also outline the use of Synopsys Sentaurus technology computer aided design (TCAD) simulations to explore the potential performance boosts, quality requirements, and design challenges in the effective implementation of a InGaP/InGaAs/SiGeSn/Ge solar cell design [16, 25]. I show that gains in solar power conversion efficiency over the InGaP/InGaAs/Ge 3J are possible for 4J solar cells incorporating reasonable quality SiGeSn. I place quality limits on the SiGeSn layer, investigate and offer solutions to the limiting factors in the design, and discuss other practical difficulties for the implementation of the novel material system. This project initially targeted the design and growth of a InGaP/InGaAs/SiGeSn/Ge solar cell, due to logistical constraints this was not possible. Consequently, my studies shifted to the simulation based study of subcell segmentation.

1.2 Subcell segmentation and segmented multi-junction solar cells

In Chapter 4 I investigate subcell segmentation, an emerging MJ solar cell design paradigm [26–34]. The different material junctions in MJ solar cells are called subcells. In segmented MJ solar cells (MJ solar cells which have undergone subcell segmentation), each subcell can be further split into multiple, absorptive, series-connected, same-material junctions called segments. This idea is schematically compared to the classical single- and multi-junction approaches in

Figure 1.1. The number of segments in each subcell offers a new design dimension which allows the simultaneous current and lattice matching requirements to be met more easily while providing a number of other benefits.

It should be noted that, in this thesis, I adopt "segment" to indicate any absorptive pn-junction in a MJ PV device [26]. The term "junction" indicates the same (as opposed to tunnel *diode*). On the other hand, (segmented) MJ solar cell subcells may be a single segment or multiple segments, they are distinguished as a subcell by their material. Throughout this thesis I take segment inclusively; MJ PPCs, segmented MJ solar cells, classic MJ solar cells, and even single junction PPCs and solar cells consist of segments. A segment is typically taken to include the front and back surface field layers which accompany the pn-junction.

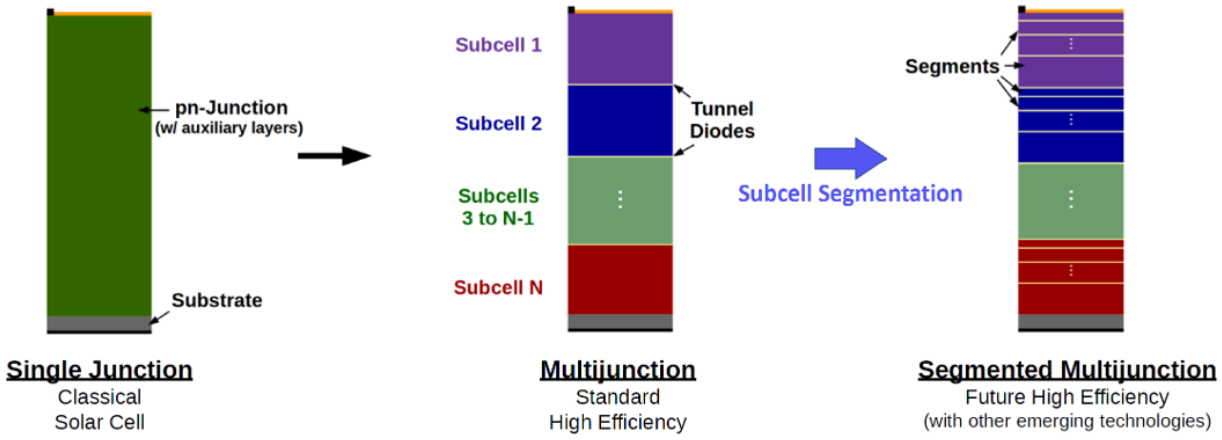

Figure 1.1: A progression of solar cell designs indicating and contextualizing the subcell segmentation technique. Different colours (purple, blue, green, red) indicate different semiconductor materials. Yellow indicates the tunnel diodes that are used to connect the segments in series. Black indicates contacts. The gold layer at the top indicates anti-reflection coating(s). Not to scale.

Chapter 4 explores the potential benefits of subcell segmentation. Specifically, I show the potential of subcell segmentation to: (1) overcome the MJ solar cell current-matching requirement and greatly expand the number of bandgap combinations which can achieve high-efficiency [26, 35], (2) ease material quality requirements for a InGaP/InGaAs/SiGeSn/Ge 4-subcell solar cell, and (3) shift power from high currents to high voltages unlocking the potential for CPV operation at extreme solar concentration factors [28, 36]. My simulation based studies are primarily completed near the detailed balance limit (DBL) using a custom modified DBL (mDBL) codebase (as detailed in Section 4.1). Synopsys Sentaurus TCAD simulations augment the SiGeSn study. Subcell segmentation is in an early stage of development with very few experimental devices realized and limited active research due to the added complexity and

constraints on crystal growth. MJ PPCs share the large segment multiplicity of segmented MJ solar cells, are the leading technology in their application space, and are the subject of active research [7]. These reasons saw me naturally joining the AIIR-Power MJ PPC project (Chapter 5) when it began and the next shift in my research focus.

1.3 Multi-junction photonic power converters

MJ PPCs and MJ solar cells are very similar devices; both employ the PV effect via a multi-layer stack of semiconductor material [7, 37–41]. As mentioned, the difference between the two is the spectrum of the light that they are optimized to absorb and convert to electrical power. MJ PPCs are optimized for small bandwidth laser light sources, typically in the infrared wavelength range. The essentially mono-chromaticity of the laser spectrum leads to the use of single absorber material stacks. In this regard, MJ PPCs are akin to a single segmented subcell in a segmented MJ solar cell.

MJ PPCs are employed in power-by-light systems where they act as the receiver/converter for power and data which is photonically transmitted in free-space or optical fiber. Photonic power and data transmission offers many advantages over the incumbent technologies (copper wires and radio telecommunications), including but not limited to: galvanic and electromagnetic isolation, higher data rates, wireless transmission, fire and explosion risk reduction, higher reliability, and faster signal propagation [42–45]. In Chapter 5, I focus on forwarding the evolution of MJ PPC design techniques. I incorporate ML into the MJ PPC design optimization by developing a framework which combines ML algorithms, databasing, optimization, batch run capabilities, and Synopsys Sentaurus TCAD simulations [46–52]. I use this framework to explore the design space of MJ PPCs which use the conventional thick on-substrate architecture as well as MJ PPCs where the substrate is removed and replaced with a flat, thin-film gold back-reflector. My framework is general purpose and allows incorporation of ML techniques into any technologies which can be simulated in Synopsys Sentaurus TCAD or other numerical solvers.

1.4 Cost-effective infrared-capable adaptive optics

In Chapter 6 I help develop a nascent cost-effective, infrared-capable adaptive optics technique for photonic data and power transmission through free-space (wirelessly) [53–56]. Free-space optical communications, typically at infrared wavelengths, unlock the bandwidth necessary for

next generation telecommunications (5G+), while free-space power-by-light offers the opportunity for remote powering of devices in hard-to-reach, sensitive, and everyday (internet of things) applications [57–64]. As mentioned, PPCs can act as the active receiver component in these photonic links.

Photonic transmission through free-space is hampered by atmospheric turbulence along the beam path [65, 66]. This turbulence causes intensity and phase distortions of the photonic wavefront and results in fast signal fading. Adaptive optics (AO) is a technique to measure and correct for wavefront distortion in real-time [67–69]. At infrared wavelengths, outside the sensitivity range of silicon, adaptive optics has been restricted by the high price of imaging devices. In Chapter 6, I advance an experimental workbench which uses a single pixel camera with compressive sensing computational imaging to overcome the cost hurdles of multi-pixel infrared imaging devices while achieving an imaging rate which is commensurate with the requirements of free-space optical communications. I obtain good agreement between single pixel, multi-pixel, and simulated images and show that the single pixel camera with compressive sensing fractions as low as 15% should perform nearly as well as a multi-pixel camera for AO applications [53].

This project was undertaken under the supervision of Drs. Oliver Pitts and Costel Fleuraru of the National Research Council of Canada's (the NRC's) Advanced Photonics and Electronics Research Centre (now the Quantum and Nanotechnologies Research Centre).

Chapter 2

Multi-junction photovoltaics and their applications

In this chapter I overview the key physics and engineering which underlie the multi-junction photovoltaic device and application research topics of this thesis. The chapter is split into four sections; photovoltaics, multi-junction photovoltaics, applications, and device design. In Section 2.1, I outline how the energy within light is harnessed by photovoltaic semiconductor devices. In Section 2.2, I detail how increasing the number of junctions offers significant benefits for PV applications and how it changes the structure and operation of the PV device. Section 2.3 then shifts into a study of application spaces for MJ PV devices. Finally, in Section 2.4, a brief outline of PV design paradigms gives context to the techniques developed in this thesis for computational device modeling.

In the interest of brevity, this chapter tailors its treatment of the background physics and engineering to the research topics covered within this thesis. It furthermore assumes a background on semiconductor physics, which has been covered elsewhere [8, 9, 70–74]. I will take as given that semiconductors are conventionally expressed within the band theory of solids, with band diagrams which are determined by the momentum-states of the electrons in the first Brillouin zone of the crystal lattice, and that the band diagrams are populated and thermally excited by Fermi-Dirac filling of the density of states. That the effect of semiconductor doping to introduce new energy levels into the band structure, and that the formation of a pn-junction as electronic band bending to equate the shifted Fermi levels of the p and n sides (which is equivalent to carrier recombination clearing a space charge region near the interface populated by dopant ions substantiating the built-in electric field), is understood.

2.1 Photovoltaics; From light to electricity

This section explains how the photovoltaic effect underlies the conversion of light to electricity in certain semiconductor devices. I first examine the nature of light and the photovoltaic effect. Then I investigate how the pn-junction semiconductor structure can leverage the photovoltaic effect to enable photonic to electrical power production. Third, I discuss the specifics of the optoelectrical operation of PV semiconductor devices. Finally, I examine differences in the spectral qualities of solar and laser light and distinguish between solar cells and PPCs, the classes of PV devices which are tailored to each light source. Coverage of multi-junction PV phenomenology is reserved for Section 2.2.

2.1.1 The photovoltaic effect; Power in light

Albert Einstein did not win his Nobel prize for special relativity, general relativity, or his contributions to quantum mechanics, but rather for "his services to Theoretical Physics, especially his work on the photoelectric effect" [1, 2, 75]. The photoelectric effect is the emission of electrons from a metal surface when illuminated by light of certain frequencies [3, 8, 9, 76]. Electron emission energies are correlated with the frequency of the light and emission populations are correlated with the light intensity. This is understood clearly now. It is the conveyance of energy in quantized photons of light, with energy proportional to frequency, which come and one-by-one interact with an electron in the metal giving it enough energy to overcome the metal's work function and escape (Figure 2.1a). However, in ∼1905, the photoelectric effect provided evidence which directly contradicted the (what is now called) classical understanding, it was a signpost pointing to new physics. With their quantum explanation of the photoelectric and other effects, Einstein and his collaborators cemented the emerging quantum worldview within which we now live. Light is a quantum wave-particle phenomena with quanta of energy called photons. A photon's frequency and energy are proportional through the Planck equation.

The photoelectric and photovoltaic effect are kin. The difference is that in the photovoltaic effect the photo-electron (photon-excited-electron) does not escape the material, it remains, energized to the photo-voltage, and is potentially conducted away [3, 8, 9]. Figure 2.1 shows the photoelectric and photovoltaic effects schematically using energy band diagrams. For the photoelectric effect, Figure 2.1a, the electron's excited energy is greater than the work function and the electron exits the material. For the photovoltaic effect, Figure 2.1b and c, the electron's excited energy is less than the work function and the electron stays in the material. In a conductor, Figure 2.1b, the overlapping valence and conduction bands lead to photo-electrons and holes which quickly thermalize and recombine. The charges are not separated and no net

current is produced. In a semiconductor, Figure 2.1c, this may not be the case. After generation (Figure 2.1c-i), recombination may occur, but because of a non-zero bandgap energy, this recombination occurs more slowly, via radiative and other means (Figure 2.1c-ii and detailed in Figure 2.3). Near the space charge region of a pn-junction, the photo-electron and hole may be separated and eventually collected (Figure 2.1c-iii).

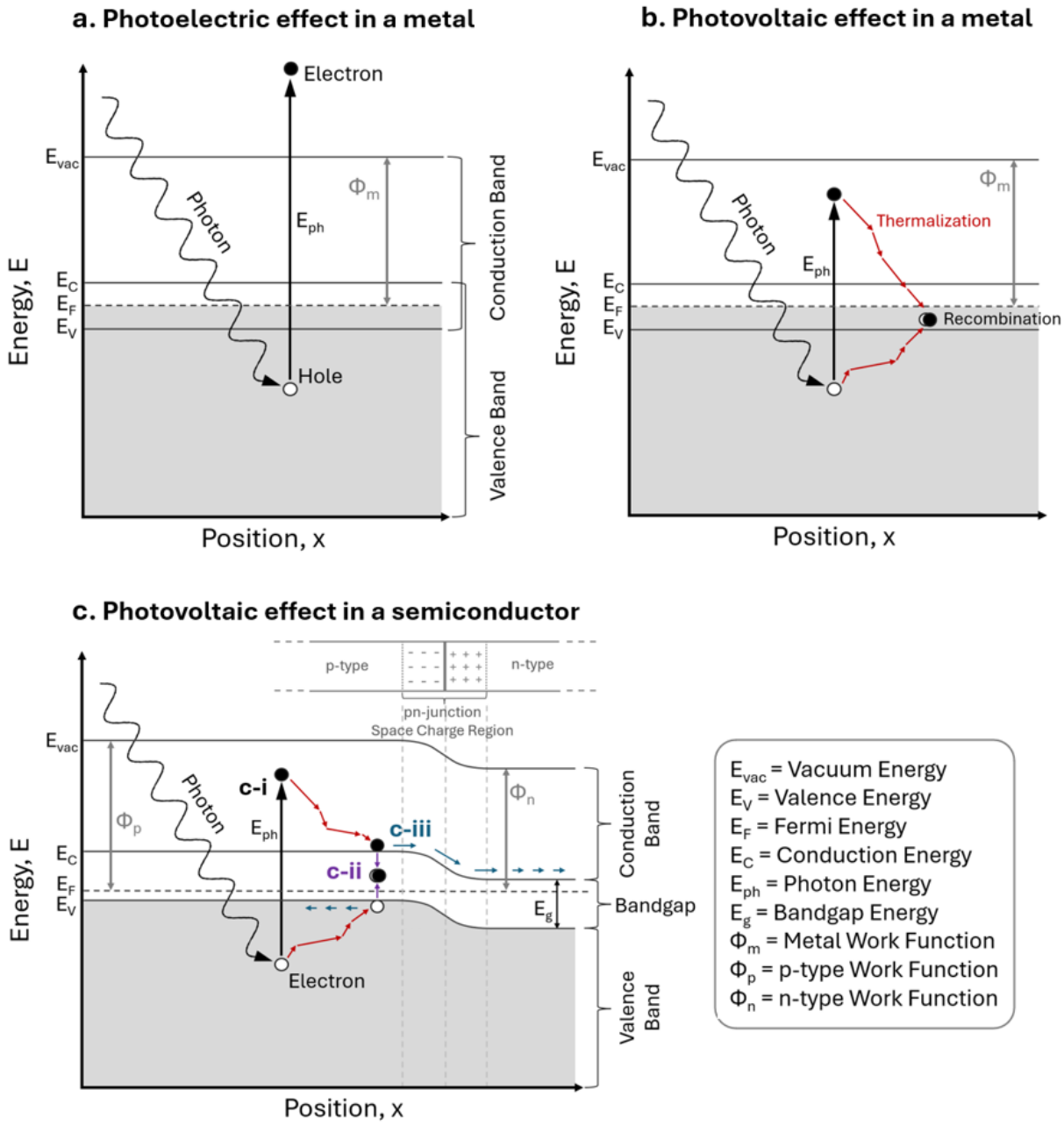

Figure 2.1: Illustrative energy band diagrams depicting the photoelectric and photovoltaic effects. In a, the photoelectric effect in a metal. In b, the photovoltaic effect in a metal. In c, the photovoltaic effect in a semiconductor. An excited electron-hole pair is generated (c-i) and may either recombine, falling back to its valence band (c-ii) or be separated by a nearby pn-junction and extracted as current (c-iii).

2.1.2 The pn-junction and semiconductor photovoltaics; Power out of light

The ability to extract power from an electrical circuit component requires a voltage and current which oppose one another (the product of the voltage and current needs to be negative). The conditions around a semiconductor pn-junction are perfect for achieving this. Figure 2.2 shows the current density-voltage (JV) curves, band-diagrams, and space charge regions of pn-junctions with and without illumination.

First considered is the pn-junction diode in the dark as shown in Figure 2.2a and b. In a, the pn-junction current-voltage characteristic across a wide voltage and current range is given. Each section of the curve is described, and the diversified utility of the pn-junction in modern society is exemplified as applications are also listed. The pn-junction dark JV characteristic is described by the diode equation [8, 9];

$$J_{dark} = J_{sat}(e^{\frac{qV}{nkT}} - 1), \tag{2.1}$$

where J_{sat} is the dark saturation current density, n is the ideality factor, q is charge (plus/minus one elementary charge for electrons and holes), k is Boltzmann's constant, and T is the temperature. The ideality factor captures the presence of recombination within the space charge region beyond the radiative baseline, if this is present n increases from its ideal value of 1 up towards 2. In Figure 2.2b, I consider the band-diagram and space charge region of the pn-junction at equilibrium. The figure shows how the built-in voltage is obtained from the different work functions of the two sides of the pn-junction.

Figure 2.2c and d show the photovoltaic effect of a pn-junction under illumination. In d, it can be seen that the valence band electrons absorb light with energy greater than the bandgap and move into the conduction band leaving behind a hole. If these charge carriers are generated within, or diffuse into, the space charge region they will be swept (at drift velocity) to the side of the region that their charge dictates. They will be separated. Furthermore, as the figure shows, the polarity of the pn-junction's built-in field is that of the minority charge carriers. A negative current (in our paradigm of Figure 2.2 and Equation 2.1) is the result.

Figure 2.2c shows a zoom of the zero region of a, including JV curves for pn-junctions under different levels of illumination. The negative photo-current is evident as a downward shift from the dark JV trend. Measured at 0 V applied, this shift is quantified by the short circuit current, J_{sc} (Section 2.1.4 details how J_{sc} can be determined). Comparing the curves, the quantum paradigm is evident; the brighter the light (number of photons) the higher the J_{sc} (number of electrons). The JV character becomes:

$$J = J_{dark} - J_{sc} = J_{sat}(e^{\frac{qV}{nkT}} - 1) - J_{sc}, \tag{2.2}$$

A careful eye shows that increased illumination also leads to a small increase in the open-circuit voltage, V_{oc}, the point where the forward bias balances the photo-generated currents. This is a logarithmic increase originating in the expansion of the space charge region under illumination [71]. This increase is accounted for in the diode equation as a rearrangement of Equation 2.2 for V_{oc} shows:

$$V_{oc} = \frac{kT}{q} ln \left\{ \frac{J_{sc}}{J_{sat}} + 1 \right\}, \tag{2.3}$$

Figure 2.2e and f highlight the maximum power producing point for one of the illumination curves from c. In e, the addition of the power density-voltage curve ($P = JV$) shows that operation in this quadrant of the pn-junction JV characteristic always leads to power production (as expected). The power density-voltage curve clearly indicates the maximum power point (MPP). The current, voltage, and power density at this point are indicated (J_{MPP}, V_{MPP}, P_{MPP}) in e. Also indicated is the fill factor, a measure of how square the JV curve is, it is given by the rectangular area defined by the dashed lines and can be calculated as the ratio of $J_{mpp}V_{mpp}$ and $J_{sc}V_{oc}$. Power conversion efficiency, often denoted η, is calculated as:

$$\eta = \frac{P_{MPP}}{P_{inc}}, \tag{2.4}$$

where P_{inc} is the power density in the incident light.

In Figure 2.2f, the band-diagram at maximum power point shows that the applied voltage has sizeably reduced the space charge region. Yet, the built-in field remains strong enough to block majority carrier currents and to separate the photon-excited minority charge carriers (as Figure 2.2e shows). Once the minority carriers drift across the space charge region they become majority carriers in the other side of the junction, they are collected at the electrodes as current and power generated.

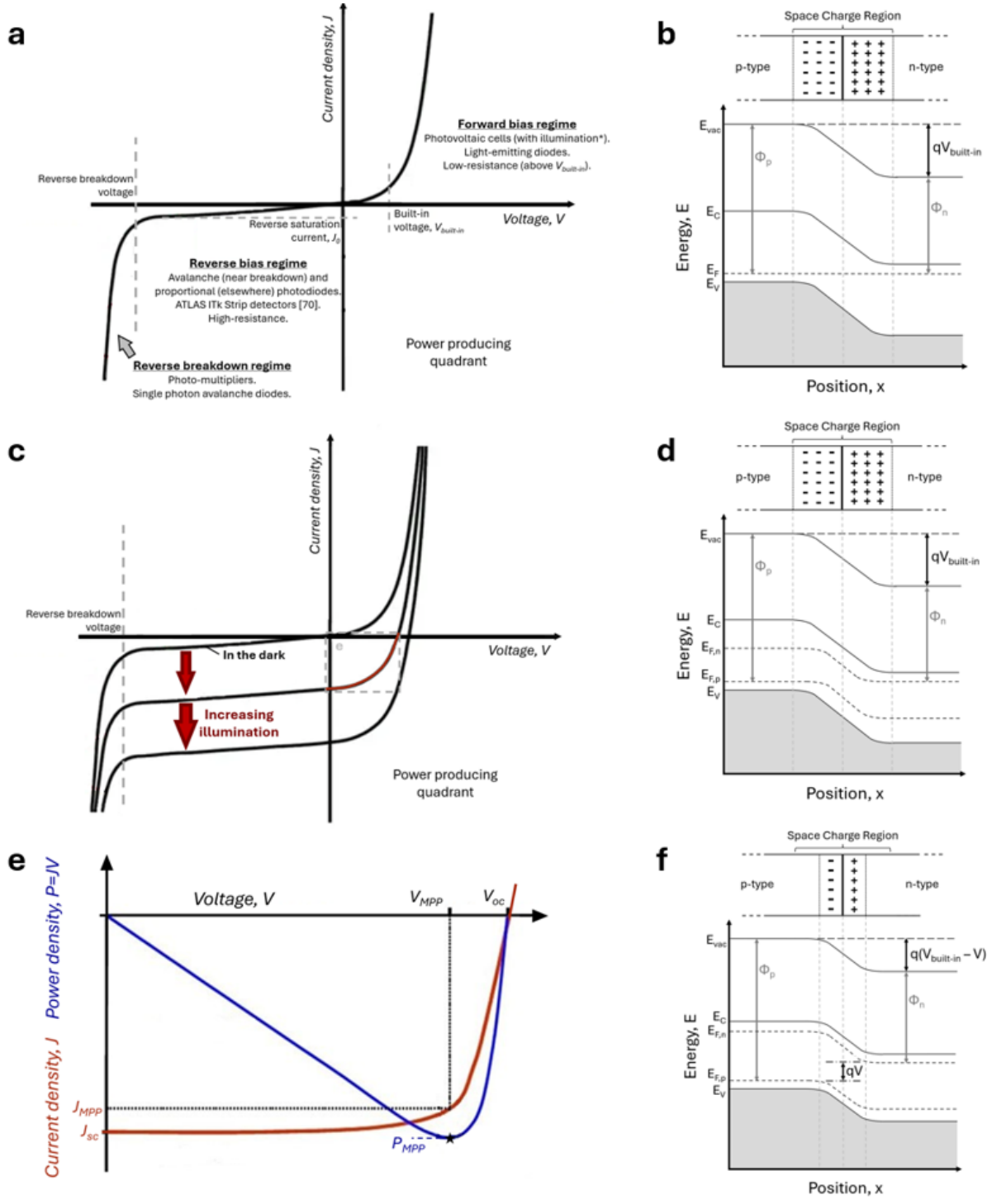

Figure 2.2: Current density - voltage, band diagram, and space charge region character of a pn-junction under various conditions. As described in the text.

Realistic accounting in the diode equation representation of the pn-junction current must account for the presence of two parasitic electrical effects in the junction. First, series resistance, R_{ser}, within the resistivity of the semiconductor itself or other portions of the circuit. R_{ser} is in series with the junction. It scales as J^2V and thus affect the highest performing regions of the power-producing JV quadrant the most, R_{ser} lowers both V_{MPP} and J_{MPP}. Second, an electrical shunt, where significant current flows through an alternate low resistance pathway to the pn-junction (like an extended crystal defect). The resistance of alternate shunt pathways is denoted R_{sh}, it is in parallel with the junction diode. The non-ideal diode representation of the single pn-junction current becomes:

$$J = J_{dark} - J_{sc} = J_{sat}(e^{\frac{q(V-JAR_{ser})}{nkT}} - 1) + \frac{V - JAR_{ser}}{R_{sh}} - J_{sc}, \tag{2.5}$$

where A is the active area of the PV device.

2.1.3 Photon and charge carrier physics

Energy arrives as photons with a given wavelength spectrum, it is absorbed by (electrons in) the semiconductor, and generates charge carrier pairs via the photovoltaic effect. These carriers move, diffusing and drifting within the junction, they may recombine or be extracted. In this section, I explore the basics of these phenomena a little deeper. Absorption is covered first, then generation and recombination mechanisms, and finally, the movement of charge carriers in the semiconductor.

Optical absorption

Optical absorption in a semiconductor obeys the empirical Beer-Lambert attenuation law [3, 8, 9, 71, 72]:

$$I(\lambda, t) = I_0(\lambda)e^{-\alpha(\lambda)t},$$

This law stipulates that the intensity of a light beam, I, after traveling through a thickness, t, of material with a known absorption coefficient, α, will have decreased exponentially from its initial intensity, I_0. The Beer-Lambert law holds across the entire wavelength (λ) spectrum of the light source although, naturally, the material's ability to absorb photons varies with wavelength ($\alpha = \alpha(\lambda)$, units of inverse distance). Absorption coefficient profiles are obtained experimentally since $\alpha(\lambda)$ varies with a number of factors, such as the material, doping concentrations, and defect concentrations [8, 9]. Ellipsometry measurements are typically employed to measure the complex refractive index of the material. Absorption coefficients of O(10^4-10^5 cm^{-1}) are

typical within a few tens of nanometers of the bandgap energy for direct bandgap materials. For indirect bandgap materials (where the highest and lowest edges of the valence and conduction band, respectively, do not align in crystal momentum space and thus the lowest photon energy excitations require an additional momentum exchange with the lattice (phonon interaction)) this value drops to O(10^1 cm^{-1} or less) [77].

A semiconductor's optical properties can be described by its complex refractive index, $\tilde{n}$:

$$\tilde{n}(\lambda) = n(\lambda) \pm i\kappa(\lambda), \tag{2.6}$$

where n and κ are the real and imaginary parts of $\tilde{n}$, respectively. The imaginary component, κ, relates directly to α:

$$\alpha(\lambda) = \frac{4\pi\kappa(\lambda)}{\lambda}, \tag{2.7}$$

The real component, n, dictates the speed of light in the semiconductor and is used in Snell's Law to determine reflection and transmission at material interfaces.

Generation and recombination

Absorption is generation. In the ideal case (no defects), this idea holds throughout the bulk of the semiconductor. The Beer-Lambert law is the statistical representation of a large number of quantum photovoltaic generation events, as have been described in the previous sections. This photo-generation mechanism is reproduced in Figure 2.3a. Light with energy greater than the bandgap is absorbed by an electron in the valence band (note: band-edge effects aside, light with energy less than the bandgap cannot be absorbed unless there are trap states, $\alpha(\lambda)$ is zero for these wavelengths). It is excited to the conduction band, leaving behind a hole (positively charged quasi-particle, an absence of an electron in the crystal lattice, which can move and behaves somewhat similarly to an oppositely charged electron). The excess photonic energy is then lost by the charge carriers to quantized vibrational excitations of the crystal lattice (phonons) in a process called thermalization. Thermalization occurs on timescales (O($<$1 ps)) shorter than that of collection or recombination (O($>$1 ns)) [8,9] (unless you introduce novelties to help extract these "hot carriers" [8]). Energetically the carriers thermalize to their respective band edge where they move (as discussed in the next subsection) or recombine (discussed below).

Charge carrier recombination is the loss of an excited electron and hole pair. The promoted electron returns to moving within the lattice valence band and the excitation energy is emitted in one form or another. Recombination may occur via a variety of mechanisms when an electron and hole are in physical proximity to each other, some common mechanisms are shown in

Figure 2.3b-e. Note that any proximate excited electrons and holes may recombine, i.e. pairs which are separated may recombine with other carriers they come into interaction with as they traverse the device.

Figure 2.3b depicts the fundamental, inescapable process of radiative recombination. It is the transition of an electron from the conduction band to recombine with a hole in the valence band, with the difference in energy emitted as a photon. This recombination mechanism is unavoidable since this emission process is the quantum mechanical equivalent to absorption generation. The emitted photon may escape the junction and is lost, or it may be reabsorbed in the junction, to produce another charge carrier pair, a process called photon recycling.

Figure 2.3c shows trap-assisted, or Shockley-Read-Hall, recombination. In this mechanism, either a hole or an electron fall into a trap state, is rendered temporarily localized and at lower energy with respect to it's valence band, the opposite carrier comes into interaction with the trapped carrier, and they recombine. These trap states are physically localized energetic levels located within the bandgap. They are associated with defects and impurities (including dopants) in the crystal lattice. The excess energy in trap-assisted recombination is lost to heat in the lattice as the carriers thermalize into the trap states.

Figure 2.3d indicates the Auger process. In this recombination mechanism, the excess energy from direct (as shown) or trap-assisted recombination is transferred to a third carrier. This may be an electron (as shown) or a valence band hole. This carrier will then thermalize back to the bandgap edge, expending the excess energy as heat in the crystal (phonon excitation).

Bulk recombination processes are quantified by their average timescale, the carrier recombination lifetime. The effective recombination lifetime, τ, can be obtained from the lifetimes of each recombination process X, τ_X. Since the processes are occurring in parallel, an inverse sum is used:

$$\frac{1}{\tau} = \frac{1}{\tau_{radiative}} + \frac{1}{\tau_{trap-assisted}} + \frac{1}{\tau_{Auger}}, \tag{2.8}$$

At the crystal termination, either outer surfaces or interfaces with other layers and materials, there is a breakdown in the crystal order which typically leads to a large number of trap states within the bandgap. This is shown in Figure 2.3e. The trap states are often associated with dangling bonds, highly reactive unpaired electrons in the broken lattice. The high trap concentration leads to an increased recombination rate at the surface compared to the bulk. This increased recombination depletes the area of minority charge carriers and leads to a diffusion-mitigated influx of carriers from the bulk towards the surface. Surface recombination is quantified by the speed of this influx; the surface recombination velocity. Larger surface recombination velocities imply greater concentration gradients and higher surface recombination

rates. Surface passivation is the chemical treatment of these surfaces to reduce the number of dangling bonds.

Recombination affects the PV device's reverse saturation current, J_{sat}. J_{sat} is reduced when there are shorter recombination lifetimes and larger surface recombination velocities. This ultimately reduces the efficiency of the device by reducing the negative current which flows through the diode (see Equation 2.5). Recombination does this by reducing the diffusion length of carriers in the device materials (the average distance a carrier will diffuse before recombination). For reasonable performance, PV devices must employ materials with good enough quality to increase the diffusion lengths up to and beyond the layer thicknesses required for sufficient photon absorption.

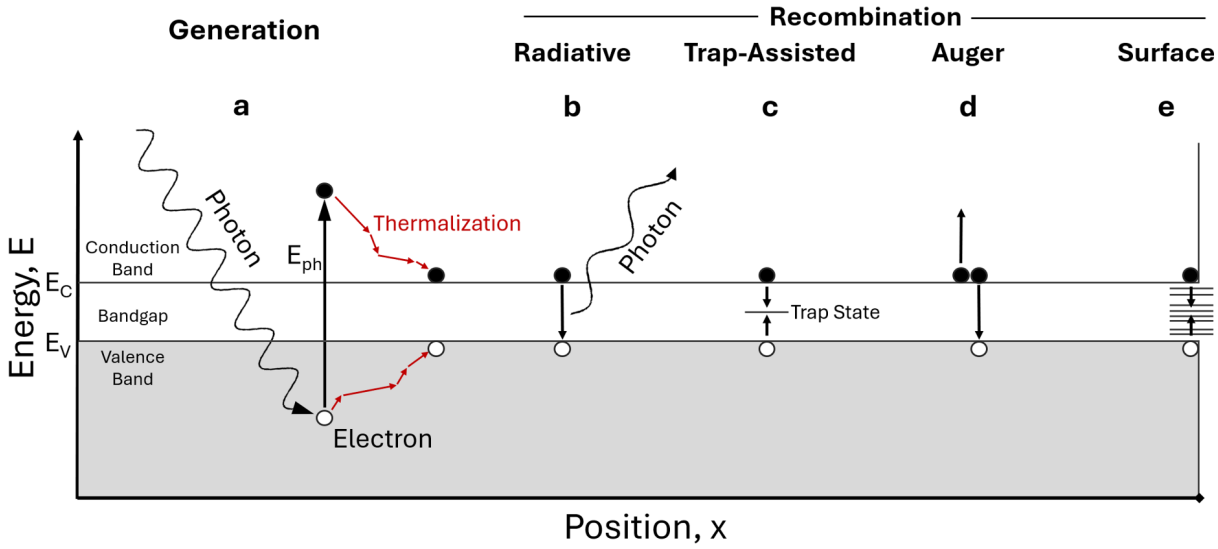

Figure 2.3: Generation and recombination mechanisms in semiconductors. This figure is a detailed expansion of Figure 2.1c-i and c-ii. In a, excited electron-hole pair generation and thermalization to the band-edges. In b, radiative recombination. When the photon emitted through radiative recombination is reabsorbed in the junction it is called photon recycling. In c, trap-assisted, also called Shockley-Read-Hall, recombination. In d, an example of Auger recombination. In e, recombination through traps states at the crystal surface.

Carrier movement

Movement of electrons and holes within the semiconductor has two contributions; drift and diffusion. Drift indicates movement under the influence of an electric field. It is predominant in

the space charge region of the pn-junction (while the junction operates in the power producing quadrant of the pn-junction JV curve this is the only location in the pn-junction with an appreciable electric field). Diffusion indicates movement under the population gradient of carriers in the device. It dominates outside the space charge region. Both currents are active for each type of charge carrier throughout the device and sum to the device's majority and minority carrier currents. Naturally, charge is conserved in these processes. The continuity equations make this accounting, tracking changes in the populations of each type of charge carrier over time [8, 9, 72, 73]. Similarly, the self-consistency of the electric field under the moving charge populations is defined by Poisson's equation which relates the density of charge carriers to the electric field [8, 9, 72, 73].

2.1.4 The light resource and photovoltaic device types

Power can be extracted from light. In this thesis I study two different light resources; solar and laser. The type of light determines the application, material(s), and type of photovoltaic device. The PV device types for solar and laser light are solar cells and photonic power converters (PPCs), respectively. While impingent light wavelengths may be vastly different (see Figure 2.6a and Figure 2.8a) the operational paradigm of solar cells and PPCs is the same; extract usable power from the light by leveraging the photovoltaic effect. For PPCs, there is an additional operational potential as a data receiver as the intensity of the laser signal may be modulated. In this section I give a brief introduction of solar and laser spectra and the consequences that each class of illumination brings for solar cell and PPC operation. In the final two subsections, I discuss: (1) the basic PV device architecture and (2) how device J_{sc} can be estimated from spectral knowledge and device characterization. The content of these two subsections applies to both solar cells and PPCs.

The solar spectrum and solar cells

Figure 2.4 shows several standard solar irradiance spectra. Due to the application spaces studied in this thesis (see Section 2.3.1), the main spectrum I consider is AM1.5 Direct, or AM1.5D. AM1.5 stands for air mass 1.5. Air mass measures the ratio of atmospheric path length for light incident at a given angle to the path length at solar noon (sun directly overhead, zenith angle of 0°). AM1.5 is a common standard indicating the sun at a zenith angle of ∼45° [78]. The direct (D) spectrum includes light which is emitted from the solar corona directly onto the PV device. The global (G) spectrum includes this contribution and a diffuse component including light which has interacted with the environment before falling on the PV cell. Also

shown in Figure 2.4, is the solar spectrum at the outer surface of Earth's atmosphere, AM0. It is observably black-body like. Differences between the terrestrial and extraterrestrial (AM0) spectra are due to absorption bands of different molecular constituents of the atmosphere (low energies <2 eV) and other phenomena such as Rayleigh scattering (high energy) [8]. Importantly, for solar applications, daily and seasonal variability and intermittency of the solar resource must be considered. The AM1.5 spectrum offers only a momentary average of this variety which is affected by such factors as install location, regional geography, system type, weather, and soiling.

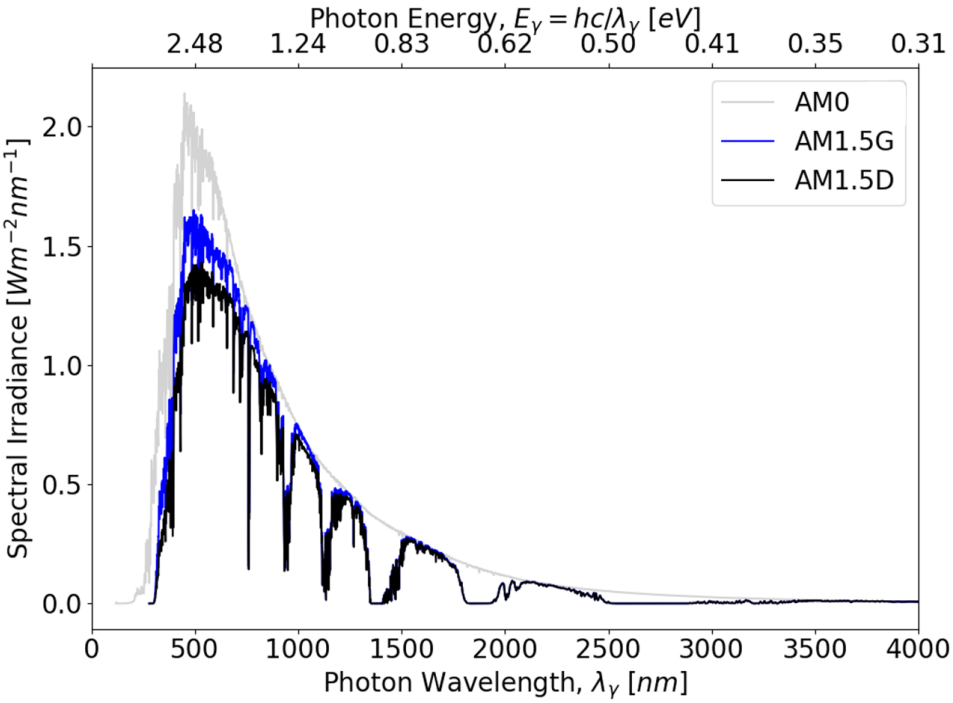

Figure 2.4: The most common standard solar spectra. Produced from the data provided at [78].

Figure 2.5 reproduces the AM1.5G solar spectrum from Figure 2.4 and aligns it with a plot of lattice constant versus bandgap energy for common semiconductors. This figure indicates the trade-offs between thermalization, absorption losses, and availability implicit in the choice of material which will be used for a solar cell absorber (it also prepares us for future discussion of multi-junction solar cells, as in Figure 2.8). In Figure 2.5b, points give group IV monotonic and III-V binary crystals, lines give ternary alloys between the two III-V end points, or binary alloys of group IV elements.

The industry standard, silicon, is highlighted in Figure 2.5. For single-junction solar cells, the application space is dominated by large-scale solar energy production. In this space the primary metric driving performance is power per dollar. Silicon leverages availability, its history, and its kin-ship with the information technology industry and has been the most economic solar cell material for several decades. Silicon has a bandgap of ∼1.12 eV (photon wavelength; ∼1107 nm) [77]. This is quite near to the optimal bandgap value to balance thermalization and absorption losses for the AM1.5G solar condition. However, unfortunately, silicon's bandgap is indirect lowering its absorption capability. In this thesis, my focus on multi-junction PV devices moves the discussion away from silicon. I offer no focused discussion of thin film (CIGS, CdTe), organic, perovskite, or silicon solar cells beyond this paragraph.

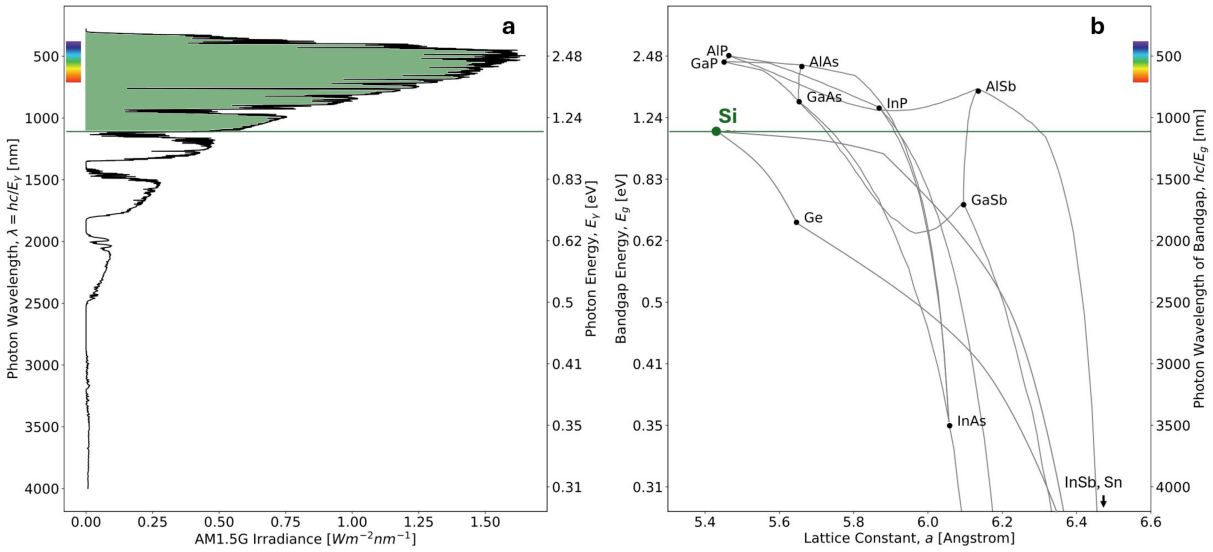

Figure 2.5: The solar resource and silicon. In a, the AM1.5G standard solar spectrum. In b, common semiconductor materials plotted as a function of crystal lattice constant and bandgap energy. Silicon, the common commercial single-junction solar cell material, is highlighted. This figure compares to Figure 2.6, the laser resource and PPCs, and to Figure 2.8, multi-junction solar cells. Figures are produced using data from [78] for a and [79] for b.

Laser transmission and photonic power converters

Figure 2.6 offers the corollary of Figure 2.5 for a laser resource. It can be immediately seen that the shape and power levels for the laser spectrum are very different from solar. Here, I show the irradiance spectrum for a 1550 nm fiber-coupled laser from QPC Lasers (the QPC Lasers 6015-A007 [80]) operating at a drive current of ∼35 A (∼11 W output). This spectrum was measured

at the University of Ottawa SUNLAB using an ASD FieldSpec3 spectrometer [81], switching between the multiple detectors employed by this spectrometer is visible in the background level changes at 1000 nm and 1800 nm in Figure 2.6a.

The optimal material choice for the PPC PV device is one which balances thermalization losses and absorption losses. The material is matched to the wavelength of the laser in operation. Laser wavelength is typically chosen by application and by laser availability. Laser signals can be transmitted through fiber optic or free space. In both cases, one encounters problems such as signal attenuation and wavefront scattering. Modality specific challenges such as atmospheric turbulence, beam divergence (free space), and power limitations (fiber optic) also exist. PPC application spaces are investigated further in Subsection 2.3.2.

Figure 2.6 shows that a potential PPC material choice for a system operating at 1550 nm is the quaternary semiconductor indium gallium arsenide phosphide (InGaAsP) lattice matched to indium phosphide (InP-LM). This is the PPC system I study in Section 5.3. PPC operation must account for potential shifts in the spectrum of the laser. The bandwidth of the laser in Figure 2.6 is $\sim$30 nm with a central wavelength of $\sim$1535 nm at the measured operating conditions. These values may change by $\sim$10 nm or more if the temperature of the laser is not managed. Typical sensitivity of the central lasing wavelength to temperature variations are on the order of 0.1 nm/$^{\circ}$C [82]. As the laser heats up the central wavelength shifts to longer values due to a decrease in bandgap energy and the bandwidth increases [71, 82].

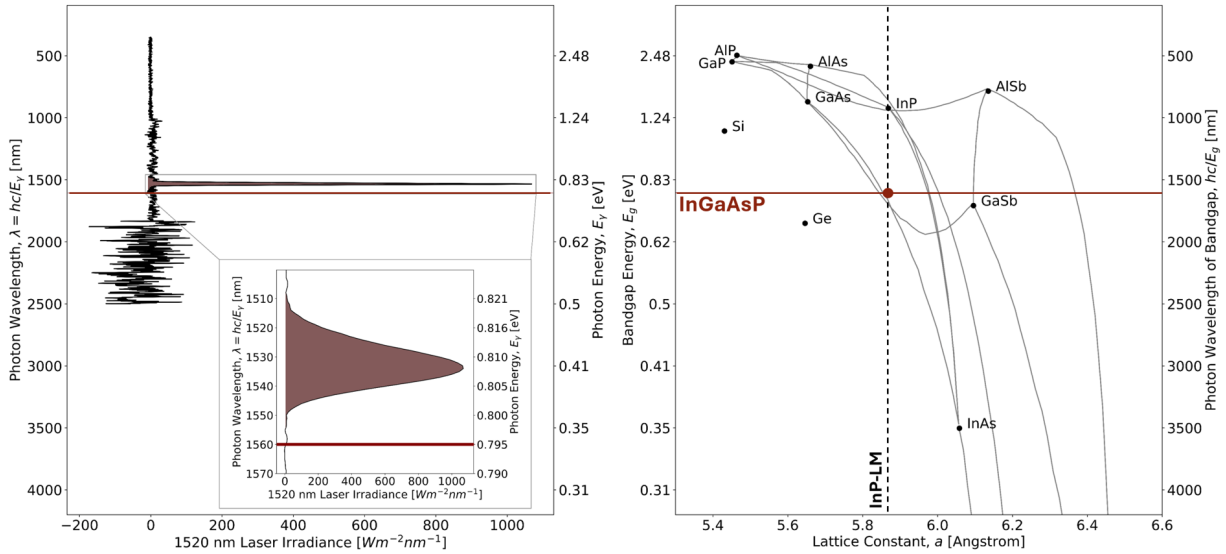

Figure 2.6: A laser resource and a suitable PPC material. In a, the spectrum of the 1550 nm QPC Lasers 6015-A007 laser. In b, common semiconductor materials plotted as a function of crystal lattice constant and bandgap energy. InP-LM InGaAsP is highlighted. With a bandgap of 0.795 eV / 1560 nm, it is chosen as a match to a 1535 nm laser wavelength. This figure compares to Figure 2.5, the solar resource and silicon, and to Figure 2.8, multi-junction solar cells. Figures are produced using data measured experimentally in the SUNLAB using an ASD FieldSpec3 spectrometer for a (courtesy of Dr. Paige Wilson) and from [79] for b.

Single-junction device architecture

Semiconductor PV devices, whether solar cell or PPC, have the same basic structure, shown in Figure 2.7. The main component is the pn-junction, as already discussed. This junction may be of any architecture; homojunction, heterojunction, pn, p-i-n, active substrate, etc., as long as it can achieve the required charge carrier separation. In Figure 2.7 a homojunction is shown. The absorbing junction is sandwiched between front and back surface field layers. By bending the valence and conduction bands upward near the contacts (Figure 2.7b) these higher doped, higher bandgap, passivating cladding layers use electric fields to block the minority carriers from approaching interfaces where surface recombination is large and thereby increase device performance. At the top (the light-exposed side) the front surface field layer is also designed to help lateral conduction to the top-side contacts which are usually arranged as a grid of fingers (see Figure 3.1). In between the grid fingers is applied one or more thin film dielectric layers. Called anti-reflection coatings (ARCs) these layers have refractive indices which are

intermediate to air (or glass, whichever is at the outer surface) and help to couple the incident light into the PV device using Snell's law. One and two layer ARCs are common, with recent trends including patterned (non-planar) ARC layers to increase the path length of light in the device (light trapping) [83–85].

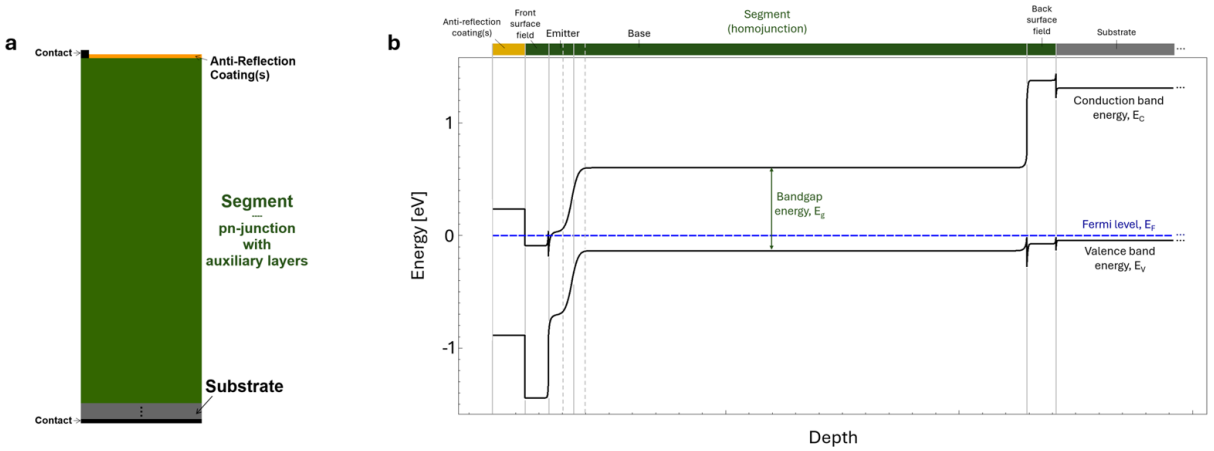

Figure 2.7: Basic single segment PV device architecture. In a, a simple cross-sectional schematic of a single segment device. The segment includes the pn-junction and the front and back surface field auxiliary layers. Not to scale. In b, the band diagram of the single segment device at equilibrium. The shown device employs a homojunction segment. The different layers of the device are labeled. Compares to Figure 2.9, the MJ solar cell schematic and band diagram.

Quantum efficiency and device photocurrent

Quantum efficiency is a measure of the current response of a PV device as a function of illumination wavelength. Specifically, it is the fraction of incoming photons, of a given wavelength, which produce charge carrier pairs collected as current [8,9]. Quantum efficiency measurements use a tunable small-bandwidth/monochromatic light beam incident on a PV device to run a wavelength survey. Input power and device current are carefully monitored. The external quantum efficiency (EQE) is then calculated as the current produced in electrons divided by the input power in photons. The "external" modifier indicates that EQE considers photons external to the device. EQE includes and is lowered by photons which are reflected or transmitted through the device without absorption. Contrastingly, internal quantum efficiency (IQE), quantifies how many carriers are collected for photons which are absorbed in the device. Calculated from the

EQE, it handles reflection, R, and transmission, T, measurements accordingly:

$$IQE(\lambda) = \frac{EQE(\lambda)}{1 - R(\lambda) - T(\lambda)} \tag{2.9}$$

Measurements of the external quantum efficiency can be combined with knowledge of the input photonic spectrum to determine the device photo-current. The device short circuit current (see Subsection 2.1.2), J_{sc}, is calculated by integrating the product of the EQE and the incident photon flux, $\Phi_{ph,inc}$, over all wavelengths, to give the total number of carriers collected as current and then multiplying this number by the carrier's charge, q:

$$J_{sc} = q \int_0^\infty EQE(\lambda)\Phi_{ph,inc}(\lambda)d\lambda \tag{2.10}$$

Quantum efficiency profiles contain a wealth of device and material quality information beyond short circuit current. For instance, they are often used to identify loss mechanisms present in the device (see Figure 3.2 and Figure 3 from Section 3.2), the peak response and bandgap of a material [8, 9, 86, 87], or to determine the current-matching point for a multi-junction device [6, 88]. More information on quantum efficiency measurements for MJ solar cells is provided in Section 2.2.3.

2.2 Multi-junction photovoltaics; More junctions, more power

This section explores the benefits and challenges of increasing the number of absorbing junctions in a PV device. First, the realization of the MJ architecture is explicated. Second, I discuss several mechanisms which are unique to the MJ device operation. Then, I distinguish how introducing more absorbing junctions differs for solar applications compared to laser applications. I introduce MJ solar cells and MJ PPCs. Their applications follow in Section 2.3.

2.2.1 MJ device architecture

The first multi-junction device challenge is including new junctions in the device. The issue is electrical polarity; how can two pn-junctions be connected in series without formation of an oppositely polarized negating np-junction? In some architectures this is achieved by maintaining electrical or physical separation between the junctions and then connecting them in series

external to the semiconductor stack (so-called >2-terminal and/or horizontally interconnected device designs [37, 89, 90]). In this thesis, the focus is on the vertically-stacked, monolithic device architecture, seen in Figure 1.1 and Figure 2.9. Any reference to a MJ PV device, MJ solar cell, or MJ PPC outside this paragraph refers to a vertically-stacked, monolithic device.

The 2-terminal, single crystal vertically-stacked approach uses tunnel diodes: very thin and highly doped pn-junctions, placed between and at opposite polarity to the absorbing junctions. The strong band bending in these layers allows carriers to non-locally tunnel between the upper pn-junction conduction band and the lower pn-junction valence band (as seen in Figure 2.9b). MJ PV tunnel diodes must be low resistance since they are opposing the output power. They must also have low parasitic absorption (i.e. be transparent at the wavelengths of operation). The MJ PV device will contain one less tunnel diode than the number of absorbing junctions since tunnel diodes are needed between each absorbing junction. The absorbing pn-junctions each have front and back surface field layers as described for the single-junction, the tunnel diodes do not. This repeating tunnel-diode-separated absorber stack has the same top and bottom "finishing" layers as the single-junction case (a lateral conduction layer, contacts, ARCs).

2.2.2 Operation of MJ PV devices

The series-connected nature of the segments dictates a good portion of the MJ PV operation and design. A chief challenge introduced is current match. A chief boon is the current to voltage power shift. Much work in this thesis aims to overcome the former and/or leverage the latter. In this section I outline these two consequences of MJ operation and briefly discuss luminescent coupling, the MJ extension of photon recycling.

Current matching

Kirchoff's current law states that current out of a point on a circuit must equal current in [91]. In a series connection the electrical current of the full MJ stack will be limited to the absorbing junction with the smallest current. For optimal performance all segments must produce the same current. They must be "current matched". When segment currents are mismatched, the excess carriers cannot be extracted from the junction, they will recombine on the timescale of the recombination lifetimes (Section 2.1.3), and, while some may be redistributed (see luminescent coupling, in Section 2.2.2 below), many will be lost, leading to lower power conversion efficiencies. To achieve the best possible performance MJ PV designers must take careful consideration of the input spectrum(s) and absorption qualities of the material(s) they will use to plan the thicknesses of the absorbing junctions.

Power shift; current for voltage

Kirchoff's voltage law states that voltages in series stack or add to one another (and that the sum in a closed loop is zero) [91]. In a MJ PV device the voltage output is found by summing the voltage of all junctions. This allows output voltages which far exceed the single-junction capability (by roughly the segment multiplicity). This voltage boost is coupled with a lower current since light absorption is shared across the junctions (approximately evenly, to attain current match) and entails a power shift from high currents and low voltages to low currents and high voltages. This effect is seen, for example, in Figure 4.2. It is central to the research of Section 4.4 and Chapter 5. As the segment multiplicity increases, the JV curve gets progressively shorter (lower current) and wider (higher voltage). The MJ power shift reduces system series resistance losses (as in Section 4.4) and boosts output voltages (as in Chapter 5). In state-of-the-art PPC devices, efficiency is nearly maintained through this shift [7]. In MJ solar cells, efficiency is increased as the number of junctions increases since it leads to more efficient collection of a greater portion of the solar spectrum (see Subsection 2.2.3).

Luminescent coupling

More absorbing junctions increases the possibility of radiative recombination reabsorption. Luminescent coupling (LC) is the multi-junction generalization of photon recycling (Section 2.1.3) [46, 51, 74, 92–99]. It is the reabsorption of photons emitted via radiative recombination in general and includes events where the recombination/emission and reabsorption are in different segments. Photon recycling, on the other hand, only describes when emission and reabsorption take place in the same segment. While photon recycling helps boost open-circuit voltages in single- and multi-junction PV devices, LC can further help raise the current in MJ PV by redistributing current-mismatch. This is a boon to MJ PV devices since a reasonably current-matched design requires non-trivially accurate and precise device modeling and manufacturing to obtain. And, since current-match operation is impossible to maintain with device heating and the ubiquitous unavoidable changes in irradiance spectra changing the current distribution (input solar spectra vary widely due to a large number factors including daily and seasonal variation in the solar resource, cloud cover, and soiling, input laser spectra vary significantly with the laser temperature). LC's redistribution of current-mismatch greatly increases MJ PV device robustness and reduces device heating by effectively reducing the total recombination. Naturally, LC effects are more significant in devices with high-quality materials, devices where radiative recombination makes up a large proportion of the recombination events (high internal radiative efficiency). Modeling LC is an area of active research, hampered by the complicated non-local balancing nature of the phenomena. LC is included in the MJ PPCs model explored

in Chapter 5 using the iterative model of Wilkins *et al.* [92].

2.2.3 MJ solar cells

In solar cells, the multi-junction approach has been to include junctions with different bandgaps to collect more of the spectrum, reduce thermalization losses, and increase device efficiency [6,8, 9,88]. A comparative look at Figure 2.5 and Figure 2.8 indicates this drawback of single-junction solar cells. As mentioned, silicon, the material indicated in Figure 2.5, is near the optimal single material bandgap to balance AM1.5G absorption and thermalization losses. Yet, the spectral figure indicates sizable transmission and thermalization losses for a great portion of the incoming energy (the spectral peak is at ∼2.5 eV, silicon's bandgap is 1.1 eV). Figure 2.8 illustrates the multi-junction solution. In this figure, the solar spectrum is now divided amongst three absorbing junctions, indicated by the three coloured areas. A larger portion of the spectrum is collected, thermalization losses have been greatly reduced, and potential maximum efficiency increases. Record one-sun efficiencies for one and three junction solar cells are 27.6% for a silicon heterojunction 1J (2024), 29.1% for a gallium arsenide (GaAs) 1J (2019), 37.9% for an InGaP/InGaAs/Ge 3J (2003), and 39.5% for an InGaP/InGaAs/InGaAs 3J with InGaP quantum wells in the second junction (max 3J one-sun efficiency, 2022) [4]. As Figure 2.9a and b indicate the junctions in an MJ solar cell are arranged with bandgap energies that decrease progressively from the top (light-side) to the bottom (substrate side) to split the absorption as indicated (Figure 2.8b and Figure 2.9b).

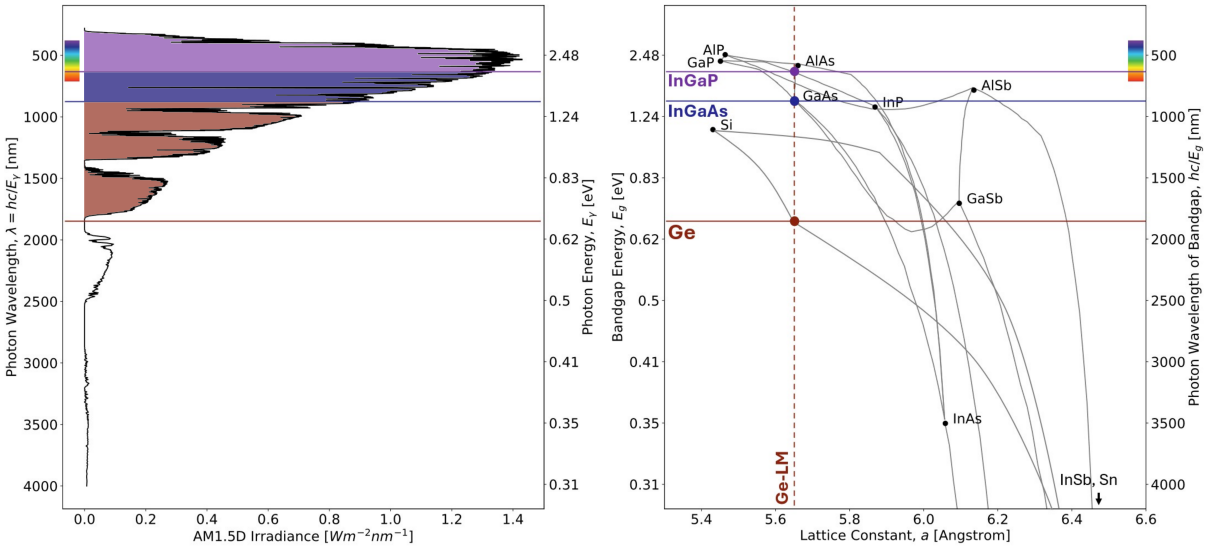

Figure 2.8: The solar resource and the InGaP/InGaAs/Ge multi-junction solar cell. In a, the AM1.5D standard solar spectrum. In b, common semiconductor materials plotted as a function of crystal lattice constant and bandgap energy. InGaP, InGaAs, and Ge, the materials for the top, middle, and bottom segments of a classical 3J solar cell are indicated. This figure compares to Figure 2.5, the solar resource and silicon, and Figure 2.6, the laser resource and PPCs. Figures are produced using data from [78] for a and [79] for b.

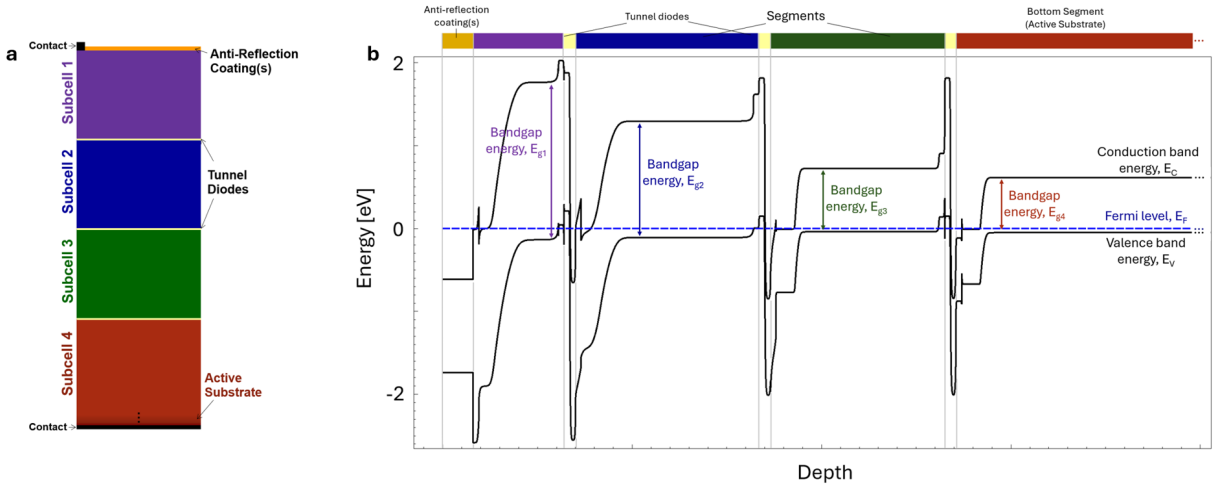

Figure 2.9: Classical unsegmented MJ solar cell device architecture. In a, a simple cross-sectional schematic of a four subcell device. This design employs an active substrate in the fourth junction, this is representative of the InGaP/InGaAs/SiGeSn/Ge material system. Each subcell segment includes the auxiliary surface field layers as in Figure 2.7. Schematic is not to scale. In b, the band diagram of the four segment device at equilibrium. As in the single-junction corollary, Figure 2.7, this device employs homojunction segments. Refer there for an example labeling of the front and back surface field layers and the pn-junction emitter and base. The progression of decreasing semiconductor bandgaps and the significant band bending of the tunnel diodes are clearly evident in b.

Design and lattice matching

Multi-junction solar cell design is a trade-off between the ideal bandgaps for the solar spectrum which the cell will experience and the actual realizable materials and their quality. As previously seen, Figure 2.8b maps the landscape for semiconductor materials. The single crystal nature of the MJ solar cell must be considered. This sets constraints on how different the size of the material lattices in the solar cell can be. The lattice constants for the materials must 'match' for a crystal with a low concentration of charge carrier removing defects (Section 2.1.3). In other words, they must be similar enough that a single crystal with multiple material layers will have minimal dislocations of atoms in the material lattices. Returning to Figure 2.8, this means designers may only choose materials which fall near a line of constant lattice constant. This restriction does not negate current matching (Section 2.2.2), which must be considered simultaneously.

The classical MJ solar cell design approach is to find high quality materials or material systems which could be leveraged for a MJ solar cell and then improve and/or extend

them [8–15, 26]. The historical industry standard high quality material system is the InGaP/InGaAs/Ge 3J design, as shown in Figure 2.8. This design employs bandgaps of 1.9 eV/1.4 eV/0.67 eV (indirect) in an epitaxial stack which is lattice matched to the active germanium substrate (Ge-LM). This design achieved great success because of its high material quality [14, 15] despite a significant overproduction of current in the germanium junction under an AM1.5D irradiance (at the detailed balance limit, see Subsection 2.4.1). Current matching can be achieved with an $\sim$ 1.0 eV third junction. However, as Figure 2.8b shows, to extend this industrially mature InGaP/InGaAs/Ge material system to include a lattice-matched, $\sim$1.0 eV bandgap third junction is not straight-forward and was long considered a holy grail for the MJ solar cell field [10, 11, 22, 34, 100–104]. In Chapter 3 of this thesis, I present research on silicon germanium tin (SiGeSn) a ternary group-IV alloy as a potential candidate for this task.

Advanced techniques exist which find novel approaches to overcoming the simultaneous lattice and current match restrictions in MJ solar cells. Two innovations on the epitaxial growth side are wafer-bonding [101, 105–108] and metamorphic buffers [101, 109–113]. Both processes find a way to connect crystals of different lattice into one monolithic structure with minimal defect generation. For wafer-bonding, the two crystals of different lattice are grown separately, with the top one grown inverted. The wafers are flattened, polished, and cleaned at the atomic level with fast argon bombardment. The clean crystals bond together naturally when brought together with sufficient force. For metamorphic buffers, a sequence of buffer layers are placed between the two portions of crystal with different lattice constant. These layers, typically of ternary or quaternary material, have a graded composition such that their lattice constants progressively shift from the one crystal's to the other's. This reduces dislocations in the lattice when sufficiently optimized. Record efficiencies (with concentration - see the previous section for one sun records) for wafer-bonded design and designs with metamorphic buffers are 47.6% (InGaP/AlGaAs/GaInAsP/InGaAs 4J, 665 suns, 2023) and 47.1% (6J, 143 suns, 2020), respectively, these are the highest solar to electrical power conversion efficiencies ever attained [4]. In Chapter 4 of this thesis, I discuss segmented MJ solar cells, another approach to decouple the lattice and current match restrictions of the MJ solar cell design space.

MJ solar cell quantum efficiency

Quantum efficiency experiments on multi-junction solar cell devices can be completed similar to single-junction quantum efficiency (Section 2.1.4) if it is the response of the full cell which is desired. Typically, however, designers would like to ascertain the response of each junction in the device separately. This requires a modification to the basic measurement due to the multiple absorbing materials in the MJ solar cell. Specifically, these experiments must use

"light biases" on the subcells which are not under study. The MJ solar cell is illuminated with a selection of small bandwidth sources with wavelength spectra which will excite carriers in each subcell alone. Each subcell is measured in turn with the light bias sources for the other subcells turned on. The light bias causes an over-production of current in all subcells but the one being surveyed, it becomes current-limiting and it's response to the monochromatic probe beam is what is measured by the quantum efficiency apparatus. For these experiments to work the light biases must be of the correct wavelengths to bias all subcells in turn without interfering with the probe and they must be strong enough to cause the current overproduction. Section 3.1 gives an example of a MJ solar cell quantum efficiency measurement collected during these doctoral studies.

2.2.4 MJ photonic power converters

For PPCs, the MJ approach is naturally quite different. The small photonic bandwidth of laser light means that one PV absorber material is ideal. It is not spectral matching but the MJ power shift (Section 2.2.2; high current, low voltage to low current, high voltage) which offers the prime advantages for PPCs [7, 37, 38, 40, 41, 114–119]. At the remote side of a power-by-light system, lower currents mean lower series resistance losses, which mean higher output powers. Larger PPC output voltages means there is no need for voltage up-converters on the remote side. And it simultaneously increases the remote load capacity by a factor of the segmentation multiplicity squared (through Ohm's Law; max load resistance is max power point voltage over current) [7]. The greater voltage range of the MJ PPC also entails higher signal fidelity compared to lower voltage single-junction operation in both fiber and free-space based data applications [63, 64, 120–123]. These benefits have led to record performance for vertically stacked MJ PPCs; output power and voltage records of >29 W (GaAs absorbers, 12J, 810 nm, ∼61% efficiency) [124] and >35 V (GaAs, 30J, 808 nm) [119]. The record (room-temperature) PPC optical power conversion efficiency is 68.9% held by a single-junction device [125]. High-quality MJ PPC efficiencies are comparable, with a record efficiency above 65% for a 5J device (GaAs, ∼830-840 nm, ∼1.25 W input power) [126]. Discussion of PPC applications continues in Subsection 2.3.2.

2.3 Applications; From electricity to societal use

Photovoltaics are a critical part of several major 21st century technological movements, such as the global energy transition, the internet-of-things, and 5G+ telecommunications paradigms. In this section, I give a brief outline of PV applications pertinent to the research topics of this

thesis. Naturally, these are split by PV device type. First, I cover MJ solar cell applications, then MJ PPCs. I also delve into the theory behind adaptive optics techniques for free space infrared communications in this section. This gives context for Chapter 6 and is an example of complementary research which must be completed to see the realization of PV applications in society.

2.3.1 Solar cells

The main application of solar cells is power production [6, 8, 9, 88, 127–129]. Solar PV offers a renewable, low emissions alternative to fossil fuels for large-scale utility power. As of 2022, <3% (4.4%) of the global energy (electricity) mix was produced by solar, this number is up significantly from the year 2000 value of <0.6% (∼0%) [127]. However, utility-scale solar installations almost always use silicon solar cells. This is the same for rooftop, vertical, building integrated, agrivoltaic, and essentially any other install that requires large areas of PV coverage. This is because silicon solar cells are orders of magnitude cheaper than MJ solar cells (0.33 US dollars per watt of DC power produced (USD/W_{DC}) compared to 69 USD/W_{DC} for a 3J, 2018 [5]) and have higher efficiencies than cost-competitive technologies, such as thin film or organic (23.6% vs. 19.2% record efficiencies for thin-film and organic respectively [4]). For MJ solar cells, utility-scale power production is only cost-competitive if concentrator technologies are leveraged, this is discussed in the first section below.

The MJ solar cell application space extends to smaller scale power production as well. The trade-off of higher performance and higher expense leads to the use of MJ solar cells in applications where space is limited, performance is valued, and/or economics are not of first concern. These include so-called niche applications [6, 88, 111, 130] such as satellites [131–133], extraterrestrial and space exploration [134], drones [135, 136], military, and electric cars [137–140]. Use of concentrating elements in these applications is possible as well.

Concentrator photovoltaic power generation

In concentrator photovoltaic (CPV) systems, optics are used to concentrate sunlight onto small MJ solar cells with the relatively cheap optics offsetting the higher MJ solar cell cost [6, 88, 141]. A simple schematic of a basic CPV module is shown in Figure 2.10a. How these modules are arranged into panels, placed on tracking systems, and fielded is shown in Figure 2.10b. The idea is simple: light is collected by a large area lens and focused down onto a comparatively small solar cell. This saves material costs as the expensive III-V semiconductor of the MJ solar cell is replaced by lenses and additional mounting. This makes CPV modules much more

cost-competitive with silicon than un-concentrated MJ operation. Since the lens must focus the light onto the MJ solar cell, the sun must remain as the lens' object. To this end CPV systems must use double-axis tracking to keep each panel perpendicular to the suns incoming rays during operation. The lenses only focus the direct portion of the solar insolation onto the cell, the vast majority of the diffuse light does not enter the lens at an angle which results in it hitting the cell. This is why AM1.5D is used as the pertinent standard solar spectrum in this thesis (see Section 2.1.4).

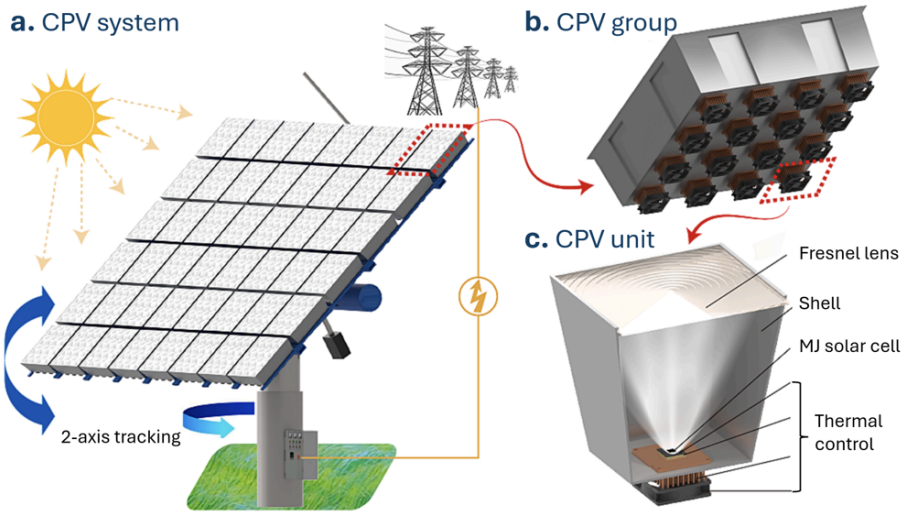

Figure 2.10: Schematic of a CPV system. In a, a large number of modules are mounted on a two-axis tracking to maintain perpendicularity to the sun. In b, modules are typically combined into groups to ease mounting. In c, the basic CPV module. A Fresnel lens focuses solar irradiation onto the MJ solar cell at its focal distance. The solar cell is mounted with thermal control to manage heating during operation. Adapted from [141] with permission from Elsevier.

The area ratio of light collection spot on the lens to illumination spot on the solar cell indicates the concentration factor. Hundreds of suns (100x) concentration factors are normal, with concentration factors exceeding a thousand suns in some cases [88,142]. As has been seen in the previous sections of this chapter (Subsection 2.1.2 and Subsection 2.1.3), increasing the level of light affects the JV characteristic of the pn-junction in two main ways. First, more photons leads to more electrons. Equation 2.5 and Equation 2.10 show that the cell current is directly proportional to the input irradiance (and, thus, concentration factor). Second, as was seen in Equation 2.3, is a logarithmic increase in the open circuit and MPP voltages with input irradiance caused by increasing chemical potential in the junction and a resultant widening of the space charge region in the junction. This voltage increase results in a power conversion efficiency

which increases logarithmically with concentration. However, the concentrated irradiance comes with the challenge of greater series resistance losses (which scales with current/concentration squared through $P = JV = J^2R$) and larger thermal loads. These two feedback effects limit system performance and must be carefully managed. The logarithmic build and then series resistance roll-off of efficiency with increasing concentration can be seen in Figures 1 through 3 of Section 4.4. Pushing the series resistance limit to greater solar concentrations using segmentation is the topic of that section.

Utility-scale CPV has declined [5, 143]. The technology was more popular in the early 2010s. At that time it was cost-competitive with silicon for large area coverage. However, the continued fall in silicon solar cell prices has rendered the competition moot at this time (2025). Advancement in CPV has been slower than silicon but continues. As Section 4.4 shows, subcell segmentation and this thesis are part of that advancement. The current trend in CPV is miniaturization; pushing the CPV advantages as far as possible by constructing cells with collection areas on the micron scale ("micro-CPV") [144–147]. Use of the concentrating principle for small-scale applications like those mentioned at the end of the previous section is an active area of research as well [131, 134, 137, 138].

2.3.2 Photonic power converters

The main PPC applications center around power and data delivery in remote, hard-to-reach, and/or sensitive systems [7, 37–41]. Figure 2.11 indicates the type of applications and electronics that PPCs can be used to power according to laser wavelength and output power of the system, as seen in [7]. Power beaming indicates free space transmission. The device types found in this figure are no coincidence, this is clear once the benefits of photonic power and data transmission are examined. First, the photonic nature of the signal entails galvanic and electromagnetic isolation. Second, fiber optics are a transmission medium which allows faster signal propagation and which is lighter and less prone to corrosion than copper wire [38]. Third, photonic power and data can be transmitted wirelessly (i.e. in free-space). Fourth, optical laser wavelengths have a large data bandwidth for telecommunications applications. And, fifth, photonic beams are highly-directional ensuring high data security. While PPCs may be used in any system where power will be extracted from a photonic signal, these benefits indicate the application spaces where PPCs and photonics have an especial advantage over the incumbent technology. For example, applications with fire risks benefit from the lack of sparking [42, 148], while safety and reliability concerns in high-voltage applications are mitigated by the photonic nature of the signal [43, 44, 149]. Heavy industry, dispersed industry or utility, geological and environmental monitoring and research, extreme environments, edge electronics, 5G+ telecommunications technologies, the internet of things, space exploration, space power systems, and more may

all profit from the safe, reliable, remote power and data transmission inherent in the photonic modality.

Figure 2.11b shows the efficiency and output power for a large variety of single and MJ PPCs from across the PPC literature [7]. This figure clearly indicates that multiple junctions are needed to achieve the output power levels required for many applications (medium and high power formats in Figure 2.11a). This is because the single-junction PPC efficiencies are limited by their ability to carry the system load ($\sim R_{MPP} = V_{MPP}/I_{MPP}$) which vanishes as the input current increases [7, 119]. High quality PPCs routinely achieve power conversion efficiencies exceeding 50%, with the highest performing devices falling within the 60-70% range. The efficiency may remain roughly unchanged as the segment multiplicity is increased. In Chapter 5 of this thesis, I discuss the design of novel MJ 1470 nm and 1550 nm PPCs, these are demarcated within Figure 2.11 by x's.

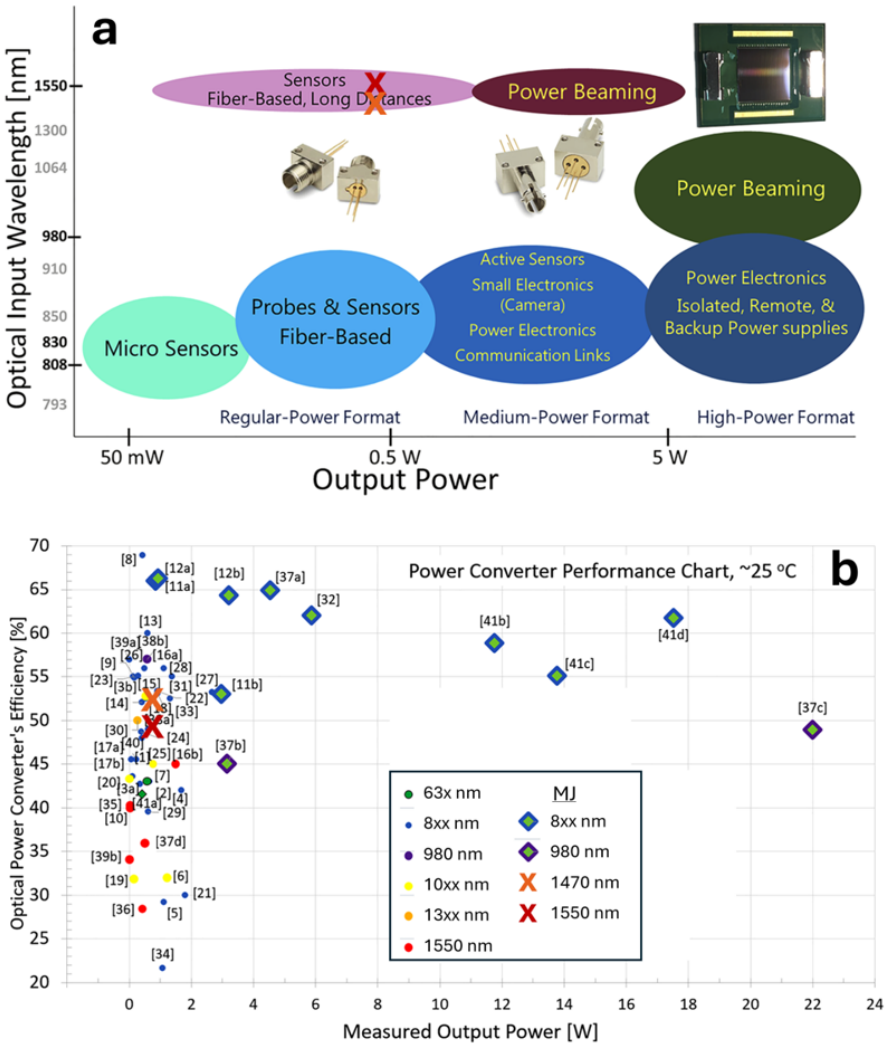

Figure 2.11: Photonic power converter perspectives. In a, PPC applications as a function of system wavelength and the PPC output power. "Power beaming" indicates free-space transmission. In b, a literature survey showing optical to electrical power conversion efficiencies and output powers for a large variety of PPCs. Colour indicates wavelength, markers indicate architecture with points denoting single-junction or horizontally-segmented MJ PPCs, and diamonds denoting vertically stacked MJ PPCs. Reference numbers within b refer to references in [7]. The x's in both figures indicate the PPCs which are the topic of Chapter 5. Both figures are adapted from [7] with minor, superficial changes (Creative Commons CC BY).

Single pixel adaptive optics for infrared free-space communications

Free-space optical links are realized by non-visual wavelength laser beams which transmit data and power in a point-to-point fashion through free-space (i.e. wirelessly) [57–62]. For links which transmit through the atmosphere, degradation of the signal occurs as the laser beam wavefront interacts with the turbulent, location and time variant, density, composition, and temperature distributions of the air. The result is not only a dimmer beam at the receiver, as some of the light is absorbed and scattered away, but, a spatially aberrant beam as well. As the beam passes through these moving volumes of air different portions of the beam are subject to different distributions of refractive index resulting in relative phase-shifts. The beam wavefront becomes out of phase with itself, and upon focusing, interacts with itself causing an interference pattern referred to as a speckle pattern. Figure 2.12 shows an example of simulated speckling from the experimental setup which is the focus of Chapter 6. In Figure 2.12a is the focal point spread function of a clean, no-turbulence, free-space laser beam signal. In Figure 2.12b is the point spread function of the same beam but with simulated atmospheric turbulence included. Wavefront speckling inhibits coherent optical processing and quickens the beam intensity loss (fast fading) limiting the reliability and throughput of optical links. For next-generation optical links these turbulence effects must be mitigated in near-real time, this is the purview of adaptive optics (AO) [65–69, 150].

Adaptive optics aims to correct for phase-distortion in the wavefront of an incoming signal using a feedback loop and a corrective optic. It progresses in an iterative manner. The wavefront of the incoming beam is measured. This may be in the pupil or focal plane as long as the phase can be extracted. Then, the phase mask required to cancel out the measured distortion and return the signal to a no-turbulence baseline is calculated. Finally, the canceling phase mask is applied to the corrective optic (e.g. a deformable mirror or spatial light modulator). This process is then repeated. AO latencies on the order of 1 ms or less are required for free-space optical communications, in accordance with the typical skew rate of low earth satellites and the environmental phase-distortion variations with time and location [151].

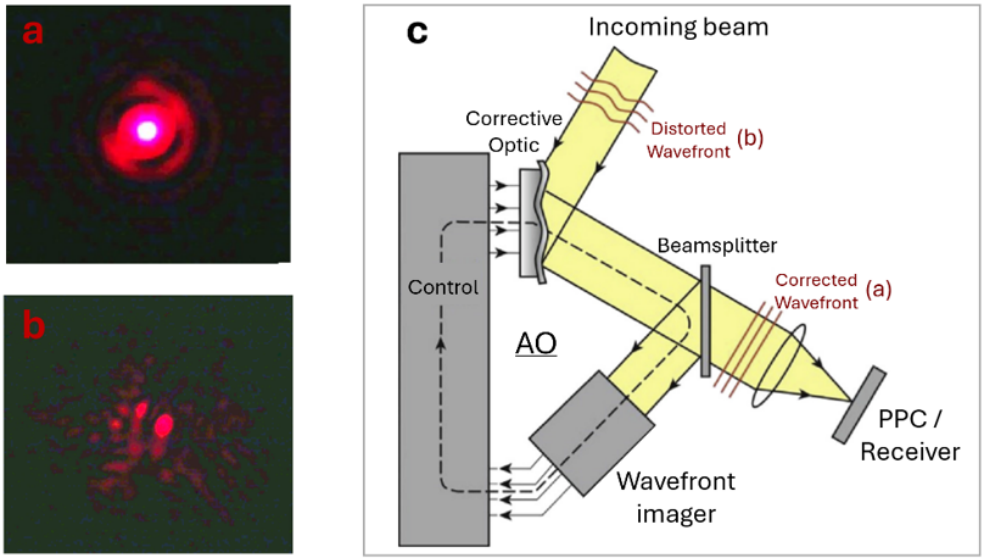

Figure 2.12: Consequences and correction of atmospheric turbulence on free-space photonic signals. In a, example focal plane point spread function of a photonic laser beam without modulation. The Airy pattern and experimental point spread response are visible. In b, focal plane point spread function for the same beam as in a but with strong atmospheric turbulence. In c, schematic representation of an adaptive optics (AO) system. Subfigures a and b are experimental images captured by the author using the test bench detailed in Chapter 6. Subfigure c is adapted from [150] with permission from Elsevier.

Adaptive optics requires an imaging component to measure the wavefront. Next-generation optical links will often use short-wave infrared wavelengths (SWIR, ∼1 - 3 micron and, specifically, 0.8 - 1.6 micron) since they are eye-safe and offer the wide-, and unlicensed/available in most regions of the globe, bandwidth necessary for 5G+ telecommunications paradigms. This wavelength regime was highlighted in Figure 2.6 and shows that detection in this bandwidth is typically achieved using InGaAs or InGaAsP. This material is available in high-quality but is up to three orders of magnitude more expensive than silicon, the conventional visual wavelength imaging material [151–153]. Unlocking the SWIR bandwidth for mainstream use will require a technology which can be economically deployed. One possibility, investigated in Chapter 6, is to use a single pixel camera to mitigate cost with compressive sensing techniques to mitigate single pixel latency [53–56, 154–156].

Single pixel cameras, as the name suggests, consist of one detecting element. Their simplicity makes them much cheaper than their multi-pixel counterparts. Single pixel cameras operate to capture a multi-pixel image using the principle of structured detection. The idea is

shown in Figure 2.13a-c. It involves the construction of the final image as the sum of the single pixel intensity weighted patterns in a sampling pattern basis. The patterns are typically applied using a digital micro-mirror device (DMD) consisting of many thousands of micron-scale mirror pixels which can each be tilted into an off or on position at rates in the thousands of hertz. A single pixel camera would be placed in the focal point of one of these modes (or both, for a differential measurement) to collect the pattern-structured image intensity. Typically, the single pixel camera needs as many measurements as there are (desired) pixels in the output image, or more, due to noise [154, 155]. Careful choice of the patterning basis and using differential measurements to reduce noise help but do not allow the single pixel camera to achieve less than a one-to-one pixel-to-measurement ratio, in other words, they cannot help break the Shannon-Nyquist sampling theorem [154, 155, 157].

Compressive sensing breaks the Shannon-Nyquist sampling theorem by realizing that resolution comes from information content rather than sampling [154, 156]. The Shannon-Nyquist theorem relates the minimum sampling rate to avoid information loss when discretizing a signal of a given maximum frequency [157]. For images (visual signals) it dictates proportionality between the image resolution and the image sampling (the number of pixels). In compressive sensing, the shift is to realize resolution is tied to information content rather than sampling. And that images are often information sparse. This can be understood viscerally when one considers an image of a face with a blank background. The image may be defined recognizably using just a few lines and shapes, it does not require a description of each pixel. Compressive sensing of images operates to find a basis in which the information content is sparse (the image is defined by a few large coefficient values, all the rest, the vast majority, are near zero). Figure 2.13d shows a suitable basis example for sparse decomposition of the focal plane speckle patterns seen in Figure 2.12b; the Hadamard patterns. Compressive sensing then exploits the sparse basis; measurements within this basis are collected and the one which has the minimum l_1-norm (coefficient sum) is identified. The magic of the sparse basis is that this minimal l_1-norm result is the true solution and that it can be found with as few as $K(log(N/K))$ measurements, where K is the size of the sparse basis and N is the full number of pixels (full image basis). Since less measurements are required, compressive sensing allows single pixel images to be collected more quickly, reducing latency for AO operations. In Chapter 6, I give experimental evidence that single pixel images with compressive sensing fractions as low as 15% may perform nearly as well as full resolution multi-pixel images when used as input for an adaptive optics algorithm which operates on the focal plane speckle patterns.

Many AO algorithms exist. The speckle-spot based AO algorithm investigated in this thesis is based on the research of Carrizo *et al.* [152, 158]. The turbulent wavefront is approximated as a linear series of plane waves, with each speckle-spot (area of coherent interference) associated with one of the plane waves. The corrective phase mask is obtained by optimizing how much of

the signal can be coupled into a fibre. It proceeds one speckle spot at a time, taking the spot intensity and location and using the periodic nature of plane waves to fit for the wavevector and phase of the plane wave associated with each speckle spot. The final solution is extracted as the series of plane waves which produce the corrected beam with the highest fibre coupling.

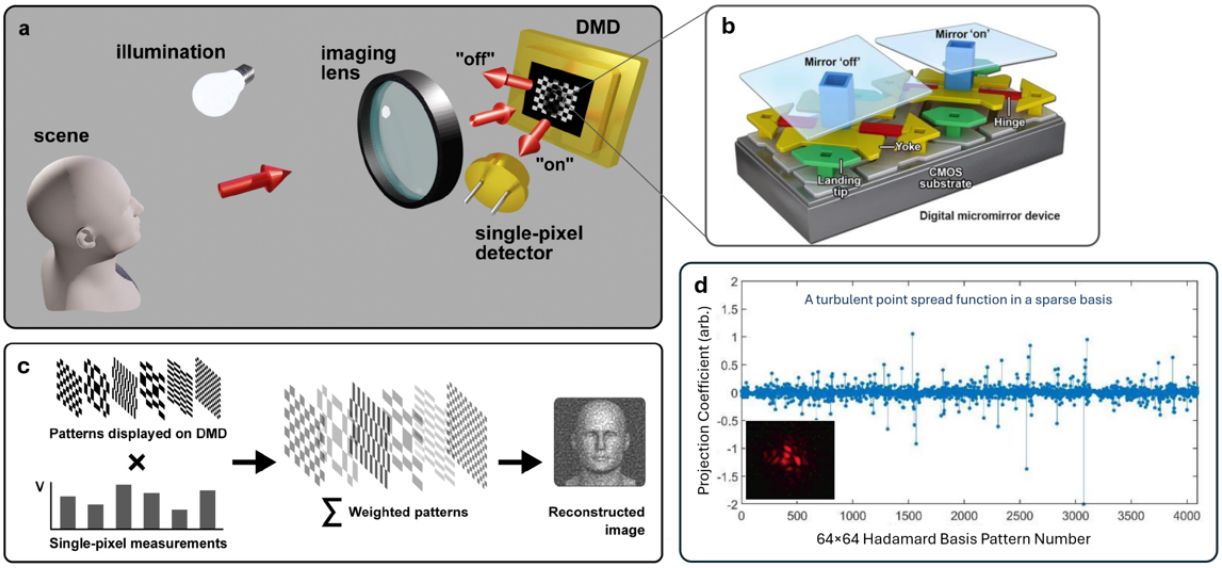

Figure 2.13: Principles of the single pixel camera (a - c) and an example of an image in a sparse basis for compressive sensing (d). In a, a representation of the imaged scene. In b, a 3D schematic view of two pixels of the DMD. In c, a visual indication of the image reconstruction process. Subfigures a-c are reproduced from [155] (©2020 Optical Society of America under the terms of the OSA Open Access Publishing Agreement). In d, a high-turbulence focal plane point spread function (inset) imaged with the single pixel camera of Chapter 6. The image is collected in the 64 × 64 Hadamard pattern set, the graph shows that this is a suitable sparse basis for compressive sensing.

2.4 Device design paradigms

Accurate optoelectronic device simulation is an important tool in the design of modern devices which feature ever-increasing complexity, shrinking sizes, greater variety, and higher performance requirements [82]. Its use typically falls in to one of two categories: (1) the use of relatively simple simulation methodologies for theoretical exploration, proof-of-concept, and "back-of-envelope" type calculations, and (2) the use of complex, well-calibrated simulation methodologies for the accurate and precise prediction of the performance of realized and realizable devices. The work in this thesis uses simulations of one type or the other. In the

subsections below I introduce the simulation methods used in this thesis. First, I will introduce the modified detailed balance limit (mDBL) calculations as an example of the former, proof-of-concept type simulation. mDBL calculations are used extensively in my research of segmented multi-junction solar cells (Chapter 4). Then, as an example of the latter, I will introduce Synopsys Sentaurus TCAD as it was used in my research on solar cells incorporating silicon-germanium-tin (Section 3.2 and Section 4.3) and MJ PPCs (Chapter 5). Finally, I briefly outline basic artificial intelligence background to provide context for its incorporation into optoelectronic device design. This is one of the main achievements of the MJ PPC project detailed in Chapter 5.

2.4.1 Proof-of-concept simulation: The detailed balance limit

Proof-of-concept simulations trade a lower model accuracy for lower computational expense. They are often based upon theoretical calculations. For PV devices the detailed balance limit, also known as the Shockley-Queisser limit and radiative efficiency limit, dictates the maximum theoretical efficiency of a single pn-junction PV device [8, 9, 159, 160]. It uses the principle of detailed balance which states that, for a device in steady-state, processes (such as photonic absorption, Figure 2.3a) are in equilibrium with their reverse (photonic emission, Figure 2.3b). This allows the PV device current to be calculated as the difference between the absorbed and emitted photon fluxes. The photon fluxes are found by considering black-body radiation profiles for the direct and diffuse components of the incoming light and the PV device itself and using a number of assumptions. The detailed balance limit assumes: (1) that all photons with energy greater than the bandgap are absorbed, generate a single electron-hole pair, and are collected as current no matter where in the device they are generated (infinite charge carrier mobility), (2) that all photons with energy less than the semiconductor bandgap are perfectly transmitted through the device, (3) that no non-radiative recombination processes are present (hence the name; radiative (recombination) efficiency limit, the junction JV is described by Equation 2.2 with an ideality factor of 1), and (4) that there are no other losses present (no parasitic absorption, reflection, contact shading, series or shunt resistances, etc.). For the AM1.5G spectrum, the detailed balance limit dictates a maximum single-junction solar cell power conversion efficiency of $\sim$33%, this is obtained with a semiconductor bandgap of $\sim$1.4 eV [8].

Modified detailed balance limit calculations extend the detailed balance limit beyond single-junction devices and refine the assumptions to produce more accurate results. In Chapter 4 of this thesis, I develop and use a mDBL simulation codebase called "Segments" to calculate theoretical JV performance of MJ solar cells with and without segmentation. It calculates the radiative recombination limited performance for each segment and connects them in series

to determine the MJ device performance. It has options to include non-unity ideality factors (approximates the effect of non-radiative recombination in the space charge region), non-unity internal quantum efficiencies (i.e. not all generated carriers are necessarily collected), reverse voltage junction breakdown (see Figure 2.2a), series resistance, and junction shunt resistances (see Equation 2.5). It also includes more realistic absorption and device thickness considerations by allowing (a specified amount) less than 100% of the incoming photons to be absorbed, and by including model-based and experimental material absorption profiles and thickness determination algorithms. Segments continues to ignore contact shading losses, reflection and interference at interfaces, parasitic absorption in any non-absorber layers including the tunnel diodes, photon recycling, and luminescent coupling. Section 4.1 presents an overview of the functionality which I added to Segments as part of this thesis work. Section 4.2 and Section 4.4 present research which use Segments to ascertain some of the potential impacts of segmentation upon the design of a InGaP/InGaAs/SiGeSn/Ge solar cell and CPV operation, respectively.

2.4.2 Predictive simulation: Synopsys Sentaurus TCAD

Proof-of-concept simulations and theoretical calculations often fail to achieve the level of realism required for the accurate prediction of PV device performance, instead designers must turn to more computationally expensive numerical methods which act to solve fundamental physics equations while including as many realistic effects as possible using phenomenological models and experimental data. For the greatest accuracy and predictive capacity, experimental data and calibration of free parameters in the models should be based off of the exact devices which will be manufactured. Hence, the typical optoelectronic device design is executed through an iterative feedback process of manufacture, evaluation, and modeling. The first iterations work to establish a well-calibrated device model which can then be used in a predictive capacity, this predicative capacity is then confirmed and refined in the next iterations. Once established, the predictive device model is used to explore the complex design space in ways that are impossible or that would be prohibitively expensive with realized devices [82, 161].

Synopsys Sentaurus TCAD is a suite of software tools for simulating semiconductor fabrication processes and devices [162]. One of its main advantages is its customizability. Any physical phenomenology which can be numerically modeled can be included in the simulation flow either through functionality present in the Synopsys Sentaurus simulation tools outright or through custom code which can be easily incorporated into the simulation environment. In this thesis, Synopsys Sentaurus TCAD is used to model MJ solar cells (Section 3.2 and Section 4.3) and PPCs (Chapter 5). Figure 2.14 presents a simplified version of the code flow in these projects. The crux of predictive simulation for PV devices is self-consistent solution of Maxwell's equations (at mesh points) throughout the device. The optical portion is solved

separately from the electrical portion. For my projects, the optical simulation benefits from the relatively simple geometry of my modeled devices. The thin, planar layer structure of the MJ solar cells in Section 3.2 and Section 4.3 allows the use of the transfer matrix method (TMM) which is derived from continuity of the electromagnetic field at the interfaces between each layer [72, 74]. The magnitude of the field can be calculated throughout the device if its incoming character is known. Alternatively, rigorous coupled wave analysis (RCWA) allows for thin, non-planar, periodically-structured-in-the-perpendicular-direction layers. It solves Maxwell's equations within the Fourier space using Bloch waves and Floquet functions (generic Bloch waves) to expand Maxwell's equations and the boundary conditions [72, 74, 163]. RCWA is used in simulation of the MJ PPCs in Chapter 5, although it should be noted that the studied MJ PPCs consist of only planar layers, in this case RCWA and TMM produce the same results. For the electrical portion of the device simulation, Sentaurus solves the Poisson and charge carrier continuity equations while accounting for all other physics modeled in the device (for example; non-radiative recombination mechanisms). For a more complete treatment of modeling PV devices in Synopsys Sentaurus TCAD please refer to [12, 72, 74, 164].

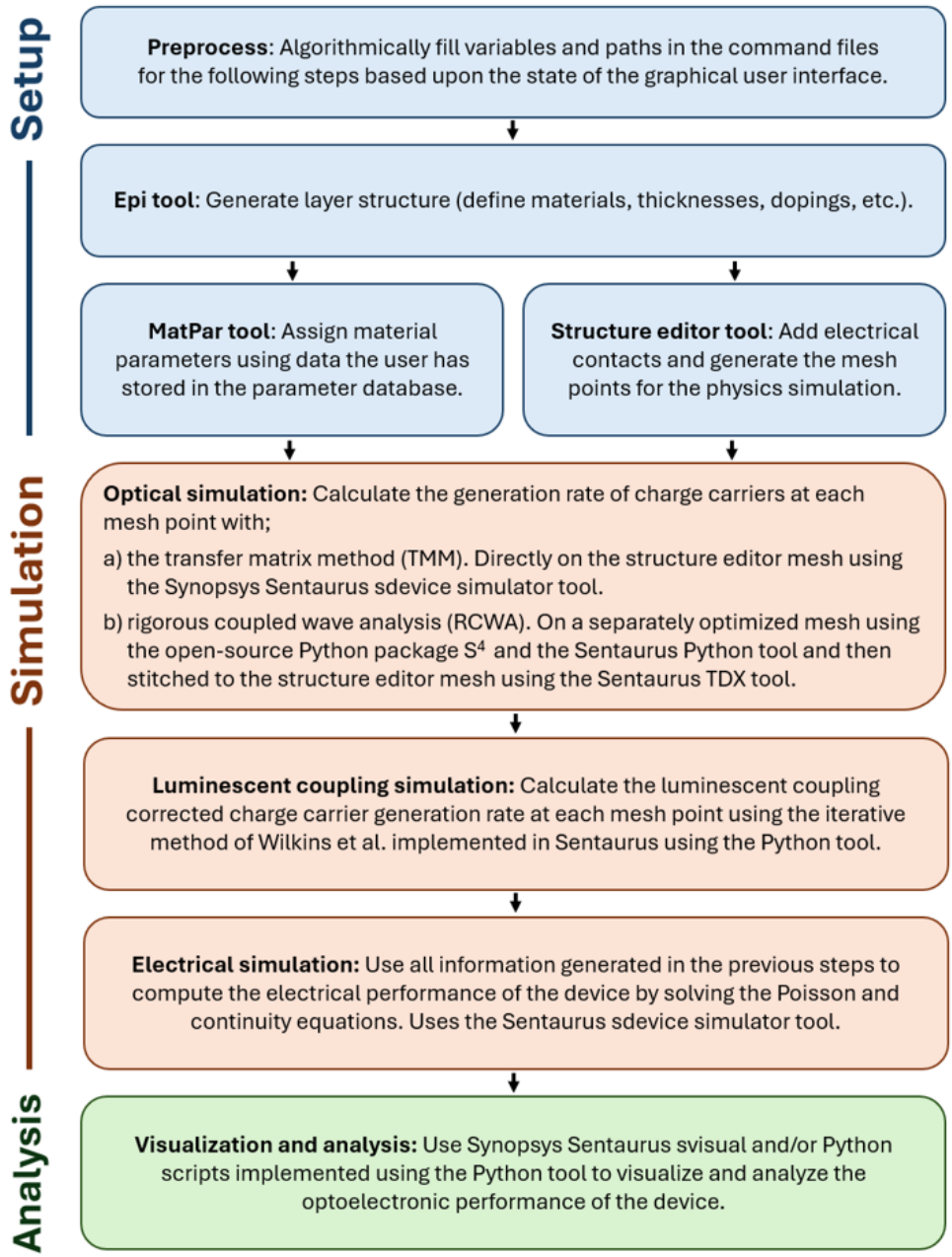

Figure 2.14: Simplified simulation flow for the Synopsys Sentaurus TCAD projects used in Section 3.2, Section 4.3, and Chapter 5. References; Synopsys Sentaurus TCAD graphical user interface [162], epi tool [165], matpar tool [165], structure editor [165], sdevice simulator [166], TDX data explorer tool [167], svisual tool [168], the S^4 RCWA package [163, 169], and the luminescent coupling method of Wilkins *et al.* [92].

2.4.3 Machine learning basics

Machine learning (ML) is the subset of artificial intelligence (AI) techniques which use data-trained algorithmic approaches. Three broad categories of ML exist; supervised, unsupervised, and reinforcement learning. Supervision refers to whether the training data includes outputs or not. Supervised ML training data includes labels (data has input and output information). It aims to determine the input-output relation which is inherent in the data. Most neural net approaches are an example of supervised learning. Unsupervised ML uses training data which is not labeled (no distinction in the data, i.e. only input data). It operates purely to recognize patterns in the training data. Clustering and dimensionality reduction are examples of unsupervised ML methods. Reinforcement learning incorporates user feedback into training the algorithm. The response of the algorithm evolves based upon whether it's action is reinforced (rewarded) or dissuaded (penalized). ML techniques generally require large amounts of accurate and clean data (where data cleanliness refers to all data being valid and having the same features). As such, establishing an efficient and efficacious data preparation pipeline is an integral component of successful ML implementation. In Chapter 5 of this thesis I implement dimensionality reduction ML techniques to enhance the design exploration, optimization, and understanding of MJ PPCs. More information on dimensionality reduction can be found therein.

Chapter 3

Silicon-germanium-tin

In this chapter I demonstrate the potential for new high-efficiency multi-junction solar cells which use SiGeSn as the third subcell in a 4J extension of the industry standard 3J. As introduced in Section 1.1, this project represents a classical approach to MJ solar cell design; develop new materials which fulfill the lattice and current matching requirements of an existing MJ material system. Higher efficiencies result as spectral matching increases and thermalization losses are reduced. In this work, this efficiency boost is targeted while simultaneously leveraging the industrial maturity of the industry standard InGaP/InGaAs/Ge 3J solar cell. I introduce the emerging SiGeSn material as a current and lattice matched third subcell. In the next section of this chapter, I briefly introduce the formal cross-Canada SiGeSn project and outline experimental measurements collected at the University of Ottawa SUNLAB. In Section 3.2, I present my Photovoltaics Specialist Conference (PVSC) 2022 evaluation abstract which delves into accurately modeling SiGeSn using Synopsys Sentaurus TCAD before reporting gains, quality limits, and challenges for the InGaP/InGaAs/SiGeSn/Ge system.

3.1 Monolithic multi-junction III-V solar cells with optimal 1 eV subcell

This section outlines my contributions to the Government of Canada's Strategic Project Grant of the same name. This project was a collaboration between Ecole Polytechnique Montréal, Université de Sherbrooke, and the University of Ottawa. It aimed to design, grow, and fabricate the first operational 4J SiGeSn solar cell. University of Ottawa's roles were device testing

and simulation. The next section describes efforts in the latter pursuit, this section the former. While no 4J devices were grown, InGaP/InGaAs 2J samples were. These prototype devices were developed and tested at Université de Sherbrooke and were also tested at the SUNLAB. This characterization is described in [24]. The reflectance and IQE measurements therein were carried out by the author, Dr. Alex Brice Poungoué Mbeunmi, and I, high concentration verification measurements were also collected at the SUNLAB. These tests contribute to the realistic growth, fabrication, and CPV application of the top two-junctions in the InGaP/InGaAs/SiGeSn/Ge stack. As a small experimental accompaniment to this simulation focused thesis I present an outline of the test and results below.

Figure 3.1 shows a magnified image of one the InGaP/InGaAs samples under test at the University of Ottawa SUNLAB. Figure 3.2 shows experimental IQE (a) and reflectance measurements (b) collected at the SUNLAB. EQE measurements were collected using an Oriel Instruments IQE200 Series [170]. Light bias of the top InGaP subcell was achieved using a 405 nm laser diode, a lamp light with red components filtered out was used for the bottom subcell. Data is collected for each subcell in separate runs, to allow switching of the light bias. Four samples are shown in Figure 3.2, they have varying grid finger pitches in the range 125-400 micron. The devices have active areas of 3.8×3.8 mm^2. Only direct reflectance is collected and considered (where direct means reflectance which is in-line with the monochromatic survey beam). Transmission and diffuse reflectance are assumed to be zero in calculation of the IQE (Equation 2.9). Non-negligible diffuse reflectance is possible and would result in a boost to the IQE if accounted for.

Figure 3.2a shows that the devices have high material quality but that there may be room for improvement in the design or growth recipe. The devices have high IQEs, around 0.9 or greater across the majority of each subcell's absorption window. The exception is in the blue (high energy) regime, here, the response is indicative of recombination in the upper layers (the shoulder from $\sim$350-475 nm). A more square response (as is observed for the lower junction) may be obtained by reducing the doping concentration in the top subcell front surface field and emitter layers. Figure 3.2b shows typical reflectance spectra for a PV device with an anti-reflection coating, here a silicon dioxide - titanium dioxide double layer ARC. Optical resonance phenomena are visible in the wave-like patterns at long wavelengths and the peak at short wavelengths. Also visible is a slight distinction between the samples; those with smaller grid finger pitches have higher reflectance, naturally, since a greater portion of the surface is covered by the metallic grid fingers.

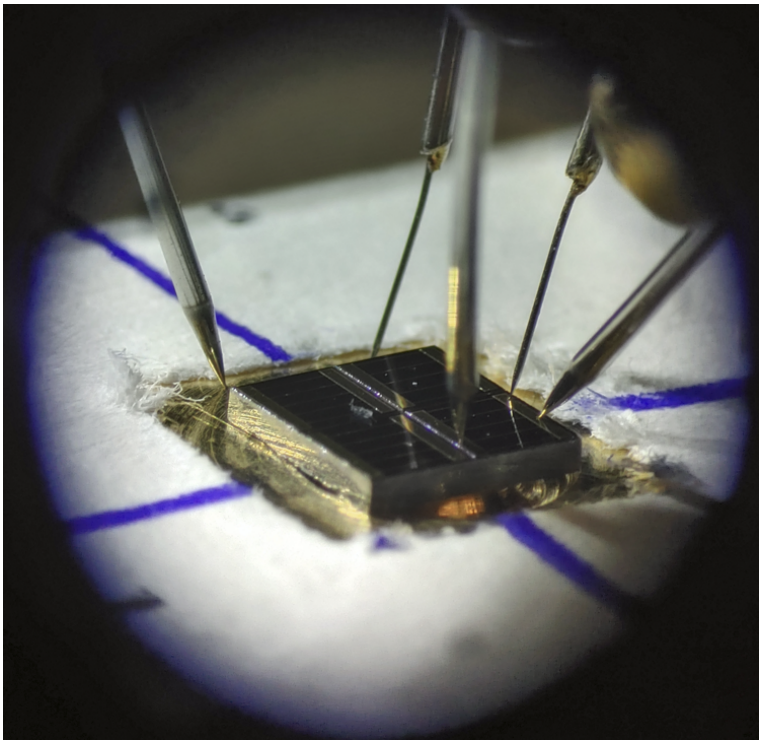

Figure 3.1: A Université de Sherbrooke InGaP/InGaAs 2J solar cell under test at the University of Ottawa SUNLAB. Micro-probe connection to the solar cell busbars and the test chuck are visible. Photograph by the author (R.F.H. Hunter).

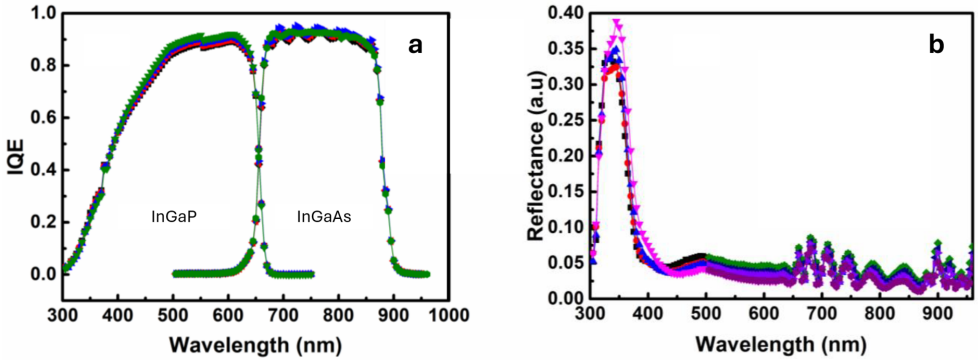

Figure 3.2: InGaP/InGaAs 2J solar cell characterization at University of Ottawa SUNLAB. In a, internal quantum efficiency. In b, (direct) reflectance. Samples with different grid finger pitches are tested. The data indicates high quality devices and avenues for improvement. Figure adapted from [24] (©2020, IEEE).

3.2 Drift-diffusion modeling of four-junction solar cells

Scope and impact

This Photovoltaics Specialist Conference 2022 evaluation abstract and oral presentation uses Synopsys Sentaurus TCAD simulations to determine the gains, material quality limits, challenges, and design guidelines for implementation of SiGeSn as the third subcell in the InGaP/InGaAs/Ge material system. The realistic composition-bandgap space is considered and a SiGeSn composition which meets the simultaneous requirements of current and lattice matching is selected. Existing calibrated 3J TCAD models are extended to include this SiGeSn with material parameters informed by literature. The simulated optoelectronic performance of 3J and 4J devices is compared to ascertain performance gains and limits. An investigation of device loss mechanisms to extract further design challenges and guidelines is executed.

The following novelties are introduced in this work:

1. Determination of a potential current and lattice matching composition for the emerging silicon-germanium-tin material: $Si_{0.14}Ge_{0.824}Sn_{0.036}$ with an indirect bandgap of 0.77 eV, direct bandgap of 1.05-1.08 eV, and germanium lattice match. Modeling of the SiGeSn composition within the Sentaurus environment using literature data creating a material parameter database which is now being used in other SUNLAB projects. Incorporation

of this material into established Sentaurus projects for the InGaP/InGaAs/Ge 3J material stack.

2. Determination of potential efficiency gains for the 4J device over the 3J when considering reasonable material quality (1.3% absolute gain in power conversion efficiency at 1000 suns concentration of the AM1.5D spectrum for SiGeSn with a trap-assisted recombination lifetime of 1 µs and 10^3 cm/s surface recombination velocities in the device). Establishment of limits on the material quality for the 4J to retain higher efficiency than the 3J (trap-assisted recombination lifetimes of 100 ns or greater, with surface recombination velocities of $5{\times}10^4$ cm/s).

3. Elucidation and discussion on the loss mechanisms and design challenges in the 4J device. Presentation of possible approaches to curb these losses such as thinning the upper junctions or introducing strain to the SiGeSn layer. Identification of current underproduction in the bottom subcell as one of the material system's limiting factors.

These results may inform the development of MJ solar cells; especially those employing the InGaP/InGaAs/SiGeSn/Ge material system, which aim to extend the InGaP/InGaAs/Ge material system, or similar material systems.

Author contributions

Laurier S. Baribeau: As a Master's student at the University of Ottawa's SUNLAB research group, Laurier developed the SiGeSn material and optoelectronic device models used in this study. Laurier finished his Master's degree without presenting this material.

Robert F.H. Hunter: As a new doctoral candidate active on the SiGeSn project I adopted Laurier's Sentaurus code. I used this code as an introduction to the field and to Sentaurus. I was lead author of this study, the conference abstract, and conference presentation.

Dr. Christopher E. Valdivia: As a senior research scientist within the University of Ottawa's SUNLAB research group, Chris helped to guide my research. He provided detailed feedback during the analysis of my simulation results and assisted in editing the manuscript.

Prof. Karin Hinzer: As the director of the University of Ottawa's SUNLAB research group and my supervisor, Karin oversaw my research. She provided detailed feedback during the analysis of my simulation results, and assisted in editing the manuscript.

Copyright

L.S. Baribeau, R.F.H. Hunter, C.E. Valdivia, and K. Hinzer, "Drift-diffusion modelling of four-junction InGaP/InGaAs/SiGeSn/Ge solar cells," *2022 IEEE 49th Photovoltaic Specialists Conference*, Philadelphia, PA, June 5-10, 2022. Oral Presentation. Proceeding; doi: 10.1109/PVSC48317.2022.9938603.

Drift-Diffusion Modelling of Four-Junction InGaP/InGaAs/SiGeSn/Ge Solar Cells

Laurier S. Baribeau, Robert F.H. Hunter, Christopher E. Valdivia, and Karin Hinzer

SUNLAB, Centre for Research in Photonics, University of Ottawa, Ottawa, Ontario, K1N 6N5, Canada

***Abstract*— The ternary alloy silicon germanium tin offers the potential to extend the industry standard lattice matched InGaP/InGaAs/Ge triple-junction solar cell to four junctions. In this work, a discussion of the compositional space for SiGeSn shows that Ge-lattice-matched alloys with an indirect bandgap of ~0.8 eV, and direct bandgap near 1.0 eV, are obtainable with current growth methods. Drift-diffusion modelling reveals a power conversion efficiency of 42.6% for a simulated InGaP/InGaAs/SiGeSn/Ge device, an increase of 1.3% absolute with respect to a comparative InGaP/InGaAs/Ge design. It is shown that current-matching in the four-junction material system requires significant thinning of the top three subcells due to inefficient absorption in the Ge bandwidth leaving room for improvement to the design. This, and other design guidelines for the InGaP/InGaAs/SiGeSn/Ge system, are outlined.**

Keywords—silicon germanium tin, drift-diffusion modelling, multijunction solar cells, materials, concentrator photovoltaics

I. Introduction

Record four-junction (4J) solar cells have achieved 46.0% and 45.7% power conversion efficiency for wafer-bonded and inverted metamorphic designs, respectively [1]. Yet, interest remains in a 4J extension of the industry standard triple-junction (3J) solar cell, germanium-lattice-matched (Ge-LM) InGaP/InGaAs/Ge. This feat would allow a boost to power conversion efficiency while leveraging the maturity of the 3J device manufacturing. We present simulation results of a 4J solar cell design containing the group-IV ternary alloy silicon germanium tin (SiGeSn). The tunable nature of the SiGeSn alloy offers the opportunity to obtain simultaneous current and lattice matching within the InGaP/InGaAs/Ge structure as a third subcell with ~1.0 eV bandgap.

The bandgap and lattice constant as a function of composition for the nascent SiGeSn material system are discussed before delving into a detailed analysis of an InGaP/InGaAs/SiGeSn/Ge design. Design guidelines for the InGaP/InGaAs/SiGeSn/Ge architecture are extracted from this simulation and from others detailed in [2]. Material parameters are modelled using literature data. Device results are obtained via drift-diffusion modelling in Synopsys Sentaurus TCAD. Calibrated 3J solar cell models are employed, as in [3].

II. Silicon-Germanium-Tin Compositional Space

In the SiGeSn material space, the amount of each element in the alloy and the layer strain can be controlled. The careful adjustment of these parameters shifts the SiGeSn lattice constant, as well as the size of the indirect and direct bandgaps. While a discussion of strained SiGeSn alloys was presented in [4], our work focuses on designs without strain.

The band structure of the alloy can be obtained from interpolation of the well-studied band structure of pure crystals of the individual elements. Deviations from the linear interpolation between pairs of components is assumed to be quadratic and is quantified using the bowing parameter, b. For the SiGeSn material system the largest bowing parameter is observed for the SiSn binary. The quadratic bowing parameter for SiSn (b_{SiSn}) has been suggested to vary significantly as a function of both growth conditions and alloy composition. Values of b_{SiSn} as dissimilar as 13.2 eV for SiSn compositions relevant for Ge-LM alloys to 3.26 eV for SiSn with ~50% Sn content have been reported [5]. While this composition dependent anomalous bowing remains a source of uncertainty for the SiGeSn material system in general, it has little effect on the bandgap of compositions which are attainable with current growth methods. Constrained by the low miscibility of Sn in Ge, SiGeSn growth is typically restricted to alloys with Sn content in the range of ~8% or less [6]. Importantly, this material space includes compositions lattice matched to Ge.

In Fig. 1, the SiGeSn bandgap (vertical axis) is shown as a function of alloy composition for Ge-LM b_{SiSn} of 13.2 eV. In this plot, the bowing parameters define the curvature of the trend plane [7]. The SiGeSn bandgap is taken as the smallest bandgap energy in the band structure. Color denotes the crystal location and direct vs. indirect nature associated with the bandgap. The composition of the ternary alloy is shown in triangular basis with silicon content aligned along the back right axis of the rectilinear

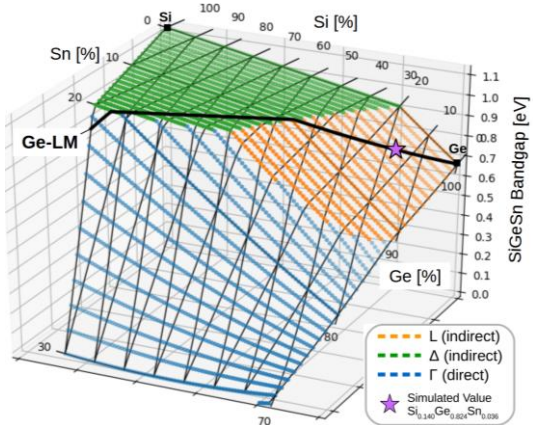

Fig. 1. Strained SiGeSn bandgap as a function of composition with a b_{SiSn} of 13.2 eV, the empirical value observed for Ge-LM SiGeSn compositions.

figure container. The compositions are shown along the edges of the trend plane. A limited extrapolation into potentially attainable compositions of SiGeSn is also shown.

The lattice constant of the SiGeSn, calculable through similar interpolation methods (Vegard's law), can be combined with the bandgap vs. composition information. This allows the Ge-LM compositional line to be included in Fig 1. An estimate of the direct bandgap value while in the indirect regime can be obtained from Fig. 1 by extrapolation of the direct Γ plane.

III. Drift-Diffusion Modelling of InGaP/InGaAs/SiGeSn/Ge Multijunction Solar Cells

One-dimensional and two-dimensional simulations of a 4J InGaP/InGaAs/SiGeSn/Ge MJSC are carried out using finite element analysis in the Synopsys Sentaurus. Optical transmission and absorption are calculated using the transfer matrix method. Electrical performance is computed using drift-diffusion modelling of charge carrier transport.

A. Model Details

Fig. 2 shows a schematic of the optimized layer structure for the modelled device. A dual layer anti-reflection coating (ARC) of MgF_2 and TiO_2 is employed. The top two subcells use standard designs for the emitter, base, front surface field (FSF), and back surface field (BSF) layers. The SiGeSn third subcell composition is Ge-LM, with 14% Si and 3.64% Sn. As indicated in Fig. 1, this corresponds to a primarily indirect bandgap, at 0.77 eV, at the L point in the crystal. A secondary direct transition at the Γ point is present at 1.05-1.08 eV. An active Ge substrate is utilized as the fourth subcell. The tunnel diodes included in the device are of standard design: AlGaAs/GaInP between the top two junctions, and AlGaAs/GaAs elsewhere. A flat gold mirror at the back surface is also used. A 3.6 µm contact width and 120 µm grid pitch are included in the 2D simulations (not shown in Fig. 2).

For materials other than SiGeSn, material parameters are obtained from literature [3]. For SiGeSn, band structure is obtained using the model outlined above, electron effective mass is calculated using linear interpolation from the longitudinal and

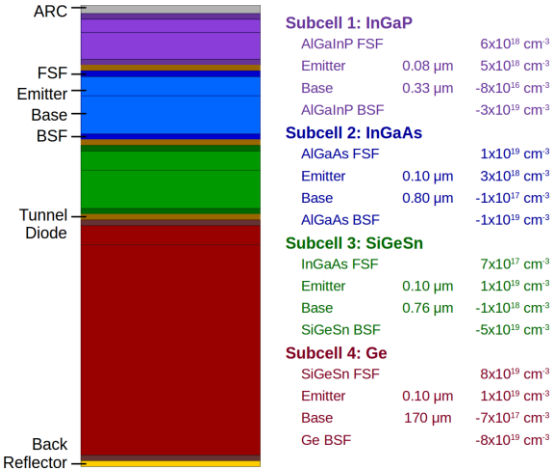

Fig. 2. Schematic view of the modelled 4J device. Not to scale. Materials and doping for the subcell layers are given along with the base and emitter thicknesses. All FSF and BSF layers are 0.30 µm thick with the exception of the Ge BSF which is 1.5 µm thick.

transverse values of the pure elements, band offsets are determined using the SiGeSn-specific model of [8], and, absorption is calculated using the empirical complex refractive index data of [9]. To ascertain the effect of the SiGeSn bulk crystal quality on the device performance, a sweep of Shockley-Read-Hall (SRH) recombination lifetimes is undertaken. Surface recombination is considered at the FSF/emitter and base/BSF interfaces in all subcells, and at the FSF/ARC interface. The device is modelled at 300 K.

B. Results and Analysis

Under 1000-sun AM1.5D illumination, the current density and electrical power density as functions of voltage are plotted in Fig. 3a for the four subcells of the InGaP/InGaAs/SiGeSn/Ge device, yielding a full device power conversion efficiency of 42.6%. This translates to an absolute efficiency gain of 1.3% compared to a like-modelled InGaP/InGaAs/Ge 3J design. These results employ a surface recombination velocity (SRV) of 10^3 cm/s. When the SRV is increased to 5×10^4 cm/s the 4J device efficiency drops to 41.6%, remaining 0.4% greater than the like-modelled industry standard 3J.

In this device simulation, the layer thicknesses have been optimized to produce current matching in all subcells. As Fig. 3a shows, 1000-sun AM1.5D short-circuit current densities (J_{sc}) vary by 0.40 A/cm^2, 3.4% relative to the current-limiting subcell's value. Current matching has been achieved by significant thinning of the top three subcells to allow enough photons to reach the Ge. This can be seen in Fig. 3b, which plots the external quantum efficiency (EQE) for subcell current generation. With this design, high current generation is obtained for a wide bandwidth. The EQE remains near 90% up to ~1.5 µm, with the EQE minima (due to reflectivity peaks) near 1.0, 1.1, and 1.3 µm, falling within atmospheric absorption bands.

Fig. 3b also shows the percent fraction of the incident photon flux which is lost to various physical processes in the device. Primary losses are absorption in the ARC, radiative recombination localized in the InGaP and InGaAs base layers, SRH recombination in the InGaAs base, and Auger recombination in the Ge. A SiGeSn SRH lifetime of 1 µs has been assumed in these results, requiring a high material quality. SiGeSn SRH lifetimes between 10 ns and 100 µs were also simulated. For a SiGeSn SRH lifetime of 10 ns, the device's power output and J_{sc} are reduced by ~20%. However, with a SRH lifetime of 100 ns the effect on subcell current generation is small (<1%) and since current matching is maintained, full device performance is minimally affected with the power conversion efficiency falling 1.25% to 41.4%. For a SiGeSn SRH lifetime of 100 µs the device power output increases by ~2%, an effect which is strongly dominated by voltage increase. In future designs, empirical data on the SRH lifetime of SiGeSn can be used as an input to help fine-tune the layer thicknesses.

The FSF and BSF layers in the simulated device have been optimized to reduce the minority carrier loss currents and improve subcell absorption. Highly doped BSF have been employed with minimum possible thicknesses. The reduced band splitting and Si-induced valence band shift of SiGeSn has been leveraged to implement an improved FSF for the Ge subcell. The incident flux fraction plot, Fig. 3b, shows that the loss currents have been significantly reduced.

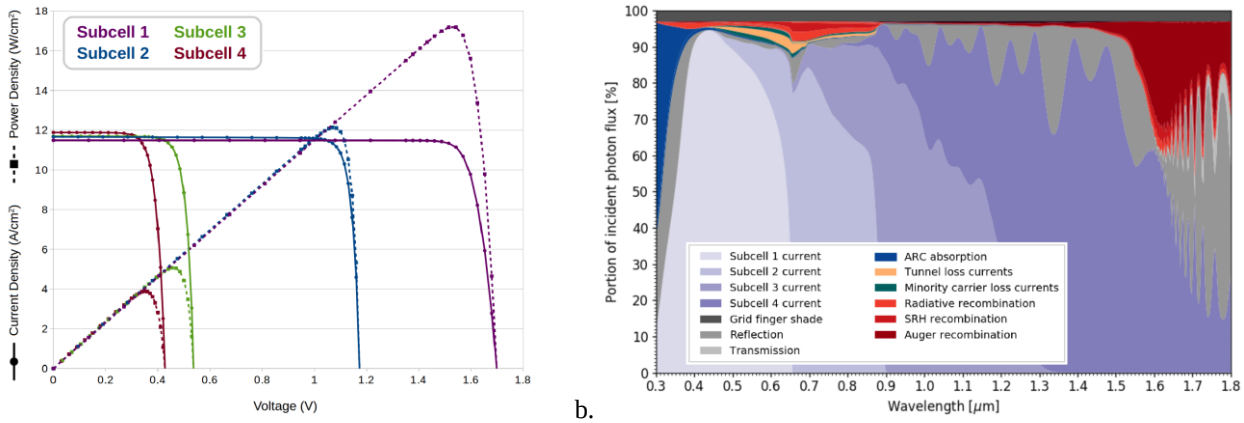

Fig. 3. a. Simulated current-voltage and power-voltage characteristic of the four subcells in the InGaP/InGaAs/SiGeSn/Ge MJSC, under 1000 suns AM1.5D illumination. b. EQE of current generation and loss mechanisms in the 4J device as a function of monochromatic illumination wavelength.

IV. Discussion and Conclusion

In this design, the difficulty to obtain current matching in the InGaP/InGaAs/SiGeSn/Ge material system is exemplified. The low absorption, high Auger recombination, and high reflectivity peaks in the Ge subcell are the primary limiting mechanisms. This necessitates significant thinning of the top three subcells, despite utilization of a thick active substrate, a consideration which increases device cost and weight. One or several design changes may be implemented to overcome this problem and boost device performance, including: improved light trapping (e.g. nanotextured back reflector); increased bandgaps of the top three subcells; replacing the Ge subcell with a strained SiGeSn composition with stronger direct bandgap absorption, and subcell segmentation [2][10]. One benefit of our proposed design is the thin SiGeSn subcell, with a thickness of only 0.86 µm, lowering the constraints on the growth of the ternary alloy.

The SiGeSn composition used in the 4J InGaP/InGaAs/SiGeSn/Ge device may benefit from the incorporation of small amounts of strain. This would allow an increase in the indirect bandgap's size and a reduction in the direct bandgap, while maintaining the same SiGeSn composition [2][4]. Keeping the indirect bandgap slightly below the direct bandgap will allow an enhancement in the absorption while minimizing the increase in radiative recombination. In this simulated device, doping levels have been chosen during the optimization process [2]. It can be noted that the doping levels used for the SiGeSn layers have been experimentally demonstrated in Ge-LM compositions [6].

With III-V species acting as dopants in group-IV materials, and vice versa, one of the main challenges of the InGaP/InGaAs/SiGeSn/Ge system is the combination of these materials in a monolithic stack. Conventionally this has required two growth reactors to avoid contamination, however, recent work shows that effective metal-organic chemical vapor deposition growth of both III-Vs and group-IV semiconductors within the same reactor is possible [11]. Despite these advances, the inclusion of a III-V compound tunnel diode between the group-IV layers, as employed here, is not considered practical with current technology. Growth of a suitable junction to use between the SiGeSn and Ge subcells has not been demonstrated to date and remains a challenge for successful implementation of the InGaP/InGaAs/SiGeSn/Ge material system.

The simulations conducted here have illuminated some of the SiGeSn quality requirements and design challenges for an effective InGaP/InGaAs/SiGeSn/Ge solar cell. It has been shown that a 1.3% absolute gain in power conversion efficiency with respect to the industry standard 3J is possible for SiGeSn with a SRH lifetime of 1 µs and 10^3 cm/s SRVs in the device. Efficiency gains remain possible for lifetimes of 100 ns or greater and with SRVs of 5×10^4 cm/s. The difficulty to achieve current matching in the material system has been highlighted and leaves room for improvements to the design.

References

[1] M.A. Green et al., "Solar cell efficiency tables (version 59)," *Prog. Photovolt. Res. Appl.*, vol. 30, no. 1, pp. 3-12, 2022.

[2] L. Baribeau, "Design of multi-junction solar cells incorporating silicon-germanium-tin alloys with finite-element annalysis and drift-diffusion model," M.A.Sc. Thesis, Univeristy of Ottawa, 2022.

[3] A.W. Walker, O. Thériault, J.F. Wheeldon, and K. Hinzer, "The effects of absorption and recombination on quantum dot multijunction solar cell efficiency," *IEEE J. of Photovolt.*, vol. 3, no. 3, pp. 1118-1124, 2013.

[4] A. Attiaoui and O. Moutanabbir, "Indirect-to-direct band gap transitions in relaxed and strained $Ge_{1-x-y}Si_xSn_y$ ternary alloys," *J. Appl. Phys.*, vol. 116, 063712, 2014.

[5] V.R. D'Costa, Y.-Y. Fang, J. Tolle, J. Kouvetakis, and J. Menéndez, "Tunable optical gap at fixed lattice constant in group-IV semiconductor alloys," *Phys. Rev. Lett.*, vol. 102, 107403, 2009.

[6] Y.-Y. Fang et al., "Practical B and P doping via $Si_xSn_yGe_{1-x-y-z}M_z$ quaternaries lattice matched to Ge: structural, electrical, and strain behaviour," *Appl. Phys. Lett.*, vol. 95, 081113, 2009.

[7] Q. Chen et al., "The effects of strain and composition on the conduction-band offset of direct band gap type-I GeSn/GeSnSi quantum dots for CMOS compatible mid-IR light source," *Semicond. Sci. Technol.*, vol. 35, no. 2, 2020.

[8] H. Wang et al., "Theoretical investigation of performance enhancement in GeSn/SiGeSn type-II staggered heterojunction tunneling FET," *IEEE Trans. Elec. Dev.*, vol. 63, no. 1, pp. 303-310, 2016.

[9] P. Pearce, T. Wilson, A. Johnson, and N. Ekins-Daukes, "Characterization of SiGeSn for use as a 1 eV sub-cell in multi-junction solar cells," *2018 IEEE 7th World Conf. Photovolt. Energy Conv.*, pp. 943-948, 2018.

[10] C.E. Valdivia and K. Hinzer, "Subcell segmentation for current matching and design flexibility in multijunction solar cells," IEEE J. Photovolt., vol. 10, no. 5, pp. 1329-1339, 2020.

[11] G. Timò et al., "Results on MOVPE SiGeSn deposition for the monolithic integration of III-V and IV elements in multi-junction solar cells," *Solar Energy Mat. and Solar Cells*, vol. 224, 111016, 2021.

Chapter 4

Subcell segmentation and segmented multi-junction solar cells

This chapter details my studies into the potential of subcell segmentation as a new design dimension in multi-junction solar cells. I present one computational modeling tool and three research contributions. Section 4.1 discusses my extensions to the Python mDBL codebase "Segments", which is used in Section 4.2 and Section 4.4. In Section 4.2, presented at the Optical Society of America (OSA) Advanced Photonics Congress 2020, I evidence the potential of subcell segmentation to alleviate the bandgap restriction of current matching for SiGeSn or a similar material. In Section 4.3, presented at the Ecolé les Houches international workshop, I present thickness considerations and optoelectronic performance of InGaP/InGaAs/SiGeSn/Ge designs with and without minimal subcell segmentation modelled in Synopsys Sentaurus TCAD. And finally, in Section 4.4, I exhibit the potential of subcell segmentation to allow one and two subcell solar cells to operate with high power conversion efficiencies at solar concentrations in the thousands of suns or more. This work demonstrates the disruptive potential of subcell segmentation as an emerging MJ solar cell design paradigm.

4.1 Segments modified detailed balance limit code

Segments is a Python based mDBL codebase originally developed by Dr. Christopher Valdivia of the SUNLAB. Detailed balance limit calculations and the Segments mDBL code were introduced in Subsection 2.4.1. In this section I outline the additional capabilities that I included in Segments. These fall under two categories: new analysis functionalities and improved accuracy

in the absorption and thicknesses calculations. Examples of the former are found in the following sections. Investigation of material systems with only one variant bandgap and of performance as a function of concentration was not possible prior to my work. I also added code to plot and analyze higher dimensional ($\geq$3-dimensional) spaces using slices and the open-source plotly module [171]. I outline consequences of the latter advancements in absorption and thickness consideration here.

The DBL approach to absorption is to assume that all photons with energy greater than the bandgap energy are absorbed while all photons with energy less than the bandgap energy are transmitted. This is not realistic, nonetheless because it entails infinitely thick absorber layers (see Section 2.1.3). As implemented by Dr. Valdivia, Segments allowed for this full DBL approach as well as a slightly more realistic approach which allowed the user to define the fraction of incident photons which would be absorbed and then calculated the segment thicknesses assuming perfect current-sharing, Beer-Lambert absorption, and generic square-root extinction coefficient profiles. To improve the accuracy of the absorption, I implemented the capability to (1) use experimental extinction coefficient data for each material in the device, (2) set maximum segment thicknesses while maintaining current-sharing, and (3) optimize subcell segmentation after the absorption has been considered.

Figure 4.1 exemplifies the effects of the added absorption and thickness accuracy on the performance of a 4-subcell MJ solar cell where the third subcell bandgap is allowed to vary between 0.75 and 1.25 eV while the other subcell bandgaps are fixed to 1.9, 1.4, and 0.67 eV. This example represents the addition of an approximately 1.0 eV third subcell into the InGaP/InGaAs/Ge LM material system. Three sets of curves are visible and are labeled α, β, and γ. The first set (α) use the initial functionality present in Segments, namely, generic extinction coefficient profiles, and finite but unrealistic thicknesses (up to 500 µm thick layers). These are given by the dashed and dotted black and blue lines. It also contains curves which use experimental absorption data but still without reasonable thickness limits, the purple and teal solid lines. The next set of results (β) show a highly degraded performance. These trends, the blue, red, and green solid lines, indicate segmented and unsegmented designs which use realistic absorption profiles as well as more realistic layer thickness limits ($\leq$5 µm). In both of these first two sets of curves (α and β) the number of segments in each subcell is optimized prior to consideration of absorption. This was the original implementation in Segments, a simplistic approach which was acceptable in the idealized absorption case but, as Figure 4.1 shows, was no longer reasonable when more realistic absorption and thicknesses were considered. Consequently, routines to optimize segmentation after the absorption is accounted for were written. The third set of curves (γ), the orange and gold solid lines, are these results. These show segmented designs which have been optimized for optical efficiency (orange) and for full optoelectronic power conversion efficiency (gold, high computational expense). Taken together

these results show the importance of considering realistic absorption and layer thicknesses in the simulation and optimization of segmented MJ solar cells.

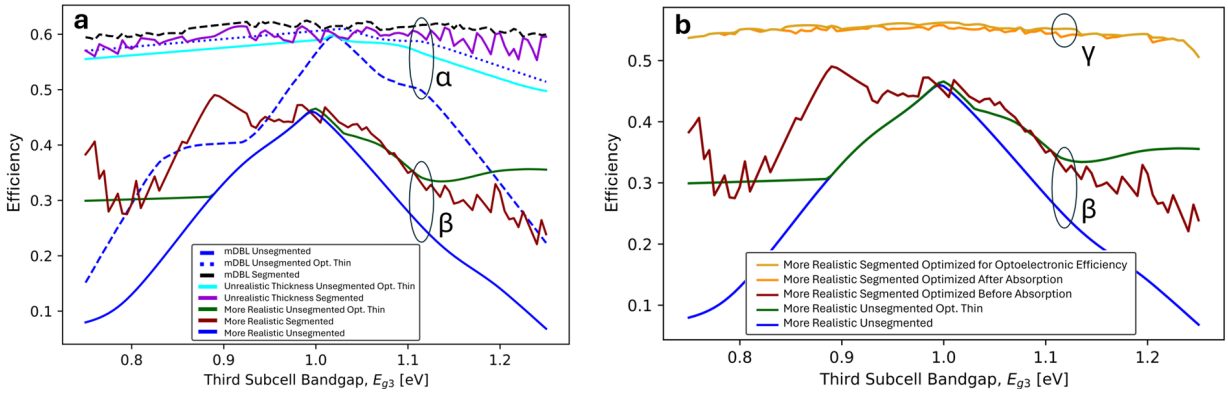

Figure 4.1: The effect of adding accuracy into the Segments mDBL codebase. The simulated performance of four-subcell MJ solar cells with and without subcell segmentation. The devices use materials with bandgaps of 1.9 eV/1.4 eV/Third/0.67 eV (variant third subcell bandgap). Three sets of curves, α, β, and γ, with different levels of realism as described in the text are visible. For clarity, α and γ are separated into subfigures a and b respectively. β is reproduced in both subfigures for comparison. Simulations are conducted at 1000 suns AM1.5D with maximum segment multiplicities of 10 segments per subcell.

To note; the unsegmented designs in Figure 4.1 have two variants distinguished by the "Opt. Thin" notifier. "Opt. Thin" designs employ the "etaOpt" photon sharing algorithm of Letay and Bett [172] which redistributes current among the subcells in the unsegmented designs by thinning the upper layers to achieve better current-matching. The etaOpt algorithm has not been applied to segmented designs to highlight the capability for better current-matching inherent in subcell segmentation alone. Subcell segmentation is optimized for each bandgap combination separately (at each x-axis point surveyed) with up to ten segments per subcell. It is this point-by-point optimization and the lack of etaOpt thinning which produces the sharp discontinuous nature of the segmented trends.

4.2 Subcell segmentation for the optimization of a four subcell multi-junction solar cell

Scope and impact

This presentation and proceeding at the Optical Society of America (OSA) Advanced Photonics Congress 2020 shows potential benefits of subcell segmentation, especially when considering a "third-of-four" subcell extension of the InGaP/InGaAs/Ge material system. I use the Segments mDBL codebase to compare the solar power conversion efficiency of 4-subcell designs with and without segmentation and as a function of CPV solar concentration factor. I compare designs where the bandgap of the third subcell material in the InGaP/InGaAs/Third/Ge stack can vary and show the expansion of high-efficiency in both bandgap and concentration space that is possible with subcell segmentation.

In this work I introduce the following novelties;

1. First study of subcell segmentation for a ∼1.0 eV third subcell extension to the InGaP/InGaAs/Ge system. Extension of the Segments modified detailed balance code.
   (a) Subcell segmentation greatly loosens the bandgap requirement of novel 3J extension materials; segmented designs from across 36% of the 0.75-1.25 eV bandgap space exceed the peak standard efficiency (with up to 10 segments per subcell at 800 suns AM1.5D)/
   (b) Subcell segmentation allows 4J devices to achieve extreme solar concentration operation.

This work informs future development of segmented MJ solar cells especially those looking to build-off of the InGaP/InGaAs/Ge material system.

Author contributions

Robert F.H. Hunter: As the lead student on this project I chose, designed, and executed this study. I used the Segments mDBL solar cell model which I extended for this work. I was lead author of the OSA 2020 conference abstract, presentation, and proceeding.

Dr. Christopher E. Valdivia: As a senior research scientist within the University of Ottawa's SUNLAB research group, Dr. Valdivia helped to guide my research. He provided detailed

feedback during the analysis of my simulation results and assisted in editing the manuscript. Dr. Valdivia is the original developer of Segments.

Laurier S. Baribeau: As a Master's student at the University of Ottawa's SUNLAB research group, Laurier provided detailed feedback on simulation results and on the manuscript.

Prof. Karin Hinzer: As the director of the University of Ottawa's SUNLAB research group and my supervisor, Prof. Hinzer oversaw my research. She provided detailed feedback during the analysis of my simulation results, and assisted in editing the manuscript.

Copyright

R.F.H. Hunter, C.E. Valdivia, L.S. Baribeau, K. Hinzer, "Subcell segmentation for the optimization of a four-subcell multijunction solar cell design," *OSA Advanced Photonics Congress*, July 13-16, 2020. Oral presentation. Proceeding; doi: 10.1364/PVLED.2020.PvM2G.6

Subcell Segmentation for the Optimization of a Four-Subcell Multijunction Solar Cell Design

Robert F.H. Hunter, Christopher E. Valdivia, Laurier S. Baribeau, Karin Hinzer
SUNLAB, Centre for Research in Photonics, University of Ottawa, 25 Templeton Street, Ottawa, ON, K1N 6N5, Canada
rhunt013@uottawa.ca

Abstract: Detailed balance calculation of subcell segmentation in the extension of the InGaP/InGaAs/Ge system to 4-subcell designs shows performance above the level of the standard optimal bandgap is achievable in conjunction with other practical advantages.

Multijunction solar cells (MJSC) hold the current record for highest solar power conversion efficiency by a wide margin. Yet, state-of-the-art designs fall far short of theoretical efficiency limits due to the simultaneous requirements of current-matching and lattice-matching. In this work the potential of the powerful design dimension of *subcell segmentation* to overcome this fundamental restriction is applied to designs with four subcells.

Subcell segmentation entails the splitting of MJSC subcells into several absorbing pn-junctions called *segments*. The basic architecture is shown in Fig. 1. The essential benefit of this new design technique is the shift of the current-limiting feature from the bandgap-dependent subcell to the thickness-dependent segment. This fundamentally decouples the lattice-matching and current-matching requirements and opens up vast new regions of practically-realizable design space to the potential of near-optimal efficiencies [1]. The thinner junctions also offer other benefits such as the reduction of series resistance power losses, greater carrier collection, greater voltages, and potential for improved radiation hardness.

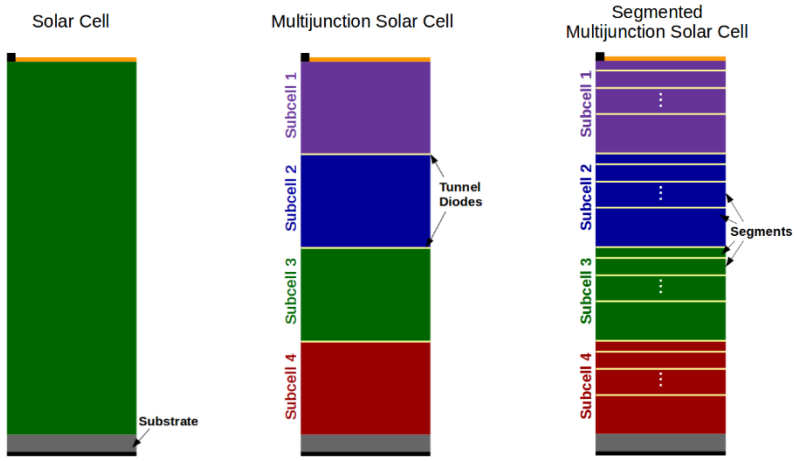

Fig. 1. Illustrative schematic view of solar cell architectures. Basic single-junction solar cell at left, conventional 4-junction MJSC at center, and a segmented 4-subcell device at right. Not to scale.

In this work we investigate the impact of segmentation for the optimization of 4-subcell multijunction solar cell designs. The extension of the standard high-efficiency MJSC material system, InGaP/InGaAs/Ge, is a natural choice of study due to the well-entrenched nature of the conventional technology. Research into 4-subcell designs using the standard stack has so far focused on materials meeting the optimal unsegmented device bandgap of ~1.0 eV [2]. In these and other new materials performance losses associated with higher defect densities may be present [3]. We will show how for materials with sub-optimal values of bandgap, diffusion length, and absorption coefficient performance losses can be mitigated with subcell segmentation.

This analysis is realized using a detailed-balance based computational model to generate idealized theoretical performance limits comparing both unsegmented and segmented variants. Current sharing is calculated using the current available to a given bandgap material from the spectrum. For unsegmented devices, photon sharing between

subcells is applied using the EtaOpt algorithm [3]. For segmented devices, we divide the photocurrent equally across all segments of a subcell (controlled via design thickness), and optimize the number of segments in each subcell by minimizing the photocurrent differences across all segments in the entire cell. This is calculated in the absence of photon sharing between subcells to highlight the benefit of segmentation alone. The number of segments is limited to 10 or less per subcell in this study. Thicknesses are computed using the absorption coefficient and the requirement that 97% of the above-bandgap-photons are absorbed. Experimental absorption coefficient data is considered as well as a generic square-root form (fit to GaAs) for energies above the bandgap.

Theoretical performances of 4-subcell designs are compared in Fig. 2. Here, the current-voltage characteristics of 1 cm^2 segmented and standard 4-subcell designs have been modelled under 1000-suns AM1.5D illumination (900 kW/m^2). A lumped sum series resistance of 15 $m\Omega \cdot cm^2$ plus 1 $m\Omega \cdot cm^2$ per tunnel diode is included in both the segmented and unsegmented designs. The generic square-root form for the absorption coefficient is used. The bandgaps of the first, second, and fourth subcells have been set at the typical values of the standard stack: 1.9 eV (disordered InGaP), 1.4 eV (InGaAs), and 0.67 (Ge), respectively. The bandgap of the third subcell is allowed to vary around the optimal ~1.0 eV point (from 0.75 eV to 1.2 eV in steps of 0.005 eV).

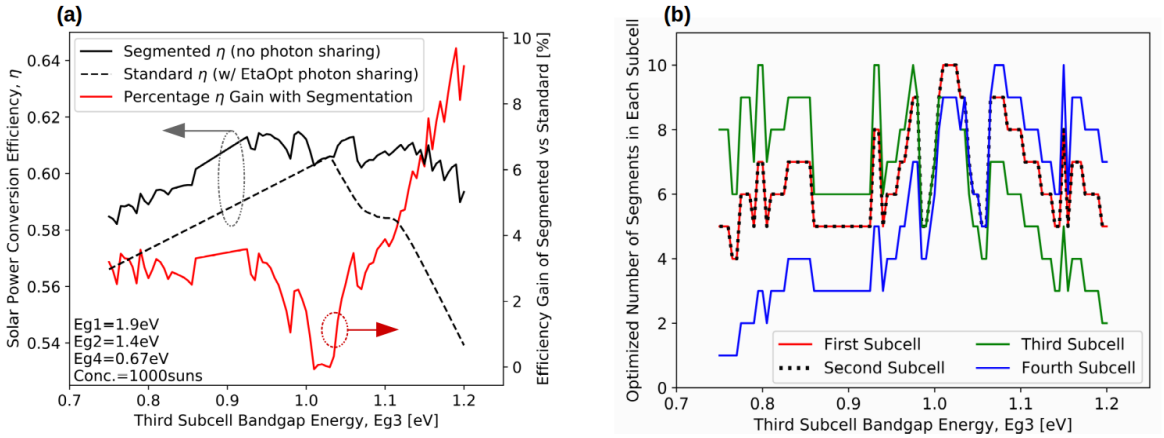

Fig. 2. (a) The solar power conversion efficiency for standard (unsegmented) and segmented 4-subcell MJSC designs using a disordered InGaP top cell, InGaAs second cell, and Ge fourth cell in conjunction with a variant bandgap third subcell. The relative efficiency gain obtained with segmentation compared to the unsegmented case is also shown.
(b) The number of segments in each subcell for the optimized segmented designs presented in Fig 2 (a).

Fig. 2 (a) shows the solar power conversion efficiency for standard and segmented designs as well as the gain in efficiency with segmentation relative to standard. With the exception of the standard design's optimal point, a significant efficiency gain is obtained due to segmentation across the investigated design space. Furthermore, an efficiency above the maximum unsegmented value (60.6% at E_{g3} of 1.03 eV) is obtained with segmentation for 45% of the considered third bandgap values. In Fig. 2 (b), the optimized number of segments in each subcell is plotted as a function of the third subcell's bandgap. The well-matched pair of 1.9 eV (disordered InGaP) and 1.4 eV (InGaAs) show a perfect overlap of their segment multiplicity curves. The standard optimal ~1.0 eV point exhibits high segment multiplicity indicating closely matched currents as expected. The study indicates that aside from a much greater design flexibility segmentation can reduce the maximum junction thicknesses to roughly 75% or less of their unsegmented values, an important consideration for novel materials which may suffer from short diffusion lengths.

A further discussion of results will be presented. More general conclusions for the extension of the InGaP/InGaAs/Ge stack to 4-subcells as well inferences on the wider applicability of the revolutionary new technique of subcell segmentation will be made.

[1] C.E. Valdivia and K. Hinzer, "Segmented multi-junction solar cells: A new opportunity for cell design & optimization," at 46th IEEE Photovoltaics Specialist Conference, 2019.
[2] P. Pearce et al., "Characterization of SiGeSn for use as a 1 eV sub-cell in multi-junction solar cells," at 7th IEEE WCPEC, 2018.
[3] M.M. Wilkins et al., "Design of thin InGaAsN(Sb) n-i-p junctions for use in four-junction concentrating photovoltaic devices", J. Photon. Energy, 7(2), 022502, 2017
[4] G. Létay and A.W. Bett, "EtaOpt – a program for calculating limiting efficiency and optimum bandgap structure for multi-bandgap solar cells and TPV cells," at 17th EUPVSEC, 2001

4.3 SiGeSn, subcell segmentation, and Synopsys Sentaurus simulations

Scope and impact

This formal international workshop poster contribution compares and contrasts the simulated performance of InGaP/InGaAs(/SiGeSn)(/Ge) 3J, 4J, 6J, and 7J solar cell designs. I use a Synopsys Sentaurus TCAD model to simulate designs with and without minimal subcell segmentation. The Synopsys Sentaurus TCAD model and SiGeSn material parameters and composition choice are informed from previous studies (Chapter 3). Here, I choose design variants within the InGaP/InGaAs/SiGeSn/Ge material system with consideration to device realization. The study outlined below was never formally published, but it is the apex of my Sentaurus TCAD simulations for SiGeSn solar cell work and is included here for completion.

I present the following novelties in this work;

1. Direct comparison of simulated optoelectronic performance for 4-subcell InGaP/InGaAs/SiGeSn/Ge solar cell without and with realistic subcell segmentation (the top two or three subcells segmented into two junctions apiece), including a comparison to a 3J InGaP/InGaAs/SiGeSn device and the 3J InGaP/InGaAs/Ge baseline.
2. Determination that the 3J InGaP/InGaAs/SiGeSn could potentially perform as well as or slightly better than the industry standard InGaP/InGaAs/Ge solar cell stack but without the use of the thick and expensive germanium substrate. The efficiency gain when adding the active substrate is 1% absolute.
3. Demonstration that segmented designs (2:2:1:1 or 2:2:2:1 top to bottom segment multiplicities) have significantly boosted (+70% or greater) open-circuit voltages and greatly reduced (-40% or greater) SiGeSn junction growth requirements compared to the unsegmented 4J variant.

This work is of interest to those developing the InGaP/InGaAs/SiGeSn/Ge material system or other extensions to the 3J InGaP/InGaAs/Ge multi-junction solar cell standard.

Author contributions

Robert F.H. Hunter: As the lead student on this project I chose, designed, and executed this study. I used the Synopsys Sentaurus TCAD model developed by Laurier for this pursuit. I was lead author of the workshop abstract and poster.

Dr. Christopher E. Valdivia: As a senior research scientist within the University of Ottawa's SUNLAB research group, Dr. Valdivia helped to guide my research. He provided detailed feedback during the analysis of my simulation results and assisted in editing the manuscript.

Laurier S. Baribeau: As a Master's student at the University of Ottawa's SUNLAB research group, Laurier developed the SiGeSn material and optoelectronic device models used in this study. Laurier finished his Master's degree without presenting this material.

Prof. Jacob J. Krich: As a professor with the University of Ottawa's SUNLAB research group, Prof. Krich provided valuable guidance and leadership to this project. He assisted in analysis of the results.

Prof. Alexandre W. Walker: As a research officer with the National Research Council of Canada's Quantum and Nanotechnologies Research Centre, adjunct University of Ottawa professor, and my supervisor, Prof. Walker has provided valuable guidance and leadership to this project and to myself. He assisted in analysis of the results.

Prof. Karin Hinzer: As the director of the University of Ottawa's SUNLAB research group and my supervisor, Prof. Hinzer oversaw my research. She provided detailed feedback during the analysis of my simulation results, and assisted in editing the manuscript.

Copyright

R.F.H. Hunter, C.E. Valdivia, L.S. Baribeau, J.J. Krich, Alex W. Walker, K. Hinzer, "Subcell Segmentation: Development and evaluation of next-generation, high-efficiency photovoltaic devices for the renewable energy transition and industry 4.0," *École de Physique des Houches Physics of Solar Cells Workshop*, April 3-8, 2022. Poster.

Research

The École les Houches poster covered general studies in subcell segmentation (such as Section 4.2 and Section 4.4), this study on subcell segmentation and SiGeSn, and outlined the AIIR-Power project on PPCs (Chapter 5). The other results from this poster are covered elsewhere in this thesis.

Figure 4.2 features the simulated current density-voltage (JV) characteristic (b) of the different solar cell designs in this study (schematically shown in (a)). High quality JV curves are observed with strong fill factors. A clear shift from higher currents (taller JV) to higher

voltages (wider JV) is present for the segmented devices. The simulation is at 1000 suns AM1.5D.

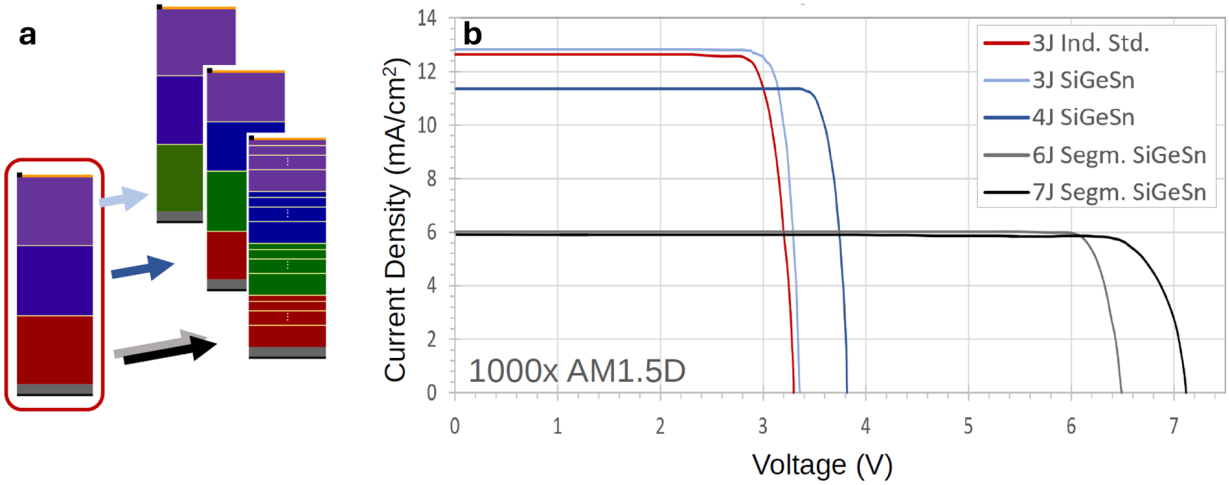

Figure 4.2: Current density-voltage curve of 3J, 4J, 6J, and 7J InGaP/InGaAs(/SiGeSn)(/Ge) solar cells with and without subcell segmentation. Curve data matches Figure 4.3. In (a), schematic representation of the test variants. In (b), current-voltage curves simulated with Sentaurus TCAD. A solar concentration of 1000 suns is used.

	3J Ind. Std.	3J SiGeSn	4J SiGeSn	6J Segm. SiGeSn	7J Segm. SiGeSn
Segments per Subcell	1:1:0:1	1:1:1:0	1:1:1:1	2:2:1:1	2:2:2:1
Thickness Note	Active Substrate	2.16µm SiGeSn	Active Substrate	550nm SiGeSn	1.32µm + SiGeSn
V_{oc} (V)	3.30	3.36	3.84	6.51	7.13
J_{sc} (mA/cm²)	12.63	12.60	11.49	5.96	5.92
Efficiency (%)	41.3	41.6	42.6	39.2	41.2

Figure 4.3: Segment multiplicities, thickness considerations, and current-voltage curve parameters for the different test variants. The corresponding JV curves are provided in Figure 4.2.

Figure 4.3 summarizes the JV curve parameters for each variant and correlates them with brief notes on thickness differences in the bottom two subcells. It shows that high efficiency is possible for all tested variants. These include designs with allowances for inactive substrates

and a 75% decrease in the required thickness of SiGeSn. The table also quantifies the current to voltage power shift of subcell segmentation.

4.4 Unlocking the potential for extreme solar concentration via subcell segmentation

Scope and impact

This conference presentation and proceeding from the 2022 International Conference on Concentrator Photovoltaic Systems offers subcell segmentation as a potential pathway to high-efficiency operation at extreme (1000+ suns) CPV solar concentrations for one and two subcell devices. I employ Segments mDBL calculations to compare one and two-subcell devices with and without segmentation as a function of illumination concentration. Varying the AM1.5D illumination spectrum between a single sun and the geometric limit of 45,600 suns solar concentration. I investigate the simulated efficiencies for fixed, optimized, and variable material bandgaps and study the effect of controlled junction multiplicities in the segmented designs.

I present the following novelties in this work;

1. Presentation of the potential for high-efficiency one- and two-subcell solar cell operation at extreme concentrations in the high hundreds, thousands, and even tens of thousands of suns. This potential is demonstrated for;

   (a) The per-concentration optimized and standard InGaP (1.7 eV)/InGaAs (1.1 eV) bandgap values.

   (b) As a function of maximum segments per subcell; here, the efficiency peak shifts from the high hundreds of suns solar concentration at segment multiplicities of $\leq$5 to tens of thousands at segment multiplicities of $\leq$15 (total junctions; $\leq$30). Gains of a few percent efficiency absolute are obtained as the peak shifts to thousands of suns illumination.

   (c) One-subcell optimized bandgap designs.

2. Demonstration of an expansion in the high-efficiency bandgap space across all concentrations. This evolution is tracked and it is shown that, even at the unsegmented peak concentration factor of 200 suns, the number of high-efficiency ($\geq$45%) designs doubles with segmentation. This advantage only grows at higher concentrations, at 2000 suns,

60% of the 2-subcell bandgap space can achieve theoretical efficiencies of 45% or higher with 15% of that achieving 50% efficiency or higher. At 2000 suns, unsegmented two-subcell solar cells have begun to succumb to series resistance losses, the peak efficiency is 40% and dropping.

These results show the theoretical feasibility of extreme CPV solar concentration operation from a cell perspective. While there are challenges; material systems which can handle high subcell segmentation, unavailability of high-bandgap tunnel diode recipes, optics which operate at 1000s of suns, module thermal management which does the same, etc., these proof-of-concept results may serve for those with an interest in extreme CPV solar concentrations.

Author contributions

Robert F.H. Hunter: As the lead student on this project I chose, designed, and executed this study. I use the Segments mDBL solar cell model which I extended for this work. I was lead author of the CPV-17 conference abstract, presentation, and proceeding.

Dr. Christopher E. Valdivia: As a senior research scientist within the University of Ottawa's SUNLAB research group, Dr. Valdivia helped to guide my research. He provided detailed feedback during the analysis of my simulation results and assisted in editing the manuscript. Dr. Valdivia is the original developer of Segments.

Laurier S. Baribeau: As a Master's student at the University of Ottawa's SUNLAB research group, Laurier provided detailed feedback on simulation results and on the manuscript.

Prof. Karin Hinzer: As the director of the University of Ottawa's SUNLAB research group and my supervisor, Prof. Hinzer oversaw my research. She provided detailed feedback during the analysis of my simulation results, and assisted in editing the manuscript.

Copyright

R.F.H. Hunter, C.E. Valdivia, L.S. Baribeau, K. Hinzer, "Unlocking the potential for extreme solar concentration via subcell segmentation," *17th International Conference on Concentrator Photovoltaic Systems (CPV-17)*, April 12-14, 2022. Oral presentation. Proceeding; doi: 10.1063/5.0099470

Unlocking the Potential for Extreme Solar Concentration via Subcell Segmentation

Robert F.H. Hunter[1, a)], Christopher E. Valdivia[1], Laurier S. Baribeau[1] and Karin Hinzer[1]

[1]SUNLAB, Centre for Research in Photonics, University of Ottawa,
25 Templeton St., Ottawa, Ontario, Canada, K1N 6N5

[a)] Corresponding author: rhunt013@uottawa.ca

Abstract. Under extreme solar concentrations, series resistance is a primary solar power loss mechanism for concentrator photovoltaic modules. In this paper, a detailed balance based approach demonstrates the mitigation of these losses by the application of subcell segmentation, a current matching architecture which divides each subcell into multiple pn junctions. By increasing the number of series-connected junctions, power extraction shifts from high current to high voltage, thus shifting theoretical efficiency peaks from hundreds to thousands of suns. Simultaneously, the high-efficiency bandgap design space expands across all concentrations by leveraging the current matching potential of subcell segmentation.

INTRODUCTION

Operation of concentrating photovoltaic (CPV) systems at extreme solar concentrations exceeding 1000 suns offers one of the most promising routes to attain cost-competitive systems based on multijunction solar cells (MJSC) [1,2]. Balance-of-system costs benefit from the reduced cell areas as well as boosted cell performance. At these very high concentrations, system performance is limited by the accumulation of series resistance losses which scale as the square of the cell current. One approach to mitigate series resistance losses in a series-connected architecture is by splitting the absorption over more pn junctions, as in MJSC designs with more subcells. This can reduce device current by a factor roughly proportional to the number of junctions while compensatingly increasing device voltage. I^2R losses are decreased while high-efficiency power collection is maintained as the device operation shifts to higher output voltages.

Increasing the number of junctions is a design strategy that has been used by a number of groups over the last two decades. The primary application has been the splitting of specific subcells in MJSC and silicon tandem solar cells to obtain higher efficiency by reducing current mismatch losses [3-9]. It has also been used to improve the carrier collection in organic photovoltaic cells [10]. A greater number of junctions is also beneficial for power conversion of narrow wavelength light. The vertically stacked photonic power converter (PPC) is a multijunction structure of single absorbing material achieving up to >65% monochromatic conversion efficiency and 35 V output voltage from a 30 junction device [11].

Subcell segmentation is the generalization of these approaches. It is a technique for systematically increasing the number of junctions in a MJSC device [12-16]. In this architecture, each subcell of a MJSC is segmented into multiple tunnel-diode-connected pn junctions called *segments*. Fig. 1a shows a simplified schematic of a segmented multijunction solar cell device. All segments in a given subcell are composed of the same material (denoted by color in Fig. 1). Each segment contains the emitter, base, front surface field, and back surface field layers.

The number and thicknesses of the segments in each subcell become powerful new design dimensions that can be tuned to obtain desired performance for a given application. Subcell segmentation may benefit applications requiring low current densities, high voltage output [11], improved radiation resistance, improved performance under non-uniform illumination [17], or which use materials with short diffusion lengths [10]. Subcell segmentation can also be used to satisfy current matching and leads to a large expansion in the volume of bandgap space that can yield near-ideal efficiencies. In the segmented MJSC, the number and thickness of the segments becomes the primary control for device current since current matching occurs at the segment level. This loosens the constraints on material systems as bandgap energies play a secondary role in current matching.

In this work a detailed balance based comparative analysis of unsegmented and segmented designs is undertaken. The ability to unlock high theoretical performance at extreme solar concentration operation exceeding 1000 suns is highlighted. The expansion of high-efficiency bandgap space as a function of concentration is also presented.

DETAILED BALANCE BASED COMPUTATIONAL MODEL

An extended detailed balance based computational model has been developed to investigate and compare unsegmented and segmented multijunction solar cell designs.

We consider 1-cm^2 sized solar cells composed of series-connected segments, each modelled as a single diode with ideality factor of one and a unity internal quantum efficiency. The reverse saturation currents are calculated at the radiative limit, at room temperature. A lumped sum series resistance penalty with magnitude typical of MJSC optimized for high-concentration is applied (15 m$\Omega\cdot$cm^2 plus 1 m$\Omega\cdot$cm^2 per tunnel diode), as well as a small shunting effect (10^7 $\Omega\cdot$cm^2).

Cells are illuminated by an AM1.5D input spectrum (900 W/m^2) with a uniform beam profile. The unsegmented devices collect and share photons following the etaOpt optical thinning algorithm [18]. The segmented devices are designed to collect 99% of available photons within the total absorber thickness of each subcell and have no optical thinning optimization applied to emphasize the current matching ability of segmentation alone. The subcell's total absorber thickness is divided to equally split the available photo-current, up to a maximum number of segments per subcell allowed. The number of segments is optimized for full cell conversion efficiency.

This idealistic model excludes several factors that would impact the performance of realistic devices, including several penalties and benefits that arise from increasing the number of junctions. This model does not include the shading losses associated with gridline surface coverage, nor internal or external reflections from layer interfaces. Parasitic absorption could increase due to the addition of auxiliary layers (front and rear surface fields) and could be especially important for tunnel diodes within the top subcell, for which novel high-transparency wide-bandgap diodes may be required. Fortunately, the reduced current densities obtained with subcell segmentation relax the requirements for high peak tunneling current and high conductivity in comparison to standard unsegmented designs. Segmentation also splits the total absorber thickness of each subcell into multiple thinner segments which each have the potential to produce logarithmically larger voltages, and to offer improved carrier collection especially for materials and designs that conventionally would be diffusion limited. The larger number of junctions allows a greater opportunity for luminescent coupling to redistribute excess current to reduce or eliminate current mismatch, as demonstrated previously for highly segmented vertically stacked PPCs [19]. For segmented solar cells, this will lead to greater robustness under nonideal bandgaps, temperature change, and spectral variation [14].

UNLOCKING EXTREME CONCENTRATIONS

With subcell segmentation, a variable number of junctions leads to a tunable cell current and voltage. This advantage is employed in the segmented MJSC to allow access to high theoretical performance at extreme concentrations above 1000 suns. This is shown for two-subcell designs with varying segmentation in Fig. 1 and Fig. 2, and one-subcell designs with up to a maximum of 30 junctions in Fig. 3.

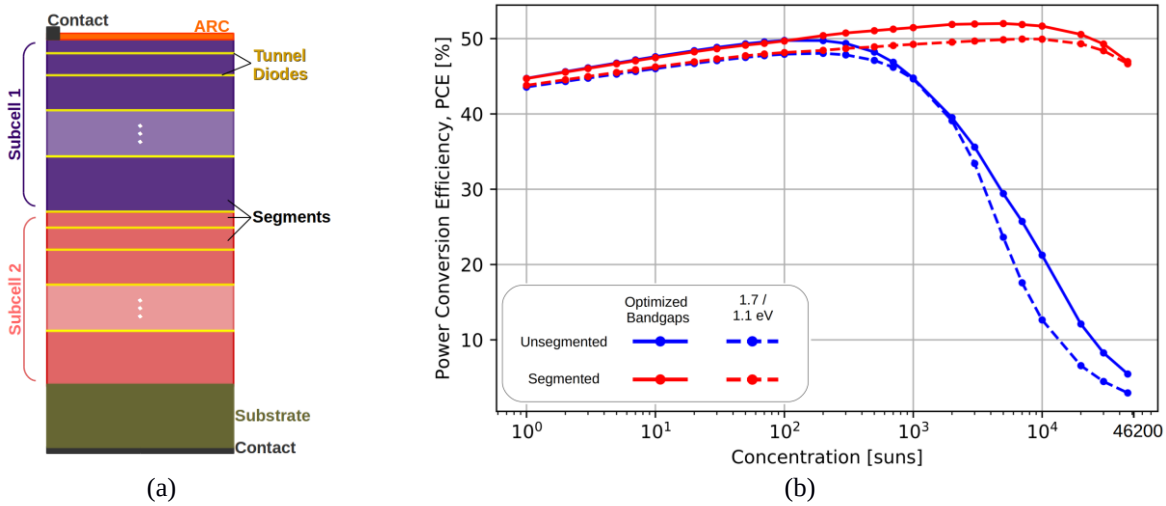

FIGURE 1. (a) Schematic illustration of a two-subcell segmented multijunction solar cell. Each segment contains an emitter, base, and front and back surface field layers. Not to scale. (b) Solar power conversion efficiencies as a function of concentration for unsegmented (blue) and segmented (red) two-subcell designs. Solid lines denote bandgap combinations optimized at each concentration. Dashed lines denote designs with subcell bandgaps fixed at 1.7 and 1.1 eV.

In Fig. 1b the solar power conversion efficiency (PCE) as a function of concentration factor has been plotted for two-subcell designs. The dashed blue line depicts the simplest case: an unsegmented device with fixed subcell bandgaps. The values of the record two-subcell device, 1.7 and 1.1 eV, are used [20]. The solid blue line depicts designs with efficiency optimized bandgaps within the ranges of 1.0 to 2.2 eV and 0.5 to 1.7 eV for the top and bottom subcell respectively. A step size of 0.05 eV is used. The bandgap combination is optimized at each concentration. At concentrations below 1000 suns, optimization leads to smaller bandgaps than 1.7 and 1.1 eV. Above 1000 suns, the optimized bandgaps climb to the upper bounds of the bandgap space investigated to reduce the I^2R electrical power losses by extracting fewer carriers but at higher voltage, a trend which is visible in the comparison between Fig. 4a and Fig. 4c.

The red curves of Fig. 1b show the efficiency of the corresponding segmented MJSC, with a maximum of ten segments per subcell. For the solid red line, bandgaps and segmentation are optimized simultaneously at each concentration. Fig. 1b shows the potential to unlock high-efficiency operation at concentrations above 1000 suns that subcell segmentation offers. For the 1.7 and 1.1 eV, devices the peak efficiency increased from 200 to 7000 suns after subcell segmentation. For the optimized bandgap devices, the peak efficiency increased from 100 suns up to 5000 suns with segmentation. An increase in the peak efficiency on the order of 2% absolute is also obtained in both cases. The sharp efficiency drop-offs in the unsegmented blue curves have been pushed to concentrations exceeding 10,000 suns due to the reduction in I^2R electrical power losses. Under these conditions, segmentation became beneficial at ~70 suns (see Fig. 2b). Beyond this, the segmentation advantage increased until saturation at ~10,000 suns when the maximum segmentation of ten segments per subcell was reached. High theoretical efficiencies up to full concentration for PV application (46,200 suns) are maintained in the segmented MJSC.

The series resistance losses can be mitigated further if a greater number of junctions is allowed. In Fig. 2a the efficiency versus concentration is plotted for two-subcell optimized designs but with a variant maximum number of segments per subcell. The unsegmented design being the special case of maximum one segment per subcell. Fig. 2b shows the total number of segments for each device. As segmentation is allowed to increase, the location of the theoretical peak efficiency can be pushed to higher concentrations. For devices with up to a total of 30 junctions, a number which has already been realized in state-of-the-art photonic power converters [11], the peak efficiency reaches 10,000 suns. For devices with up to a total of 40 junctions the peak efficiency reaches 20,000 suns and is achieved by a device with 35 junctions.

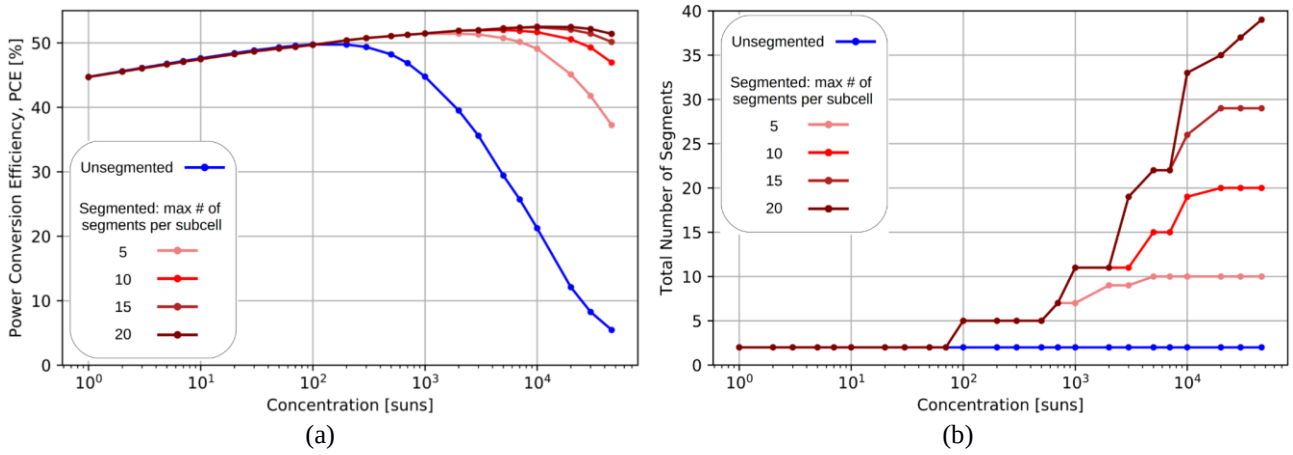

(a) (b)

FIGURE 2. (a) Solar power conversion efficiencies as a function of concentration for two-subcell designs with optimized bandgap combinations. Unsegmented designs shown in blue and segmented designs with an increasing number of maximum segments per subcell shown in progressively darker red. (b) The total number of segments in each design.

Subcell segmentation can be applied to devices with any number of subcells. Fig. 3a shows the efficiency variation with concentration for one-subcell (single absorbing material) devices. This is an identical architecture to the vertically stacked photonic power converter [11] but optimized for the solar spectrum rather than a narrow wavelength source. Here, the bandgaps are optimized at each concentration within the bandgap space of 0.5 to 2.2 eV in 0.05 eV steps. A maximum of 30 segments is allowed. The same ability to unlock extreme concentrations is observed, with the peak efficiency shifting from 50 to 10000 suns. Similar analysis has been performed previously for three- and four-subcell devices [12].

Fig. 3b shows the number of subcells in the optimized one-subcell designs. Segmentation becomes advantageous above 30 suns for the simulated devices. The number of junctions increases quickly in the hundreds and thousands of suns before saturating at ~10,000 suns at the maximum of 30 segments.

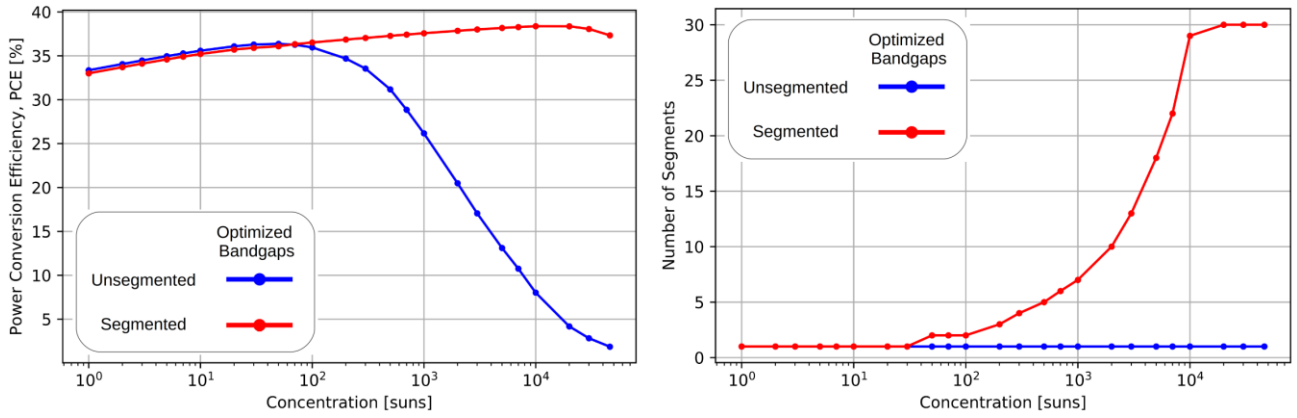

(a) (b)

FIGURE 3. (a) Solar power conversion efficiencies as a function of concentration for unsegmented (blue) and segmented (red) one-subcell designs. Bandgap combinations are optimized at each concentration. (b) The number of segments in each design.

In the above studies, the cell resistance was fixed to 15 m$\Omega \cdot cm^2$ plus 1 m$\Omega \cdot cm^2$ per tunnel diode and shading losses were not considered. This is a simplified illustrative scenario. In a realistic device, the grid pattern would be optimized to determine the best trade-off between shading and resistive losses for each concentration and design (bandgaps, segmentation). As solar concentration is increased, cell performance becomes more sensitive to changes in the resistance through the I^2R electrical power loss. The increased current density requires greater grid coverage [2]. This results in a lower series resistance but increases the shading losses. The reduced currents that subcell segmentation brings allow a reduction in grid coverage and the associated shading losses. At extreme concentrations this effect will be amplified.

While thermal variation was not considered in these simulations (fixed cell temperature of 25ºC), a secondary benefit for resistive thermal effects is also expected. The lower current in segmented devices leads to lower thermal loads via a reduction in current-induced Joule heating, enabling higher efficiencies or less need for cooling.

EXPANDING HIGH-EFFICIENCY BANDGAP SPACE

By shifting current matching from the design of the subcell to the design of the segment, subcell segmentation boasts a prodigious potential for increasing the number of bandgap combinations that could achieve near-ideal performance [12]. This expansion of high-efficiency bandgap space is visualized in Fig. 4 and Fig. 5. Two-subcell designs with a maximum of ten segments per subcell are considered

In the top row of Fig. 4 the solar PCE at 200 suns concentration for (a) unsegmented and (b) segmented designs is plotted over the investigated bandgap space. The black points and white stars give the optimal and 1.7/1.1 eV bandgap combinations and associated efficiencies. An identical color scale in the two plots illuminates the differences in the shape of the power conversion efficiency trends. The unsegmented designs feature a sharp angular climb which is softened by the optical thinning for like-valued bandgap combinations. More resemblant of a plateau, the current matching freedom of segmentation leads to a wider high-efficiency landscape of similar or greater height compared to the peak of the unsegmented trend. Further widening of the high-efficiency plateau is possible if optical thinning is considered or if the segmentation is increased.

The 200 suns condition is a best case scenario for the unsegmented designs, corresponding to the point right before series resistance losses begin to dominate. In contrast, the bottom row of Fig. 4 shows the corresponding plots for 5000 suns concentration, well beyond the conventional operational limit of unsegmented MJSCs. The color scale is retained and shows immediately that the advantages of segmentation have increased with concentration. The shift of the unsegmented peak's bandgap combination with concentration is visible, moving from 1.55/0.95 eV at 200 suns to 2.00/1.55 eV at 5000 suns. The optimal segmented bandgaps vary up to 0.15 eV but with no distinguished concentration trend.

In Fig. 5 the shape of the high-efficiency region is investigated as a function of solar concentration. The fraction of bandgap space exceeding power conversion efficiency thresholds of 20% to 50%, in steps of 5%, is plotted for (a) unsegmented and (b) segmented designs. In both cases, the high-efficiency bandgap space expands with concentration factor and is widest at the optimal concentration. At 200 suns, the unsegmented design's peak, 0.40 of the unsegmented design space exceeds 40% power conversion efficiency. This fraction is nearly doubled, to 0.78, with subcell segmentation. At 5000 suns, the maximum efficiency for unsegmented designs is 29%, meanwhile 0.83 of the segmented bandgap space exceeds 40% efficiency and 0.15 exceeds 50% power conversion efficiency.

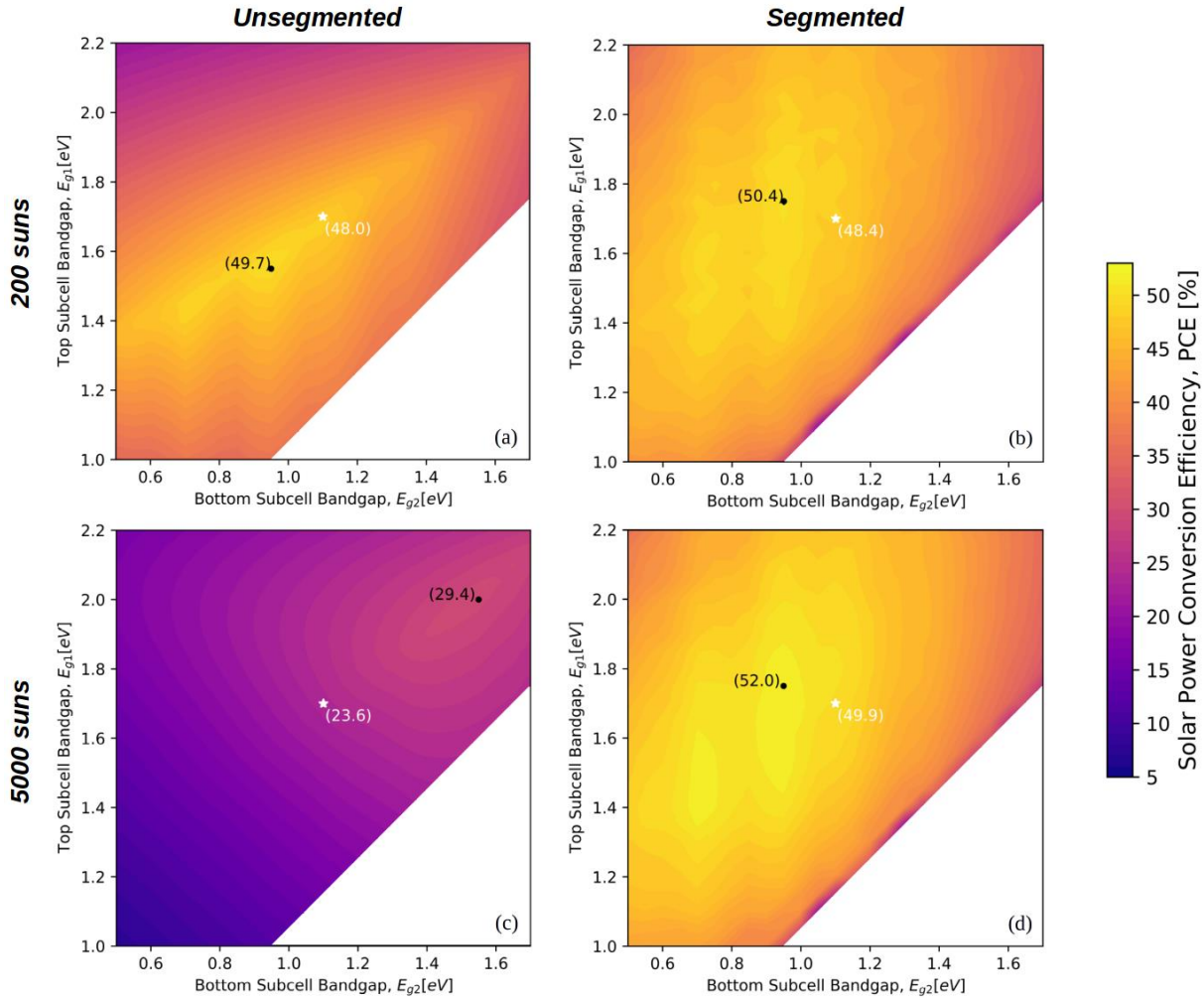

FIGURE 4. Solar power conversion efficiency as a function of bandgap combination for two-subcell designs. Unsegmented MJSC with optical thinning are shown in the left column. Segmented MJSC with a maximum of ten segments per subcell in the right. The top row shows performance at a 200 suns AM1.5D. The bottom row shows performance at 5000 suns. Black dots show the peak efficiency in the bandgap space while white stars signify the bandgap combination of 1.7 and 1.1 eV.

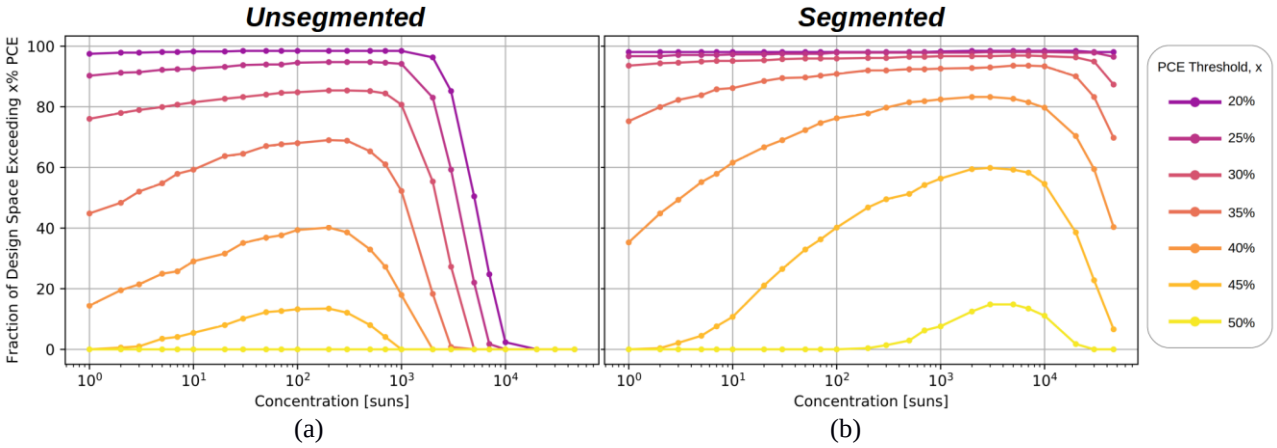

FIGURE 5. High-efficiency bandgap space visualized using absolute solar power conversion efficiency thresholds. Fraction of bandgap space exceeding threshold is plotted as a function of concentration. (a) Unsegmented MJSC with etaOpt optical thinning. (b) Segmented MJSC with efficiency optimized segmentation and a maximum of ten segments per subcell.

DISCUSSION AND CONCLUSIONS

An important challenge for the adoption of subcell segmentation is a present lack of wide bandgap tunnel diodes with simultaneous high transparency and low resistance for use within the top subcell. However, for the tunnel diodes lower in the epitaxial stack, established materials and designs have been exemplified in PPC devices with up to 30 junctions [11].

In this work detailed balance based calculations have demonstrated the potential to operate CPV cells at extreme concentrations far above 1000 suns using subcell segmentation. Its larger and variant number of junctions increases the maximum efficiency (+2.0% abs.), increases the concentration yielding the peak efficiency (shifts from 200 to 5000 suns), and expands the high-efficiency volume of the bandgap space (doubling even for the optimal 200-suns concentration of the unsegmented design). These advantages offer a pathway to the development of new applications and new materials for concentrator photovoltaic systems, with a potential for cost-competitive integration into the mainstream power generation market under extreme concentrations [1,2]. As the III-V manufacturing and material technology continues to mature, subcell segmentation can become an increasingly powerful tool for high efficiency multijunction solar cell design.

REFERENCES

1. M. El-Gahouchi *et al.*, "Cost-effective energy harvesting at ultra-high concentration with duplicated concentrated photovoltaic solar cells," in *Energy Science & Engineering*, 2020, vol. 8, p. 2760–2770.
2. A. Vossier *et al.*, "Very high fluxes for concentrating photovoltaics: considerations from simple experiments and modeling," in *Renewable Energy*, 2012, vol. 38, p. 31–39.
3. D.J. Aiken, "InGaP/GaAs/Ge multi-junction solar cell efficiency improvement using epitaxial germanium," in *Proc. 28th IEEE Photovolt. Spec. Conf.*, 2000, p. 994–997.
4. R.R. King et al., "High-voltage, low-current GaInP/GaInP/GaAs/GaInNAs/Ge solar cells," in *Proc. 29th IEEE Photovolt. Spec. Conf.*, 2002, p. 852–855.
5. M.P. Lumb et al., "Drift-diffusion modeling of InP-based triple junction solar cells," in *Proc. Photon. West - Phys., Simul. Photonic Eng. Photovolt. Devices II*, 2013, paper 86201G.
6. M.K. Yakes et al., "Split InAlAs top cell enabled four-junction solar cell lattice matched to InP," in *Proc. 43rd IEEE Photovolt. Spec. Conf.*, 2016, p. 2836–2838.
7. Y. Huang and H. Yang, "Design of InP-based metamorphic high-efficiency five-junction solar cells for concentrated photovoltaics," in *Semiconductor Science and Technology*, 2015, vol. 30, art. no. 105031.
8. Z. Ren et al., "The GaAs/GaAs/Si solar cell – Towards current matching in an integrated two terminal tandem," in *Solar Energy Materials & Solar Cells*, 2017, vol. 160, p. 94–100.
9. R. Garrison and R. Kleiman, "Higher efficiency tandem solar cells through composite-cell current matching," in *Optical Express*, 2019, vol. 27, no. 8, p. A543–A571.
10. M. Ryyan Khan, B. Ray, and M.A. Alam, "Prospects of layer-split tandem cells for high-efficiency opv" in *Solar Energy Materials & Solar Cells*, 2014, vol. 120, p. 716–723.
11. S. Fafard *et al.*, "Ultrahigh efficiency optical power convertors based on the vertical epitaxial heterostructure architecture (vehsa) design," in *1st Opt. Wirel. Fiber Power Transm. Conf.*, 2019.
12. C.E. Valdivia and K. Hinzer, "Subcell segmentation for current matching and design flexibility in multi-junction solar cells," in *IEEE Journal of Photovoltaics*, 2020, vol. 10, issue 5, p. 1329–1339.
13. C.E. Valdivia and K. Hinzer, "Current-matching of high-voltage multijunction solar cells via subcell segmentation," in *Proc. 7th Photon. West – Phys., Simul., Photon. Eng. Photovolt. Devices*, 2018.
14. C.E. Valdivia and K. Hinzer, "Subcell segmentation: a novel method to current match multi-junction solar cells," in *Proc. 14th Int. Conf. Concentrator Photovolt. Syst.*, 2018.
15. C.E. Valdivia and K. Hinzer, "Segmented multi-junction solar cells: a new opportunity for cell design & optimization," in *Proc. 46th IEEE Photovolt. Spec. Conf.*, 2019, p. 1–4.
16. R.F.H. Hunter *et al.*, "Subcell segmentation for the optimization of a four-subcell multijunction solar cell design," in *OSA Advanced Photonics Congress (AP) 2020 (IPR, NP, NOMA, Networks, PVLED, PSC, SPPCom, SOF)*, 2020, paper PvM2G.6.
17. C.E. Valdivia *et al.* "Many-junction photovoltaic device performance under non-uniform high-concentration illumination," in *Proc. 13th Int. Conf. Concentrator Photovolt. Syst.*, 2017.
18. G. Létay and A. W. Bett, "EtaOpt—A program for calculating limiting efficiency and optimum bandgap structure for multi-bandgap solar cells and TPV cells," in *Proc. 17th Eur. Photovolt. Sol. Energy Conf.*, 2001, p. 1–4.
19. M. Wilkins *et al.*, "Luminescent coupling in planar opto-electronic devices," in *Journal of Applied Physics*, 2015, vol. 118, art. no. 143102.
20. N. Jain *et al.*, "High-efficiency inverted metamorphic 1.7/1.1 eV GaInAsP/GaInAs dual-junction solar cells," in *Applied Physics Letters*, 2018, vol. 112, art. no. 053905.

Chapter 5

Multi-junction photonic power converters

In this chapter I highlight my contributions to the AI-enhanced design of photonic power converters (PPCs) an innovation which is motivated by the highly complex and correlated design spaces of MJ PPCs. In Section 5.1, I describe the international collaboration, AIIR-Power, that achieved this feat and my place within it. In Section 5.2, I introduce "aiirmap", an AI/ML-enhanced python-based simulation environment that I designed and built for AIIR-Power but which has more general utility, as will be shown. Finally, in Section 5.3, I present work which is currently under peer review with Scientific Reports. Therein I compare and contrast standard Beer-Lambert 10J 1550 nm PPC designs and those optimized with and without ML enhancement. I show how machine learning can be a powerful tool for MJ PPC design: simultaneously helping us to understand the design landscape while providing significant optimization acceleration. This work indicates the beginnings of a paradigm shift towards ML-enhanced design of active optoelectronic devices such as MJ PPCs.

5.1 AIIR-Power: Record setting photonic power converter design

AIIR-Power is a Canadian-German collaboration between the University of Ottawa, the National Research Council of Canada, Optiwave Systems Inc. (Ottawa), Broadcom Canada, AIXTRON SE (Germany), and the Fraunhofer Institute for Solar Energy Research (Germany). The full project name is descriptive and apt; *A*rtificial *I*ntelligence Enhanced Design and Manufacturing

of *I*nfra*r*ed Photonic Power Converters for *Power* and Telecom [173, 174]. The University of Ottawa involvement was on the AI-enhanced design side of the project. This involved developing a calibrated optoelectronic device model [51, 175], with luminescent coupling [92, 98, 99], which can be implemented within an AI-capable environment [46, 48–50]. My work focused on the third of these tasks. Clear overlap exists between the three tasks and I am grateful to my fellow developers, Drs. Gavin Forcade and Paige Wilson, for their contributions and expertise. The achievements of AIIR-Power have been disseminated in seven conference contributions and two journal papers so far and include the achievement of record PPC efficiency at 1445 nm illumination wavelength [51].

Journal papers;

G.P. Forcade, D.P. Wilson, M.N Beattie, H. Helmers, R.F.H. Hunter, O. Hohn, LP. St-Arnaud, C.E. Valdivia, D. Lackner, A.W. Walker, J.J. Krich, and K. Hinzer, "Multi-junction laser power converters exceeding 50% efficiency in the short wavelength infrared", *Cell Reports Physical Science*, 6(6):102610. May 2025. https://doi.org/10.1016/j.xcrp.2025.102610 [51]

*R.F.H. Hunter, G.P. Forcade, Y. Grinberg, D.P. Wilson, M.N. Beattie, C.E. Valdivia, M. de Lafontaine, L.-P. St-Arnaud, H. Helmers, O. Höhn, D. Lackner, C. Pellegrino, J.J. Krich, A.W. Walker, K. Hinzer, "Machine learning enhanced design optimization and knowledge discovery for multi-junction photonic power converters", *Scientific Reports*. In peer-review. July 2025. [46]

*This journal paper is discussed in Section 5.3 below.

Conference contributions;

G.P. Forcade, M.N. Beattie, C.E. Valdivia, H. Helmers, O. Hohn, P. Wilson, L-P. St-Arnaud, R.F.H. Hunter, D. Lackner, J.J. Krich, A.W. Walker, and K. Hinzer, "High-Performance Multi-Junction C-Band Photonic Power Converters: Calibrated Optoelectronic Model for Next Generation Designs", *50th IEEE Photovoltaic Specialists Conference (PVSC)*, San Juan, Puerto Rico, 2023. [Oral, Best student finalist] [175]

P. Wilson, G.P. Forcade, R.F.H. Hunter, M.N. Beattie, A.W. Walker, Y. Grinberg, H. Helmers, O. Hohn, D. Lackner, J.J. Krich, K. Hinzer, "Quantifying the luminescent coupling process in C-band multi-junction photonic power converters", *Photonics West*, San Fransisco, USA, 2024. [Oral] [98]

**R.F.H. Hunter, G.P. Forcade, Y. Grinberg, D.P. Wilson, M.N. Beattie, C.E. Valdivia, M. de Lafontaine, L.-P. St-Arnaud, H. Helmers, O. Höhn, D. Lackner, C. Pellegrino, J.J. Krich, A.W. Walker, K. Hinzer, "Using machine learning to optimize multi-junction photonic power converters", *SPIE OPTO 2024*, San Francisco, California, United States, 2024. [Oral] [47]

**K. Hinzer, R.F.H. Hunter, D.P. Wilson, G.P. Forcade, M.N. Beattie, C.E. Valdivia, O. Hohn, L-P. St-Arnaud, C. Pellegrino, D. Lackner, Y. Grinberg, J.J. Krich, A.W. Walker, H. Helmers, "Multi-junction photonic power converters: AI enhanced design optimization", *52nd IEEE Photovoltaic Specialists Conference (PVSC)*, Seattle, USA, 2024. [Poster] [48]

**K. Hinzer, R.F.H. Hunter, D.P. Wilson, G.P. Forcade, M.N. Beattie, C.E. Valdivia, O.Hohn, L-P.St-Arnaud, D. Lackner, Y. Grinberg, M. de Lafontaine, C. Pellegrino, J.J. Krich, A.W. Walker, H. Helmers, "C-band Multi-Junction Photonic Power Converters: AI Techniques for Optimized Designs and Role of Luminescent Coupling", *6th Optical Wireless and Fiber Power Transmission Conference (OWPT)*, Japan, 2024. [Invited talk] [49]

**Y. Grinberg, D.-X. Xu, M.Al-Digeil, D. Melati, R.F.H. Hunter, A.W. Walker, G.P. Forcade, J.J. Krich, K. Hinzer, M.M. Masnad, O. Liboiron-Ladoceur, P. Cheben, J.H. Schid, and S. Janz, "Dimensionality Reduction in Photonics Design – New Methods and Applications", *Photonics North 2024*, Vancouver, Canada, 2024. [Invited talk] [50]

P. Wilson, G.P. Forcade, R.F.H. Hunter, A.W. Walker, Y. Grinberg, J.J. Krich, and K. Hinzer, "Impact of Luminescent Coupling on Multijunction InGaAs Photonic Power Converters under Current Mismatched Conditions in the C-Band", *Photonics North 2025*, Ottawa, Canada, 2025. [Oral] [99]

**These conference presentations specifically feature my work (as outlined in the sections below).

5.2 aiirmap: Python based framework for machine learning enhanced photonic device design

My central contribution to the AIIR-Power project was inception and creation of the computational framework which combines ML techniques with the predictive device model. I call this Python based framework "aiirmap". I previously introduced the predictive simulation model, written in Synopsys Sentaurus TCAD, in Subsection 2.4.2. Likewise, I introduced basic ML concepts in Subsection 2.4.3. In this section I outline the basic functionality and features of aiirmap. The aiirmap user's manual is provided in A.

The aiirmap framework features high-throughput batch run, optimization, databasing, and ML capabilities which can be combined with any simulation software which can interact with Python. For AIIR-Power I have included Synopsys Sentaurus TCAD interfaces and the principal component analysis dimensionality reduction algorithm. In aiirmap I consciously chose to employ the Python coding language and standard Python modules such as pandas for databasing

[176, 177] and scikit-learn for optimization and ML [178] to improve it's adoptability. aiirmap is organized in such a way that implementation of new ML algorithms and simulation software interfaces is as easy as possible. Users need only to define new subclasses of existing classes which are already incorporated into the central codebase functionality. aiirmap is offered as an open-source software [179]. It features nearly 29,000 lines of commented code.

ML is a tool, to leverage it properly aiirmap is highly customizable and versatile. Datasets are substantiated as databases which use pandas DataFrames at their core, with each row of the DataFrame indicating a different design and each column recording the input and output variables. Databases are easily generated, sent to and collected from Sentaurus, manipulated (cleaned, split, combined, thresholded, etc.), subjected to dimensionality reduction, and analyzed using user-defined Python run files. Databases and dimensionality reduction instances are saved for later use with comma separated value files and pickle compressed binary format respectively.

aiirmap interacts with Synopsys Sentaurus TCAD in two ways: collection of results and batch run control. Collection of results is instantiated in the Sentaurus project using the Python tool. The collector script directly records input parameter values and Sentaurus workbench node numbers for each experiment during preprocessing (see Figure 2.14). Due to the Sentaurus code flow (Figure 2.14), output variable values are collected from the Sentaurus gvars.dat file. This occurs when the project run is finished or when requested by aiirmap. It is at this point that they are matched with the input parameters and saved to an aiirmap database. The aiirmap Sentaurus collection protocol allows for use of the Sentaurus gopt optimization tool [180] which creates child projects for the optimization of each design. These are tracked and linked to their parent algorithmically in the collection code. The Sentaurus batch run control is instantiated through protocols which directly write the Sentaurus project's gtree.dat file which codifies the state of the Sentaurus workbench [162]. aiirmap runs an automatic procedure which takes an input database, splits it into easy to handle subset databases, which it runs sequentially, collecting and collating the results as it goes. This functionality was integral to running large datasets since the Synopsys Sentaurus workbench suffers memory issues if more than a few tens of experiments are run at any one time. This high-throughput batch run capability allowed the computation and analysis of over 345,000 MJ PPCs designs and 72 instances of dimensionality reduction over the course of my AIIR-Power work.

The general applicability of the aiirmap framework has already been demonstrated. aiirmap was adopted by fellow SUNLAB researchers for studies outside the scope of AIIR-Power. Specifically, Prof. Mathieu de Lafontaine has used aiirmap to run particle swarm optimizations of betavoltaic devices simulated using multiple software (Monte Carlo simulation of beta particle energy deposition, custom ionization radiation to carrier conversion, and Synopsys Sentaurus TCAD simulation of carrier drift-diffusion in the device). More information can be found in the

research contributions listed below [181–183].

M. de Lafontaine, R.F.H. Hunter, G.P. Forcade, J.P.D. Cook, D. Drouin, J.J. Krich, K. Hinzer, "p-i-n Betavoltaic Cells under 63Ni Irradiation: Quantifying Carrier Collection and Power Output", *52nd IEEE Photovoltaic Specialists Conference (PVSC)*, Seattle, USA, 2024. [Oral] [181]

M. de Lafontaine, R.F.H. Hunter, G.P. Forcade, J.P.D. Cook, J. Patel, B. Ellis, H. Fritzsche, K. Hinzer, "Optimizing Tritium Powered GaAs p-i-n and p-n Betavoltaic Cells", *14th International Conference on Tritium Science and Technology*, Ottawa, Canada, 2025. [Oral] [182]

M. de Lafontaine, C. Succar, R.F.H. Hunter, G.P. Forcade, J.P.D. Cook, J. Patel, B. Ellis, H. Fritzsche, J.J. Krich, K. Hinzer, "Figures of merit to quantify carrier collection in betavoltaics: Gain and gain efficiency," *Cell Reports Physical Science*. In print. July 2025. [183]

5.3 Machine learning enhanced design and knowledge discovery for multi-junction photonic power converters

Scope and impact

This first-author journal article currently in the late stages of peer-review with Scientific Reports demonstrates the multidimensional utility of a dimensionality reduction enhanced MJ PPC design optimization compared to classical optimization and conventional design approaches. I use calibrated Synopsys Sentaurus TCAD device models, embedded within the AI/ML-enhanced Python environment aiirmap, to investigate 10J 1550 nm PPC on-substrate designs. I conduct tens of thousands of optical optimizations and compare the optimal designs for datasets which include dimensionality reduction enhancement to those which did not. I analyze the reduced dimensional subspace construction for physical phenomenology in the design space. I contrast the simulated optoelectronic performance of the ML-enhanced optima, to classically obtained optima, and to the industry standard approach.

In this work I introduce the following novelties;

1. First-ever application of dimensionality reduction to the design of active III-V optoelectronic devices. Development of a novel simulation environment, aiirmap, with an integrated calibrated device model and machine learning (ML) capabilities.
2. Demonstration that the ML-enhanced method accelerates the design optimization of the MJ PPCs. It produces a much greater number of designs which attain the highest

optical performance, which have greater layer thickness variability, and which have a lower computational cost than those found using classical optimization algorithms alone.

3. Demonstration of the potential for knowledge discovery inherent in the ML-enhanced method by showing that the reduced dimensional subspace construction encodes fundamental physics in the design space.

4. Determination that the conventional design approach to MJ PPC design (Beer-Lambert law absorber thicknesses with optimized anti-reflection coatings (ARCs)) is sufficient for the on-substrate 10J 1550 nm PPCs in this work. It achieves comparable optoelectronic performance to the top designs from the ML and classical optimizations.

In general, this work informs the future paradigms of optoelectronic device design. With high-versatility, high-interpretability, high synergistic potential, and low computational cost, dimensionality reduction serves as a unique and powerful tool in the modern AI toolbox. In particular, this work dictates the design of the record efficiency AIIR-Power PPCs [51].

Author contributions

Robert F.H. Hunter: As a doctoral candidate with the University of Ottawa, I was the lead student for the machine learning portion of the AIIR-Power project. I created the aiirmap simulation framework which is used in these studies. I am the lead author of this study and manuscript.

Dr. Gavin P. Forcade: As a doctoral candidate with the University of Ottawa SUNLAB research group, Dr. Forcade led the development and calibration of the multi-junction photonic power converter Synopsys Sentaurus TCAD model. He also assisted in the experimental characterization used in the model calibration, analysis of results, and editing this manuscript.

Prof. Yuri Grinberg: As a research officer with the National Research Council of Canada's Digital Technologies Research Centre, and adjunct University of Ottawa professor, Prof. Grinberg offered his machine-learning expertise to this project. He provided valuable input to the development of the methodology and analysis of results. He assisted in editing the manuscript.

Dr. D. Paige Wilson: As a post-doctoral research scientist within the University of Ottawa SUNLAB research group, Dr. Wilson worked to integrate and update the luminescent coupling part of the Sentaurus model. Paige also assisted in experimental characterization of the devices used in the Sentaurus model calibration.

Dr. Megan N. Beattie: As a former post-doctoral research scientist within the University of Ottawa's SUNLAB research group, Dr. Beattie helped to guide in the design of this project. She constructed the initial Synopsys Sentaurus model for PPCs. Dr. Beattie assisted in editing the manuscript.

Dr. Christopher E. Valdivia: As a former senior research scientist within the University of Ottawa's SUNLAB research group, Dr. Valdivia helped to guide the design of this project. He assisted in the editing of the manuscript.

Dr. Mathieu de Lafontaine: As a post-doctoral research scientist with the University of Ottawa's SUNLAB research group, Dr. de Lafontaine provided feedback on the manuscript. He provided early feedback on the model development.

Louis-Philippe St-Arnaud: As a late year undergraduate summer student with the University of Ottawa SUNLAB Louis-Philippe assisted in the experimental characterization of the devices used in the Sentaurus model calibration.

Dr. Henning Helmers: As the Deputy Head of the Fraunhofer ISE III-V Photovoltaics and Concentrator Technology Department, Dr. Helmers provided valuable guidance and leadership to this project. He was part of the team which grew and fabricated the project devices. He assisted in device characterization and in editing the manuscript.

Dr. Oliver Höhn: As the Head of the Fraunhofer ISE III-V Semiconductor Technology Group, Dr. Höhn provided valuable guidance to this project. He was part of the team which grew and fabricated the project devices. He assisted in device characterization and in editing the manuscript.

Dr. David Lackner: As the Head of the Fraunhofer ISE III-V Epitaxy and Material Development Group, Dr. Lackner provided valuable guidance to this project. He was part of the team which grew and fabricated the project devices. He assisted in device characterization and in editing the manuscript.

Dr. Carmine Pellegrino: As a research scientist with Fraunhofer ISE, Dr. Pellegrino provided was part of the team which grew and fabricated the project devices. He assisted in device characterization and in editing the manuscript.

Prof. Jacob J. Krich: As a professor with the University of Ottawa's SUNLAB research group, Prof. Krich provided valuable guidance and leadership to this project. He assisted in analysis of the results and in editing the manuscript.

Prof. Alexandre W. Walker: As a research officer with the National Research Council of Canada's Quantum and Nanotechnologies Research Centre, adjunct University of Ottawa professor, and my supervisor, Prof. Walker has provided valuable guidance and leadership to this project and to myself. He assisted in analysis of the results and in editing the manuscript.

Prof. Karin Hinzer: As the director of the University of Ottawa's SUNLAB research group and my supervisor, Prof. Hinzer oversaw my research. She provided detailed feedback during the analysis of my simulation results, and assisted in editing the manuscript.

Copyright

Machine learning enhanced design and knowledge discovery for multi-junction photonic power converters

Robert F. H. Hunter[1,*], Gavin P. Forcade[1], Yuri Grinberg[2], D. Paige Wilson[1], Meghan N. Beattie[1], Christopher E. Valdivia[1], Mathieu de Lafontaine[1], Louis-Philippe St-Arnaud[1], Henning Helmers[3], Oliver Höhn[3,4], David Lackner[3], Carmine Pellegrino[3], Jacob J. Krich[1], Alexandre W. Walker[5], and Karin Hinzer[1]

[1]SUNLAB, Nexus for Quantum Technologies Institute, University of Ottawa, Ottawa, ON, Canada
[2]Digital Technologies Research Centre, National Research Council of Canada, Ottawa, ON, Canada
[3]Fraunhofer Institute for Solar Energy Systems ISE, 79110 Freiburg, Germany
[4]Department of Sustainable Systems Engineering (INATECH), University of Freiburg, 79110 Freiburg, Germany
[5]Quantum and Nanotechnologies Research Centre, National Research Council of Canada, Ottawa, ON, Canada
[*]rhunt013@uottawa.ca

ABSTRACT

Machine learning is proving to be a revolutionary tool across many disciplines, including optoelectronic device design. In this report, we compare classical and machine-learning enhanced design optimization methodologies. We investigate, as an example case, the design of the complex structures of ten-junction InP lattice matched photonic power converters with $In_{0.53}Ga_{0.47}As$ absorbers optimized for operation at 1550 nm. We find that the implicit pattern recognition capabilities of dimensionality reduction using principal component analysis accelerate design discovery, optimization, and the understanding of complex optical phenomena in the simulated devices. The dimensionality reduction approach offers over twenty times as many optimal designs with greater variability and with a 15% reduction in computational cost compared to a classical optimization method. Furthermore, we find that the representation of the reduced dimensionality subspace offers an intuitive interpretation of optical phenomena expected to occur in this design problem. This method is general and offers the potential for knowledge discovery, expanded design perspective, and optimization acceleration in conjunction with a significant reduction in computational expense in systems which can be numerically modeled.

Keywords: machine learning, dimensionality reduction, design discovery, optimization acceleration, knowledge discovery, multi-junction photonic power converters

Introduction

Optoelectronic device design relies upon the expertise of the design team to guide the process towards a desired outcome. However, the complexity of many devices quickly makes this process intractable as the number of parameters to consider is large and their correlations non-trivial. Classical optimization strategies, such as brute-force[1–3], genetic[2,3], or multiobjective optimization algorithms[4], are employed but come with several drawbacks[5]. First, their large computational expense scales with the number of varied parameters in the design space, exponentially in the worst cases. Second, there is no guarantee of finding an adequate solution since they are sensitive to the designer's initial assumptions and to the complexity of the input-output relation. And third, they cannot efficiently handle multi-objective problems, which is standard for most optoelectronic applications. Contemporary tools based on machine-learning (ML) algorithms offer a way forward in these complex design problems, expanding the design perspective by reducing computational load and dependence upon the design team's input while simultaneously bolstering the understanding of the physics underlying the problem.

Supervised learning and dimensionality reduction are two common machine learning strategies for optoelectronic design. Supervised learning methods typically employ neural networks, which reduce computational cost by learning the input-output relation. This contributes to the great success of neural network based approaches in the inverse design problem, where

the device design is obtained from the desired response[2,3,6–11]. However, these methods are; 1) not interpretable, 2) do not reliably represent the many-to-one problem, where many sets of design parameters produce the same output response, which includes the design of many optoelectronic devices[9,12], and, 3) in the case of high-dimensional spaces, may still require computationally expensive data collection efforts to train. On the other hand, dimensionality reduction is a machine learning method to significantly reduce the computational cost of optimization while simultaneously identifying and encapsulating relationships in the data, enabling knowledge discovery. It operates to find the most compact representation of high-dimensional data with minimal information loss, greatly reducing the complexity of the problem. The reduced dimensional space offers fertile ground for efficient optimizations or multi-objective parameter sweeps[12–22]. The construction of the reduced dimensional space provides insights to supplement the design team's understanding of the device and design landscape. This expansion in design perspective may speed up, improve, or lead to entirely new paradigms in the device design[12,17,23–25].

In this work, we extend the dimensionality reduction based method of Melati et al.[13]. We compare this machine learning (ML) enhanced method to a classical optimization strategy and the conventional "Beer-Lambert" approach for the chosen example design problem: multi-junction photonic power converters (PPCs). We study the nature of the optimized devices and explain the systematic deviations away from the typical approach that are observed. Comparing optimizations, we find that the ML-enhanced method offers over twenty times as many top designs with greater variability and at lower computational cost than the classical optimization approach. Ultimately, we identify that the top optimized designs from both methods and the Beer-Lambert design have comparable optoelectronic power conversion efficiencies (due to luminescent coupling and high material quality). Nonetheless, the variety of high-performance designs discovered, especially in the ML approach, is advantageous to applications where multiple figures of merit (FOM) are considered, as is often the case in reality. We further examine the construction of the reduced dimensional space and link features of the dimensionality reduction to the physical phenomenology of the design space. To the best of our knowledge, this is the first application of machine learning to the design of photonic power converters. It also constitutes an in-depth examination of dimensionality reduction based design for knowledge discovery following the examples of Melati et al.[16] and Kiarashinejad et al.[12,23–25].

Multi-junction Photonic Power Converter Design Optimization

Background and Conventional Design Approach

Photonic power converters (PPCs) are photovoltaic devices optimized to convert laser light into electrical power. They are part of the receiver unit in power-by-light systems and some optical-wavelength telecommunications links, with many modern applications in 5G, internet-of-things, remote power, and more[26–44]. Vertically-stacked monolithic multi-junction device architectures with several p-n junctions connected in series using tunnel diodes are state-of-the-art. They enable operation under higher optical power densities than other architectures and, thus, enable the highest electrical output powers. Simultaneously, their increased voltage output negates the need for step-up voltage converters on the remote side improving system efficiency[27,45–50]. When compared to single-junction designs, they allow lower current densities, reducing series resistance losses, and have thinner junctions that loosen material diffusion length constraints and reduce bulk recombination losses[27,50–54]. Multi-junction devices have achieved record efficiencies above 65% (GaAs absorbers, 5-junction, ~830-840 nm, ~1.25 W input power, at 25°C[55]) and output powers in excess of 29 W (GaAs absorbers, 12-junction, ~810 nm, efficiency of ~61%[56]). PPCs with 30 junctions are commercially available[50]. In this work, we consider ten-junction (10J) PPCs with an absorber material of $In_{0.53}Ga_{0.47}As$ lattice matched to an InP substrate, hereafter referred to as InGaAs. The InGaAs absorber material (bandgap $\approx$ 0.736 eV) has been chosen for system operation at a laser wavelength of ~1550 nm, which benefits from the advantageous free space and fibre optic transmission properties at this wavelength[27,28,48,57,58]. We choose ten junctions to allow output voltages greater than 5 V as desirable for powering downstream electronics. This junction multiplicity matches the state-of-the-art devices in this material system[45].

The simplest design approach to vertically stacked multi-junction PPCs employs the Beer-Lambert law to calculate the absorber layer thicknesses. This law stipulates that the optical power decreases exponentially as a function of depth into a semiconductor material. Due to the current matching constraints of series-connected junctions, Beer-Lambert designs have junctions, which increase in thickness from the light-incident side down (see Fig. 1). This serves as a reasonable first-order estimate and has been used to achieve high device performance[45]. In its simplest application, the Beer-Lambert method does not account for auxiliary non-absorbing layers, optical effects such as interference, interfaces, doping, and parasitic absorption. Additional to the absorber layers, PPCs employ anti-reflection coatings (ARCs), top-side dielectric layers which help couple light into the device. The thicknesses of the ARC layers are often designed by maximizing the transmission into a simple material stack with a uniform refractive index, neglecting the optical coupling of these layers to the full device structure. In this paper, we consider Beer-Lambert absorber designs with double-layer ARCs optimized using simple structures and those

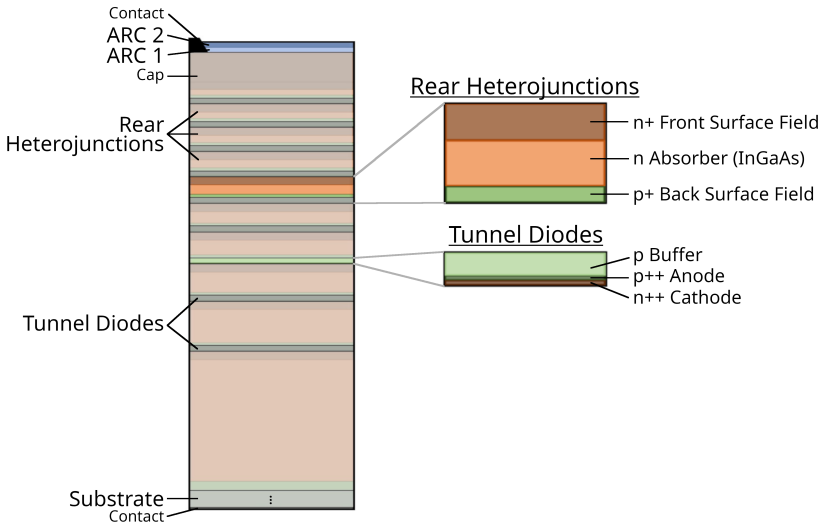

Figure 1. Simplified schematic of the modeled devices, to scale with 98% total absorption Beer-Lambert absorber thicknesses (1550 nm illumination). Zoomed views (right) show the junction and tunnel diode construction. Colors indicate doping sign and concentration.

optimized using the full active stack, and compare these designs to the top results from the optimization methods. We ascertain that the approximations implicit in these conventional approaches do not significantly affect the optoelectronic power conversion efficiency for our 10J device. We attribute this to the weak optical coupling present in the structure and to luminescent coupling. Beer-Lambert designs are specified in the text by the fraction of incident light absorbed in the full device.

Device Model and Calibration

We evaluate devices using an accurate and predictive one-dimensional Poisson/drift-diffusion device model built in Synopsys Sentaurus TCAD[59]. We simulate optical absorption, including interference effects in layers thinner than the wavelength of incident light, using a rigorous coupled wave analysis (RCWA) optical solver, S4[60,61]. For computational efficiency, we implement scikit-learn[62] optimization capabilities directly in the S4 python interface to Sentaurus. We assume standard one-to-one conversion of absorbed photons to electron-hole pairs and couple the resulting optical carrier generation rates from the RCWA calculation into Sentaurus' device solver using the Sentaurus Data Explorer[63], with a linear interpolation between the separately optimized optical and device meshes. We calculate electrical device performance considering Shockley-Read-Hall, Auger, and radiative recombination mechanisms. We include photon recycling and luminescent coupling, where photons originating in radiative recombination of carriers are reabsorbed in the device, with a custom python plugin using the iterative method of Wilkins et al.[64]. We calibrate the device model using experimental measurement of 1J, 2J, and 10J on-substrate PPCs[48,65] using PPCs grown and fabricated at Fraunhofer ISE[66] and experimentally characterized at Fraunhofer ISE[67] and the University of Ottawa SUNLAB[68,69]. Our rigorous calibration ensures accurate optimization results[48,70].

Figure 1 shows a schematic view of the 10J PPC devices in this paper including all modeled layers. We adopt the "segment" naming convention for same material subcells[53]; in this paper, using segment to refer to the subcell absorber layers specifically. We consider rear-heterojunction segments with high-bandgap front- and back-surface-field layers for efficient carrier extraction. The back-surface-field layer plays the role of emitter. The modeled tunnel diodes have negligible series resistance. We base their structure on Soresi et al.[71]. Allowing the ARC and these absorber layer thicknesses to vary under optimization results in the 12-dimensional (12D) design landscape of this study.

Optics-Based Photocurrent Figure of Merit

The typical figure of merit (FOM) in the design of PPCs is the optical to electrical power conversion efficiency, η_P, the ratio of electrical power out to photonic power in. In our model, the computational expense of the RCWA optical simulations is two to three orders of magnitude less than full optoelectronic device simulations. We introduce a FOM based on the optical part of the device simulation alone, this allows this study to be conducted with sufficient sample sizes in a reasonable time period. We

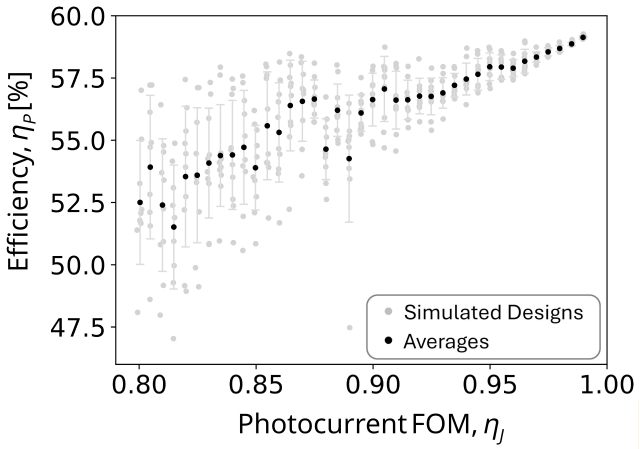

Figure 2. Correlation between full optoelectronic device efficiency, η_P, and the optical-only FOM, η_J, for a large variety of designs. Ten different randomly generated or partially optimized designs are simulated at each sampled η_J value, given by the gray markers. Black markers indicate the average for each set of ten. RMSE error bars are given. Excellent correlation for the highest performing designs exists.

calculate and report the full optoelectronic, η_P, for the top-performing designs only. Our optical-only photocurrent FOM, η_J,

$$\eta_J = \text{Photocurrent FOM} = \frac{\text{device photocurrent } [e/s]}{\text{incident photons per segment } [\gamma/s]}, \tag{1}$$

is the device photocurrent in number of electrons, e, per second calculated by the RCWA optical solver divided by one tenth of the input power in number of photons, γ, per second (the input power perfectly shared in the series-connected 10J device). The RCWA calculation accounts for reflection and transmission at all interfaces, as well as optical interference effects. The η_J accounts for current matching between the segments by taking the limiting segment photocurrent for the device. It has an ideal value of 1, which indicates the possibility of converting 100% of the incident light into equal numbers of carriers in each segment of the device.

The η_J proves to be a good proxy for full optoelectronic device efficiency under current matching conditions. Figure 2 shows the modeled η_P as a function of η_J for a large number of device designs over a wide η_J range. We simulate ten different randomly generated or partially optimized designs at each of 39 η_J values, given by the gray markers. The black markers indicate the average for each set of ten designs. The root-mean-square-error (RMSE) over each set is used for gray error bars. For this study, we consider the designs with the highest η_J. Figure 2 shows that these designs have the highest efficiencies and sit in a region of the plot where there is good correlation between the full optoelectronic η_P and the optical-only η_J. At lower η_J values, a greater variety in the optoelectronic performance of the designs emerges. This originates in the greater physical variety in the surveyed designs which can attain a given η_J when including luminescent coupling. Luminescent coupling naturally redistributes current when segments are current mismatched allowing a larger variety of designs to achieve high performance. In Fig. 2, this effect is especially evident in the device designs which achieve high η_P despite having non-optimal photocurrent FOM and is the reason why the correlation over the full η_J range is flatter than the highly current matched region ($\eta_J \geq 0.98$). Luminescent coupling is not included in the optical simulations.

Machine Learning Enhanced Optimization Implementation

Our dimensionality reduction based design method is given in Fig. 3. It involves a four-step process. First, any classical multi-start optimization method produces a sparse set of high-performance designs (Optimization 1). Second, the top designs are used to train the dimensionality reduction algorithm, and a reduced dimensional subspace is constructed. Third, a grid of designs are generated in the reduced dimensional subspace. And fourth, these designs are used as starting points for a second stage of classical optimization in the full dimensional design space (Optimization 2). Previously, the first three steps of this method were used by Melati et al. to assist in the design of nanoscale silicon-on-insulator vertical grating couplers and power splitters[13–17,72]. We add the second optimization step to mitigate loss of information during the dimensionality reduction step (see the Results section and the first section of Supplementary 1 and Supplementary Fig. S1 for more information).

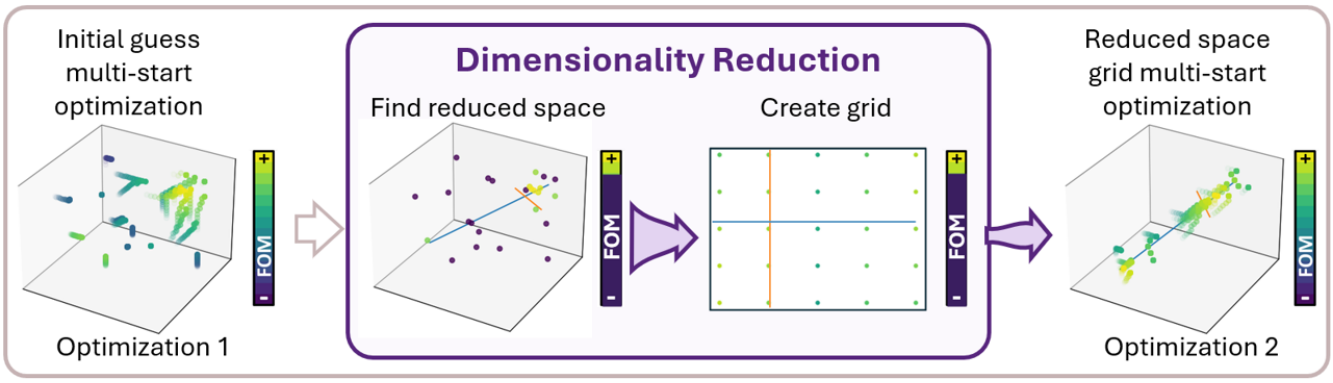

Figure 3. Simplified design flow for the machine learning enhanced design optimization. Step 1; classical multi-start optimization. Step 2; top designs from step 1 according to a chosen figure of merit (FOM) are used to train a dimensionality reduction algorithm and generate a reduced dimension subspace. Step 3; the reduced dimensional subspace is used to generate start points. Step 4; extension of the method, classical multi-start optimization from the step 3 grid points to mitigate information loss during steps 2 and 3.

In this work, we generate the starting points for the first stage of optimization randomly in a hyperbox centered around the 98% total absorption Beer-Lambert absorber thicknesses and the ARC thicknesses from the calibration device[48]. We survey a wide area of the design landscape with the hyperbox edges at ±40% for the InGaAs layers and ±90% for the ARC layers. We generate 10,000 random designs. For optimization, we employ the Nelder-Mead simplex method, as we observe it to reach better performing designs compared to gradient based techniques. The optimizations are run until convergence for each design assuming default convergence tolerances[62]. We use the top 200 designs as training data for dimensionality reduction representing a η_J cutoff of 0.984.

The dimensionality reduction algorithm we use here is principal component analysis (PCA)[73,74]. As equation (2) shows, in PCA the reduced space dimensions, or "components", y_i, are created by linear combination of the input dimensions, x_j, which are standardized using a mean, μ_j, subtraction and standard deviation, σ_j, normalization. The algorithm operates to find the coefficients, a_{ij}, for the linear sums of the standardized input dimensions, x'_j, with the a_{ij} chosen to retain the maximal amount of variance in the data. In other words, PCA operates to find the best linear dimensionality reduction solution with respect to the mean squared error measure of information loss leading to a_{ij} which are the coefficients for the ordered eigenvectors of the covariance matrix.

$$y_i = \sum_j a_{ij}\left(\frac{x_j - \mu_j}{\sigma_j}\right) = \sum_j a_{ij} x'_j, \tag{2}$$

We select the dimensionality of the reduced space based upon the ability to reconstruct the training data. We project the training data points into and back out of reduced spaces of different dimensionality and calculate the average error in their reconstruction. The blue trend in Fig. 4 shows the result of this analysis. The red trend in Fig. 4 shows a related measure: the percentage of training data variance each reduced space retains. In this study, we choose a reduced space dimensionality of three, as the smallest reduced space in the plateau of the reconstruction error trend. The average reconstruction error for this reduced space is 0.085 μm and the training data variance retained is ∼88%.

We generate a grid of approximately 10,000 new designs spread across the identified subspace, bounded by the extremities of the training data. We project these designs out into the original space where they are used as the starting points for the second stage of optimization. We then gather the final designs from both stages of optimization and apply constraints of 5 μm maximum for a single segment thickness and 8 μm maximum for the total absorber thickness. These constraints originate in practical limits on the total time and thermal budget allowances for growth of the epitaxial semiconductor structure.

The classical optimization only baseline uses the same simulation framework. To ensure a fair comparison, it uses two stages of optimization with the end points from the first stage used as the starting points for the second stage. This choice is equivalent to running the results from Optimization 1 directly into Optimization 2 without the dimensionality reduction steps

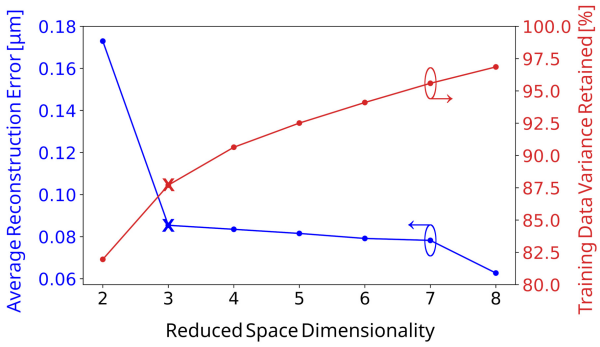

Figure 4. Average reconstruction error of the 12-dimensional training data (blue, left axis) and percentage of training data variance retained (red, right axis) for reduced spaces of different dimensionality. The trends flatten out indicating a level of stability in the complexity of the data. The x's show the selected reduced space.

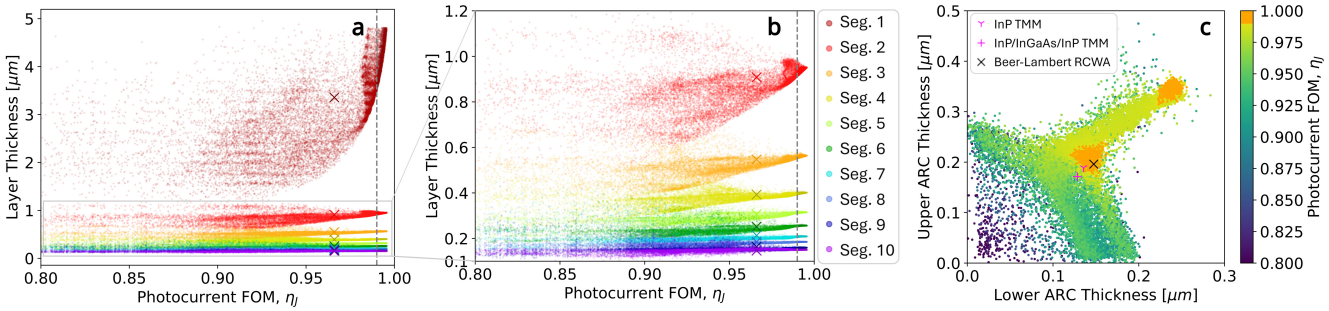

Figure 5. Optimized layer thicknesses for the ML-enhanced method. **a** Segment absorber layer thicknesses as a function of η_J. **b** Zoom of **a** highlighting segments 2-10. The highest η_J designs show narrow distributions for all but segment 1 absorber thickness. **c** the η_J for all designs as a function of the double-layer anti-reflection coating thicknesses. Purple markers ($\curlyvee$ and $+$) indicate ARC designs which use a simpler structure and optimization method (as detailed in the text). In all panels, the designs exceeding a η_J of 0.99 are indicated using darker markers. X's indicate the 99.5% total absorption Beer-Lambert absorber design.

in Fig. 3. The second optimization stage once again uses the Nelder-Mead algorithm with default convergence criteria. Both the ML-enhanced and classical-only methods use the same first stage data. We run our design optimization using common packages in a python environment called aiirmap[75]. We use scikit-learn[62] for machine learning and optimization algorithms. Databasing of the model results leverages pandas[76,77].

Results

Nature of ML-Enhanced Optimization and Comparison to the Conventional Design

We show the nature of the optimized results from both optimization stages of the ML-enhanced method in Fig. 5. Supplementary Fig. S2 shows qualitatively similar results for the classical optimization. Figures 5a and 5b plot the InGaAs segment absorber layer thicknesses against η_J. Figure 5a shows all absorber layer thicknesses, while Fig. 5b zooms in on the thinner layers . In Fig. 5c, we plot the optimized on-substrate designs as a function of the double layer ARC thicknesses. Figure 5 shows over 19,000 designs. These are the designs which pass the growth constraints minus the few (197) optimized designs which have an η_J less than 0.80. We highlight the top designs, $\eta_J \geq 0.99$, on these plots using a vertical line and darker markers in Figs. 5a and 5b and orange markers in Fig. 5c. Nearly 4,000 designs meet this criteria. Using x's, we include a conventional Beer-Lambert design with 99.5% total absorption and η_J of 0.966. The highest performing designs achieve an η_J of 0.996.

Two features drive the η_J optimization: current matching between segments and maximizing absorber thickness. The former dominates with direct proportionality; any current mismatch directly lowers the total device current. Meanwhile, the latter inherits the logarithmic relation between thickness and absorption encoded in the physics of the Beer-Lambert relationship. Consequently, thin current matched devices with only ~4.5 μm of absorber material can achieve reasonable η_J (~0.95), while

the highest η_J require current-matching and the exponentially thicker layers (most clearly observed in the segment 1 trend). The exponential-like absorption trend also reflects in the smaller thickness spread in the upper layers; they are more tightly constrained to obtain current matched values under the higher photon fluxes they experience. For the absolute highest η_J designs ($\sim$0.996) a single solution for the absorber thicknesses exists. This solution differs systematically from the Beer-Lambert trend, as Fig. 6 will explore.

The segment 1 trend in Fig. 5a shows evidence of optical interference phenomena in the large number of horizontal ridges. These preferential thicknesses occur at half-wavelength optical path length intervals of the incident light indicating where the optimization stabilizes when the rate of change in the interference pattern and generation rate in the bottom segment are minimized. There is indication that segment 2 is also thick enough for this effect to occur. The maximum of 5 μm in Fig. 5a indicates the growth-informed design constraints.

The ML-enhanced optimization converges to two unique ARC designs, the two orange peaks in Fig. 5c. Figure 5c also shows several features associated with optical interference. Linear peaks of higher η_J extend outward from the x and y axes along lines which maximize transmission through the ARCs. The intersection at the y-axis is at the expected location, where the upper ARC has a quarter wavelength optical depth (refractive index of the upper ARC is 1.38 at 1.550 μm) and thus purely destructive interference upon reflection at the first interface. On the other hand, the intersection at the x-axis has been split to either side of the quarter wavelength optical depth in the lower ARC due to the presence of the InP window layer. The near half wavelength optical depth of the window leads to the small split and strong optical coupling which produces a second linear peak of high-performance. We find near-optimal performance along another linear trend which connects the two orange optimal performance peaks. This is associated with the current match layer pattern, with the two peaks indicating the designs where this layer pattern couples to an $\sim$5 μm thick segment 1. The second peak designates the interference modified half wavelength shift at which destructive interference between reflected waves is once again maximized.

The simple approach of optimizing the ARC layers separately from the absorber layers proves to be sufficient in this device architecture. The purple markers in Fig. 5c indicate double layer ARC thicknesses optimized using the transfer matrix method on-top of simpler epitaxial layer stacks. For the purple tri marker ($\curlyvee$), the underlying structure is an InP substrate only, for the purple plus marker (+) the ARCs sit atop 1 μm InP, 2 μm InGaAs, and an InP substrate. The black x indicates the fully modeled layer stack with Beer-Lambert absorber thicknesses (as in Fig. 1). These three ARC designs are similar, with single-layer ARC thicknesses differing by 25 nm or less. Under optoelectronic simulation using the Beer-Lambert absorber design, we obtain negligible performance loss for devices where the ARCs were optimized using the simpler structure.

The ML-enhanced optimized absorber thicknesses systematically deviate away from the simple Beer-Lambert exponential absorption trend. Figure 6 shows the percent difference between the top ($\eta_J \geq 0.99$) ML-enhanced optimized segment thicknesses compared to the 99.5% absorption Beer-Lambert design shown by the x's in Fig. 5. This Beer-Lambert design is chosen such that the bottom segment thickness aligns with the mean optimized value. It corresponds to a Beer-Lambert device with total absorber thickness of 7.4 μm. In Figure 6, segments 10, 6, and 5 are, on average, slightly thicker than the Beer-Lambert while the remaining upper segments are up to $\sim$3% thinner. The maximal average percent difference is 3.3%, this was obtained for segment 9 and corresponds to a 6 nm thickness difference. Spreads in the optimized thickness remain $\sim$5% for all but the thickest segments, where they increase to 8% and $\sim$31% (+14% to -17%) in segments 2 and 1 respectively. Similar results are found for the classically optimized dataset (see Supplementary Fig. S3). We attribute these deviations to optical interference effects in the multilayer cavity which are strongest at the thinner top segments (see Supplementary Fig. S4 for more information). This optical interference arises from differences in refractive index between layers which produce multiple reflections and a weak Fabry-Perot type resonance effect. Features which are not captured in the Beer-Lambert approach. The design differences do not prove meaningful under full optoelectronic simulation with luminescent coupling. The natural current redistributing recovery of the luminescent coupling process (see Fig. 2) leads to equivalent optoelectronic power conversion efficiencies for the Beer-Lambert design and the top ML-optimized devices from each ARC cluster. Furthermore, the deviations observed in the mean optimized layer thicknesses in Fig. 6 fall within the typical uncertainty arising in the epitaxial growth which leads to layer thicknesses that vary by up to 5% of their nominal value. While these results remain of theoretical interest only for the 10J on-substrate InGaAs devices studied here, optimal layer thickness modulation due to optical interference effects may play a larger role in PPC devices with different materials, junction multiplicities, refractive index variations, auxiliary layer designs, or device architectures (such as thin film PPCs with a back-reflector instead of the substrate[78]). In this design and with efficiency as the target figure of merit, these results give confidence to designers employing the Beer-Lambert approach for the absorber layer thicknesses.

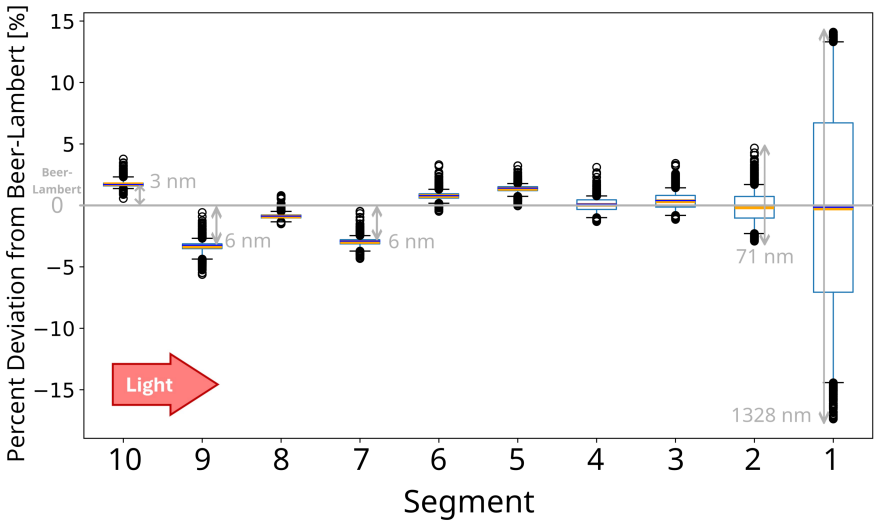

Figure 6. Deviation of layer thicknesses of the top ($\eta_J \geq 0.99$) ML-enhanced designs from the 99.5% Beer-Lambert design. Orange lines denote mean values, blue lines denote medians, and the box gives the first and third quartiles. The whiskers show the two sigma extent of the data and open circles the designs falling outside these limits. Several segments (10, 9, and 7), have optimal layer thicknesses that are significantly (∼2-3%) different from the Beer-Lambert thicknesses.

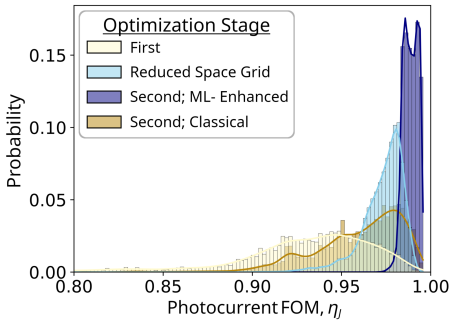

Optimization Stage	Total Population	Average η_J	Population $\eta_J \geq 0.99$
First	9922	0.928	24 (0.2%)
Reduced Space Grid	10316	0.973	70 (0.7%)
Second; ML-Enhanced	9423	0.989	3890 (41.3%)
Second; Classical	9718	0.959	417 (4.3%)

Figure 7. Photocurrent FOM population probability histograms for designs from different stages of the ML-enhanced and classical optimization scenarios. The total design populations meeting the growth constraints, the number and percentage of these designs with a η_J greater than or equal to 0.99, and average η_J for each stage are also given. This shows the much larger number and percentage of high-η_J designs produced by the ML-enhanced method.

Comparison between ML-Enhanced and Classical Design Optimizations

By comparing the η_J and variety of the optimized designs we find that the ML-enhanced method outperforms the classical optimization method in a number of ways. Figure 7 shows the η_J population probability distributions for the designs after the first stage of optimization (yellow, Fig. 3 Optimization 1), from the reduced dimensional space grid (light blue), after the second stage of optimization starting from the reduced space grid (dark blue, ML-enhanced, Fig. 3 Optimization 2), and after the second stage of optimization starting from the first stage end-points (brown, classical). We do not include the initial random starting point designs, they had a normally distributed η_J histogram with a mean of ∼0.58 and a standard deviation of ∼0.08. The differences in the populations arise from the application of the growth constraints, the reduced space grid granularity, and from simulations which fail to converge.

The reduced dimensional subspace is highly effective at generating second stage optimization starting points and accelerates design discovery further down the optimization pathway. As Fig. 7 shows, over forty percent of the points from the ML-enhanced second stage reach the highest η_J (≥ 0.99). This compares to only ∼4% for the classical optimization second stage. The very top performing designs from both methods have nearly equivalent performance (η_J of 0.995 (classical) and 0.996 (ML-enhanced)) but there are over 20 times as many designs at this level for the ML-enhanced method compared to the classical method. The lowest performing design after the ML-enhanced second stage has an η_J of 0.971; ∼60% of the designs

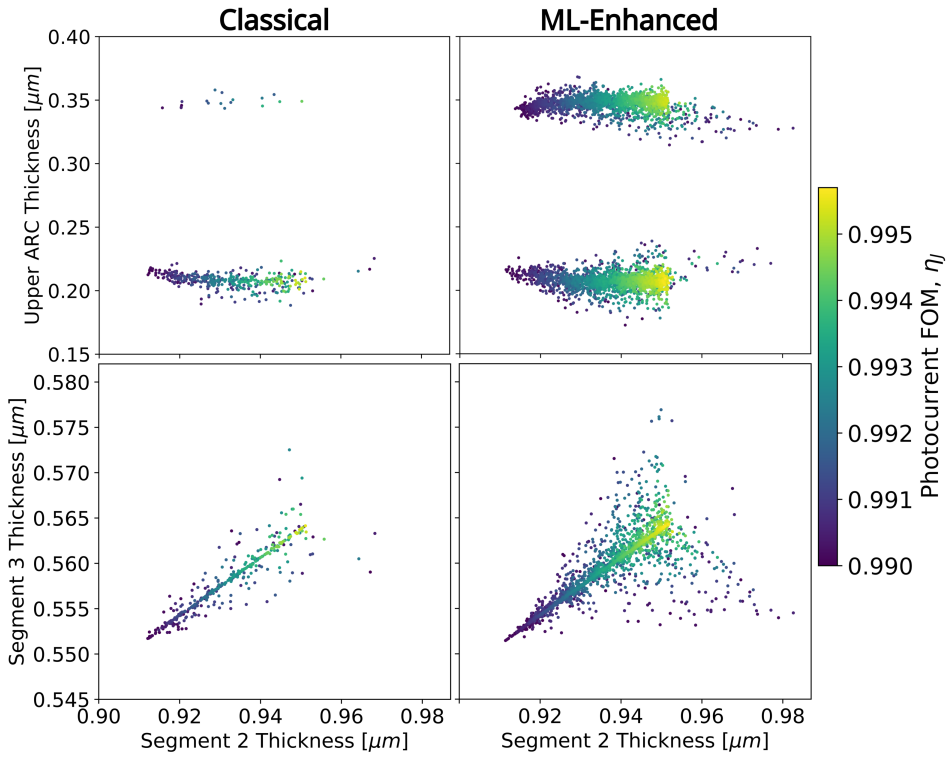

Figure 8. Two-dimensional projections, selected from the 12-dimensional design space. The high-η_J (≥ 0.99) designs from the classical optimization (left) and ML-enhanced (right) second stages of optimization. The thicknesses of the upper ARC (top) and segment 3 (bottom) are shown against the the segment 2 thickness. The larger number of designs, higher η_J , and larger diversity of designs from the ML-enhanced method is clear.

from the classical second stage do not reach this mark. The ML method also produces more significantly thicker devices (e.g. 43% of designs thicker than 7 µm, comparing to 9% for classical second stage) indicating it has proceeded further along the optimization pathway. In Fig. 7, the double peak in the ML-enhanced second stage data reflects results which straddle the saddle region within the ARC subspace (the yellow area between the two orange peaks in Fig. 5c). The peaks are centered at η_J of 0.986 and 0.994.

We obtain the optimized designs from the ML-enhanced second stage of optimization with 30% less computational effort compared to the classical second stage of optimization, as measured by the average number of iterations until convergence. The total reduction in computational cost is 15% for the full method (steps 1 through 4 of Fig. 3) compared to the classical optimization method since both approaches use the same first stage data which had a similar computational cost as the classical second stage. The dimensionality reduction step itself is computationally inexpensive.

The reduced dimensional subspace grid survey, light blue in Fig. 7, produces a large quantity of near-optimal designs (≥ 0.95). The reduced space is constructed from first stage training data with an η_J cutoff of 0.984. We attribute the η_J tail below the training data threshold to a small loss of meaningful information which occurs during the grid creation and results in a reduced space which includes the high performance peak as well as a slightly lower performance volume (in this case, the saddle region within the ARC subspace). This loss of information motivates our second stage of optimization (see the first section of Supplementary 1).

The ML-enhanced optimization also demonstrates greater variability of top performing designs when we compare to those generated using the classical two-stage optimization. Fig. 8 shows the designs with η_J greater than or equal to 0.99 after the ML-enhanced and classical second stage for two 2D projections of the 12D design space. Shared xy axes highlight the extended variety of the designs that the ML-enhanced procedure attains. In the ARCs (top row of Fig. 8 and Fig. 5c) we find that the ML-enhanced method generates a much greater population of designs with thicker ARC layers. While this thicker ARC design is expected from simple optics and is not typically considered in fabrication of real devices, this result shows the potential of

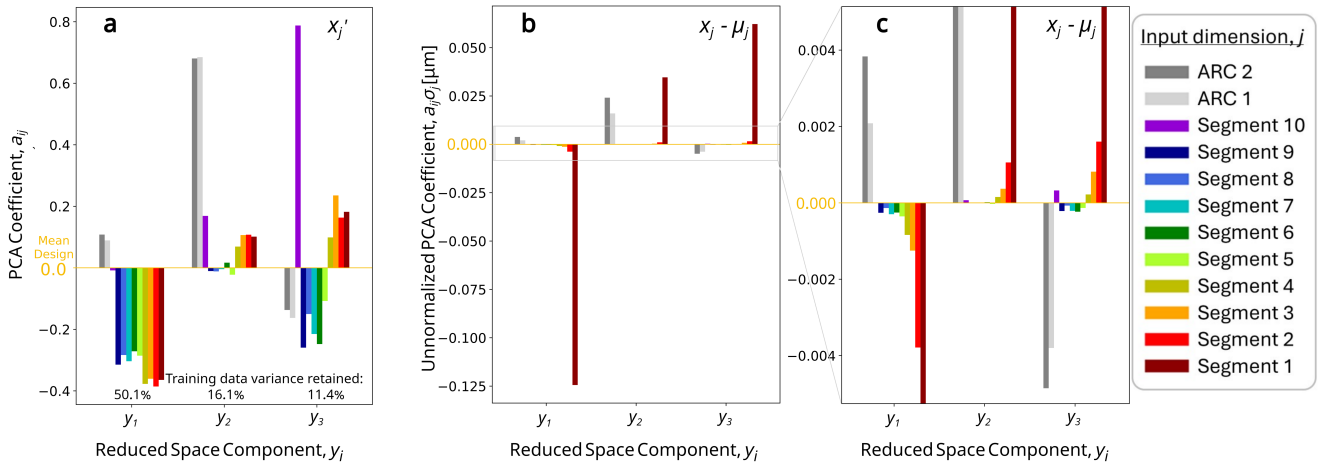

Figure 9. Reduced dimensionality subspace construction for the first three principal components that principal component analysis identifies. **a** PCA coefficient, a_{ij} of equation (2), for each standardized input dimension, x_j'. **b** PCA coefficient times the standard deviation, $a_{ij} * \sigma_j$, in micron, for each mean subtracted input dimension, $x_j - \mu_j$. **c** Y-scale zoom on the zero region of **b**. The percent of training data variance which each of principal component retains is given along the bottom of **a**. The primary optical phenomena in the design space are visibly encoded in the construction of the reduced space.

the dimensionality reduction enhanced method to move out, discover, and populate new high performance regions of the design space. The thicker ARC peak being in an area outside the range of the initial guesses and only sparsely present in the training data. The segment 2 - segment 3 projections (bottom row of Fig. 8) show a variation which is mirrored across the absorber design space and arises as all layers shift according to the interference patterns to maintain segment current matching. This variety may allow discovery of designs which satisfy multiple performance metrics and/or are less sensitive to typical design parameter variations in realistic devices and their operation (e.g. temperature, wavelength, absorber composition, thickness accuracy and precision).

Knowledge Discovery through Reduced Dimensional Subspace Construction

Dimensionality reduction compresses this multi-junction PPC design space to one-quarter of its original size while maintaining an average reconstruction error of less than 100 nm. A number which is weighted by the thick bottom segments. The total training data variance that the three-dimensional space retains is 88%. Figure 9 presents the composition of the three principal components, the y_i in equation (2). Fig. 9a gives the reduced space construction in terms of the PCA coefficients, a_{ij}, for each standardized input dimension, x_j'. Fig. 9b and 9c remove the standard deviation normalization from the input dimensions to show the physical nature of the component composition. Due to the mean subtraction in equation (2), the zero of these plots represents the mean design, given by the orange lines in Fig. 6.

PCA determines the sets of correlations which account for the most variance in the training data. Components are constructed as orthonormal representations of these correlations. Within one component, same (opposite) sign coefficients indicate positive (negative) correlation between input dimensions, and the magnitude of each coefficient indicates how strongly each input dimension contributes to the trend. The sign and magnitude differences of the input dimension coefficients from one component to another have little physical meaning. The component ordering gives the relevant ordering of which trend contributes more to overall data variance[73]. We consider this when interpreting the reduced space construction for knowledge discovery.

The first principal component, y_1 in Fig. 9, encodes the most basic relationship in terms of the thickness dependencies between segments. It says that if one layer thickness increases, the others tend to increase to maintain current matching. As Fig. 9b shows, it implicitly encodes the Beer-Lambert like exponential relation between segment thicknesses. The first principal component accounts for ∼69% of the training data variance.

The two ARC layers dominate the construction of the second principal component, y_2. Fig. 9a shows that over 13% of the variance in the training data was contained in these two dimensions alone. This signifies PCA's recognition of the two ARC

peaks in the training data and the construction of a component which linearly spans the space between them.

The third principal component, y_3, forms the secondary axis of the ARC saddle (Fig. 5c). It also seems to encode a wave-like pattern through the absorber layers. This suggests the appearance of the optical interference phenomena we observed in the previous figures. Here, combined with the Beer-Lambert trend in y_1. Further testing suggests that 5-15% of the training data variance is attributable to optical interference phenomena (see Supplementary Fig. S5).

Discussion and Conclusion

We study a ML-enhanced method which accelerates the design optimization of multi-junction PPCs. It produces a much greater number of designs attaining the highest η_J, these have a greater design variability, and are obtained at a lower computational cost than those found using classical optimization algorithms alone. These advantages, coupled with the demonstrated knowledge discovery, exemplify an expansion in the design perspective which empowers the design choice under external constraints and preferences (e.g. different or multiple performance metrics, growth parameters, or cost). In this study, the reduced space grid is conservatively bounded by the training data. Extending the grid beyond these bounds, or increasing the resolution of the grid survey, could lead to the generation of greater numbers of high-performance designs with larger variability.

We show the potential for knowledge discovery implicit in the construction of the reduced dimensional subspace. Figure 9 confirms the basic understanding of the multi-junction PPC design space. The major contributions to η_J are (y_1) the requirement for good current matching with Beer-Lambert like absorption, (y_2) the optimization of the ARC, and (y_3) a fine-tuning of absorber thicknesses suggestive of optical interference effects within the multi-layer semiconductor stack. We attribute the deviations away from the Beer-Lambert design, as observed in Fig. 6, to this optical interference. Further knowledge discovery is possible within the on-substrate PPC context by including more design parameters, such as layer doping and auxiliary layer design, in the analysis.

The ML-enhanced method does not identify designs with higher optoelectronic efficiency than the conventional and classical approaches. This result is not unusual since the ML method relies on the same classical optimization algorithms to generate its designs. However, the larger variety in the ML-enhanced designs indicate that our method has led to a wider characterization of the high performance design space and lends stronger support to the conclusion that the Beer-Lambert approach is sufficient for the multi-junction PPC design problem when power conversion efficiency is the target figure of merit. In general, it is difficult to know apriori whether the ML-enhanced method will lead to new knowledge beyond what is known through classical or individually optimized means. In any case, dimensionality reduction offers an efficient pathway for a more complete characterization of the design space ensuring that nothing has been missed while simultaneously offering new design perspectives through knowledge discovery and a reduction in computational cost.

Optical-based design optimization of multi-junction PPCs ignores the important optoelectronic phenomenon known as luminescent coupling. As Fig. 2 shows, luminescent coupling can expand the pertinent design space if the highest efficiency is not the only performance criterion. Having multiple FOMs is often the case in reality, as applications, cost, manufacturing uncertainties, and operational uncertainties impose challenges and considerations beyond what can be easily simulated. Forcade et al.[48] show that PPCs optimized with luminescent coupling converge toward a layer structure with current limiting top and bottom junctions which take advantage of the physics of radiative recombination recapture. Future dimensionality reduction studies could use devices optimized with luminescent coupling, leading to an even larger diversity of high efficiency structures.

Machine learning is a toolbox of empowering methods which expands the design perspective in photovoltaics, optoelectronics, and beyond. By allowing a significant reduction in the complexity of a problem in a meaningful manner, dimensionality reduction simultaneously reduces computational cost while unlocking new pathways for exploration and fundamental understanding. It is an indispensable tool in the emerging field of ML-enhanced design, especially for high-dimensional problems. The general dimensionality reduction method we present here is applicable to problems that can be accurately numerically modeled. It does not require assumptions about the nature of the design space or on the optimization figure of merit but it requires an accurate model and a reasonably efficient optimization pipeline. This pipeline must generate a sufficient number of optimized and unbiased designs required for effective training. The general dimensionality reduction method can also be augmented by including other dimensionality reduction algorithms in place of principal component analysis, such as non-linear techniques[18,20–22,79] or feature selection[79,80]. It can be combined with other machine learning techniques such as neural networks and advanced optimization algorithms[2,3,6–9].

Data Availability

Data underlying the results presented in this paper are not publicly available at this time but may be obtained from the authors upon reasonable request.

References

1. Chen, H., Jia, H., Wang, T. & Yang, J. A gradient-oriented binary search method for photonic device design. *J. Light. Technol.* **39**, 2407–2412, DOI: 10.1109/JLT.2021.3050771 (2021).
2. Mao, S. *et al.* Inverse design for silicon photonics: From iterative optimization algorithms to deep neural networks. *Appl. Sci.* **11**, 3822, DOI: 10.3390/app11093822 (2021).
3. Yao, K., Unni, R. & Zheng, Y. Intelligent nanophotonics: merging photonics and artificial intelligence at the nanoscale. *Nanophotonics* **8**, 339–366, DOI: 10.1515/nanoph-2018-0183 (2019).
4. Ngatchou, P., Zarei, A. & El-Sharkawi, A. Pareto multi objective optimization. vol. 2005, 84– 91, DOI: 10.1109/ISAP.2005.1599245 (2005).
5. Ma, W. *et al.* Deep learning for the design of photonic structures. *Nat. photonics* **15**, 77–90 (2021).
6. Ren, Y. *et al.* Genetic-algorithm-based deep neural networks for highly efficient photonic device design. *Photonics Res.* **9**, B247, DOI: 10.1364/PRJ.416294 (2021).
7. Deng, L., Xu, Y. & Liu, Y. Hybrid inverse design of photonic structures by combining optimization methods with neural networks. *Photonics Nanostructures - Fundamentals Appl.* **52**, 101073, DOI: 10.1016/j.photonics.2022.101073 (2022).
8. Jiang, J., Chen, M. & Fan, J. A. Deep neural networks for the evaluation and design of photonic devices. *Nat. Rev. Mater.* **6**, 679–700, DOI: 10.1038/s41578-020-00260-1 (2020).
9. Hegde, R. S. Deep learning: a new tool for photonic nanostructure design. *Nanoscale Adv.* **2**, 1007–1023, DOI: 10.1039/C9NA00656G (2020).
10. Adibnia, E., Ghadrdan, M. & Ali Mansouri-Birjandi, M. Chirped apodized fiber bragg gratings inverse design via deep learning. *Opt. Laser Technol.* **181**, 111766, DOI: https://doi.org/10.1016/j.optlastec.2024.111766 (2025).
11. Adibnia, E., Ghadrdan, M. & Mansouri-Birjandi, M. A. Inverse design of fbg-based optical filters using deep learning: A hybrid cnn-mlp approach. *J. Light. Technol.* **43**, 4452–4461, DOI: 10.1109/JLT.2025.3534275 (2025).
12. Kiarashinejad, Y., Abdollahramezani, S. & Adibi, A. Deep learning approach based on dimensionality reduction for designing electromagnetic nanostructures. *npj Comput. Mater.* **6**, 12, DOI: 10.1038/s41524-020-0276-y (2020).
13. Melati, D. *et al.* Mapping the global design space of nanophotonic components using machine learning pattern recognition. *Nat. Commun.* **10**, 4775, DOI: 10.1038/s41467-019-12698-1 (2019).
14. Kamandar Dezfouli, M. *et al.* Perfectly vertical surface grating couplers using subwavelength engineering for increased feature sizes. *Opt. Lett.* **45**, 3701, DOI: 10.1364/OL.395292 (2020).
15. Melati, D. *et al.* Design of multi-parameter photonic devices using machine learning pattern recognition. In Baets, R. G., O'Brien, P. & Vivien, L. (eds.) *Integrated Photonics Platforms: Fundamental Research, Manufacturing and Applications*, 7, DOI: 10.1117/12.2559583 (SPIE, 2020).
16. Melati, D. *et al.* Design of compact and efficient silicon photonic micro antennas with perfectly vertical emission. *IEEE J. Sel. Top. Quantum Electron.* **27**, 1–10, DOI: 10.1109/JSTQE.2020.3013532 (2021).
17. Melati, D. *et al.* Subwavelength metamaterial devices with optimization and machine learning. In He, S. & Vivien, L. (eds.) *Smart Photonic and Optoelectronic Integrated Circuits 2023*, vol. PC12425, PC1242509, DOI: 10.1117/12.2649953. International Society for Optics and Photonics (SPIE, 2023).
18. Al-Digeil, M. *et al.* Pca-enhanced autoencoders for nonlinear dimensionality reduction in low data regimes. In *Proceedings of the 36th Canadian Conference on Artificial Intelligence*, DOI: 10.21428/594757db.05a13011 (Canadian Artificial Intelligence Association, 2023).
19. Zandehshahvar, M., Hemmatyar, O., Kiarashinejad, Y., Abdollahramezani, S. & Adibi, A. Dimensionality reduction based method for design and optimization of optical nanostructures using neural network. In *Frontiers in Optics + Laser Science APS/DLS*, FM5C.2, DOI: 10.1364/FIO.2019.FM5C.2 (OSA, 2019).
20. Kudyshev, Z. A., Kildishev, A. V., Shalaev, V. M. & Boltasseva, A. Machine learning–assisted global optimization of photonic devices. *Nanophotonics* **10**, 371–383, DOI: 10.1515/nanoph-2020-0376 (2020).

21. Liu, Z., Raju, L., Zhu, D. & Cai, W. A hybrid strategy for the discovery and design of photonic structures. *IEEE J. on Emerg. Sel. Top. Circuits Syst.* **10**, 126–135, DOI: 10.1109/JETCAS.2020.2970080 (2020).

22. Liu, Z. *et al.* Compounding meta-atoms into metamolecules with hybrid artificial intelligence techniques. *Adv. Mater.* **32**, 1904790, DOI: 10.1002/adma.201904790 (2020).

23. Kiarashinejad, Y., Abdollahramezani, S., Zandehshahvar, M., Hemmatyar, O. & Adibi, A. Deep learning reveals underlying physics of light–matter interactions in nanophotonic devices. *Adv. Theory Simulations* **2**, 1900088, DOI: 10.1002/adts.201900088 (2019).

24. Kiarashinejad, Y. *et al.* Knowledge discovery in nanophotonics using geometric deep learning. *Adv. Intell. Syst.* **2**, 1900132, DOI: 10.1002/aisy.201900132 (2020).

25. Hemmatyar, O., Abdollahramezani, S., Kiarashinejad, Y., Zandehshahvar, M. & Adibi, A. Full color generation with Fano-type resonant HfO_2 nanopillars designed by a deep-learning approach. *Nanoscale* **11**, 21266–21274, DOI: 10.1039/C9NR07408B (2019).

26. Matsuura, M. Recent advancement in power-over-fiber technologies. *Photonics* **8**, 335, DOI: 10.3390/photonics8080335 (2021).

27. Fafard, S. & Masson, D. P. Perspective on photovoltaic optical power converters. *J. Appl. Phys.* **130**, 160901, DOI: 10.1063/5.0070860 (2021).

28. Algora, C. *et al.* Beaming power: Photovoltaic laser power converters for power-by-light. *Joule* **6**, 340–368, DOI: 10.1016/j.joule.2021.11.014 (2022).

29. Putra, E. P. *et al.* Technology update on patent and development trend of power over fiber: a critical review and future prospects. *J. Photonics for Energy* **13**, DOI: 10.1117/1.JPE.13.011001 (2023).

30. Spillman, W., Crowne, D. & Woodward, D. Optically powered and interrogated rotary position sensor for aircraft engine control applications. *Opt. Lasers Eng.* **16**, 105–118, DOI: 10.1016/0143-8166(92)90003-P (1992).

31. Worms, K. *et al.* Reliable and lightning-safe monitoring of wind turbine rotor blades using optically powered sensors. *Wind. Energy* **20**, 345–360, DOI: 10.1002/we.2009 (2017).

32. De Nazare, F. V. B. & Werneck, M. M. Hybrid optoelectronic sensor for current and temperature monitoring in overhead transmission lines. *IEEE Sensors J.* **12**, 1193–1194, DOI: 10.1109/JSEN.2011.2163709 (2012).

33. Zheng, Y. *et al.* Wireless laser power transmission: Recent progress and future challenges. *Space Sol. Power Wirel. Transm.* S2950104023000020, DOI: 10.1016/j.sspwt.2023.12.001 (2024).

34. Ding, J., Liu, W., I, C.-L., Zhang, H. & Mei, H. Advanced progress of optical wireless technologies for power industry: An overview. *Appl. Sci.* **10**, 6463, DOI: 10.3390/app10186463 (2020).

35. Zin, A. M., Bongsu, M. S., Idrus, S. M. & Zulkifli, N. An overview of radio-over-fiber network technology. In *International Conference On Photonics 2010*, 1–3, DOI: 10.1109/ICP.2010.5604429 (IEEE, 2010).

36. Aboelala, O., Lee, I. E. & Chung, G. C. A survey of hybrid free space optics (FSO) communication networks to achieve 5g connectivity for backhauling. *Entropy* **24**, 1573, DOI: 10.3390/e24111573 (2022).

37. Goto, K., Nakagawa, T., Nakamura, O. & Kawata, S. An implantable power supply with an optically rechargeable lithium battery. *IEEE Transactions on Biomed. Eng.* **48**, 830–833, DOI: 10.1109/10.930908 (2001).

38. Vazquez, C. *et al.* Multicore fiber scenarios supporting power over fiber in radio over fiber systems. *IEEE Access* **7**, 158409–158418, DOI: 10.1109/ACCESS.2019.2950599 (2019).

39. Al-Zubaidi, F. M. A., Lopez-Cardona, J. D., Sanchez Montero, D. & Vazquez, C. Optically powered radio-over-fiber systems in support of 5g cellular networks and IoT. *J. Light. Technol.* **39**, 4262–4269, DOI: 10.1109/JLT.2021.3074193 (2021).

40. Grandidier, J. *et al.* Feasibility of power beaming through the venus atmosphere. *Acta Astronaut.* **211**, 376–381, DOI: 10.1016/j.actaastro.2023.06.042 (2023).

41. Malaviya, P., Sarvaiya, V., Shah, A., Thakkar, D. & Shah, M. A comprehensive review on space solar power satellite: an idiosyncratic approach. *Environ. Sci. Pollut. Res.* **29**, 42476–42492, DOI: 10.1007/s11356-022-19560-w (2022).

42. Guiomar, F. P., Fernandes, M. A., Nascimento, J. L., Rodrigues, V. & Monteiro, P. P. Coherent free-space optical communications: Opportunities and challenges. *J. Light. Technol.* **40**, 3173–3186, DOI: 10.1109/JLT.2022.3164736 (2022).

43. Jahid, A., Alsharif, M. H. & Hall, T. J. A contemporary survey on free space optical communication: Potentials, technical challenges, recent advances and research direction. *J. Netw. Comput. Appl.* **200**, 103311, DOI: 10.1016/j.jnca.2021.103311 (2022).

44. Dahrouj, H., Douik, A., Rayal, F., Al-Naffouri, T. Y. & Alouini, M.-S. Cost-effective hybrid RF/FSO backhaul solution for next generation wireless systems. *IEEE Wirel. Commun.* **22**, 98–104, DOI: 10.1109/MWC.2015.7306543 (2015).

45. Fafard, S. & Masson, D. P. High-efficiency and high-power multijunction InGaAs/InP photovoltaic laser power converters for 1470 nm. *Photonics* **9**, 438, DOI: 10.3390/photonics9070438 (2022).

46. Lozano, J. F. *et al.* A new path towards ultra-high efficient laser power converters: Silicon carbide-based multijunction devices. *Results Eng.* **21**, 101987, DOI: 10.1016/j.rineng.2024.101987 (2024).

47. Helmers, H. *et al.* Photovoltaic cells with increased voltage output for optical power supply of sensor electronics. In *Proceedings SENSOR 2015*, 519–524, DOI: 10.5162/sensor2015/D1.4 (AMA Service GmbH, Von-Münchhausen-Str. 49, 31515 Wunstorf, Germany, 2015).

48. Forcade, G. P. *et al.* 53.6% efficient multi-junction laser power converter for extended telecom range operation. *"* (2024). Manuscript submitted for publication.

49. Zhao, Y., Sun, Y., He, Y., Yu, S. & Dong, J. Design and fabrication of six-volt vertically-stacked GaAs photovoltaic power converter. *Sci. Reports* **6**, 38044, DOI: 10.1038/srep38044 (2016).

50. Fafard, S. *et al.* Power and spectral range characteristics for optical power converters. *Energies* **14**, 4395, DOI: 10.3390/en14154395 (2021).

51. Fafard, S. *et al.* High-efficiency photovoltaic power converters and application to optical power transmission. In *2021 26th Microoptics Conference (MOC)*, 1–2, DOI: 10.23919/MOC52031.2021.9598073 (IEEE, 2021).

52. Hunter, R. F. H., Valdivia, C. E., Baribeau, L. S. & Hinzer, K. Unlocking the potential for extreme solar concentration via subcell segmentation. In *17th International Conference on Concentrator Photovoltaic Systems (CPV))*, 020006, DOI: 10.1063/5.0099470 (2022).

53. Valdivia, C. E. & Hinzer, K. Subcell segmentation for current matching and design flexibility in multijunction solar cells. *IEEE J. Photovoltaics* **10**, 1329–1339, DOI: 10.1109/JPHOTOV.2020.3005630 (2020).

54. Baribeau, L. S., Hunter, R. F., Valdivia, C. E. & Hinzer, K. Drift-diffusion modelling of four-junction ingap/ingaas/sigesn/ge solar cells. In *2022 IEEE 49th Photovoltaics Specialists Conference (PVSC)*, 1031–1031, DOI: 10.1109/PVSC48317.2022.9938603 (2022).

55. Fafard, S. *et al.* Ultrahigh efficiencies in vertical epitaxial heterostructure architectures. *Appl. Phys. Lett.* **108**, 071101, DOI: 10.1063/1.4941240 (2016).

56. Fafard, S. & Masson, D. Vertical multi-junction laser power converters with 61% efficiency at 30 w output power and with tolerance to beam non-uniformity, partial illumination, and beam displacement. *Photonics* **10**, DOI: 10.3390/photonics10080940 (2023).

57. Mukherjee, J., Jarvis, S., Perren, M. & Sweeney, S. J. Efficiency limits of laser power converters for optical power transfer applications. *J. Phys. D: Appl. Phys.* **46**, 264006, DOI: 10.1088/0022-3727/46/26/264006 (2013).

58. Beattie, M. N. *et al.* InP- and GaAs-based photonic power converters under o-band laser illumination: Performance analysis and comparison. *IEEE J. Photovoltaics* **13**, 113–121, DOI: 10.1109/JPHOTOV.2022.3218938 (2023).

59. Synopsys Inc. Sentaurus TCAD user guide version S-2021.06 (2021).

60. Liu, V. & Fan, S. S^4 : A free electromagnetic solver for layered periodic structures. *Comput. Phys. Commun.* **183**, 2233–2244, DOI: 10.1016/j.cpc.2012.04.026 (2012).

61. Pearce, P. & Liu, V. S4 - RCWA. *github* https://github.com/phoebe-p/S4 (retrieved Jan. 2023).

62. Pedregosa, F. *et al.* Scikit-learn: Machine learning in python. *J. Mach. Learn. Res.* **12**, 2825–2830, DOI: 10.5555/1953048.2078195 (2011).

63. Synopsys Inc. Sentaurus data explorer user guide version S-2021.06 (2021).

64. Wilkins, M. *et al.* Luminescent coupling in planar opto-electronic devices. *J. Appl. Phys.* **118**, 143102, DOI: 10.1063/1.4932660 (2015).

65. Forcade, G. P. *et al.* High-performance multi-junction c-band photonic power converters: Calibrated optoelectronic model for next generation designs. In *2023 IEEE 50th Photovoltaic Specialists Conference (PVSC)*, DOI: 10.1109/PVSC48320.2023.10359786 (2023).

66. Helmers, H. *et al.* Advancing solar energy conversion efficiency to 47.6% and exploring the spectral versatility of III-V photonic power converters. In Freundlich, A., Collin, S., Hinzer, K. & Sellers, I. R. (eds.) *Physics, Simulation, and Photonic Engineering of Photovoltaic Devices XIII*, vol. 12881, 1288103, DOI: 10.1117/12.3000352. International Society for Optics and Photonics (SPIE, 2024).

67. Helmers, H. *et al.* Unlocking 1550 nm laser power conversion by ingaas single- and multi-junction pv cells. In *2022 IEEE 49th Photovoltaics Specialists Conference (PVSC)*, 9938627, 1235–1235, DOI: 10.1109/PVSC48317.2022.9938627 (2022).

68. Beattie, M. N. *et al.* EQE measurement technique for multi-junction photovoltaics with overlapping subcell absorptance. In Freundlich, A., Collin, S., Hinzer, K. & Sellers, I. R. (eds.) *Physics, Simulation, and Photonic Engineering of Photovoltaic Devices XIII*, vol. PC12881, PC1288107, DOI: 10.1117/12.3001662. International Society for Optics and Photonics (SPIE, 2024).

69. Wilson, P. *et al.* Quantifying the luminescent coupling process in C-band multi-junction photonic power converters. In Freundlich, A., Collin, S., Hinzer, K. & Sellers, I. R. (eds.) *Physics, Simulation, and Photonic Engineering of Photovoltaic Devices XIII*, vol. PC12881, PC128810J, DOI: 10.1117/12.3000797. International Society for Optics and Photonics (SPIE, 2024).

70. Piprek, J. Simulation-based machine learning for optoelectronic device design: perspectives, problems, and prospects. *Opt. Quantum Electron.* **53**, DOI: 10.1007/s11082-021-02837-8 (2021).

71. Soresi, S. *et al.* Inp:s/alinas:c tunnel junction grown by movpe for photovoltaic applications. *physica status solidi (a)* **215**, 1700427, DOI: https://doi.org/10.1002/pssa.201700427 (2018).

72. Melati, D. *et al.* Machine learning design of subwavelengh integrated photonic devices. In *2019 International Conference on Numerical Simulation of Optoelectronic Devices (NUSOD)*, 135–136, DOI: 10.1109/NUSOD.2019.8806835 (IEEE, 2019).

73. Jolliffe, I. T. & Cadima, J. Principal component analysis: a review and recent developments. *Philos. Transactions Royal Soc. A: Math. Phys. Eng. Sci.* **374**, 20150202, DOI: 10.1098/rsta.2015.0202 (2016).

74. Pearson, K. LIII. on lines and planes of closest fit to systems of points in space. *The London, Edinburgh, Dublin Philos. Mag. J. Sci.* **2**, 559–572, DOI: 10.1080/14786440109462720 (1901).

75. Hunter, R. F. H. aiirmap. *github* https://github.com/rfhhunter/aiirmap (2024).

76. Wes McKinney. Data Structures for Statistical Computing in Python. In Stéfan van der Walt & Jarrod Millman (eds.) *Proceedings of the 9th Python in Science Conference*, 56 – 61, DOI: 10.25080/Majora-92bf1922-00a (2010).

77. The pandas development team. pandas-dev/pandas: Pandas, version 2.2.2, DOI: 10.5281/zenodo.3509134 (Apr. 2024).

78. Helmers, H. *et al.* 68.9% efficient GaAs-based photonic power conversion enabled by photon recycling and optical resonance. *physica status solidi (RRL) - Rapid Res. Lett.* **15**, 2100113, DOI: 10.1002/pssr.202100113 (2021).

79. Ayesha, S., Hanif, M. K. & Talib, R. Overview and comparative study of dimensionality reduction techniques for high dimensional data. *Inf. Fusion* **59**, 44–58, DOI: https://doi.org/10.1016/j.inffus.2020.01.005 (2020).

80. How, W. B., Wang, B., Chu, W., Tkatchenko, A. & Prezhdo, O. V. Significance of the chemical environment of an element in nonadiabatic molecular dynamics: Feature selection and dimensionality reduction with machine learning. *The J. Phys. Chem. Lett.* **12**, 12026–12032, DOI: 10.1021/acs.jpclett.1c03469 (2021).

Acknowledgments

Funding provided by: Government of Canada's AI for Design National Research Council Collaborative Science, Technology, and Innovation Program under Grant INT-014-1. Government of Canada's National Research Council under Grant HSTN-645. National Sciences and Engineering Research Research Council of Canada Discovery Research Program under Grant RGPIN-2022-03877. National Sciences and Engineering Research Research Council of Canada under Grant 497981. The Canadian Foundation for Innovation. The Government of Ontario. The German Federal Ministry of Education and Research under Grant 01DM21006A. ERC grant PHASE (No. 101125948).

We acknowledge Dr. Daniel Poitras of the National Research Council of Canada for his help in generating the anti-reflection coating designs with simpler underlying epitaxial stacks. We also acknowledge CMC Microsystems for the provision of products and services that facilitated this research, including Synopsys Sentaurus TCAD.

Author Contributions

R.F.H.H. built the optimization framework and conducted the simulations. G.P.F. built the calibrated optoelectronic Sentaurus model. D.P.W. provided the updated luminescent model, adapted from[64]. All authors contributed to the design of the experimental devices, which were grown by H.H., O.H., D.L., and C.P.. All authors contributed to the design of the study. Manuscript prepared by R.F.H.H. All authors reviewed the manuscript.

Additional Information

Supplementary Material

See Supplementary 1 for supporting content.

Competing Interests

Karin Hinzer and Christopher E. Valdivia are president and chief technical officer of Enurgen Inc., respectively. The authors declare no other conflicts of interest.

Supplementary 1

Machine learning enhanced design optimization and knowledge discovery for multi-junction photonic power converters

Robert F. H. Hunter[1,*], Gavin P. Forcade[1], Yuri Grinberg[2], D. Paige Wilson[1], Meghan N. Beattie[1], Christopher E. Valdivia[1], Mathieu de Lafontaine[1], Louis-Philippe St-Arnaud[1], Henning Helmers[3], Oliver Höhn[3,4], David Lackner[3], Carmine Pellegrino[3], Jacob J. Krich[1], Alexandre W. Walker[5], and Karin Hinzer[1]

[1]SUNLAB, Nexus for Quantum Technologies Institute, University of Ottawa, Ottawa, ON, Canada
[2]Digital Technologies Research Centre, National Research Council of Canada, Ottawa, ON, Canada
[3]Fraunhofer Institute for Solar Energy Systems ISE, 79110 Freiburg, Germany
[4]Department of Sustainable Systems Engineering (INATECH), University of Freiburg, 79110 Freiburg, Germany
[5]Quantum and Nanotechnologies Research Centre, National Research Council of Canada, Ottawa, ON, Canada
[*]rhunt013@uottawa.ca

Motivation for the Second Stage of Optimization

Our work adds the second stage of optimization to the machine learning (ML) enhanced design method (Step 4 of Fig. 3 of the main text). This second optimization is added to recover a small but meaningful loss of information that occurs during the dimensionality reduction. The information loss occurs because of the finite size of the training dataset and because the reduced dimensional subspace fails to perfectly capture the high-performance manifold. It results in; 1) the inability to accurately reconstruct data (a non-zero reconstruction error), and, 2) a reduced dimensional subspace which includes regions of lower performance. The second stage of optimization corrects for both manifestations of information loss in design spaces with continuous optimization FOM landscapes.

We observe information loss in our study in Fig. 7 (reproduced in Supplementary Fig. S1a for ease of comparison). Specifically, it appears as a low-η_J tail for the reduced subspace histogram (light blue) which extends below the training data threshold of 0.984. Our information loss has two components. First is the intersection of the reduced dimensional subspace with lower performance design volumes. For the ARCs, the linear dimensionality reduction algorithm cannot isolate the two distinct peaks (the orange designs in Supplementary Fig. S2c and f) and the reduced dimensional subspace includes the area around and between them (the saddle region) where the η_J drops due to non-optimal transmission through the ARC layers. For the absorbers, the dimensionality reduction fails to capture all the Beer-Lambert and interference-related nonlinearities leading to a reduced space of approximated curves. The second component is the reconstruction error. The 3D reduced dimensional subspace chosen in this study has an average segment reconstruction error of 85 nm. Supplementary Figure S1b shows the effect of this information loss on the η_J of the training data, presenting the η_J histogram before (black) and after (red) reconstruction. A low-η_J tail below the training data threshold of 0.984 is evident in the reconstructed trend. This effect combines with the population of the ARC saddle region to produce the tail in the reduced space trend. For our dataset, the second stage of optimization recovers the vast majority of information loss yielding an extremely high-performing population (dark blue in Supplementary Fig. S1a).

Nature of the Results from the Classical Optimization

The optimized designs from the classical design optimization are qualitatively very similar to the results from the ML-enhanced method. Supplementary Figures S2 and S3 provide comparisons of the ML-enhanced (top row of each figure) and classical (bottom row of each figure) results. The ML-enhanced results are reproduced from Figures 5 and 6 of the main text and included here for ease of comparison. The same 99.5% total absorption Beer-Lambert design is used as baseline in both sets of plots. Slightly more than 400 classically optimized designs exceed a η_J of 0.99. These high-performing designs are indicated by the dashed lines and orange markers in Supplementary Fig. S2d, e, and f. This compares to ∼3,900 designs for the ML-enhanced

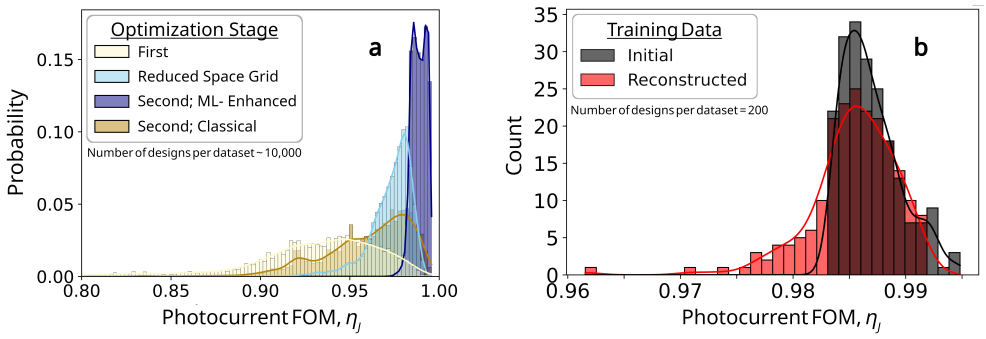

Supplementary Figure S1. The effect of reconstruction error information loss on the optical performance of the training data and its contribution to information loss in the reduced dimensional subspace. **a** Photocurrent FOM population probability histograms for designs from different stages of the ML-enhanced and classical optimization scenarios. *Reproduced from Fig. 7.* **b** Photocurrent FOM population histograms for the 200 training data designs before ("Initial", black) and after projection into and out of the reduced dimensional space ("Reconstructed", red). A small low-η_J tail emerges after reconstruction.

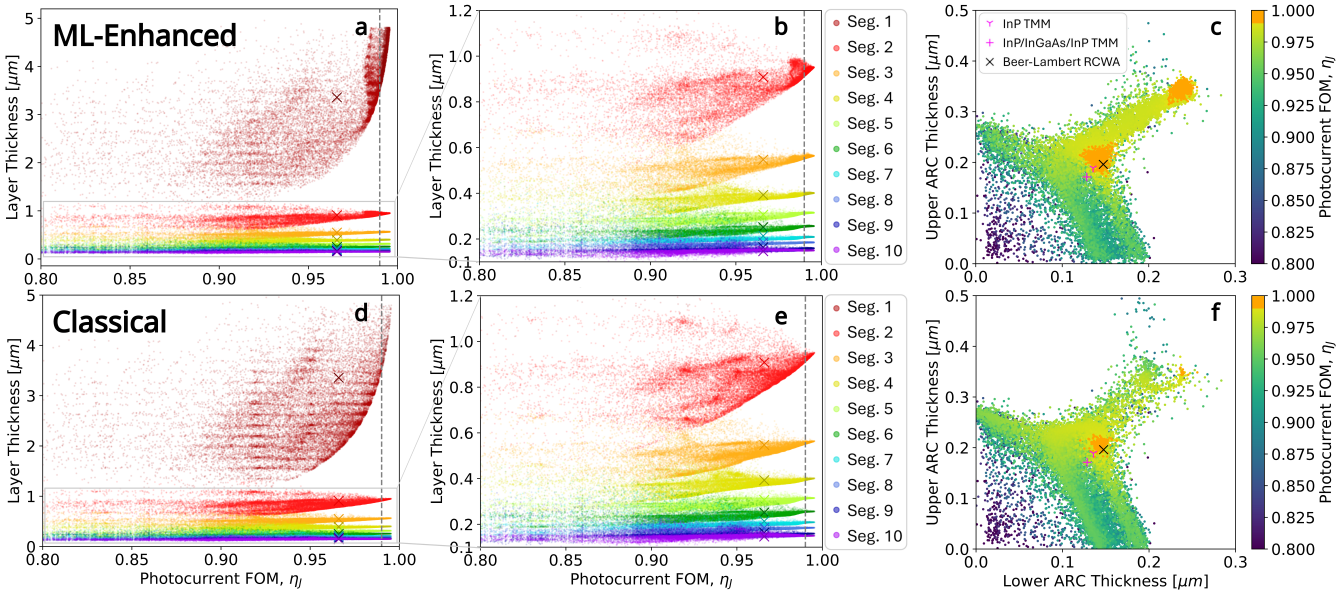

Supplementary Figure S2. Comparison of the the optimized layer thicknesses for the ML-enhanced (top) and classical (bottom) methods. *The ML-enhanced results (**a**,**b**,**c**) are reproduced from Fig. 5.* **a** and **d**: All absorber layers as a function of η_J. **b** and **e**: zooms of **a** and **d**, respectively, which focus on segments 2-10. **c** and **f**: η_J for all designs as a function of the double-layer anti-reflection coating thicknesses. Purple markers ($\curlyvee$ and $+$) indicate ARC designs which use a simpler structure and optimization method (as detailed in the main text). In all panels, the designs exceeding a η_J of 0.99 are indicated using darker markers. X's indicate the 99.5% Beer-Lambert absorber design used in the plots of Supplementary Fig. S3.

method (subfigures a, b, and c).

There are a few important differences between the two sets of results. The first is the larger density of higher performance designs in the second optimization stage of the ML-enhanced method (9,728 designs have $\eta_J > 0.98$, this compares to 2,597 for the classical method). This is visible in Fig. 7 (Supplementary Fig. S1a) but also appears in a comparison of the two sets of plots in Supplementary Fig. S2, most easily discerned in the segment 1 trend. The plots also show an indication of the greater variety of high performing ML-enhanced designs. Finally, they show a greater number of ML-enhanced designs with thicker ARCs (Supplementary Fig. S2 subfigure c vs. subfigure f). We note that the same optical interference pattern of horizontal lines in the segment 1 thicknesses emerges in both the ML-enhanced and classical optimization results.

Both the ML-enhanced and classical optimization methods converge to the same globally optimal solution for the absorber

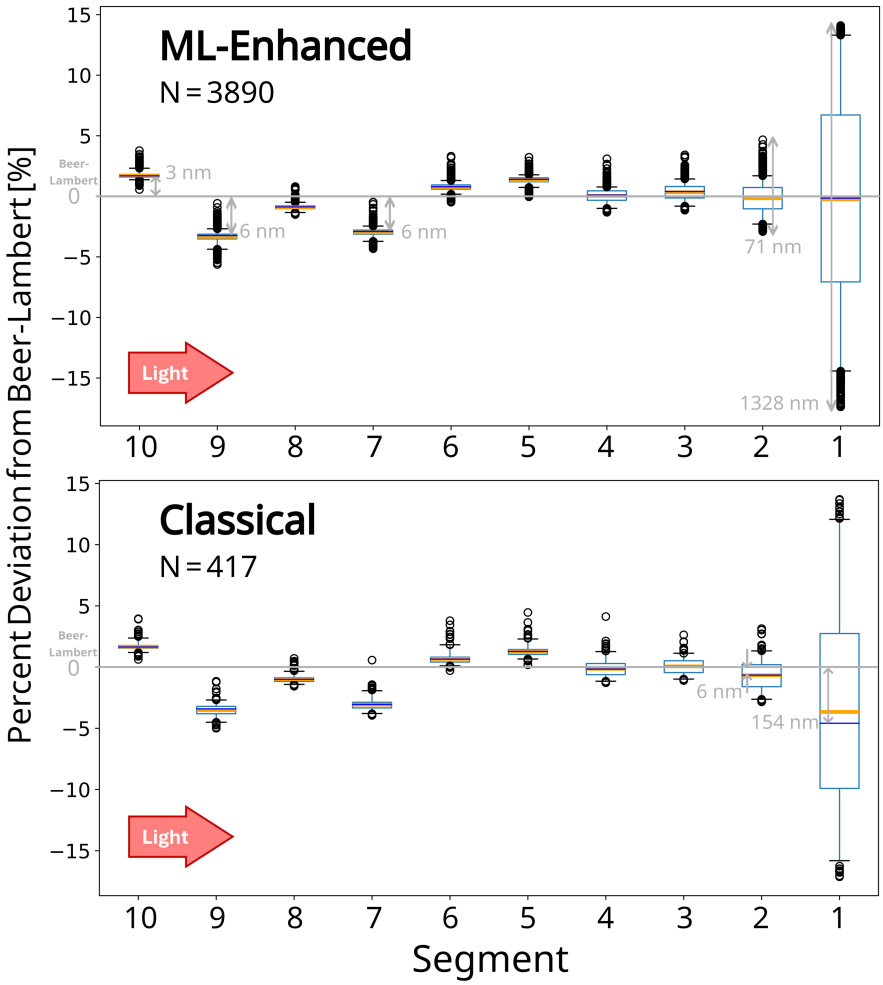

Supplementary Figure S3. Comparison of layer thickness deviations from the 99.5% Beer-Lambert design for ML-enhanced (top) and classical (bottom) optimization methods. *The ML-enhanced result (top) is reproduced from Fig. 6.* The top designs ($\eta_J \geq 0.99$) are included with the populations as indicated. Orange lines denote mean values, blue lines denote medians, and the box gives the first and third quartiles. The whiskers show the two sigma extent of the data and open circles the designs falling outside these limits. Light is incident from the left.

layers. The ML-enhanced method generates a greater diversity and density of solutions in the vicinity of this optimum. A comparison of the two plots in Supplementary Fig. S3 shows this. The mean thickness for the top designs ($\eta_J \geq 0.99$) from both methods are within a couple nanometers of each other for segments 3-10 and within 10 nm of each other for segment 2. The only segment with appreciable differences is segment 1. There, we see thinner results for the classical method compared to the ML-enhanced, once again pointing to the fact that the classical optimization has not progressed quite as far down the optimization pathway (specifically the trend towards thicker devices with its exponentially decreasing absorption gains).

Observation of Interference Effects in the Device

We attribute the systematic deviation away from the simple Beer-Lambert exponential absorption trend that is observed in Figs. 6 and S3 to interference phenomena in the multilayer cavity. Supplementary Figure S4 shows the generation rate in the segments as a function of depth obtained by the RCWA optical solver for a well performing design. Generation rate is given on a log scale. Optical interference patterns are visible throughout the device causing significant variation in the generation rate across a segment (for example, >50% in segment 8) and non-linearity from one segment to another. It should be noted that these interference effects may be smaller in realized devices since realistic material and doping changes at the interfaces are less abrupt than they are in our device model.

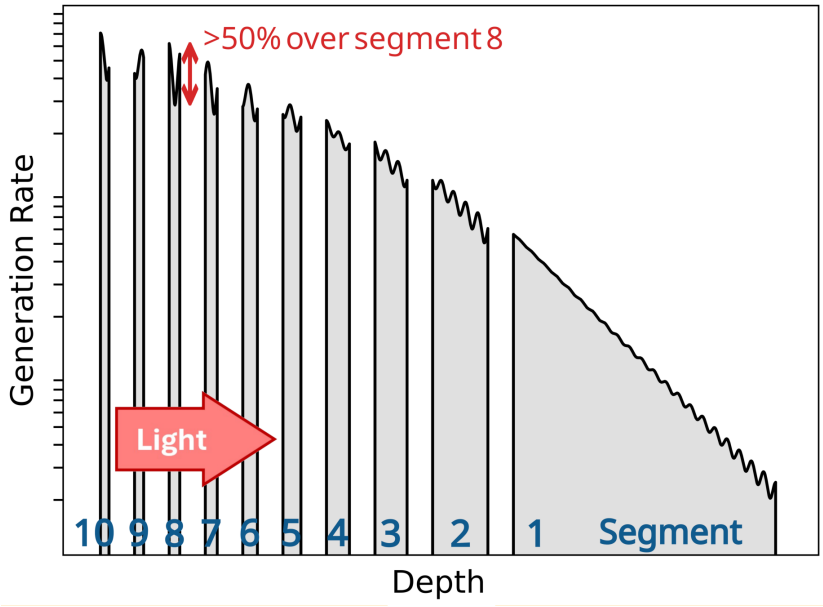

Supplementary Figure S4. Segment generation rates as a function of depth as calculated by the RCWA optical solver. Generation rate is on a log-scale, depth is on a linear scale. Segment numbers are indicated. Light is incident from the left. Optical interference effects within the absorbers are visible.

Reduced Spaces Using More Optimized Training Data

The construction of the reduced space naturally relies on the nature of the training data. The bottom row of Supplementary Fig. S5 shows a reduced space based on the top 200 designs after a first stage of optimization which consisted of two back-to-back RCWA optimizations. The top row of this figure is a reproduction of Fig. 9 from the main text. It uses a single RCWA optimization and is included here for ease of comparison. Supplementary Fig. S5 shows that with better quality data the PCA construction can more cleanly express the trends associated with the different physical phenomena in the design landscape. When we compare the two sets of plots, we see the exponential Beer-Lambert trend in the unnormalized construction of y_1 more clearly in the reduced space based off of the more highly optimized training data. That reduced space also shows optical interference effects which seem to be almost entirely isolated in y_3, with only minor leakage into, the still-ARC dominated, y_2.

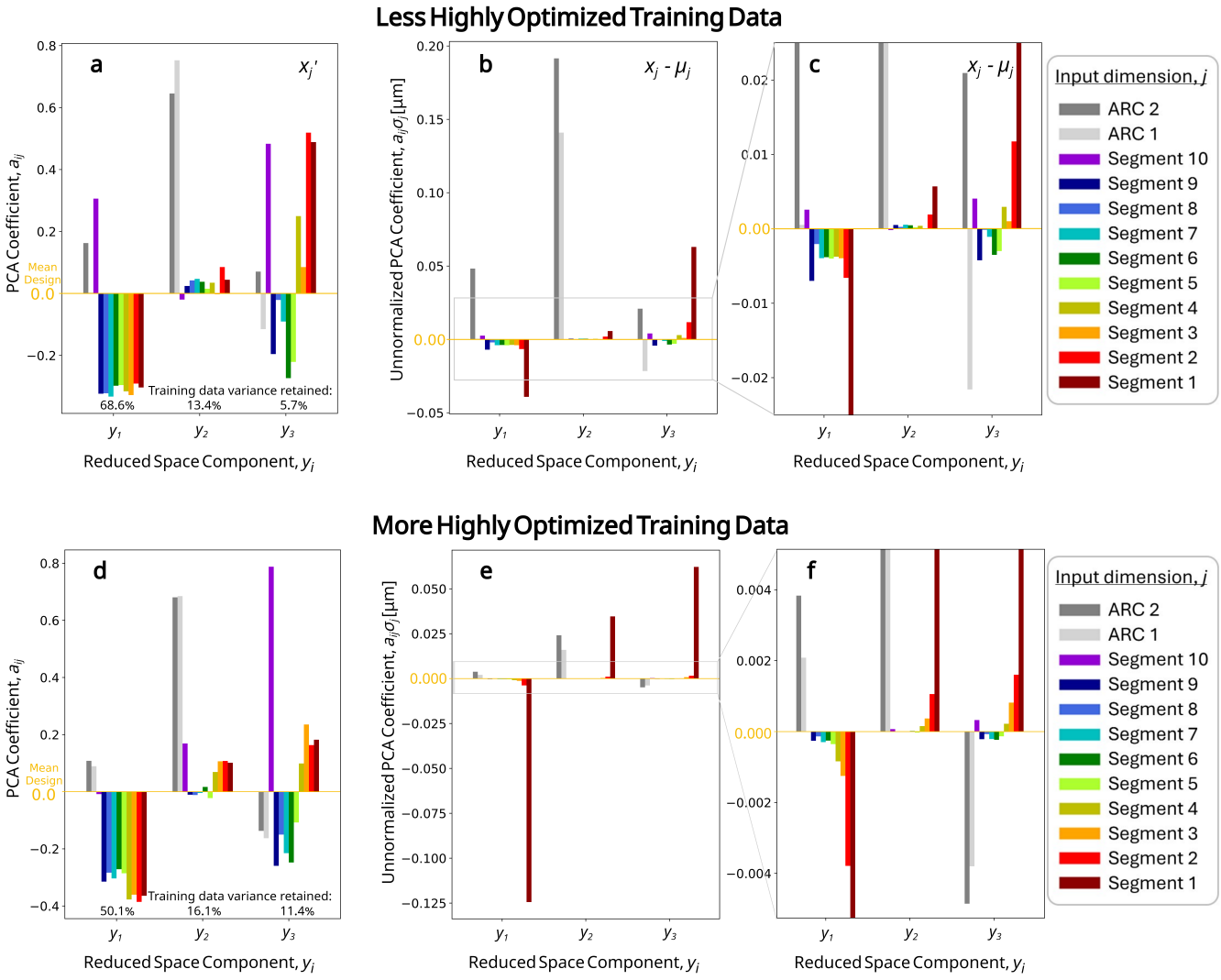

Supplementary Figure S5. Comparison of reduced dimensionality subspaces for less (top) and more (bottom) highly optimized training data. *Subfigures **a**,**b**,**c** are reproduced from Fig. 9.* Principal component construction for the first three components is shown. **a** and **d**: the PCA coefficient, a_{ij}, of equation (2), for each standardized input dimension, x'_j. **b** and **e**: PCA coefficient times the standard deviation, $a_{ij} * \sigma_j$, in micron, for each mean subtracted input dimension, $x_j - \mu_j$. **c** and **f**: y-scale zoom on the zero regions of **b** and **e**, respectively. The percent of training data variance which is captured by each of the principal components is given along the bottom of **a** and **d**. The primary optical phenomena in the design space are visibly encoded in the construction of the reduced spaces.

5.4 ML-enhanced study of MJ PPCs with flat back-reflector architecture

This section outlines ongoing research that I am conducting which is a natural complementary extension to the study presented in the last section. This work falls under the purview of the AIIR-Power BR project which runs until March 2026. In this project I use aiirmap and Synopsys Sentaurus TCAD to investigate and optimize the design of a 10J PPC with a flat back-reflector. Flat back-reflector architectures remove the substrate from the bottom of the MJ PV device and replace it with a thin-film reflector (mirror) layer (typically gold). This offers a significant increase in the light-trapping capabilities of the PPC, unlocking higher efficiencies and greatly reducing absorber thickness requirements [125, 184–186]. The thinner back-reflector devices ease material-quality and epitaxial-growth constraints, offering a design paradigm more commensurate with cost-effective, high-throughput manufacturing techniques. As the last section clearly showed the design landscape of MJ PPCs is high dimensional and highly correlated with strong optical, electrical, and optoelectronic effects mediating complex interactions between the many layers. In the case of back-reflector architectures these interactions are amplified by the thinner junctions and more complex photonic paths. Preliminary results show that these effects result in a nonlinear optimal design manifold in the parameter space, as opposed to convergence to simple solutions as was found for the on-substrate designs in the last section. These high-performing back-reflector designs offer significant flexibility to realize application specific systems.

Figure 5.1 shows some of these preliminary results of studies into 10J flat back-reflector PPCs. Similar to Figure 8 in the main document of Section 5.3, this figure shows the top (photocurrent figure-of-merit ≥ 0.99) optimized results in two pairs of 2-dimensional projections of the higher dimensionality design space. Examples of thinner segments, segment 10 vs. segment 7 thicknesses, are shown across the top row. The thickest layers, segment 2 vs. segment 1, are shown in the bottom row. The left column shows designs optimized using the same classical methods as described in Section 5.3 above. The right column shows the designs optimized using the ML-enhanced method using linear dimensionality reduction. The projections in Figure 5.1 use the same xy and colour scales and use red markers to highlight the higher performance and greater variety in the ML-enhanced designs. These preliminary results indicate that flat back-reflector designs with up to 40% reduction in the absorber thickness compared to a design which employs the Beer-Lambert law and a perfect back-mirror may be possible without any loss in efficiency. This study shows that dimensionality reduction is an effective method to identify, explore, and understand the non-linear optimal design manifold. This project will build off of the aiirmap codebase and calibrated Synopsys Sentaurus TCAD model introduced in the previous section. The model will be refined to obtain better calibration with back-reflector

devices and non-linear dimensionality reduction techniques using auto-encoder neural nets as in [187] will be included into aiirmap. Record efficiency flat back-reflector samples are an end target, as are non-conventional (thinned total absorber) designs and knowledge discovery in the emergent flat back-reflector MJ PPC design space.

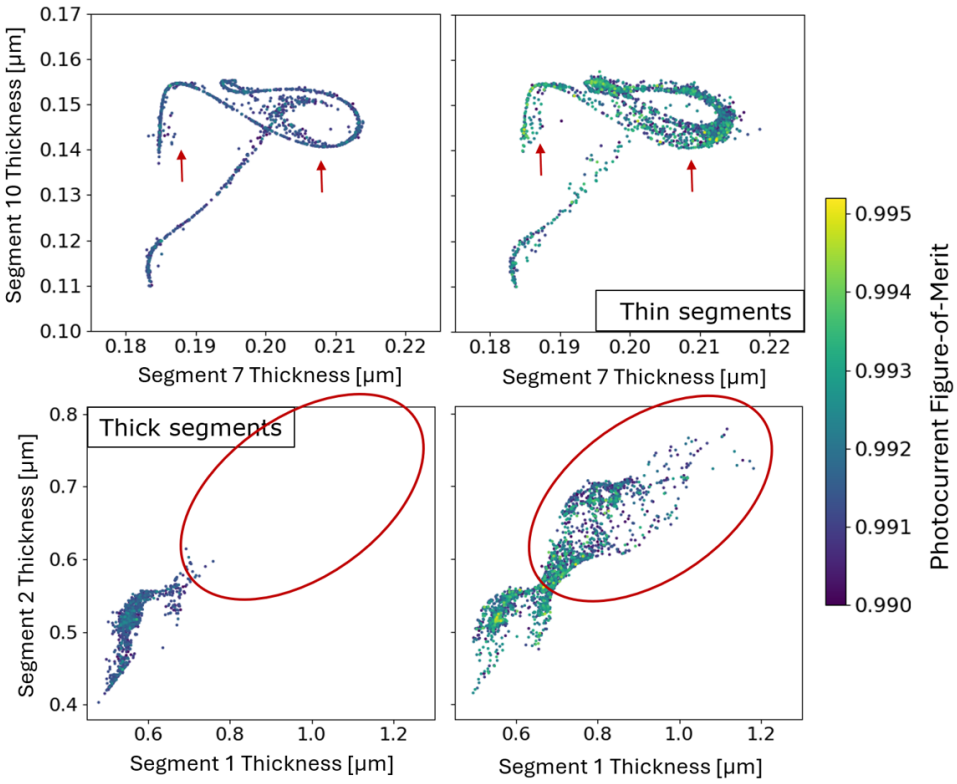

Figure 5.1: Two-dimensional projections selected from the higher dimensional design space. High performance designs (photocurrent figure-of-merit ≥ 0.99) from the classical optimization (left) and ML-enhanced optimization (right) methods described in Section 5.3 are shown. The projections are of two thinner segments, segment 10 and segment 7, in the top row and the two thickest segments, segment 2 and segment 1, in the bottom row. For ease of comparison, each pair shares xy axes and all four share the colour scale. Red markers indicate areas of difference.

Chapter 6

Cost-effective, infrared-capable adaptive optics

In this chapter I detail my efforts towards the experimental achievement of an AO system which can handle compressive sensing single pixel images as input. It consists of one contribution, presented at the IEEE Sensors Applications Symposium (SAS) 2023 conference. This work provides witness for a functioning experimental test bench (see Figure 2 in the next section) and evidence for the viable operation of speckle spot based adaptive optics algorithms on single pixel images with compressive sensing fractions as low as 15%. It indicates the feasibility of the single pixel adaptive optics approach as a cost-effective, infrared-capable AO technique.

6.1 Experimental point spread function imaging of turbulent wavefronts using compressive sensing

Scope and impact

This conference presentation and proceeding from SAS 2023 uses experimental and computational data to indicate the feasibility of single pixel images with and without compressive sensing as input for speckle spot based adaptive optics algorithms. I revitalize an experimental test bench which includes a spatial light modulator to simulate atmospheric phase-distortion and single pixel, multi-pixel cameras, and a Shack-Hartmann wavefront sensor for observation. Beam images are obtained using the variable methods with Kolmogorov phase screens used to simulate high atmospheric turbulence conditions (where the beam diameter is ten times

larger than the atmospheric coherence length). I compare the single pixel, multi-pixel, and wave-propagation-simulated focal plane patterns, the so-called 'speckle spot' patterns of static atmospheric turbulence. I consider speckle spot based adaptive optics an emerging technique which may respond well to compressive sensing images and introduce computational tools and metrics to analyze and compare the speckle spot content of the images. I contrast the speckle spot information from multi-pixel, simulated, and single pixel images with (simulated a-posteri Walsh-ordered or random down-sampled) compressive sensing fractions between 15% and 100% (the full 64x64 basis) and discuss the results.

In this work I introduce the following novelties;

1. Development of a fully functional, well-calibrated test bench with the capability to simulate and capture the phase-distortion caused by atmospheric turbulence using a Shack-Hartmann wavefront sensor in the pupil plane and both single pixel and multi-pixel cameras at the focal plane. Collection of single pixel images with a 64x64 Hadamard basis. Exemplification of clear visual congruence between single pixel, multi-pixel, and simulated focal plane wavefront speckle patterns.

2. Provision of evidence that speckle spot-based adaptive optics algorithms should perform just as well with single pixel images as standard multi-pixel images and that single pixel images with compressive sensing fractions as low as 15% may perform almost as well. Walsh down-sampling of the single pixel camera basis outperforms random across essentially all down-sampling rates between 45% and 15%. The metrics show that Walsh down-sampled images are better at retaining general (as indicated by higher structural similarity index measures) and speckle spot related information (as indicated by lower intensity-weighted average pairwise distances and relative intensity errors).

This work contributes to the development of adaptive optics systems which use single pixel architectures and/or compressive sensing. It falls under the initiative of the National Research Council of Canada's High-Throughput and Secure Networks Challenge and contributes to the goals given therein (e.g. high-speed internet access in remote communities of the Canadian north delivered through free-space infrared telecommunications links).

Author contributions

Robert F.H. Hunter: As a doctoral candidate with the University of Ottawa and intern with the National Research Council of Canada's Quantum and Nanotechnologies (then Advanced

Electronics and Photonics) Research Centre, I was the lead student on the experimental setup for this project. I revitalized the experimental test bench and greatly improved its performance and capabilities. I am the lead author of this study and manuscript.

Dr. Mohamadreza Pashazanoosi: As a doctoral candidate with the University of McMaster, Dr. Pashazanoosi was the lead active researcher on the compressive sensing application side of the single pixel camera adaptive optics project. He provided valuable feedback to the manuscript.

Prof. Steve Hranilovic: As a professor with the University of McMaster, Prof. Hranilovic contributed valuable guidance and leadership to this project. He provided valuable feedback to the manuscript.

Prof. Costel Flueraru: As a senior research officer with the National Research Council of Canada's Quantum and Nanotechnologies Research Centre, and adjunct University of Ottawa professor, Prof. Flueraru provided valuable guidance and leadership to this project. He assisted in analysis of the results and in editing the manuscript. Along with Dr. Pitts, Prof. Flueraru supervised my internship at the National Research Council.

Dr. Antony Orth: As a research officer with the National Research Council of Canada, Dr. Orth led his expertise to the conception of this project. He provided valuable feedback while editing the manuscript.

Dr. Oliver J. Pitts: As a senior research scientist with the National Research Council of Canada's Quantum and Nanotechnologies Research Centre, Dr. Pitts has provided valuable guidance and leadership to this project and to myself. He assisted in analysis of the results and provided key contributions to the manuscript. Along with Prof. Flueraru, Dr. Pitts supervised my internship at the National Research Council.

Copyright

R.F.H. Hunter, M. Pashazanoosi, S. Hranilovic, C. Flueraru, A. Orth, O.J. Pitts, "Experimental point spread function imaging of turbulent wavefronts using compressive sensing," *2023 IEEE Sensors Applications Symposium (SAS)*, July 18-20, 2023. Oral Presentation. Proceeding; doi: 10.1109/SAS58821.2023.10254074

Experimental Point Spread Function Imaging of Turbulent Wavefronts using Compressive Sensing

Robert F. H. Hunter[1,3], Mohamadreza Pashazanoosi[2], Steve Hranilovic[2], Costel Flueraru[3], Antony Orth[3], Oliver J. Pitts[3]

[1]*School of Electrical Engineering and Computer Science, University of Ottawa*
Ottawa, ON, Canada
rhunt013@uottawa.ca

[2]*Dept. of Electrical & Computer Engineering, McMaster University*
Hamilton, ON, Canada

[3]*National Research Council of Canada*
Ottawa, ON, Canada

***Abstract*—Wavefront distortion of free-space optical beams propagating through atmospheric turbulence leads to signal fading in communications applications. The wavefront distortion can be compensated by adaptive optics, but conventional methods based on wavefront sensing may fail to ensure adequate signal coupling in typical communications scenarios. Alternative methods rely on focal plane intensity measurements. In this work, we apply computational imaging using a digital micromirror device to reconstruct the focal plane intensity image of a beam distorted by simulated atmospheric turbulence generated by a phase-only spatial light modulator. The image fidelity of the experimental focal plane images is compared to calculated point spread functions as a function of the compression ratio for undersampled images.**

Keywords—Free-space Optical Communication, Atmospheric Turbulence, Single-Pixel Imaging, Wavefront Sensors

I. Introduction

There is increasing interest in free-space optical communication (FSOC) as a solution to increase the available bandwidth of inter-satellite and ground-satellite communication links. Establishing reliable ground-satellite communications using FSOC is seen as a mechanism to improve data transmission rates of feeder links, compared to current radio frequency (RF) solutions [1, 2]. However, optical transmission through the atmosphere is affected by atmospheric turbulence. In the context of FSOC, this results in intensity and phase distortions leading to signal fading [3, 4]. Adaptive optics (AO) techniques have been used to improve the performance of FSOC links through the atmosphere by sensing, and correcting for, the wavefront distortions caused by turbulence [5 - 7].

Traditional wavefront sensing approaches used in astronomical AO, such as the Shack-Hartmann wavefront sensor (SH-WFS), can fail under the strong turbulence conditions expected at ground station locations, particularly for low-angle elevations or when tracking a satellite at a high slew rate, as is required for communications with low earth orbit (LEO) satellites [8, 9]. Alternative methods have been proposed to improve AO performance in strong turbulence, including sensorless approaches, in which the corrective element is iteratively updated to optimize the optical beam to fiber coupling efficiency [10, 11]. However, the sensorless approach requires a large number of iterations, which may not be feasible for short coherence times, *e.g.* ~ 1 ms, which are typical for LEO downlinks [12]. Recently, a method has been proposed using imaging of the point spread function (PSF) in the focal plane to significantly reduce the number of iterations required [13]. This approach requires an imaging camera operating at both high speed and high sensitivity, which may present challenges, for example where the beam to be imaged is at a typical infrared telecommunications wavelength such as the C-band. It has been proposed that the PSF in the focal plane may be imaged using a single pixel imaging approach based on a digital micromirror device (DMD) [14]. This approach has the advantage of high sensitivity due to the optical integration of a large area of the image plane, and can be implemented over a wide range of wavelength bands using relatively inexpensive hardware. The PSF images are reconstructed from intensity measurements sequentially collected while projecting a sequence of patterns on the DMD, using for example the Hadamard basis. Based on the principles of compressive sensing (CS), the image can be reconstructed using significantly fewer data points than the number of image pixels [15]. An adaptive optics system using such a single pixel imager has been proposed [16], and a preliminary experimental demonstration was reported [17].

In this work, the design and construction of a benchtop turbulence simulation setup, using a phase-only liquid crystal spatial light modulator (SLM), and a DMD-based PSF imaging system, are described. The recorded PSF images reconstructed from both full and partial (CS) Hadamard pattern sets are compared with the simulated focal plane images obtained by calculating the propagated complex field from the known phase distribution projected on the SLM. The precision of the PSF information obtained is evaluated by comparing the locations and intensities of the speckle pattern spots computed by an image processing routine.

II. Experimental method

The schematic of the experimental test-bench is shown in Fig. 1. The light source for our setup is linearly polarized 635 nm laser light. It enters the system through a polarization maintaining fiber and is passed through a fixed collimator, linear polarizer, and half-wave plate which act to align the polarization axis of the laser light to the superordinal axis of the SLM. The beam is expanded by a factor of ten to overfill the SLM area using a fixed beam expander and is then masked down to fit on

Funding for this work was provided through the High Throughput and Secure Networks Challenge program at the National Research Council of Canada.

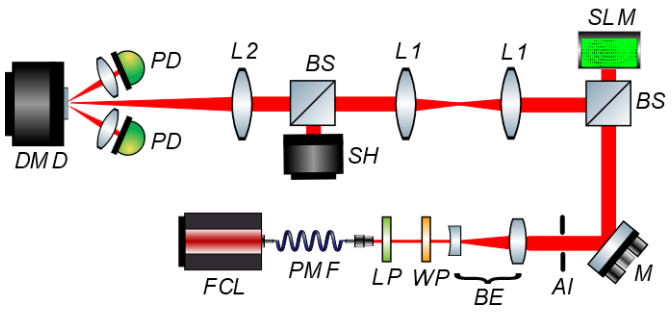

Fig. 1: Schematic of the experimental test-bench for development of an adaptive optics system employing a single-pixel camera imaging component. *FCL*: fiber coupled laser; *PMF*: polarization maintaining fiber; *LP*: linear polarizer; *WP*: half wave plate; *BE*: beam expander; *AI*: adjustable iris; *M*: beam steering mirror; *BS*: beam splitters; *SLM*: spatial light modulator; *L1*: relay lenses; *SH*: Shack Hartmann wavefront sensor; *L2*: imaging lens; *DMD*: digital micromirror device; *PD*: photodiodes.

the SLM screen using an adjustable iris. The beam is reflected and directed through a non-polarizing 50 / 50 beam splitter before impinging upon the reflective SLM screen which carries a phase screen which simulates atmospheric turbulence. The turbulent wavefront is reflected by the beam splitter and directed out to the imaging components using a 4*f* relay. At this pupil-plane, conjugate with the SLM plane, is located another non-polarizing 50 / 50 beam splitter which directs a portion of the beam intensity into the reference SH-WFS, and the other portion of the beam to the focusing lens. At the focal plane of this focusing lens is the DMD. Photodiodes are placed at both of the ± 24º reflection orientations of the DMD mirrors, each with a collimating lens. Subtracting the signals from these photodiodes allows a differential measurement for each modulation pattern to be collected in one measurement interval [18]. This data collection mode will be referred to as the single pixel camera (SPC). As an additional reference measurement, a standard CMOS camera, referred to as the multi-pixel camera (MPC) can be moved into the focal plane in place of the DMD.

Optical alignment of the system is eased by the use of standard 30 and 60 mm cages throughout the assembly, by standard optical mounting, and by the use of separate stage-mounted breadboards for the focal plane and pupil plane. Fine displacement, tip, and tilt control is given by the laser collimator, corner mirror, and SLM. Focus at the DMD is easily achieved, with repeatability, by placing the DMD mount on a micrometer-driven stage with translation along the optical axis. Instrument control, for all components except the SH-WFS, is implemented in a Python framework using vendor supplied software development kits. Control of the SH-WFS is executed using the vendor graphical user interface.

A. *Atmospheric turbulence simulation*

Atmospheric turbulence is simulated using Kolmogorov phase screens approximated using the inverse fast fourier transform (IFFT) plus subharmonics method [19]. In this work, three low frequency subharmonics are used. The strength of atmospheric turbulence captured by the phase screen is set by defining the desired D / r_0, where D is the beam diameter measured at the SLM and r_0 is the atmospheric coherence length (Fried's parameter). The phase screen is then generated using an r_0 scaled to the experimental beam diameter on the SLM. The effect of compensation optics typically present in AO systems is simulated by removing the average tip-tilt across the beam profile. Phase screens are generated on a 2048 × 2048 grid which is then cropped to the SLM format (1920 × 1200), phase wrapped modulo 2π and converted to a 10 bit integer and displayed on the SLM.

B. *Imaging techniques and beam propagation simulation*

The focal plane region of interest is determined by considering the focusing lens, beam size, and maximum turbulence strength. For these results, a focusing lens with a focal length of 500 mm was used. With a beam diameter of roughly 7 mm, prior to focusing, this lens yields a diffraction limited spot size of about 110 µm at the focal plane. Considering a maximum turbulence strength of $D / r_0 = 10$ and the scaling of the speckle pattern size with D / r_0 leads to a focal plane region of interest of ~ 1100 µm × 1100 µm.

The image capture area for all methods is defined by the SPC since the DMD has a larger pixel size than the MPC. A Texas Instruments DLP4500 employs square mirrors with a 7.8 µm side-length, rotated at 45° to form a diamond pattern [20]. The 1140 rows of the device are pitched at the 5.4 µm, half of the single mirror diagonal length, however, the 912 columns use a 10.8 µm, full mirror diagonal, pitch (for a visualization see Fig 6. in [17]). This disparity is taken into consideration when constructing the DMD display patterns, which incorporate an equal number of mirrors in each dimension (but half as many columns as rows). In this regard, we consider a region of interest of 1382.4 µm × 1382.4 µm, which encompasses 256 rows and 128 columns. Hadamard patterns were used as the SPC modulation basis due to their binary nature, orthogonality, and the existence of a fast Walsh-Hadamard transform. A full basis set of 64 × 64 pixel Hadamard patterns is used to collect the SPC image (4096 patterns), with four DMD mirrors used for each pattern pixel. The same region of interest is also captured by the other measurement methods; by selecting a correctly sized sub-region of the MPC pixel array, and by scaling the simulation pixel grid to cover this area. For the SPC and MPC, a calibration procedure is used to place the beam spot (without a turbulence phase screen) at the center of the region of interest prior to further data collection.

The effect of compressive sensing is simulated by a retroactive down-sampling of the collected full basis data set. Two down-sampling methods are considered. In the first approach, the retained indices are the first x % of the Walsh (sequency) ordered Hadamard basis [21]. In the second approach, a fixed proportion, x %, of the Hadamard indices are retained at random. In order to minimize the computational overhead, the image reconstructions are performed via an inverse fast Walsh-Hadamard transform with the non-sampled indices set to zero. This approach has been shown to be suitable for high frame rate reconstruction when a suitable basis ordering is selected [22].

The fast Walsh-Hadamard transform is applied to the full or down-sampled differential Hadamard data to obtain the

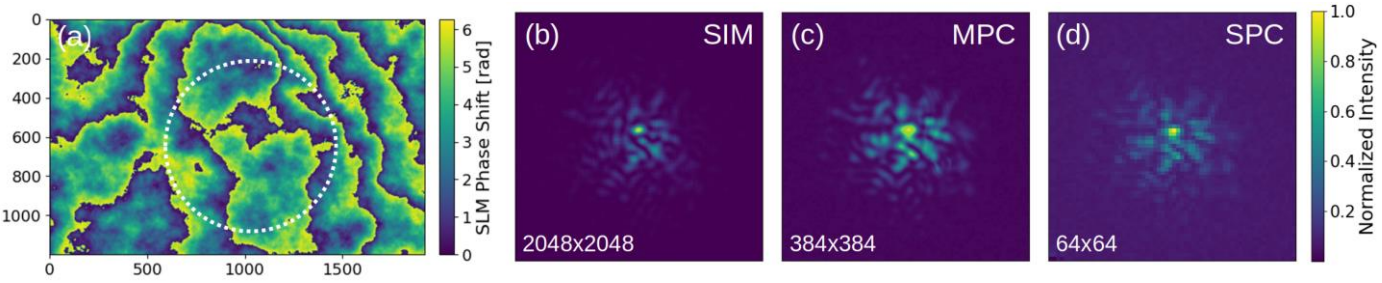

Fig. 2: (a) Simulated atmospheric turbulence phase screen with a turbulence strength of $D / r_0 = 10$ as displayed on the SLM. The phase is wrapped modulo 2π and represented using 10-bit integers. The dashed circle denotes the beam profile on the SLM. (b) Simulated, (c) MPC image, and (d) full basis SPC image of the corresponding focal plane PSF.

reconstructed SPC images. The differential data are obtained as the difference between the normalized, mean-subtracted intensity values from each photodiode. The mean subtraction is applied to account for background light and DC offset. A measurement artifact observed as bright pixels in the leftmost column and uppermost row of the reconstructed image is corrected by replacing this column and row by their neighbors, retaining the image contrast. These measurement artifacts may be associated with detector drift over the measurement period. However, no other imaging cleaning was applied to the full and down-sampled SPC images, so that the effect of the CS sampling fraction on the image quality could be compared for the as-reconstructed images. In practice, the resolution of these images could be improved, for example, by using a filter which is informed with the D / r_0 dependent power spectral density function.

System alignment and further image quality comparison is facilitated by a numerical simulation of the beam propagation and speckle pattern. In this work, the methodology of [23] is used. The pupil plane electric field is constructed as a plane wave with unity amplitude, travelling perpendicular to the pupil plane, and with a phase given by the beam profile masked phase screen. Simulations are carried out on a 2048 × 2048 grid which is scaled to the SLM's larger pixel dimension. The focal distance is used as a free parameter to produce the desired scaling of the focal plane simulation area to the imaging region of interest.

III. Results and Discussion

A. System alignment

A first test of the system alignment is the simulation and experimental capture of the diffraction limited spot which is produced when a flat zero phase screen is applied to the SLM. All images show a well-formed circular spot at the image center and a barely distinguishable first order Airy ring at the default capture contrast (as used in the figures below). However, minor tip-tilt misalignment is detectable in the shift of the SPC intensity maximum to the bottom left of the diffraction limited spot. Furthermore, a close examination of the Airy rings in the MPC image shows that the system retains a small amount of 0 / 90° astigmatism. The tip-tilt misalignment is visible again in the slight rotation of the astigmatism flares away from the 0 / 90° axes. Finally, observable in high exposure MPC images, are ghost Airy disks to the left and right of the primary pattern. These arise from diffraction of the beam off of the SLM pixel edges along its superordinal axis. This extra diffraction also leads to a brighter primary disk which appears in clear distinction to simulation in some turbulence degraded PSF images.

B. The effect of compressive sensing on image quality

Phase screens simulating an atmospheric turbulence strength of $D / r_0 = 10$ were generated. Here, we focus on the results from one of these phase screens. This phase screen as it is displayed on the SLM is shown in Fig. 2 (a). The beam profile location is marked with a dashed circle. Fig. 2 (b - d) show simulated and experimental images of the turbulence degraded speckle pattern PSF. In (b) the full resolution simulation is given, (c) shows the MPC image capture, and (d) shows the full 64 × 64 Hadamard basis reconstruction. All PSF images have been intensity normalized and set in the same color scale.

A good agreement between the location, size, and shape of the speckle spots is observed, both in the bright central and the finer outlying patterns. An increased contrast in the experimental images is observed due to the finite exposure periods compared to simulation which offers a single snapshot of the focal plane PSF. The structural similarity index measure (SSIM) was calculated as described in [24], as a metric to compare the images in Fig. 2. The SSIM between the full basis SPC image and the full resolution calculated PSF for the single phase screen is 0.86. For the MPC image and calculated PSF it is 0.31. This difference is attributable in part to the higher exposure of the MPC with respect to the SPC and simulation which affects both the luminance and contrast comparison functions of the SSIM. There is also evidence of the static aberration and SLM pixel related diffraction mentioned previously in the speckle spot smearing and extra bright central spot in the experimental results. It should be noted that the full resolution simulation (a) remains at much higher resolution than the MPC (b) and SPC (c) images (2048 × 2048, 384 × 384, and 64 × 64 respectively).

In Figs. 3 and 4 the centroids of the 30 brightest speckle spots have been identified using the peak_finder_max algorithm implemented in the Python scikit-image library [25]. The results of this search are shown in each image using red dots. Speckle spot finding has been carried out at a resolution of 128×128 using an intensity threshold of 2 % and a minimum spot

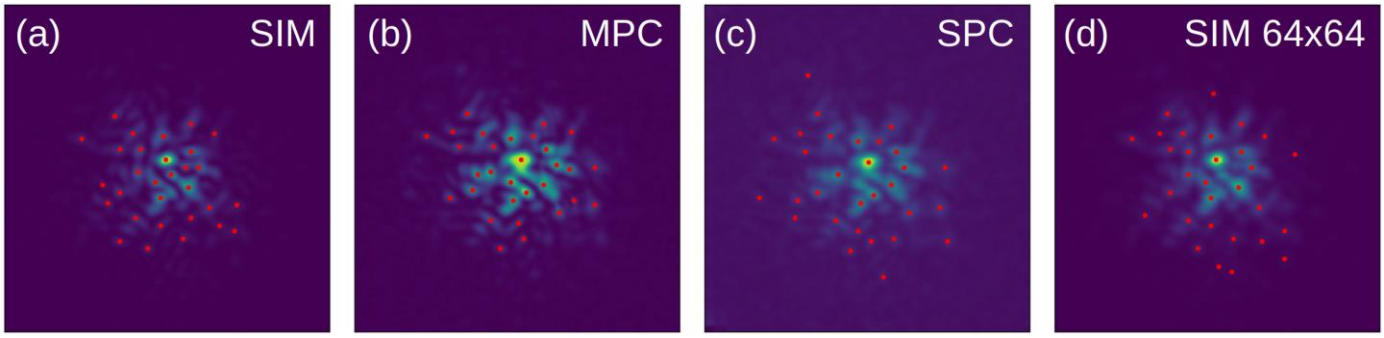

Fig. 3: Focal plane PSFs at the speckle spot finder resolution of 128 × 128 with the 30 brightest speckle spot centroids identified with red points: (a) full resolution simulation, (b) MPC, (c) SPC without CS, and (d) simulation downscaled to SPC resolution source images.

separation of three pixels. Fig. 3 (a-c) shows the speckle spot centroids for the PSF images in Fig. 2 (b-d). Fig. 3 (d) shows the speckle spot centroids for the simulation when it is downscaled to 64 × 64 before being upscaled to 128 × 128 for the centroid identification. This figure is included for comparison to the SPC.

The addition of the speckle spot centroid points allows a more detailed comparison of the simulated and experimental PSF images. We observe, that as the source image resolution is decreased there is a spreading out of the identified centroids, as spots merge and smear into one another. It can also be seen that the increased exposure of the experimental images has led to the identification of a different set of speckle spot centroids. For example, in the spots directly below the central point. The tilted 0 / 90° astigmatism present in the system may also contribute to the redistribution of spots from the top left and bottom right in the simulated images to the top right and bottom left in the experimental images.

In Fig. 4, the full 64 × 64 Hadamard basis SPC image has been down-sampled using Walsh (a-e) and random (f-j) ordering. The compressive sensing percentage, *i.e.*, the fraction of measurements which are retained, is given in the Figure for each image. CS percentages of 15, 25, 35, and 45% are included corresponding to 614, 1024, 1434, and 1843 measurements out of the full 4096 Hadamard basis set. The rightmost image in each row (subfigures (e) and (j)) shows the full basis SPC image reconstruction. It is identical to Fig. 4 (c) and is included for comparison. Each of the CS images is intensity normalized after down-sampling.

First, the effect of these down-sampling methods on the image itself can be observed. As expected, the Walsh-ordered down-sample appears primarily as a loss of resolution along the *x* and *y* directions. While resolution is lost, the brightest region of the image remains centered. This is not the case for the random down-sampling method which sees a blurring and pixelating effect occur across the whole image area. The speckle

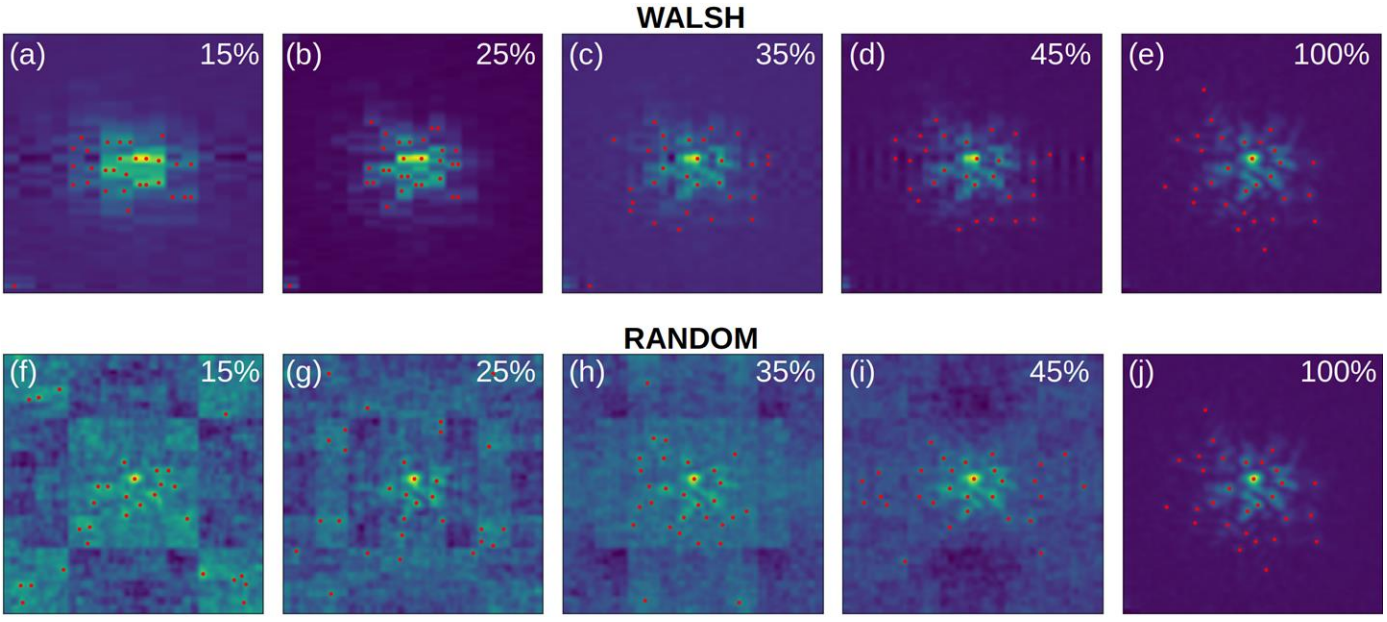

Fig. 4: Focal plane PSFs at the speckle spot finder resolution of 128 × 128 with the 30 brightest speckle spot centroids identified by red points. For SPC images down-sampled using the (a-e) Walsh or (f-j) random method. The percentage of measurements retained in each image is given in the figure.

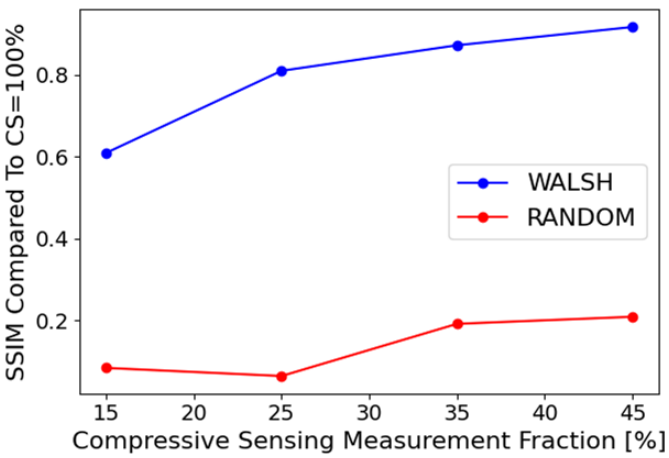

Fig. 5: Structural similarity index measure (SSIM) for the images with the given CS fraction in comparison to the full basis SPC image, for the Walsh (blue) and random (red) down-sampling methods, respectively.

pattern is successively buried under this noise becoming less and less recognizable as the compressive sensing fraction is reduced.

The identified speckle spot centroid locations corroborate these observations. For the Walsh ordered down-sampled results the centroid locations remain central, coming closer as the compressive sensing fraction is reduced to 25%, as the bright central spots are blurred together, and then, spreading apart again at a compressive sensing fraction of 15%, when not enough information is retained. A spurious spot is identified in the bottom left corner of the images at the lower CS fractions due to the smearing of the first column measurement artifact which is corrected only after reconstruction of the down-sampled spectra. For the random down-sampling method the loss of signal to noise is clear in the identification of speckle spot centroids which do not have any correlation with speckle spots in the full basis image. This is especially evident in the outlying regions of the image. Due to the random nature of this method the number and location of speckle spots attributable to noise does not follow a specific trend with respect to the compressive

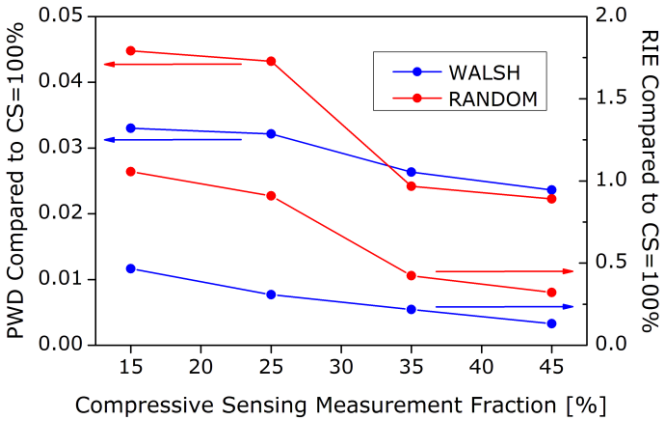

Fig. 6: Intensity-weighted average pairwise distance (PWD) and relative intensity error (RIE) between the normalized, intensity ordered speckle spot centroids for the images with the given CS fraction in comparison to the full basis SPC image, for the Walsh (blue) and random (red) down-sampling methods, respectively.

sensing fraction. For instance, for this phase screen PSF the measurements retained with a compressive sensing fraction of 15% accentuate the brightness in the center of the image and seem to lead to a better collection of identified speckle spot centroids than the CS 25% image. The random nature leads to a large variation in the quality of the CS images from one phase screen PSF to another (or even for a subsequent down-sampling of the same phase screen PSF). On the other hand, the Walsh down-sampled CS images for other phase screens tend to follow the same trend as the phase screen PSF presented here.

Fig. 5 shows the SSIM metric calculated for the down-sampled CS images, with the full-basis (100%) image used as the reference. For both the Walsh-ordered and random down-sampling, the SSIM increases as the measurement fraction increases, reflecting increasing similarity to the reference image. However, the SSIM is significantly higher for all of the images using Walsh-ordered down-sampling, compared to the ones using random down-sampling. This is likely due to a large influence of background noise on the SSIM metric for the images using random down-sampling.

C. Speckle-based comparison of the image quality

For applications in wavefront sensing and AO, visual comparison, or general image quality metrics such as the SSIM, for the reconstructed image quality may not be as relevant, since the ultimate aim is to accurately correct the wavefront rather than to output a high-quality image. For example, in the method outlined in [13], the only parameters retained from the focal plane image are speckle spot centroid locations and intensities. Furthermore, in that method the plane waves applied as the basis for the wavefront correction are weighted on the basis of the spot intensities. As a proposed pair of metrics to evaluate the PSF image quality for AO purposes, we therefore computed the intensity-ordered pairwise distances between nearest spots, and the relative errors in the corresponding intensities, for the spot locations and intensities obtained from a reference and comparison image, respectively. Average values were then calculated using an intensity-weighted average, as shown in (1):

$$PWD = \Sigma_i I_{0i} \cdot ((x_i - x_{0i})^2 + (y_i - y_{0i})^2)^{1/2} / \Sigma_i I_{0i}, \quad (1)$$

where the pairwise distances are calculated with the x and y locations normalized to the image size, *i.e.* a distance value of 1 corresponds to the image side length, and (2):

$$RIE = \Sigma_i I_{0i} \cdot | (I_i - I_{0i}) / I_{0i} | / \Sigma_i I_{0i}, \quad (2)$$

where in both (1) and (2) the sums are calculated over the 30 brightest spot centroids, and (x_i, y_i, I_i) and (x_{0i}, y_{0i}, I_{0i}) denote the positions and intensities of the ith spot in the comparison and reference images, respectively.

Fig. 6 shows the averaged pairwise distance (PWD) and relative intensity error (RIE) metrics defined in (1) and (2) as a function of the CS measurement fraction, with the non-compressive or 100 % measurement fraction image as the reference. As would be expected, the general trend is an increase in the PWD and RIE as the CS measurement fraction decreases. However, it is not clear whether these differences are significant: for comparison, the same metrics were calculated for three of

the experimental PSF images using the 2048 × 2048 resolution simulated PSF as the reference, again using *x* and *y* length scales normalized to the image size for all images. The PWD between the MPC image and the simulated PSF is 0.023, and the RIE is 0.79. For the SPC non-compressive image (100% measurement fraction) compared to the simulated PSF, the PWD is 0.026 and the RIE is 0.23, and for the SPC image using Walsh down-sampling at 15% measurement fraction, the PWD is 0.035 and the RIE is 0.916. This suggests that the SPC would perform nearly as well as the MPC when used to feed an adaptive optics algorithm based on speckle spot finding, even for CS fractions as low as 15 %. Based on the PWD and RIE metrics, the down-selection of measurement indices using Walsh ordering is also seen to perform better than the random ordering, although the difference is not as significant as for the SSIM. This is likely a reflection of the greater background noise in the images reconstructed from randomly selected Hadamard basis vectors, leading to the image processing routine identifying spots in the background noise.

IV. Conclusions

We applied a computational imaging approach, using a digital micromirror device projecting Hadamard patterns, to reconstruct the focal plane intensity images of beams distorted by simulated atmospheric turbulence, which was generated by a phase-only spatial light modulator. Good agreement was obtained between the reconstructed images, standard CMOS camera images, and the calculated point spread functions obtained by numerical propagation of the applied phase screens to the focal plane. Image processing of the reconstructed focal plane images was applied to find the brightest spots in the speckle patterns. Comparison of the speckle spot positions and intensities as a function of the compressive sensing fraction in under-sampled images, and of the reconstructed image with the numerically calculated PSF, indicates that the computational imaging method should perform as well as a standard camera for non-compressive imaging, and almost as well at compressive fractions as low as 15 %, where the images are used as the input to a speckle spot-based adaptive optics algorithm.

References

[1] W. S. Rabinovich *et al.*, "Free-space optical communications research and demonstrations at the US Naval Research Laboratory," Applied optics 54.31 (2015): F189-F200.

[2] R. Saathof *et al*., "Optical technologies for terabit/s-throughput feeder link," 2017 IEEE International Conference on Space Optical Systems and Applications (ICSOS). IEEE, 2017.

[3] J. E. Kaufmann, "Performance limits of high-rate space-to-ground optical communications through the turbulent atmospheric channel," Free-Space Laser Communication Technologies VII. Vol. 2381. SPIE, 1995.

[4] Y. Dikmelik and F. M. Davidson, "Fiber-coupling efficiency for free-space optical communication through atmospheric turbulence," Applied Optics 44.23 (2005): 4946-4952.

[5] M. W. Wright, J. F. Morris, J. M. Kovalik, K. S. Andrews, M. J. Abrahamson, and A. Biswas, "Adaptive optics correction into single mode fiber for a low Earth orbiting space to ground optical communication link using the OPALS downlink," Opt. Express, vol. 23, no. 26, pp. 33705–33712, 2015.

[6] R. M. Calvo, *et al.*, "Optical technologies for very high throughput satellite communications," Free-Space Laser Communications XXXI. Vol. 10910. SPIE, 2019.

[7] Y. Liang, X. Su, C. Cai, L. Wang, J. Liu, H. Wang, J. Wang, 'Adaptive turbulence compensation and fast auto-alignment link for free-space optical communications," Optics Express 29.24 (2021): 40514-40523.

[8] J. D. Barchers, D. L. Fried, D. J. Link, G. A. Tyler, W. Moretti, T. J. Brennan, and R. Q. Fugate, "The performance of wavefront sensors in strong scintillation," Proc. SPIE 4839, 217 (2003).

[9] T. R. Ellis and J. D. Schmidt, "Wavefront Sensor Performance in Strong Turbulence with an Extended Beacon," in Proceedings of Aerospace Conference (IEEE, 2010).

[10] M. Segel and S. Gladysz. "Optimal, blind-search modal wavefront correction in atmospheric turbulence. Part I: simulations," Optics Express 29.2 (2021): 805-820.

[11] P. Taghinia, R. Clare, S. Weddell, L. Yang, "Direct model-based wavefront sensorless method with a fixed number of measurements," Optics Continuum, 1(12), 2460-2479 (2022).

[12] N. Perlot, M. Knapek, D. Giggenbach, J. Horwath, M. Brechtelsbauer, Y. Takayama, T. Jono, "Results of the optical downlink experiment KIODO from OICETS satellite to optical ground station Oberpfaffenhofen (OGS-OP)," Proc. SPIE 6457, 645704 (2007).

[13] C. E. Carrizo, R. M. Calvo, A. Belmonte, "Intensity-based adaptive optics with sequential optimization for laser communications," Opt. Expr. 26(13), pp. 16044-16053 (2018).

[14] M. D. A. Mohamed and S. Hranilovic, "Diversity reception for deep space optical communication using linear projections," IEEE J. Sel. Top.Quantum Electron., vol. 16, no. 5, pp. 1071–1083, 2010.

[15] M. F. Duarte, M. A. Davenport, D. Takhar, J. N. Laska, T. Sun, K. F. Kelly, R. G. Baraniuk, "Single-pixel imaging via compressive sampling," IEEE Signal Process. Mag. 25, 83–91 (2008).

[16] M. Pashazanoosi, M. Taylor, O. Pitts, C. Flueraru, A. Orth, S. Hranilovic, "Maximizing Atmospheric-Disturbed Fiber Coupling Efficiency with Speckle-based Phase Retrieval and a Single-Pixel Camera," Applied Optics, in press. DOI: 10.1364/AO.485172

[17] M. Taylor, M. Pashazanoosi, S. Hranilovic, C. Flueraru, A. Orth, O. Pitts, "Experimental setup for single-pixel imaging of turbulent wavefronts and speckle-based phase retrieval," in Proceedings of 2022 IEEE International Conference on Space Optical Systems and Applications (ICSOS, 2022), pp. 78-84.

[18] F. Soldevila, P. Clemente, E. Tajahuerce, N. Uribe-Patarroyo, P. Andrés P, J. Lancis, "Computational imaging with a balanced detector," Scientific Reports. 2016 Jun 29;6(1):29181.

[19] R. G. Lane, A. Glindemann, J. C. Dainty, "Simulation of a Kolmogorov phase screen," Waves in Rand. Media 2(3), pp. 209-224 (1992).

[20] "DLP4500 data sheet, product information and support | TI.com." https://www.ti.com/product/DLP4500 (accessed Apr. 4, 2023).

[21] C. Zhuoran, Z. Honglin, J. Min, W. Gang, S. Jingshi, "An improved Hadamard measurement matrix based on Walsh code for compressive sensing," In 2013 9th International Conference on Information, Communications & Signal Processing, pp. 1-4. IEEE, 2013.

[22] M. J. Sun, L. T. Meng, M. P. Edgar, M. J. Padgett, N. Radwell, "A Russian Dolls ordering of the Hadamard basis for compressive single-pixel imaging," Scientific reports, 7(1), 3464, 2017.

[23] D. G. Voelz, Computational Fourier Optics: A MATLAB Tutorial (SPIE, 2011).

[24] Z. Wang, A. C. Bovik, H. R. Sheikh, and E. P. Simoncelli, "Image quality assessment: from error visibility to structural similarity," IEEE Trans. on Image Proc., 13(4), pp. 600-612 (2004).

[25] S. van der Walt, J. L. Schönberger, J. Nunez-Iglesias, F. Boulogne, J. D. Waner, N. Yager, E. Gouillart, T. Yu, and the scikit-image contributors, "scikit-image: image processing in Python," PeerJ 2, e453 (2014).

Chapter 7

Summary and outlook

Harnessing the power in light has already begun to revolutionize our modern society. Solar power generation at utility and smaller scales energizes the global energy transition. Meanwhile, photonic power and data transmission in free-space and fibre optics powers 5G+ telecommunications, the internet of things, and safer, more reliable remote sensing. MJ PV offers the highest performance in both solar and laser based applications but is more expensive than other PV technologies. This thesis investigates new materials, new design paradigms, and technical challenges in the application of MJ PV devices to improve their efficacy and competitiveness. My research demonstrates a number of pathways to improve MJ PV performance: through the extension of the industry standard MJ solar cell to include a SiGeSn third junction, development of the subcell segmentation architecture, and incorporation of ML techniques into PV device design optimization. It also contributes to the development of a cost-effective, infrared-capable AO technique, an integral technology required to overcome fast signal fading in free-space photonic power and data transmission.

Chapter 3 gave an example of a classical approach to improving the solar power conversion efficiency of MJ solar cells; extension of an existing material system to include a new material. SiGeSn was explored as an emerging material which could be used as a third junction in the InGaP/InGaAs/Ge material system. Chapter 3 showed that a lattice-matched and current-matched system is possible with a $Si_{0.14}Ge_{0.824}Sn_{0.036}$ composition. That for the InGaP/InGaAs/SiGeSn/Ge device to outperform the 3J baseline, the SiGeSn must have trap-assisted recombination lifetimes longer than 100 ns when the surface recombination velocity is $5{\times}10^4$ cm/s. It further discussed the loss mechanisms and design challenges in the 4J device. For instance, an under-production of current in the germanium subcell due to low absorption, high Auger recombination, and high reflectivity peaks which hinders the device performance through current limiting.

Future researchers looking to develop SiGeSn and/or extend the InGaP/InGaAs/Ge material system can use my findings on SiGeSn material limits in their process consideration. The next step for this project would be to enter into an iterative simulation/design/manufacture loop, as described in Subsection 2.4.2. This would allow a more accurately calibrated device model but more importantly moves towards a physical prototype device which may be developed further to increase its technological readiness level eventually leading to its deployment in societal application. This pathway will require reliable high-quality growth of the pertinent SiGeSn compositions, which still requires further development [17,188]. Future researchers may overcome current under-production in the Ge subcell by investigating the use of nanotextured light trapping surfaces at the front- and/or back-side, increasing the bandgaps of the three top subcells, replacing the Ge with strained SiGeSn to increase the direct bandgap absorption, or by employing subcell segmentation. Since III-Vs and group-IV atoms act as dopants in semiconductors of the other type, growth of a monolithic structure with both classes of material typically requires two growth reactors to avoid contamination. This increases cost and complexity and potentially reduces material quality. Same reactor growth of III-Vs and group-IV semiconductors has been demonstrated [189], but requires further proof. One of the main hurdles for a SiGeSn inclusive 4J device is that a suitable material for the tunnel diode connecting the third and fourth subcells has not been developed. Future researchers must overcome this issue before a SiGeSn extension of the industry standard InGaP/InGaAs/Ge can reach fruition.

Chapter 4 shifted focus to subcell segmentation, an emerging design paradigm for MJ solar cells. I explained how segmented MJ solar cells ease the simultaneous lattice-matching and current-matching requirements by introducing a new design dimension: the number of segments in each subcell. In Chapter 4 I detail the work I completed to advance a custom mDBL code for segmented MJ solar cells, and the use of this codebase and other simulation modalities to investigate the potential benefits of subcell segmentation. Specifically, I showed how subcell segmentation expands the number of bandgap combinations which can achieve high efficiency; in the case of a third subcell extension to the InGaP/InGaAs/Ge material system I show that 36% of the segmented designs across the 0.75-1.25 eV interval can achieve better performance than their peak unsegmented counterpart ($\sim$1.0 eV) and for generic two-subcell devices I quantify the expansion in high-performance design space as a function of concentration factor. I also showed that minimal subcell segmentation can lead to $\geq$40% reductions in the thickness of the SiGeSn layers and $\geq$70% increases in open-circuit voltage while maintaining comparable power conversion efficiencies to the unsegmented design. Finally, I demonstrated how subcell segmentation unlocks the potential for CPV operation at extreme solar concentrations by leveraging the power shift from high currents to high voltages inherent in the segmented architecture. I showed how peak efficiencies can be pushed into the thousands of suns and even tens of thousands of suns for one and two junction solar cells and ascertained

the ideal bandgaps for each concentration and device type.

Segmented MJ solar cells are currently at an early stage of development and much further research is required to improve their technological readiness. While my research clearly demonstrates the disruptive potential of the design technique, further study with detailed predictive simulation and experimental devices is needed to confirm that this potential will translate into the real world. The commercialization of PPCs with up to 30 junctions indicates that the complexity inherent in the segmented design can be overcome [119]. Due to the growth restrictions inherent in the subcell segmentation modality, its application will realistically be targeted to specific applications and/or established high-quality material systems. One example, pertinent to this thesis is subcell segmentation of the InGaP/InGaAs/Ge material system to obtain better current matching. This is an interesting option but requires epitaxial growth of germanium and the inclusion of suitable tunnel diodes for the germanium subcell. As for the realization of SiGeSn MJ solar cells this requires further development of same reactor III-V and group-IV growth methods and development of suitable (ideally group-IV) materials to use as the tunnel diode in the germanium subcell. Other examples include GaAs/GaAs/silicon which takes advantage of minimal segmentation of high-quality materials which would otherwise be current mismatched [32], indium aluminum arsenide / indium aluminum arsenide / indium aluminum gallium arsenide / InGaAs to obtain current-matched wide spectral absorption in an InP-LM system [31], InGaP/InGaP/InGaAsP/InGaAsP/InGaAs for a current-matched high material quality 5J design with InP-LM bottom segments and a metamorphic buffer connected top subcell (the InGaP) [33], and so on. These examples show how subcell segmentation can be a useful tool in the MJ solar cell design toolbox. Future researchers can look to develop these minimal segmentation systems further or to use them as inspiration for their own targeted application.

Chapter 5 moves from solar to laser based PV. I outlined how MJ PV devices' have high dimensional and highly correlated design spaces and how modern artificial learning paradigms can be harnessed to help explore and understand these designs. I target the ML-enhanced design optimization of MJ PPCs. My central achievement in this project was the construction of aiirmap, a Python based framework which combines dimensionality reduction, batch run, databasing, optimization, and Synopsys Sentaurus TCAD simulation capabilities in an easy to use module. Chapter 5 explained how this framework has already been used by SUNLAB collaborators to achieve record PPC power conversion efficiency at 1446 nm illumination wavelength [51], to explore the effects of luminescent coupling on MJ PPC performance [98, 99], and to optimize GaAs betavoltaic devices [181–183]. Personally, I used the ML-enhanced framework to optimize and explore the design space of 10J InGaAs PPCs for operation at 1550 nm. I showed how the ML-enhanced framework produces over twenty times as many optimal designs with greater variability and with a 15% reduction in computational cost compared to a classical optimization method. And, how the construction of the reduced dimensionality subspace implicitly encodes

device physics and can be used to supplement the design team's understanding of the design.

The research presented in Chapter 5 opens a door to a new design paradigm for device design. The ML-enhanced approach allows a larger and more informed perspective of complex design spaces. The next step for this project, which is part of ongoing studies, is the use of the aiirmap framework to study MJ PPCs with a flat back-reflector architecture (see Section 5.4) and will augment its capabilities by including non-linear dimensionality reduction. Further use of the ML-enhanced approach in the optimization and study of MJ PPCs and betavoltaics by SUNLAB collaborators is anticipated, as is its use in the design of lasers and single and MJ solar cells. aiirmap is offered as an open-source module where it can be used to enhance the optimization of any problems which can be numerically modeled in software which can communicate with Python. It has been designed and communicated as general purpose and written to allow easy extension for more simulation softwares and machine learning techniques.

Finally, in Chapter 6, I turn directly to the application of MJ PV, and forward the development of a cost-effective, infrared-capable AO technique. AO technology is required to avoid fast signal fading due to atmospheric turbulence in free-space photonic links for 5G+ telecommunications and power-by-light systems. The ubiquity and transmission properties of free-space require that this solution be cost-effective and infrared-capable, a challenge since this operation is outside the response range of silicon. Chapter 6 outlined my work to increase the efficacy and capabilities of an experimental single pixel compressive sensing adaptive optics system. I achieved previously unattainable high level of agreement between single pixel, multi-pixel, and simulated focal point spread function imaging methods. And, I demonstrated the potential of single pixel imaging with compressive sensing fractions as low as 15% to perform almost as well as multi-pixel imaging when used as input for a speckle spot based AO algorithm.

The development of the experimental single pixel camera compressive sensing adaptive optics test bench is ongoing. Some next steps for this project include implementation of the AO algorithm in the test bench, dynamic simulated atmospheric turbulence and its correction, and latency optimization. Free-space experimentation with a static transmitter-receiver system on the National Research Council grounds will follow, then, drone or high-altitude balloon based receiver prototypes as this technology matures towards telecommunication applications in the real-world. Other avenues for future research include exploration and optimization of the single pixel imaging basis exploration and optimization, the compressive sampling method, and the adaptive optics algorithm. For cost and experimental ease (visibility), the current study uses a 650 nm visible wavelength laser, eventually this system will need to run infrared wavelengths in the targeted telecommunications bands, this functionality remains to be tested.

Overall, this thesis has demonstrated several pathways to improving the applicability and competitiveness of MJ PV. New materials and new design paradigms for MJ PV are explored and

technical challenges in the realization of free-space photonic links are addressed. Applications of this research range from small and utility-scale power generation for the global energy transition to 5G+ telecommunications, internet of things, remote power and sensing, and more. These technologies capture the power in light harnessing it for humanity's growth.

References

[1] A. Einstein, "On a heuristic point of view regarding the production and transformation of light," *Annalen der Physik*, vol. 322, no. 6, pp. 132–148, 1905. doi: 10.1002/andp.19053220607

[2] A. B. Arons and M. B. Peppard, "Einstein's proposal of the photon concept—a translation of the annalen der physik paper of 1905," *American Journal of Physics*, vol. 33, no. 5, pp. 367–374, 05 1965. doi: 10.1119/1.1971542

[3] J. Brehm and W. Mullin, *Introduction to the structure of matter*. New York: John Wiley and Sons, 1989.

[4] National Renewable Energy Laboratory (NREL), "Best research-cell efficiency chart," last accessed April 22nd, 2025. https://www2.nrel.gov/pv/cell-efficiency

[5] K. Horowitz, A. Ptak, B. Smith, and T. Remo, "A techno-economic analysis and cost reduction roadmap for III-V solar cells," 2018.

[6] M. Wilkins and K. Hinzer, *Multijunction solar cells*. CRC Press, 2017, vol. 2.

[7] S. Fafard and D. P. Masson, "Perspective on photovoltaic optical power converters," *Journal of Applied Physics*, vol. 130, no. 16, p. 160901, 2021. doi: 10.1063/5.0070860

[8] J. Nelson, *The physics of solar cells*. Imperial College Press, 2003.

[9] A. Reinders, P. Verlinden, W. van Sark, and A. Freundlich, *Photovoltaic solar energy: From fundamentals to applications*. John Wiley and Sons, 2017.

[10] R. R. King, A. Boca, W. Hong, X. Liu, D. Bhusari, D. Larrabee, K. Edmondson, D. Law, C. Fetzer, S. Mesropian *et al.*, "Band-gap-engineered architectures for high-efficiency multijunction concentrator solar cells," in *24th European Photovoltaic Solar Energy Conference and Exhibition, Hamburg, Germany*, vol. 21, 2009, p. 55.

[11] R. R. King, W. Hong, C. Fetzer, D. Law, D. Larrabee, R. King, D. Bhusari, A. Boca, D. Larrabee, X. Liu *et al.*, "Fundamental efficiency losses in next-generation multijunction solar cells," in *25th European Photovoltaic Solar Energy Conference Proceeding*, 2010, pp. 1–4.

[12] A. W. Walker, "Bandgap engineering of multi-junction solar cells using nanostructures for enhanced performance under concentrated illumination," Ph.D. dissertation, Université d'Ottawa/University of Ottawa, 2013.

[13] J. Zeitouny, E. A. Katz, A. Dollet, and A. Vossier, "Band gap engineering of multi-junction solar cells: Effects of series resistances and solar concentration," *Scientific Reports*, vol. 7, no. 1, p. 1766, 2017.

[14] J. Olson, S. Kurtz, A. Kibbler, and P. Faine, "A 27.3% efficient $Ga_{0.5}In_{0.5}P$/GaAs tandem solar cell," *Applied physics letters*, vol. 56, no. 7, pp. 623–625, 1990.

[15] K. Nishioka, T. Takamoto, T. Agui, M. Kaneiwa, Y. Uraoka, and T. Fuyuki, "Annual output estimation of concentrator photovoltaic systems using high-efficiency InGaP/InGaAs/Ge triple-junction solar cells based on experimental solar cell's characteristics and field-test meteorological data," *Solar Energy Materials and Solar Cells*, vol. 90, no. 1, pp. 57–67, 2006. doi: https://doi.org/10.1016/j.solmat.2005.01.011

[16] L. Baribeau, "Design of multi-junction solar cells incorporating silicon-germanium-tin alloys with finite-element analysis and drift-diffusion model," Master's thesis, Université d'Ottawa/University of Ottawa, 2022.

[17] A. Attiaoui and O. Moutanabbir, "Indirect-to-direct band gap transition in relaxed and strained $Ge_{1-x-y}Si_xSn_y$ ternary alloys," *Journal of Applied Physics*, vol. 116, no. 6, 2014.

[18] V. D'Costa, Y.-Y. Fang, J. Tolle, J. Kouvetakis, and J. Menendez, "Tunable optical gap at a fixed lattice constant in group-IV semiconductor alloys," *Physical Review Letters*, vol. 102, no. 10, p. 107403, 2009.

[19] V. D'Costa, Y.-Y. Fang, and J. Tolle, "Ternary GeSiSn alloys: New opportunities for strain and band gap engineering using group-IV semiconductors," *Thin Solid Films*, vol. 518, no. 9, pp. 2531–2537, 2010.

[20] S. Wirths, D. Stange, R. Geiger, Z. Ikonic, T. Stoica, G. Mussler, J.-M. Hartmann, H. Sigg, D. Grützmacher, S. Mantl, and D. Buca, "Strain engineering for direct bandgap GeSn alloys," in *11th International Conference on Group IV Photonics (GFP)*, 2014. doi: 10.1109/Group4.2014.6962004

[21] Q. Chen, L. Zhang, H. Zhou, W. Li, B. K. Son, and C. S. Tan, "The effects of strain and composition on the conduction-band offset of direct band gap type-I GeSn/GeSnSi quantum dots for CMOS compatible mid-IR light source," *Semiconductor Science and Technology*, vol. 35, no. 2, p. 025008, 2020.

[22] P. Pearce, T. Wilson, A. Johnson, and N. Ekins-Daukes, "Characterization of SiGeSn for use as a 1 eV sub-cell in multi-junction solar cells," in *2018 IEEE 7th World Conference on Photovoltaic Energy Conversion (WCPEC) (A Joint Conference of 45th IEEE PVSC, 28th PVSEC and the 34th EU PVSEC)*, 2018. doi: 10.1109/PVSC.2018.8547764

[23] P. M. Pearce, C. A. Broderick, M. P. Nielsen, A. D. Johnson, and N. J. Ekins-Daukes, "Electronic and optical properties of $Si_xGe_{1-x-y}Sn_y$ alloys lattice-matched to Ge," *Physical Review Materials*, vol. 6, no. 1, p. 015402, 2022.

[24] A. B. P. Mbeunmi, A. Turala, R. Arvinte, A. Jaouad, V. Aimez, R. Arès, A. Boucherif, and S. Fafard, "High performance dual junction GaInP/GaAs for concentrator photovoltaic quad-junction," in *2020 47th IEEE Photovoltaic Specialists Conference (PVSC)*, 2020. doi: 10.1109/PVSC45281.2020.9300758

[25] L. S. Baribeau, R. F. H. Hunter, C. E. Valdivia, and K. Hinzer, "Drift-diffusion modelling of four-junction InGaP/InGaAs/SiGeSn/Ge solar cells," in *2022 IEEE 49th Photovoltaics Specialists Conference (PVSC)*, 2022. doi: 10.1109/PVSC48317.2022.9938603 pp. 1031–1031, [Oral].

[26] C. E. Valdivia and K. Hinzer, "Subcell segmentation for current matching and design flexibility in multijunction solar cells," *IEEE Journal of Photovoltaics*, vol. 10, no. 5, pp. 1329–1339, 2020. doi: 10.1109/JPHOTOV.2020.3005630

[27] C. E. Valdivia and K. Hinzer, "Segmented multi-junction solar cells: A new opportunity for cell design & optimization," in *2019 IEEE 46th Photovoltaic Specialists Conference (PVSC)*. IEEE, 2019, pp. 0045–0048.

[28] M. El-Gahouchi, M. R. Aziziyan, R. Arès, S. Fafard, and A. Boucherif, "Cost-effective energy harvesting at ultra-high concentration with duplicated concentrated photovoltaic solar cells," *Energy Science & Engineering*, vol. 8, no. 8, pp. 2760–2770, 2020.

[29] R. Garrison and R. Kleiman, "Higher efficiency tandem solar cells through composite-cell current matching," *Optics Express*, vol. 27, no. 8, pp. A543–A571, 2019.

[30] M. Lumb, M. González, C. Bailey, I. Vurgaftman, J. Meyer, J. Abell, M. Yakes, R. Hoheisel, J. Tischler, P. Stavrinou *et al.*, "Drift-diffusion modeling of InP-based triple junction solar cells," in *Physics, Simulation, and Photonic Engineering of Photovoltaic Devices II*, vol. 8620. SPIE, 2013, pp. 314–322.

[31] M. K. Yakes, K. J. Schmieder, M. P. Lumb, M. F. Bennett, L. C. Hirst, N. A. Kotulak, M. Gonzalez, S. Tomasulo, N. J. Ekins-Daukes, and R. J. Walters, "Split InAlAs top cell enabled four-junction solar cell lattice matched to InP," in *2016 IEEE 43rd Photovoltaic Specialists Conference (PVSC)*. IEEE, 2016, pp. 2836–2838.

[32] Z. Ren, H. Liu, Z. Liu, C. S. Tan, A. G. Aberle, T. Buonassisi, and I. M. Peters, "The GaAs/GaAs/Si solar cell: Towards current matching in an integrated two terminal tandem," *Solar Energy Materials and Solar Cells*, vol. 160, pp. 94–100, 2017.

[33] Y. Huang and H. Yang, "Design of InP-based metamorphic high-efficiency five-junction solar cells for concentrated photovoltaics," *Semiconductor Science and Technology*, vol. 30, no. 10, p. 105031, 2015.

[34] D. J. Aiken, "InGaP/GaAs/Ge multi-junction solar cell efficiency improvements using epitaxial germanium," in *Conference Record of the Twenty-Eighth IEEE Photovoltaic Specialists Conference-2000 (Cat. No. 00CH37036)*. IEEE, 2000, pp. 994–997.

[35] R. F. H. Hunter, C. E. Valdivia, L. S. Baribeau, and K. Hinzer, "Subcell segmentation for the optimization of a four-subcell multijunction solar cell design," in *OSA Advanced Photonics Congress (AP) 2020 (IPR, NP, NOMA, Networks, PVLED, PSC, SPPCom, SOF)*. Optica Publishing Group, 2020. doi: 10.1364/PVLED.2020.PvM2G.6 p. PvM2G.6, [Oral].

[36] R. F. H. Hunter, C. E. Valdivia, L. S. Baribeau, and K. Hinzer, "Unlocking the potential for extreme solar concentration via subcell segmentation," *AIP Conference Proceedings*, vol. 2550, no. 1, p. 020006, 09 2022. doi: 10.1063/5.0099470 [Oral].

[37] C. Algora, I. García, M. Delgado, R. Peña, C. Vázquez, M. Hinojosa, and I. Rey-Stolle, "Beaming power: Photovoltaic laser power converters for power-by-light," *Joule*, vol. 6, no. 2, pp. 340–368, 2022. doi: 10.1016/j.joule.2021.11.014

[38] M. Matsuura, "Recent advancement in power-over-fiber technologies," *Photonics*, vol. 8, no. 8, p. 335, 2021. doi: 10.3390/photonics8080335

[39] E. P. Putra, R. Theivindran, H. Hasnul, H. J. Lee, P. J. Ker, M. Z. Jamaludin, R. Awang, and F. A. Mohd Yusof, "Technology update on patent and development trend of power

over fiber: A critical review and future prospects," *Journal of Photonics for Energy*, vol. 13, no. 1, 2023. doi: 10.1117/1.JPE.13.011001

[40] Y. Zheng, G. Zhang, Z. Huan, Y. Zhang, G. Yuan, Q. Li, G. Ding, Z. Lv, W. Ni, Y. Shao, X. Liu, and J. Zu, "Wireless laser power transmission: Recent progress and future challenges," *Space Solar Power and Wireless Transmission*, p. S2950104023000020, 2024. doi: 10.1016/j.sspwt.2023.12.001

[41] J. Ding, W. Liu, C.-L. I, H. Zhang, and H. Mei, "Advanced progress of optical wireless technologies for power industry: An overview," *Applied Sciences*, vol. 10, no. 18, p. 6463, 2020. doi: 10.3390/app10186463

[42] W. Spillman, D. Crowne, and D. Woodward, "Optically powered and interrogated rotary position sensor for aircraft engine control applications," *Optics and Lasers in Engineering*, vol. 16, no. 2, pp. 105–118, 1992. doi: 10.1016/0143-8166(92)90003-P

[43] K. Worms, C. Klamouris, F. Wegh, L. Meder, D. Volkmer, S. P. Philipps, S. K. Reichmuth, H. Helmers, A. Kunadt, J. Vourvoulakis, A. W. Bett, C. Koos, W. Freude, J. Leuthold, and W. Stork, "Reliable and lightning-safe monitoring of wind turbine rotor blades using optically powered sensors," *Wind Energy*, vol. 20, no. 2, pp. 345–360, 2017. doi: 10.1002/we.2009

[44] F. V. B. De Nazare and M. M. Werneck, "Hybrid optoelectronic sensor for current and temperature monitoring in overhead transmission lines," *IEEE Sensors Journal*, vol. 12, no. 5, pp. 1193–1194, 2012. doi: 10.1109/JSEN.2011.2163709

[45] K. Goto, T. Nakagawa, O. Nakamura, and S. Kawata, "An implantable power supply with an optically rechargeable lithium battery," *IEEE Transactions on Biomedical Engineering*, vol. 48, no. 7, pp. 830–833, 2001. doi: 10.1109/10.930908

[46] R. F. H. Hunter, G. P. Forcade, Y. Grinberg, D. P. Wilson, M. N. Beattie, C. E. Valdivia, M. de Lafontaine, L.-P. St-Arnaud, H. Helmers, O. Höhn, D. Lackner, C. Pellegrino, J. J. Krich, A. W. Walker, and K. Hinzer, "Machine learning enhanced design optimization and knowledge discovery for multi-junction photonic power converters," *Scientific Reports*, July 2025, In peer-review.

[47] R. F. H. Hunter, G. P. Forcade, Y. Grinberg, M. N. Beattie, D. P. Wilson, C. E. Valdivia, M. de Lafontaine, L.-P. St-Arnaud, H. Helmers, O. Höhn, D. Lackner, C. Pellegrino, J. J. Krich, A. W. Walker, and K. Hinzer, "Using machine learning to optimize multi-junction photonic power converters," in *Physics, Simulation, and Photonic Engineering of Photovoltaic Devices XIII*, A. Freundlich, S. Collin, K. Hinzer, and I. R. Sellers,

Eds., vol. PC12881, International Society for Optics and Photonics. SPIE, 2024. doi: 10.1117/12.3002658 p. PC1288109, [Oral].

[48] K. Hinzer, R. F. H. Hunter, D. P. Wilson, G. P. Forcade, M. N. Beattie, C. E. Valdivia, O. Hãhn, L.-P. St-Arnaud, C. Pellegrino, D. Lackner, Y. Grinberg, J. J. Krich, A. W. Walker, and H. Helmers, "Multi-junction photonic power converters: AI enhanced design optimization," in *2024 IEEE 52nd Photovoltaic Specialist Conference (PVSC)*, 2024. doi: 10.1109/PVSC57443.2024.10749088 pp. 1642–1642, [Poster].

[49] K. Hinzer, R. F. H. Hunter, D. P. Wilson, G. P. Forcade, M. N. Beattie, C. E. Valdivia, O. Hãhn, L.-P. St-Arnaud, C. Pellegrino, D. Lackner, Y. Grinberg, J. J. Krich, A. W. Walker, and H. Helmers, "C-band multi-junction photonic power converters: AI techniques for optimized designs and role of luminescent coupling," in *6th Optical Wireless and Fiber Power Transmission Conference (OWPT)*, 2024, [Invited talk].

[50] Y. Grinberg, D.-X. Xu, M. AI-Digeil, D. Melati, R. F. H. Hunter, A. W. Walker, G. P. Forcade, J. Krich, K. Hinzer, M. M. Masnad, O. Liboiron-Ladoceur, P. Cheben, J. H. Schmld, and S. Janz, "Dimensionality reduction in photonics design - new methods and applications," in *2024 Photonics North (PN)*, 2024. doi: 10.1109/PN62551.2024.10621802 [Invited talk].

[51] G. P. Forcade, D. P. Wilson, M. N. Beattie, C. Pellegrino, H. Helmers, R. F. H. Hunter, O. Höhn, D. Lackner, L.-P. St-Arnaud, T. N. Tibbits, D. Poitras, C. E. Valdivia, A. W. Walker, J. J. Krich, and K. Hinzer, "Multi-junction laser power converters exceeding 50% efficiency in the short wavelength infrared," *Cell Reports Physical Science*, vol. 6, no. 6, May 2025. doi: 10.1016/j.xcrp.2025.102610

[52] D. Melati, Y. Grinberg, M. Kamandar Dezfouli, S. Janz, P. Cheben, J. H. Schmid, A. Sánchez-Postigo, and D.-X. Xu, "Mapping the global design space of nanophotonic components using machine learning pattern recognition," *Nature Communications*, vol. 10, no. 1, p. 4775, 2019. doi: 10.1038/s41467-019-12698-1

[53] R. F. H. Hunter, M. Pashazanoosi, S. Hranilovic, C. Flueraru, A. Orth, and O. J. Pitts, "Experimental point spread function imaging of turbulent wavefronts using compressive sensing," in *2023 IEEE Sensors Applications Symposium (SAS)*, 2023. doi: 10.1109/SAS58821.2023.10254074 [Oral].

[54] O. J. Pitts, M. Pashazanoosi, I. A. Ali, C. Flueraru, A. Orth, and S. Hranilovic, "Focal plane intensity-based adaptive optics with low-resolution image acquisition," in *Optica*

Imaging Congress 2024 (3D, AOMS, COSI, ISA, pcAOP). Optica Publishing Group, 2024. doi: 10.1364/AOPT.2024.OF4F.3

[55] M. Taylor, M. Pashazanoosi, S. Hranilovic, C. Flueraru, A. Orth, and O. Pitts, "Experimental setup for single-pixel imaging of turbulent wavefronts and speckle-based phase retrieval," in *2022 IEEE International Conference on Space Optical Systems and Applications (ICSOS)*, 2022. doi: 10.1109/ICSOS53063.2022.9749732

[56] M. Pashazanoosi, M. Taylor, O. Pitts, C. Flueraru, A. Orth, and S. Hranilovic, "Maximizing atmospheric-disturbed fiber coupling efficiency with speckle-based phase retrieval and a single-pixel camera," *Appl. Opt.*, vol. 62, no. 23, pp. G43–G52, Aug 2023. doi: 10.1364/AO.485172

[57] W. S. Rabinovich, C. Moore, R. Mahon, P. Goetz, H. Burris, M. Ferraro, J. Murphy, L. Thomas, G. Gilbreath, M. Vilcheck *et al.*, "Free-space optical communications research and demonstrations at the US Naval Research Laboratory," *Applied optics*, vol. 54, no. 31, pp. F189–F200, 2015.

[58] R. Saathof, R. Den Breeje, W. Klop, S. Kuiper, N. Doelman, F. Pettazzi, A. Vosteen, N. Truyens, W. Crowcombe, J. Human *et al.*, "Optical technologies for terabit/s-throughput feeder link," in *2017 IEEE International Conference on Space Optical Systems and Applications (ICSOS)*. IEEE, 2017, pp. 123–129.

[59] H. Dahrouj, A. Douik, F. Rayal, T. Y. Al-Naffouri, and M.-S. Alouini, "Cost-effective hybrid RF/FSO backhaul solution for next generation wireless systems," *IEEE Wireless Communications*, vol. 22, no. 5, pp. 98–104, 2015. doi: 10.1109/MWC.2015.7306543

[60] A. Jahid, M. H. Alsharif, and T. J. Hall, "A contemporary survey on free space optical communication: Potentials, technical challenges, recent advances and research direction," *Journal of Network and Computer Applications*, vol. 200, p. 103311, 2022. doi: 10.1016/j.jnca.2021.103311

[61] F. P. Guiomar, M. A. Fernandes, J. L. Nascimento, V. Rodrigues, and P. P. Monteiro, "Coherent free-space optical communications: Opportunities and challenges," *Journal of Lightwave Technology*, vol. 40, no. 10, pp. 3173–3186, 2022. doi: 10.1109/JLT.2022.3164736

[62] O. Aboelala, I. E. Lee, and G. C. Chung, "A survey of hybrid free space optics (FSO) communication networks to achieve 5G connectivity for backhauling," *Entropy*, vol. 24, no. 11, p. 1573, 2022. doi: 10.3390/e24111573

[63] F. M. A. Al-Zubaidi, J. D. Lopez-Cardona, D. Sanchez Montero, and C. Vazquez, "Optically powered radio-over-fiber systems in support of 5G cellular networks and IoT," *Journal of Lightwave Technology*, vol. 39, no. 13, pp. 4262–4269, 2021. doi: 10.1109/JLT.2021.3074193

[64] C. Vazquez, J. D. Lopez-Cardona, P. C. Lallana, D. S. Montero, F. M. A. Al-Zubaidi, S. Perez-Prieto, and I. Perez Garcilopez, "Multicore fiber scenarios supporting power over fiber in radio over fiber systems," *IEEE Access*, vol. 7, pp. 158 409–158 418, 2019. doi: 10.1109/ACCESS.2019.2950599

[65] J. E. Kaufmann, "Performance limits of high-rate space-to-ground optical communications through the turbulent atmospheric channel," in *Free-Space Laser Communication Technologies VII*, vol. 2381. SPIE, 1995, pp. 171–182.

[66] Y. Dikmelik and F. M. Davidson, "Fiber-coupling efficiency for free-space optical communication through atmospheric turbulence," *Applied Optics*, vol. 44, no. 23, pp. 4946–4952, 2005.

[67] M. W. Wright, J. F. Morris, J. M. Kovalik, K. S. Andrews, M. J. Abrahamson, and A. Biswas, "Adaptive optics correction into single mode fiber for a low earth orbiting space to ground optical communication link using the OPALS downlink," *Optics Express*, vol. 23, no. 26, pp. 33 705–33 712, 2015.

[68] R. M. Calvo, J. Poliak, J. Surof, A. Reeves, M. Richerzhagen, H. F. Kelemu, R. Barrios, C. Carrizo, R. Wolf, F. Rein *et al.*, "Optical technologies for very high throughput satellite communications," in *Free-Space Laser Communications XXXI*, vol. 10910. SPIE, 2019, pp. 189–204.

[69] Y. Liang, X. Su, C. Cai, L. Wang, J. Liu, H. Wang, and J. Wang, "Adaptive turbulence compensation and fast auto-alignment link for free-space optical communications," *Optics Express*, vol. 29, no. 24, pp. 40 514–40 523, 2021.

[70] R. F. H. Hunter, "Development and evaluation of novel, large area, radiation hard silicon microstrip sensors for the ATLAS ITk experiment at the HL-LHC," Master's thesis, Carleton University, 2017.

[71] S. Sze and K. Ng, *Physics of Semiconductor Devices, third edition*. John Wiley and Sons, 2007.

[72] G. P. Forcade, "High-efficiency III-V semiconductor device and system optimization for photovoltaic applications," Ph.D. dissertation, Université d'Ottawa/University of Ottawa, 2025.

[73] E. M. Tonita, "High bifaciality and vertical photovoltaic technologies for a solar-powered north," Ph.D. dissertation, Université d'Ottawa/University of Ottawa, 2025.

[74] M. Wilkins, "Multi-junction solar cells and photovoltaic power converters: High-efficiency designs and effects of luminescent coupling," Ph.D. dissertation, Université d'Ottawa/University of Ottawa, 2017.

[75] Nobel Prize Outreach, "The nobel prize in physics 1921," 2025, last accessed March 21st, 2025. https://www.nobelprize.org/prizes/physics/1921/summary/

[76] H. Jho, B. Lee, Y. Ji, and S. Ha, "Discussion for the enhanced understanding of the photoelectric effect," *European Journal of Physics*, vol. 44, no. 2, p. 025301, 2023.

[77] S. Adachi, *Properties of semiconductor alloys: Group-IV, III-V and II-VI semiconductors*. John Wiley and Sons, 2009.

[78] National Renewable Energy Laboratory (NREL), "Reference air mass 1.5 spectra," last accessed April 22nd, 2025. https://www.nrel.gov/grid/solar-resource/spectra-am1.5.html

[79] A. Clarke, M. Darnon, K. Hinzer, and M. de Lafontaine, "Review of plasma etching processes for III-V semiconductors," *Micro and Nano Engineering*, 2025, In print.

[80] QPC Lasers, "1550nm, 15W fiber-coupled laser module, integrated fiber sensor," last accessed on Apr. 14th, 2025. https://www.laserdiodesource.com/shop/1550nm-15w-fiber-coupled-laser-module-QPC-Laser

[81] Analytical Spectral Devices Inc., "ASD FieldSpec 3 user manual," 2005, last accessed on Apr. 14th, 2025. https://fsf.nerc.ac.uk/assets/documents/ASD/FieldSpec3.pdf

[82] J. Piprek, *Semiconductor Optoelectronic Devices: Introduction to Physics and Simulation*. Elsevier Academic Press, 2003.

[83] A. M. Law, L. O. Jones, and J. M. Walls, "The performance and durability of anti-reflection coatings for solar module cover glass: A review," *Solar Energy*, vol. 261, pp. 85–95, 2023.

[84] C. E. Valdivia, E. Desfonds, D. Masson, S. Fafard, A. Carlson, J. Cook, T. J. Hall, and K. Hinzer, "Optimization of antireflection coating design for multijunction solar cells and concentrator systems," in *Photonics North 2008*, vol. 7099. SPIE, 2008, pp. 320–329.

[85] N. Nouri, "Design, modeling, and optimization of thin and ultra-thin photonic power converters operating at 1310 nm laser illumination," Ph.D. dissertation, Université d'Ottawa/University of Ottawa, 2022.

[86] H. Helmers, C. Karcher, and A. W. Bett, "Bandgap determination based on electrical quantum efficiency," *Applied Physics Letters*, vol. 103, no. 3, p. 032108, 07 2013. doi: 10.1063/1.4816079

[87] O. Almora, C. I. Cabrera, J. Garcia-Cerrillo, T. Kirchartz, U. Rau, and C. J. Brabec, "Quantifying the absorption onset in the quantum efficiency of emerging photovoltaic devices," *Advanced energy materials*, vol. 11, no. 16, p. 2100022, 2021.

[88] P. Pérez-Higueras and E. F. Fernández, *High concentrator photovoltaics: Fundamentals, engineering and power plants*. Springer, 2015.

[89] K. Araki, H. Tawa, H. Saiki, Y. Ota, K. Nishioka, and M. Yamaguchi, "The outdoor field test and energy yield model of the four-terminal on Si tandem PV module," *Applied Sciences*, vol. 10, no. 7, p. 2529, 2020.

[90] J. Schubert, E. Oliva, F. Dimroth, W. Guter, R. Loeckenhoff, and A. Bett, "High-voltage GaAs photovoltaic laser power converters," *IEEE Transactions on Electron Devices*, vol. 56, no. 2, pp. 170–175, 2009.

[91] H. D. Young, R. A. Freedman, A. L. Ford, and F. W. Sears, *Sears and Zemansky's University Physics: with Modern Physics, 13th Edition*. San Francisco: Pearson Addison-Wesley, 2012.

[92] M. Wilkins, C. E. Valdivia, A. M. Gabr, D. Masson, S. Fafard, and K. Hinzer, "Luminescent coupling in planar opto-electronic devices," *Journal of Applied Physics*, vol. 118, no. 14, p. 143102, 2015. doi: 10.1063/1.4932660

[93] M. Wilkins, C. E. Valdivia, S. Chahal, M. Ishigaki, D. P. Masson, S. Fafard, and K. Hinzer, "Performance impact of luminescent coupling on monolithic 12-junction phototransducers for 12 V photonic power systems," in *Physics, Simulation, and Photonic Engineering of Photovoltaic Devices V*, vol. 9743. SPIE, 2016, pp. 127–132.

[94] M. M. Wilkins, A. M. Gabr, A. H. Trojnar, H. Schriemer, and K. Hinzer, "Effects of luminescent coupling in single-and 4-junction dilute nitride solar cells," in *2014 IEEE 40th Photovoltaic Specialist Conference (PVSC)*. IEEE, 2014, pp. 3601–3604.

[95] D. Xia and J. J. Krich, "Efficiency increase in multijunction monochromatic photovoltaic devices due to luminescent coupling," *Journal of Applied Physics*, vol. 128, no. 1, p. 013101, 2020. doi: 10.1063/5.0009870

[96] D. J. Friedman, J. F. Geisz, and M. A. Steiner, "Effect of luminescent coupling on the optimal design of multijunction solar cells," *IEEE Journal of Photovoltaics*, vol. 4, no. 3, pp. 986–990, 2014. doi: 10.1109/JPHOTOV.2014.2308722

[97] M. A. Steiner, J. F. Geisz, T. E. Moriarty, R. M. France, W. E. McMahon, J. M. Olson, S. R. Kurtz, and D. J. Friedman, "Measuring IV curves and subcell photocurrents in the presence of luminescent coupling," *IEEE Journal of Photovoltaics*, vol. 3, no. 2, pp. 879–887, 2013. doi: 10.1109/JPHOTOV.2012.2228298

[98] P. Wilson, G. P. Forcade, R. F. H. Hunter, M. N. Beattie, A. W. Walker, Y. Grinberg, H. Helmers, O. Hohn, D. Lackner, J. J. Krich, and K. Hinzer, "Quantifying the luminescent coupling process in C-band multi-junction photonic power converters," in *Physics, Simulation, and Photonic Engineering of Photovoltaic Devices XIII*, A. Freundlich, S. Collin, K. Hinzer, and I. R. Sellers, Eds., vol. PC12881, International Society for Optics and Photonics. SPIE, 2024. doi: 10.1117/12.3000797 p. PC128810J, [Oral].

[99] P. Wilson, G. P. Forcade, R. F. H. Hunter, A. W. Walker, Y. Grinberg, J. J. Krich, and K. Hinzer, "Impact of luminescent coupling on multijunction InGaAs photonic power converters under current mismatched conditions in the C-band," photonics North 2025, Ottawa, Canada, May 2025. [Oral].

[100] G. M. Wilson, M. Al-Jassim, W. K. Metzger, S. W. Glunz, P. Verlinden, G. Xiong, L. M. Mansfield, B. J. Stanbery, K. Zhu, Y. Yan, J. J. Berry, A. J. Ptak, F. Dimroth, B. M. Kayes, A. C. Tamboli, R. Peibst, K. Catchpole, M. O. Reese, C. S. Klinga, P. Denholm, M. Morjaria, M. G. Deceglie, J. M. Freeman, M. A. Mikofski, D. C. Jordan, G. TamizhMani, and D. B. Sulas-Kern, "The 2020 photovoltaic technologies roadmap," *Journal of Physics D: Applied Physics*, vol. 53, no. 49, p. 493001, sep 2020. doi: 10.1088/1361-6463/ab9c6a

[101] D. Lackner, O. Höhn, A. W. Walker, M. Niemeyer, P. Beutel, G. Siefer, M. Schachtner, V. Klinger, E. Oliva, K. Hillerich *et al.*, "Status of four-junction cell development at Fraunhofer ISE," in *E3S Web of Conferences*, vol. 16. EDP Sciences, 2017, p. 03009.

[102] G. Timò, G. Abagnale, N. Armani, M. Calicchio, and B. Schineller, "MOVPE SiGeSn development for the next generation four junction solar cells," *AIP Conference Proceedings*, vol. 2012, no. 1, p. 040011, 09 2018. doi: 10.1063/1.5053519

[103] M. Wilkins, A. Walker, J. F. Wheeldon, G. Arbez, H. Schriemer, and K. Hinzer, "Design constraints of n-p InGaAsN dilute nitride sub-cells for 3- and 4- junction solar cell applications under concentrated illumination," in *2013 IEEE 39th Photovoltaic Specialists Conference (PVSC)*, 2013. doi: 10.1109/PVSC.2013.6744897

[104] R. Roucka, A. Clark, T. Wilson, T. Thomas, M. Führer, N. Ekins-Daukes, A. Johnson, R. Hoffman, and D. Begarney, "Demonstrating dilute-tin alloy SiGeSn for use in multijunction photovoltaics: Single- and multijunction solar cells with a 1.0-eV SiGeSn junction," *IEEE Journal of Photovoltaics*, vol. 6, no. 4, pp. 1025–1030, 2016. doi: 10.1109/JPHOTOV.2016.2559785

[105] F. Dimroth, M. Grave, P. Beutel, U. Fiedeler, C. Karcher, T. N. D. Tibbits, E. Oliva, G. Siefer, M. Schachtner, A. Wekkeli, A. W. Bett, R. Krause, M. Piccin, N. Blanc, C. Drazek, E. Guiot, B. Ghyselen, T. Salvetat, A. Tauzin, T. Signamarcheix, A. Dobrich, T. Hannappel, and K. Schwarzburg, "Wafer bonded four-junction GaInP/GaAs//GaInAsP/GaInAs concentrator solar cells with 44.7% efficiency," *Progress in Photovoltaics: Research and Applications*, vol. 22, no. 3, pp. 277–282, 2014. doi: https://doi.org/10.1002/pip.2475

[106] F. Dimroth, T. N. D. Tibbits, M. Niemeyer, F. Predan, P. Beutel, C. Karcher, E. Oliva, G. Siefer, D. Lackner, P. Fuß-Kailuweit, A. W. Bett, R. Krause, C. Drazek, E. Guiot, J. Wasselin, A. Tauzin, and T. Signamarcheix, "Four-junction wafer-bonded concentrator solar cells," *IEEE Journal of Photovoltaics*, vol. 6, no. 1, pp. 343–349, 2016. doi: 10.1109/JPHOTOV.2015.2501729

[107] S. van Riesen, M. Neubauer, A. Boos, M. M. Rico, C. Gourdel, S. Wanka, R. Krause, P. Guernard, and A. Gombert, "New module design with 4-junction solar cells for high efficiencies," in *11th International Conference on Concentrator Photovoltaic Systems: CPV-11*, ser. American Institute of Physics Conference Series, vol. 1679. AIP, Sep 2015. doi: 10.1063/1.4931553

[108] K. Araki, Y. Ota, H. Saiki, H. Tawa, K. Nishioka, and M. Yamaguchi, "Super-multi-junction solar cells—device configuration with the potential for more than 50% annual energy conversion efficiency (non-concentration)," *Applied Sciences*, vol. 9, no. 21, p. 4598, 2019.

[109] R. R. King, D. C. Law, K. M. Edmondson, C. M. Fetzer, R. A. Sherif, G. S. Kinsey, D. D. Krut, H. L. Cotal, and N. H. Karam, "Metamorphic and lattice-matched solar cells under concentration," in *2006 IEEE 4th World Conference on Photovoltaic Energy Conference*, vol. 1, 2006. doi: 10.1109/WCPEC.2006.279567

[110] R. R. King, D. C. Law, K. M. Edmondson, C. M. Fetzer, G. S. Kinsey, H. Yoon, R. A. Sherif, and N. H. Karam, "40% efficient metamorphic GaInP/GaInAs/Ge multijunction solar cells," *Applied Physics Letters*, vol. 90, no. 18, p. 183516, 05 2007. doi: 10.1063/1.2734507

[111] A. Bett, D. Frank, W. Guter, R. Hoheisel, E. Oliva, S. Philipps, J. Schöne, G. Siefer, M. Steiner, A. Wekkeli, E. Welser, M. Meusel, W. Köstler, and G. Strobl, "Highest efficiency multi-junction solar cell for terrestrial and space applications," *24th European Photovoltaic Solar Energy Conference and Exhibition*, 01 2009.

[112] R. R. King, D. Bhusari, D. Larrabee, X.-Q. Liu, E. Rehder, K. Edmondson, H. Cotal, R. K. Jones, J. H. Ermer, C. M. Fetzer, D. C. Law, and N. H. Karam, "Solar cell generations over 40% efficiency," *Progress in Photovoltaics: Research and Applications*, vol. 20, no. 6, pp. 801–815, 2012. doi: https://doi.org/10.1002/pip.1255

[113] J. F. Geisz, R. M. France, K. L. Schulte, M. A. Steiner, A. G. Norman, H. L. Guthrey, M. R. Young, T. Song, and T. Moriarty, "Six-junction III–V solar cells with 47.1% conversion efficiency under 143-suns concentration," *Nature Energy*, vol. 5, pp. 326–335, 2020. doi: 10.1038/s41560-020-0598-5

[114] Y. Zhao, Y. Sun, Y. He, S. Yu, and J. Dong, "Design and fabrication of six-volt vertically-stacked GaAs photovoltaic power converter," *Scientific Reports*, vol. 6, no. 1, p. 38044, 2016. doi: 10.1038/srep38044

[115] M. N. Beattie, H. Helmers, G. P. Forcade, C. E. Valdivia, O. Hohn, and K. Hinzer, "InP- and GaAs-based photonic power converters under O-band laser illumination: Performance analysis and comparison," *IEEE Journal of Photovoltaics*, vol. 13, no. 1, pp. 113–121, 2023. doi: 10.1109/JPHOTOV.2022.3218938

[116] S. Fafard and D. P. Masson, "High-efficiency and high-power multijunction InGaAs/InP photovoltaic laser power converters for 1470 nm," *Photonics*, vol. 9, no. 7, p. 438, 2022. doi: 10.3390/photonics9070438

[117] S. Fafard and D. P. Masson, "74.7% efficient GaAs-based laser power converters at 808 nm at 150 K," *Photonics*, vol. 9, no. 8, p. 579, 2022. doi: 10.3390/photonics9080579

[118] S. Fafard, M. York, F. Proulx, M. Wilkins, C. Valdivia, M. Bajcsy, D. Ban, R. Arès, V. Aimez, K. Hinzer, M. Ishigaki, and D. Masson, "Ultra-efficient N-junction photovoltaic cells with VOC exceeding 14V at high optical input powers," in *2016 IEEE Photovoltaics Specialist Conference (PVSC)*, 06 2016. doi: 10.1109/PVSC.2016.7750065

[119] S. Fafard, D. Masson, J.-G. Werthen, J. Liu, T.-C. Wu, C. Hundsberger, M. Schwarzfischer, G. Steinle, C. Gaertner, C. Piemonte, B. Luecke, J. Wittl, and M. Weigert, "Power and spectral range characteristics for optical power converters," *Energies*, vol. 14, no. 15, p. 4395, 2021. doi: 10.3390/en14154395

[120] M. Wilkins, M. Ishigaki, P.-O. Provost, C. Valdivia, S. Fafard, D. Masson, E. Dede, and K. Hinzer, "Ripple-free boost-mode power supply using photonic power conversion," *IEEE Transactions on Power Electronics*, vol. PP, pp. 1–1, 06 2018. doi: 10.1109/TPEL.2018.2843158

[121] B. Majlesein, S. Babadi, I. Osahon, O. Younus, R. Nacke, C. Pellegrino, D. Lackner, G. Siefer, I. Tavakkolnia, H. Helmers, and H. Haas, "Efficient protocols for simultaneous optical wireless power transfer and communication," in *Optical Power Delivery*, B. Jalali, Ed., vol. 13359, International Society for Optics and Photonics. SPIE, 2025. doi: 10.1117/12.3043151

[122] C. Pellegrino, R. Nacke, D. Lackner, G. Siefer, B. Majlesein, O. Younus, I. Osahon, S. Babadi, I. Tavakkolnia, H. Haas, and H. Helmers, "Simultaneous optical power and data transfer using photonic power converter devices: Modeling and measurements," in *Optical Power Delivery*, B. Jalali, Ed., vol. 13359, International Society for Optics and Photonics. SPIE, 2025. doi: 10.1117/12.3042920

[123] R. Nacke, C. Pellegrino, D. Lackner, G. Siefer, B. Majlesein, O. Younus, I. N. O. Osahon, I. Tavakkolnia, A. W. Bett, H. Haas, and H. Helmers, "Application scenarios for simultaneous optical power and data transfer," in *Optical Power Delivery*, B. Jalali, Ed., vol. 13359, International Society for Optics and Photonics. SPIE, 2025. doi: 10.1117/12.3042965

[124] S. Fafard and D. Masson, "Vertical multi-junction laser power converters with 61% efficiency at 30 W output power and with tolerance to beam non-uniformity, partial illumination, and beam displacement," *Photonics*, vol. 10, no. 8, 2023. doi: 10.3390/photonics10080940

[125] H. Helmers, E. Lopez, O. Höhn, D. Lackner, J. Schön, M. Schauerte, M. Schachtner, F. Dimroth, and A. W. Bett, "68.9% efficient GaAs-based photonic power conversion

enabled by photon recycling and optical resonance," *physica status solidi (RRL) - Rapid Research Letters*, vol. 15, no. 7, p. 2100113, 2021. doi: 10.1002/pssr.202100113

[126] S. Fafard, M. C. A. York, F. Proulx, C. E. Valdivia, M. M. Wilkins, R. Arès, V. Aimez, K. Hinzer, and D. P. Masson, "Ultrahigh efficiencies in vertical epitaxial heterostructure architectures," *Applied Physics Letters*, vol. 108, no. 7, p. 071101, 2016. doi: 10.1063/1.4941240

[127] International Energy Agency, "World energy mix," last accessed on Apr. 14th, 2025. https://www.iea.org/world/energy-mix

[128] Intergovernmental Panel on Climate Change (IPCC), "Climate change 2023: Synthesis report. contribution of working groups I, II and III to the sixth assessment report of the intergovernmental panel on climate change," 2023.

[129] A. C. Lazaroiu, M. Gmal Osman, C.-V. Strejoiu, and G. Lazaroiu, "A comprehensive overview of photovoltaic technologies and their efficiency for climate neutrality," *Sustainability*, vol. 15, no. 23, p. 16297, 2023. doi: 10.3390/su152316297

[130] A. Baiju and M. Yarema, "Status and challenges of multi-junction solar cell technology," *Frontiers in Energy Research*, vol. Volume 10 - 2022, 2022. doi: 10.3389/fenrg.2022.971918

[131] M. J. O'Neill, "Chapter fifteen - space photovoltaic concentrators for outer planet and near-sun missions using ultralight Fresnel lenses," in *Photovoltaics for Space*, S. G. Bailey, A. F. Hepp, D. C. Ferguson, R. P. Raffaelle, and S. M. Durbin, Eds. Elsevier, 2023, pp. 411–432. ISBN 978-0-12-823300-9

[132] J. Li, A. Aierken, Y. Liu, Y. Zhuang, X. Yang, J. H. Mo, R. K. Fan, Q. Y. Chen, S. Y. Zhang, Y. M. Huang, and Q. Zhang, "A brief review of high efficiency III-V solar cells for space application," *Frontiers in Physics*, vol. Volume 8 - 2020, 2021. doi: 10.3389/fphy.2020.631925

[133] H. Yoon, J. E. Granata, P. Hebert, R. R. King, C. M. Fetzer, P. C. Colter, K. M. Edmondson, D. Law, G. S. Kinsey, D. D. Krut, J. H. Ermer, M. S. Gillanders, and N. H. Karam, "Recent advances in high-efficiency III–V multi-junction solar cells for space applications: Ultra triple junction qualification," *Progress in Photovoltaics: Research and Applications*, vol. 13, no. 2, pp. 133–139, 2005. doi: https://doi.org/10.1002/pip.610

[134] Y. Zhang, P. Guo, M. Tian, H. Chen, R. Liu, Z. Deng, and L. Li, "A review of solar concentration technology applications in deep space exploration: Environmental adaptability

and performance comparison," *Space Solar Power and Wireless Transmission*, vol. 2, no. 1, pp. 43–53, 2025. doi: https://doi.org/10.1016/j.sspwt.2025.02.001

[135] N. El-Atab, R. B. Mishra, R. Alshanbari, and M. M. Hussain, "Solar powered small unmanned aerial vehicles: A review," *Energy Technology*, vol. 9, no. 12, p. 2170121, 2021. doi: https://doi.org/10.1002/ente.202170121

[136] K. Sornek, J. Augustyn-Nadzieja, I. Rosikoń, R. Łopusiewicz, and M. Łopusiewicz, "Status and development prospects of solar-powered unmanned aerial vehicles: A literature review," *Energies*, vol. 18, no. 8, p. 1924, 2025. doi: 10.3390/en18081924

[137] H. Vu, N. H. Vu, and S. Shin, "Static concentrator photovoltaics module for electric vehicle applications based on compound parabolic concentrator," *Energies*, vol. 15, no. 19, p. 6951, 2022. doi: 10.3390/en15196951

[138] T. Masuda, K. Araki, K. Okumura, S. Urabe, Y. Kudo, K. Kimura, T. Nakado, A. Sato, and M. Yamaguchi, "Static concentrator photovoltaics for automotive applications," *Solar Energy*, vol. 146, pp. 523–531, 2017. doi: https://doi.org/10.1016/j.solener.2017.03.028

[139] T. Masuda, M. Yamaguchi, S. Iwasaki, T. Nakado, T. Takamoto, and K. Nishioka, "Public road driving tests of Toyota Prius equipped with high-efficiency III-V triple-junction PV modules," *EPJ Photovoltaics*, vol. 16, no. 20, 2025. doi: https://doi.org/10.1051/epjpv/2025008

[140] S. El Ayane and A. Ahaitouf, "Performance analysis of a micro-photovoltaic concentrator designed for automotive applications," *Energies*, vol. 17, no. 24, p. 6470, 2024. doi: 10.3390/en17246470

[141] Z. Wu, G. Xie, F. Gao, W. Chen, Q. Zheng, and Y. Liu, "Experimental study of a self-cooling concentrated photovoltaic (CPV) system using thermoelectric modules," *Energy Conversion and Management*, vol. 299, p. 117858, 2024. doi: https://doi.org/10.1016/j.enconman.2023.117858

[142] D. T. Vu, N. M. Kieu, T. Q. Tien, T. P. Nguyen, H. Vu, S. Shin, and N. H. Vu, "Solar concentrator bio-inspired by the superposition compound eye for high-concentration photovoltaic system up to thousands fold factor," *Energies*, vol. 15, no. 9, p. 3406, 2022. doi: 10.3390/en15093406

[143] V. Benda and L. Černá, "PV cells and modules – state of the art, limits and trends," *Heliyon*, vol. 6, no. 12, p. e05666, 2020. doi: https://doi.org/10.1016/j.heliyon.2020.e05666

[144] N. Jost, T. Gu, J. Hu, and I. Antón, "Review of micro concentrator photovoltaics technology: Optics," in *Nonimaging Optics: Efficient Design for Illumination and Concentration XIX*, R. Winston, L. Jiang, H. J. D. Johnsen, and T. A. Cooper, Eds., vol. 13132, International Society for Optics and Photonics. SPIE, 2024. doi: 10.1117/12.3028934

[145] M. Wiesenfarth, D. Iankov, J. F. Martínez, P. Nitz, M. Steiner, F. Dimroth, and H. Helmers, "Technical boundaries of micro-CPV module components: How small is enough?" *AIP Conference Proceedings*, vol. 2550, no. 1, p. 030008, 09 2022. doi: 10.1063/5.0099878

[146] P. Albert, A. Jaouad, G. Hamon, M. Volatier, C. E. Valdivia, Y. Deshayes, K. Hinzer, L. Béchou, V. Aimez, and M. Darnon, "Miniaturization of InGaP/InGaAs/Ge solar cells for micro-concentrator photovoltaics," *Progress in Photovoltaics: Research and Applications*, vol. 29, no. 9, pp. 990–999, 2021. doi: https://doi.org/10.1002/pip.3421

[147] M. de Lafontaine, G. Gay, E. Pargon, C. Petit-Etienne, R. Stricher, S. Ecoffey, A. Turala, M. Volatier, A. Jaouad, S. Fafard, V. Aimez, and M. Darnon, "Micro-scale III-V/Ge multijunction solar cell with through cell via contacts," in *2022 IEEE 49th Photovoltaics Specialists Conference (PVSC)*, 2022. doi: 10.1109/PVSC48317.2022.9938702

[148] Y. Zhou, C. Guan, H. Lv, Y. Zhang, R. Zhou, W. Chu, P. Lv, H. Qin, S. Li, and X. Li, "Design and research of laser power converter (LPC) for passive optical fiber audio transmission system terminal," *Photonics*, vol. 10, no. 11, p. 1257, 2023. doi: 10.3390/photonics10111257

[149] F. V. B. De Nazare and M. M. Werneck, "Temperature and current monitoring system for transmission lines using power-over-fiber technology," in *2010 IEEE Instrumentation & Measurement Technology Conference Proceedings*. IEEE, 2010. doi: 10.1109/IMTC.2010.5488198. ISBN 978-1-4244-2832-8

[150] A. T. Tokunaga, *Chapter 51 - New Generation Ground-Based Optical/Infrared Telescopes*. Boston: Elsevier, 2014, pp. 1089–1105. ISBN 978-0-12-415845-0

[151] N. Perlot, M. Knapek, D. Giggenbach, J. Horwath, M. Brechtelsbauer, Y. Takayama, and T. Jono, "Results of the optical downlink experiment KIODO from OICETS satellite to optical ground station Oberpfaffenhofen (OGS-OP)," in *Proceedings SPIE*, vol. 6457, 02 2007. doi: 10.1117/12.708413. ISBN 9780819465733

[152] C. Carrizo, R. Mata Calvo, and A. Belmonte, "Intensity-based adaptive optics with sequential optimization for laser communications," *Optics Express*, vol. 26, pp. 16 044–16 053, 06 2018. doi: 10.1364/OE.26.016044

[153] M. D. A. Mohamed and S. Hranilovic, "Diversity reception for deep-space optical communication using linear projections," *IEEE Journal of Selected Topics in Quantum Electronics*, vol. 16, no. 5, pp. 1071–1083, 2010. doi: 10.1109/JSTQE.2010.2046397

[154] M. F. Duarte, M. A. Davenport, D. Takhar, J. N. Laska, T. Sun, K. F. Kelly, and R. G. Baraniuk, "Single-pixel imaging via compressive sampling," *IEEE Signal Processing Magazine*, vol. 25, no. 2, pp. 83–91, 2008. doi: 10.1109/MSP.2007.914730

[155] G. M. Gibson, S. D. Johnson, and M. J. Padgett, "Single-pixel imaging 12 years on: A review," *Opt. Express*, vol. 28, no. 19, pp. 28 190–28 208, Sep 2020. doi: 10.1364/OE.403195

[156] D. Mackenzie, "Compressed sensing makes every pixel count," in *Computer Science, Engineering, Physics*, 2009. https://api.semanticscholar.org/CorpusID:566312

[157] C. E. Shannon, "A mathematical theory of communication," *The Bell System Technical Journal*, vol. 27, no. 3, pp. 379–423, 1948. doi: 10.1002/j.1538-7305.1948.tb01338.x

[158] C. E. Carrizo, "Advanced adaptive compensation system for free-space optical communications," Ph.D. dissertation, Universitat Politecnica de Catalunya, BarcelonaTech, 2019.

[159] W. Shockley and H. J. Queisser, "Detailed balance limit of efficiency of p-n junction solar cells," *Journal of Applied Physics*, vol. 32, no. 3, pp. 510–519, 03 1961. doi: 10.1063/1.1736034

[160] T. Tiedje, E. Yablonovitch, G. D. Cody, and B. G. Brooks, "Limiting efficiency of silicon solar cells," *IEEE Transactions on Electron Devices*, vol. 31, no. 5, 1984.

[161] J. Piprek, "Simulation-based machine learning for optoelectronic device design: Perspectives, problems, and prospects," *Optical and Quantum Electronics*, vol. 53, no. 175, 2021. doi: 10.1007/s11082-021-02837-8

[162] Synopsys Inc., "Sentaurus workbench user guide version S-2021.06," 2021.

[163] V. Liu and S. Fan, "S^4 : A free electromagnetic solver for layered periodic structures," *Computer Physics Communications*, vol. 183, no. 10, pp. 2233–2244, 2012. doi: 10.1016/j.cpc.2012.04.026

[164] M. Beattie, "Semiconductor materials and devices for high efficiency broadband and monochromatic photovoltaic energy conversion," Ph.D. dissertation, Université d'Ottawa/University of Ottawa, 2021.

[165] Synopsys Inc., "Epi/matpar user guide," Apr. 2008.

[166] Synopsys Inc., "Sentaurus device user guide version S-2021.06," 2021.

[167] Synopsys Inc., "Sentaurus data explorer user guide version S-2021.06," 2021.

[168] Synopsys Inc., "Sentaurus visual user guide version S-2021.06," 2021.

[169] P. Pearce and V. Liu, "S4 - RCWA," *github* https://github.com/phoebe-p/S4, retrieved Jan. 2023.

[170] Newport Corporation, "Quantum efficiency measurement system, 350-1100 nm wavelength range," 2024, last accessed on Apr. 22, 2025. https://www.newport.com/p/IQE-200B?srsltid=AfmBOorvZhsriT-qfzQi0x5QGIT3f2FQUJ1JOAa_5EamuYtQI5q4jJfn

[171] Plotly Technologies Inc. (2015) Collaborative data science. Montreal, QC. https://plot.ly

[172] G. Letay and A. Bett, "EtaOpt – a program for calculating limiting efficiency and optimum bandgap structure for multi-bandgap solar cells and TPV cells," in *Proceedings of the 17th European Photovoltaic Solar Energy Conference and Exhibition*, 10 2001.

[173] National Research Council of Canada, "Supporting collaborative projects between Canada and Germany in artificial intelligence and value-added manufacturing," 2021. https://nrc.canada.ca/en/stories/supporting-collaborative-projects-between-canada-germany-artificial-intelligence-value-added

[174] Fraunhofer Institute for Solar Energy Research, "AI-assisted design and fabrication of photonic infrared power converters for energy and telecommunication," 2021. https://www.ise.fraunhofer.de/en/research-projects/aiir-power.html

[175] G. P. Forcade, M. N. Beattie, C. E. Valdivia, H. Helmers, O. Höhn, P. Wilson, L.-P. St-Arnaud, R. F. H. Hunter, D. Lackner, J. J. Krich, A. W. Walker, and K. Hinzer, "High-performance multi-junction C-band photonic power converters: Calibrated opto-electronic model for next generation designs," in *2023 IEEE 50th Photovoltaic Specialists Conference (PVSC)*, 2023. doi: 10.1109/PVSC48320.2023.10359786 [Oral].

[176] Wes McKinney, "Data Structures for Statistical Computing in Python," in *Proceedings of the 9th Python in Science Conference*, Stéfan van der Walt and Jarrod Millman, Eds., 2010. doi: 10.25080/Majora-92bf1922-00a

[177] The pandas development team, "pandas-dev/pandas: Pandas, version 2.2.2," Apr. 2024.

[178] F. Pedregosa, G. Varoquaux, A. Gramfort, V. Michel, B. Thirion, O. Grisel, M. Blondel, P. Prettenhofer, R. Weiss, V. Dubourg, J. Vanderplas, A. Passos, D. Cournapeau, M. Brucher, M. Perrot, and E. Duchesnay, "Scikit-learn: Machine learning in python," *Journal of Machine Learning Research*, vol. 12, pp. 2825–2830, 2011. doi: 10.5555/1953048.2078195

[179] R. F. H. Hunter, "aiirmap," *github* https://github.com/rfhhunter/aiirmap, 2024.

[180] Synopsys Inc., "Sentaurus workbench optimization framework user guide version S-2021.06," 2021.

[181] M. de Lafontaine, R. F. H. Hunter, G. Forcade, J. Cook, D. Drouin, J. Krich, and K. Hinzer, "p-i-n betavoltaic cells under Ni63 irradiation: Quantifying carrier collection and power output," 06 2024. doi: 10.1109/PVSC57443.2024.10748690 pp. 0662–0662.

[182] M. de Lafontaine, R. F. H. Hunter, G. P. Forcade, J. P. D. Cook, J. Patel, B. Ellis, H. Fritzsche, and K. Hinzer, "Optimizing tritium powered GaAs p-i-n and p-n betavoltaic cells," 14th International Conference on Tritium Science and Technology, Ottawa, Canada, 2025. [Oral].

[183] M. de Lafontaine, C. Succar, R. F. H. Hunter, G. Forcade, J. Cook, J. Patel, B. Ellis, H. Fritzsche, J. Krich, and K. Hinzer, "How to quantify energy conversion in betavoltaics: Capture efficiency, gain and gain efficiency," *Cell Reports Physical Science*, July 2025, In print.

[184] E. Lopez, O. Höhn, M. Schauerte, D. Lackner, M. Schachtner, S. K. Reichmuth, and H. Helmers, "Experimental coupling process efficiency and benefits of back surface reflectors in photovoltaic multi-junction photonic power converters," *Progress in Photovoltaics: Research and Applications*, vol. 29, no. 4, pp. 461–470, 2021. doi: 10.1002/pip.3391

[185] N. Nouri, C. E. Valdivia, M. N. Beattie, J. J. Krich, and K. Hinzer, "Light management in ultra-thin photonic power converters for 1310 nm laser illumination," *Opt. Express*, vol. 30, no. 13, pp. 23 417–23 427, Jun 2022. doi: 10.1364/OE.459680

[186] E. Camarillo Abad, H. J. Joyce, and L. C. Hirst, "Light management for ever-thinner photovoltaics: A tutorial review," *APL Photonics*, vol. 9, no. 1, p. 011101, 2024. doi: 10.1063/5.0176458

[187] M. Al-Digeil, Y. Grinberg, D. Melati, J. H. Schmid, P. Cheben, S. Janz, and D.-X. Xu, "PCA-enhanced autoencoders for nonlinear dimensionality reduction in low data regimes,"

in *Proceedings of the 36th Canadian Conference on Artificial Intelligence*. Canadian Artificial Intelligence Association, 2023. doi: 10.21428/594757db.05a13011

[188] Y.-Y. Fang, J. Tolle, A. V. G. Chizmeshya, J. Kouvetakis, V. R. D'Costa, and J. Menendez, "Practical B and P doping via $Si_xSn_yGe_{1xyz}M_z$ quaternaries lattice matched to Ge: Structural, electrical, and strain behavior," *Applied physics letters*, vol. 95, no. 8, 2009.

[189] G. Timò, M. Calicchio, G. Abagnale, N. Armani, E. Achilli, M. Cornelli, F. Annoni, N. Castagnetti, M. Patrini, L. C. Andreani, L. Nasi, and B. Schineller, "Results on MOVPE SiGeSn deposition for the monolithic integration of III-V and IV elements in multi-junction solar cells," *Solar Energy Materials and Solar Cells*, vol. 224, p. 111016, 2021. doi: https://doi.org/10.1016/j.solmat.2021.111016

APPENDICES

Appendix A

aiirmap User's Manual

A Framework for Machine Learning Enhanced Design

User's Manual

Robert F. H. Hunter

August 2025, v1

Contents

1 Overview

aiirmap is available as a github repo: https://github.com/rfhhunter/aiirmap

aiirmap is a codebase which interfaces simulation softwares with Python databasing, machine learning, and optimization capabilities. It was originally designed to couple optoelectronic device simulations in Synopsys Sentaurus TCAD [1] with principle component analysis [2, 3] dimensionality reduction. It is written to be easily extendable to new simulation softwares and machine learning methods. To ease adoption, aiirmap is built upon standard Python packages; such as pandas [4, 5], scikit-learn [6], tensorflow [7], scipy [8], numpy [9], and matplotlib [10].

The basic functionality of aiirmap is as a databasing tool. Large sets of experiments can be easily defined using pandas DataFrame based *DataBases*. They are sent to and collected from the simulation softwares, manipulated (split, merged, sorted, thresholded, cleaned, etc.), subjected to machine learning, and analyzed with user-defined runfiles. This highly versatile run paradigm facilitates comprehensive design of experiments and problem space exploration. It also empowers machine learning approaches which hinge upon large datasets and flexible, reliable data pipeline control. *DataBases* and machine learning instances are saved for later use with csv and pickle format, respectively.

The remainder of this document is organized as follows: Section 2 provides an operational overview including install and setup (Section 2.1), an outline of the project structure (Section 2.2), the basic aiirmap objects (Section 2.3), and an outline of the runfile paradigm (Section 2.4). Section 3 describes how aiirmap interacts with simulation softwares such as Synopsys Sentaurus TCAD (Section 3.1). Section 4 discusses implementation of machine learning algorithms in the aiirmap code. Section 5 gives instructions on how to include new simulation softwares and machine learning functionalities. Section 6 provides some anecdotal notes on running aiirmap. Finally, in Section 7 is a list of publications which employ aiirmap and, in Section 8, persons and entities who contributed to the development of aiirmap are gratefully acknowledged.

Issues with the code or documentation can be reported in the github repository.

2 Running aiirmap

This section overviews how to install and setup aiirmap (Section 2.1). It then outlines the project structure (Section 2.2) and custom objects (Section 2.3) to give context to the run paradigm (Section 2.4), which is built around user-defined "runfiles".

2.1 Install and Setup

"Installation" of aiirmap is straightforward. Retrieve the aiirmap project from the github repo (https://github.com/rfhhunter/aiirmap) and clone it to your machine. aiirmap uses Python 3. The specific version is restricted only by the requirements of the packages that it uses. It has

been verified on Python 3.9, 3.11, 3.12, and 3.13. The remainder of the aiirmap installation is to install any Python packages it includes, if you do not have them already. The majority of these are listed at the top of the *aiirmapCommon.py* file. No specific versioning of the included Python packages is required. aiirmap operation is verified with up-to-date packages at the time of the writing of this document (Aug. 2025).

Setup of aiirmap is likewise very easy. All aiirmap requires is a folder with three subfolders to save output files. This folder is referred to as the filing folder. It can be located anywhere which is read-write accessible while running the codebase. In aiirmap its location is defined in *config.py* using the variable *filingdir*. Filing folder subfolders are used to organize the output files. Defined immediately below *filingdir* in *config.py* they include a folder for databases and machine learning instance pickles (*dbdir*), copies of simulation files (*sfdir*), and plots (*pldir*). No other setup is required to run aiirmap. The remaining variables in *config.py* set the defaults for other aspects of the codebase, as described below.

2.2 Project Structure

This section gives a very brief overview of the project structure, primarily to give context to the runfiles paradigm. For more information on the functions and code architecture please refer to the extensive comments in the code itself.

The main folder of aiirmap contains the files with configuration variables (*config.py*), an import file (*aiirmapCommon.py*), bash terminal wrappers for a few of the functions (*pyDBCollector.py, pyProjectCollector.py, grid-runner.py*), and the files for creating Sentaurus command files (*py<2/3>prepper.py*).

Several subfolders exist. The *utilities* folder contains the heart of aiirmap functionality. Functions are the split topically into different files with relevant names. The *runfiles* folder is the location where users can drop their control scripts. A couple example runfiles are included in the aiirmap repository. The *user_manual* folder contains the latex files for this document. And the *archive* offers a location to drop old files for safekeeping.

2.3 Project Objects

There are two main aiirmap objects; *DataBases* and *aiirMappings*. These objects are substantiated as Python classes located in the files *utilities/databasing.py* and *utilities/ml/machine_learning.py*, respectively. This section briefly overviews their intended operation and attributes. For further details please refer to comments in the py files.

2.3.1 DataBases

aiirmap *DataBases* are how sets of simulations are realized in the code. They are defined in the file *utilities/databasing.py* and this is also where all the functions for their creation and manipulation are located. The aiirmap *DataBase* is based upon the pandas DataFrame allowing

large datasets to be easily and quickly defined and manipulated (cleaned, split, combined, sorted, thresholded, etc.). aiirmap *DataBases* are saved as csv files in the database filing folder for later use. Their attributes are as follows, provided in the order they appear in the csv file:

- **grid** [boolean]:
  Whether or not the *DataBase* includes only simulation inputs. This is determined by whether or not the *experiment-outputs* column exists in the *DataBase.dataframe* (see below for more information). *DataBases* with only reference and/or simulation input columns are referred to as "Grids". The first line in a *DataBase* csv is the comment "#AiirMap DataBase". The next line will contain the text "GRID FILE" if the *DataBase* is a Grid or will be empty if not.

- **dbfilename** [string ending in .csv]:
  The identifier for the dataset; its filename. One line in the csv file.

- **dbFile** [path string]:
  The path to the dataset. Note that this does *not* need to match its actual location on your machine, when a *DataBase* is loaded the accurate *dbFile* will be used in the code (and will be recorded if the *DataBase* is saved). One line in the csv file.

- **lineage** [list with format of [[datetime string, action description str], ...]]:
  A recording of past manipulations of the *DataBase*. This is saved in the csv file using multiple lines; one line for each entry in the list with a header line reading "Lineage:". Lineage inheritance is also implemented. For *DataBases* created through merging of other *DataBases* a few lines of the lineage of these ancestors is recorded in the new database csv file and distinguished by »» and «« (the size of the inherited lineage can be set in *config.py*).

- **dataframe** [pandas DataFrame]:
  The main attribute for the *DataBase*. This is where your dataset data goes. Simulation inputs and outputs are given by the columns and are typically indexed with text (for instance with the parameter and variable names used in a Synopsys Sentaurus TCAD model). Different experiments (simulation instances) are given by the rows and are indexed with integers. The *DataBase.dataframe* has two special columns which act to separate the dataframe into three sections; reference, inputs, and outputs. These two columns are defined as *experiment-inputs* and *experiment-outputs* (this default can be changed or added to by editing *<in/out>putStartStrs* in *config.py*). They are placed at the left-side of each section resulting in a column structure which looks like; *db_idx*|reference columns|*experiment-inputs*|input parameter columns|*experiment-outputs*|output variable columns (where *db_idx* is the dataframe index). Note that *db_idx* begins at 0, while *experiment-<in/out>puts* begin at 1 (are the experiment number rather than its index).

2.3.2 aiirMappings

aiirMappings are the objects which codify instances of machine learning application when data is transformed. They include the inputs and outputs to the machine learning algorithm as well as the mapping between them. Information on which algorithm has been employed and

how (its hyperparameters) are also recorded here. The *aiirMapping* class is defined in the file *utilities/ml/machine_learning.py*. *aiirMappings* are saved using the pickle (.pkl) binary file format. The attributes of the *aiirMapping* object, in the order given in the code, are as follows:

- **mapType** [(a specific) string]:
  The label for the machine learning algorithm which was used. The labels for the implemented algorithm are *pca* and *ae*. *pca* is the label for principle component analysis, a linear dimensionality reduction technique [2, 3]. *ae* is the label for nonlinear dimensionality reduction using autoencoder architecture neural nets [11].

- **mapName** [string]:
  Descriptor for the *aiirMapping* instance. As opposed to *DataBase.dbfilename* this string should not end in .pkl.

- **mapFolder** [string path]:
  The path to the folder containing the *aiirMapping* pickle file. Note that this does *not* need to match the actual location of the pickle file in the code, when the *aiirMapping* is loaded then the accurate location is used in the code and will be written to file if the *aiirMapping* is saved.

- **settings** [dictionary]:
  These are the hyperparameters for the given machine learning algorithm. Each algorithm has different hyperparameter options and thus different *settings* dictionary structure. For the *aiirMapping.settings* structures specific to each algorithm see the comments at the top of the *aiirMapping* class definition.

- **ml** [machine learning object]:
  Also located in *utilities/ml/machine_learning.py* is the definition of classes for each type of machine learning algorithm (so far only *DimensionalityReduction*). These objects package the actual machine learning objects created by the scikit-learn or tensorflow (or other package) functions for later access.

- **filteredInputDB** [DataBase]:
  This is the aiirmap *DataBase* with the input data for the machine learning algorithm. Filtering refers to the fact that the experiments in this dataset have been cleaned and thresholded, it contains only the data which is actually being used as input to the algorithm. This *DataBase* contains all columns present in the original *DataBase* for this filtered data.

- **filteredInputGrid** [(Grid) DataBase]:
  Very similar to the previous attribute but now the reference and outputs columns have been removed. Input columns which are extraneous to the machine learning training have also been removed in a process called column cleaning (see the function *dbDRCleanCols* in *utilities/databasing.py* for more information). This is the training data (only).

- **results** [dict]:
  The outputs from the machine learning algorithm. Each algorithm will have different outputs according to type and intended operation. For the *aiirMapping.results* structures specific to each algorithm see the comments in the *aiirMapping* class definition.

2.4 Runfiles

aiirmap provides the functions and objects for a versatile simulation flow control. It is up to the user how to they want to use this functionality and, indeed, the exploratory nature of design and machine learning enhanced design means that this use will evolve. "Runfiles" are simply the user scripts written to access aiirmap functionality. Users may also directly use the Python terminal if they prefer. All aiirmap capabilities are imported by including *aiirmapCommon.py* at the start of your script (*from aiirmapCommon import **).

Typical runfile operations are listed below. These are just examples offered to spark the user's imagination. Any desired functionality can be included in runfiles and organized as the user sees fit. Runfile functions may also be loaded as modules into other runfiles. General useful functionality can be ported into the aiirmap utilities and shared if the user wishes.

Potential runfile operations: Creating a new *DataBase* and filling it with data to send as input to the simulation software. Creating a new *DataBase* from one or more other *DataBases*. Loading a *DataBase* and running analysis or machine learning and potentially outputting a new *DataBase* for further simulation. Comparing performance across *DataBases*. Designing specific investigations. Creating sequential simulation run operations. etc.

3 Simulation Software Interactions

This section outlines how aiirmap interacts with the simulation softwares which have been implemented in its environment. As mentioned, aiirmap has been designed in a manner which allows it to be extended to include other simulation softwares. The procedure for adding new softwares into the code is outlined in Section 5 below. Users may add subsections here outlining their software interface.

3.1 Synopsys Sentaurus TCAD Interaction

Synopsys Sentaurus TCAD is an finite element analysis optoelectronics device simulator [1]. aiirmap was originally written to interface Python with Sentaurus to provide databasing and machine learning capabilities. Sentaurus interacts with Sentaurus in two ways; collection of simulation results and (batch-capable) run control.

Collection of results is instantiated in the Sentaurus project flow using the Sentaurus Python tool. aiirmap includes a script (*py2prepper.py*) which writes the command file for this tool during preprocessing to allow maximum flexibility in the strict Sentaurus operation flow. One creates the Python tool in their project and then includes the following line in their project tooldb file: '*set WB_tool(gsub,prologue) { exec python $wdir/path/to/py2prepper.py $wdir }*' (do not include the quotation marks). Due to the order of operations in Sentaurus, the collector tool first writes the input parameter values and the nodes associated with each experiment into a csv file in the Sentaurus folder, this occurs during preprocessing. The rest of the operations occur when the project is finished or when requested by the aiirmap user (using *pyProjectCollector.py*, *pyDBCollector.py*, or other scripts which run the functions for which

those files are bash wrappers). At that point, the output variable values are collected from the Sentaurus gvars.dat file, matched with the input parameters using the node numbers in the collector csv file, and together saved to an aiirmap *DataBase* (see *utilities/sReadAndInteract.py* for more information). aiirmap also writes a second csv in the Sentaurus project folder which records the execution times of the nodes. Pertinent Sentaurus files, as defined in *config.py*, are then copied to a project subfolder in the simulation files filing folder.

It can be noted that the aiirmap Sentaurus collection protocol allows for use of the Sentaurus gopt optimization tool which creates child projects for the optimization of each design. These are tracked and linked to their parent algorithmically in the collection code.

The second functionality, Sentaurus run control, was written for two reasons; 1) the ease at which one can define experiments, including large numbers of experiments, in a Python environment, as compared to the Sentaurus GUI, and 2) to enable large dataset runs using a batching functionality which was required to overcome memory issues inherent to the version of Sentaurus which was being used. The Sentaurus batch run control is instantiated through protocols which directly write the Sentaurus project's gtree.dat file which codifies the state of the Sentaurus workbench. The *grid-runner.py* wrapper file runs an automatic procedure which takes an input database, splits it into easy to handle subset databases, which it runs sequentially, collecting and collating the results as it goes.

Further details on Sentaurus interaction are found in the comments in the code (specifically, see *py2prepper.py* and the wrappers in the main aiirmap folder).

4 Machine Learning Algorithm Implementations

This section outlines the different machine learning algorithms which have been implemented in the aiirmap framework. Users may add subsections here for added functionality. Comments on adding new machine learning functionality are provided in Section 5.

Implementation of machine learning follows two methods depending upon the class of machine learning algorithm. First, for machine learning algorithms which act upon a dataset adding information or providing analysis but not necessarily transforming the data, a simple file with functions may be used. A number of **clustering** algorithms have been implemented this way. These include DBSCAN [12], HDBSCAN [13], KMeans [14], and Agglomerative Hierarchical [15]. This functionality is located in *utilities/ml/clustering.py*. Functions apply clustering to a *DataBase*, compute centroids and simple statistics, and auto-split *DataBases* according to cluster. Please see the code for more information. The second machine learning implementation is used for algorithms which transform the data. The included example being principle component analysis [2, 3] and autoencoder-based [11] **dimensionality reduction**. These implementations use the *aiirMapping* object described in Section 2.3. A brief outline of aiirmap dimensionality reduction is below.

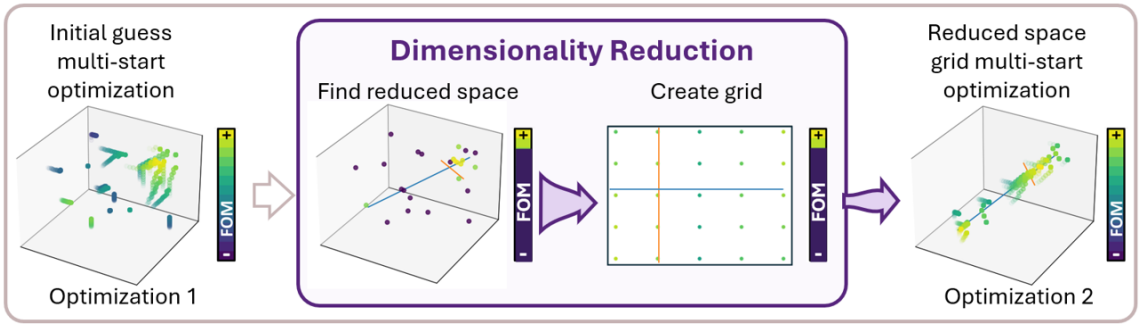

Figure 1: aiirmap dimensionality reduction enhanced design schema. FOM indicates a chosen figure of merit. Figure sourced from [16].

4.1 Dimensionality Reduction

aiirmap dimensionality reduction was designed to execute the schema shown in Figure 1 [16]. Top designs from a first stage of multi-start optimization are used to train the dimensionality reduction algorithm which identifies a latent high-performance design subspace of reduced dimensionality. A grid of points are generated to survey this subspace and are projected back out into the full design space and used as start points for a second stage of optimization. More information on this method and its advantages can be found in [16].

The dimensionality reduction implementation is located in *utilities/ml/machine_learning.py*. This functionality, including the *aiirMapping* object, reflect the schema shown in Figure 1. Functions take a *DataBase* clean and threshold it, apply dimensionality reduction, and then use the reduced space to generate a grid of designs which is projected back into the original design space. This is completed via the *applyDR* function. The exploratory nature of machine learning application led to the further development of so-called "DR investigations". These are sets of multiple dimensionality reduction (DR) runs with differing parameters which are applied to the same input data and saved together in the form of a pickle and pandas dataframe csv. See the code, specifically *investigateDR*, for more info. A wrapper which automatically detects whether a single or multiple/investigation dimensionality reduction is being run is found in *runNewDR*. Some functions for analyzing the reduced space and the reconstruction of data (when datapoints are projected into and then back out of the reduced space) are also provided.

5 Adding New Simulation Software or Machine Learning Algorithms

The design philosophy of aiirmap is for it to be a general purpose framework which allows any simulation softwares which can communicate with Python to be coupled to all of the powerful databasing, optimization, machine learning, analysis, visualization, control, etc. capabilities written in Python packages. New simulation softwares can be added, as can new machine learning algorithms. This section will briefly outline the procedures for each.

Adding new simulation softwares into aiirmap will depend highly upon the context. Specif-

ically, how the new software communicates with Python. The main functionality of the new interface is to be able to collect a correctly formatted *DataBase* csv. It is suggested that the user familiarize themselves with the *DataBase* format as described in Section 2.3 above and in *utilities/databasing.py*. Other functionality may be added, such as run control and/or storage of simulation files but is not required (although the author does suggest run control to allow two-way communication between aiirmap and your software). Interaction with Sentaurus provides all three of these functionalities and may be used as an example, see Section 3.1 and *utilities/sReadAndInteract.py* for more information. As the Sentaurus TCAD section outlines, the interaction between Sentaurus and aiirmap is a bit convoluted due to the operational paradigm of Sentaurus, new software implementations may contain many less functions than was required in *sReadAndInteract.py*. Sharing the added software functionality in the github repository is greatly appreciated! Please write a new utility file similar to *sReadAndinteract.py* with the new interface and feel free to add a section to this document outlining its use (locate it in Section 3).

Adding new machine learning algorithms into aiirmap can be done two ways. If the new algorithm use is light, exploratory, or time-constrained the user may find it sufficient to implement the new algorithm only within their personal runfiles. On the other hand, if the new algorithm use is substantial, requires standardization, or if the user has the intent to share implementation of the new algorithm involves the creation of new *aiirMapping* variants or addition of similar objects, as the user sees fit. The description of *aiirMapping* objects in Section 2.3 above and the architecture and comments in *utilities/ml/machine_learning.py* are pertinent in this case (take care to note how two different dimensionality reduction methods are included). The hope is that a large majority of machine learning algorithms will be able to fit into the *aiirMapping* form factor which would act as a standardized frontispiece for machine learning functionalities which transform the data. Sharing of added functionality in the github repository is greatly appreciated! Please include a brief overview of how to run the new algorithm as a subsection in Section 4.

6 Notes

Please be aware of the following points:

- The plotting subfolder (*pldir*) is not used by a great number of the plotting functions. Suggested practice for these functions is to screenshot or save your plots directly from the matplotlib figure window. This course of action allows the user to adjust the aspect ratio and make sure all figure components are visible for each image.
- The *amverbose* variable (found in *config.py*) is meant as a global switch to turn off or on extra terminal output. It is only partially implemented.

7 Publications

The following peer-reviewed publications have utilized the aiirmap framework, listed from newest to oldest:

- R.F.H. Hunter, "Next-Generation Multi-Junction Photovoltaic Design Paradigms and Adaptive Optics Techniques for Telecommunications Applications and the Global Energy Transition," Ph.D. Thesis, University of Ottawa, Aug. 2025.
- R.F.H. Hunter *et al.*, "Machine learning enhanced design optimization and knowledge discovery for multi-junction photonic power converters," *Scientific Reports*, Aug. 2025. doi: https://doi.org/10.1038/s41598-025-16408-4
- M. de Lafontaine *et al.*, "Figures of merit to quantify carrier collection in betavoltaics: Gain and gain efficiency," *Cell Reports Physical Science*, 102789, Aug. 2025. doi: https://doi.org/10.1016/j.xcrp.2025.102789
- G.P. Forcade *et al.*, "Multi-junction laser power converters exceeding 50% efficiency in the short wavelength infrared", *Cell Reports Physical Science*, 6(6):102610, May 2025. doi: https://doi.org/10.1016/j.xcrp.2025.102610

The following scientific conference presentations (some with proceedings) have utilized the aiirmap framework:

- M. de Lafontaine *et al.*, "Optimizing Tritium Powered GaAs p-i-n and p-n Betavoltaic Cells," *14th International Conference on Tritium Science and Technology*, Ottawa, Canada, 2025.
- P. Wilson *et al.*, "Impact of Luminescent Coupling on Multijunction InGaAs Photonic Power Converters under Current Mismatched Conditions in the C-Band," *Photonics North 2025*, Ottawa, Canada, 2025.
- P. Wilson *et al.*, "Quantifying the luminescent coupling process in C-band multi-junction photonic power converters," *Photonics West*, San Fransisco, USA, 2024.
- R.F.H. Hunter, "Using machine learning to optimize multi-junction photonic power converters," *SPIE OPTO 2024*, San Francisco, California, United States, 2024.
- K. Hinzer *et al.*, "Multi-junction photonic power converters: AI enhanced design optimization," *52nd IEEE Photovoltaic Specialists Conference (PVSC)*, Seattle, USA, 2024.
- K. Hinzer *et al.*, "C-band Multi-Junction Photonic Power Converters: AI Techniques for Optimized Designs and Role of Luminescent Coupling," *6th Optical Wireless and Fiber Power Transmission Conference (OWPT)*, Japan, 2024.
- Y. Grinberg *et al.*, "Dimensionality Reduction in Photonics Design – New Methods and Applications," *Photonics North 2024*, Vancouver, Canada, 2024.
- M. de Lafontaine *et al.*, "p-i-n Betavoltaic Cells under 63Ni Irradiation: Quantifying Carrier Collection and Power Output," *52nd IEEE Photovoltaic Specialists Conference (PVSC)*, Seattle, USA, 2024.
- G.P. Forcade *et al.*, "High-Performance Multi-Junction C-Band Photonic Power Converters: Calibrated Optoelectronic Model for Next Generation Designs," *50th IEEE Photovoltaic Specialists Conference (PVSC)*, San Juan, Puerto Rico, 2023.

Users may feel free to add their publications and presentations to the lists. These lists are not considered exhaustive.

8 Acknowledgments

aiirmap was originally developed as part of the AIIR-Power project [17, 18]. The author is grateful to the agencies which provided funding to the AIIR-Power project and to the members of the consortium for their guidance. While its design diverged significantly over time, aiirmap got its initial inspiration from the project spacemap, developed by AIIR-Power collaborators at the National Research Council of Canada. spacemap is available at https://github.com/NRC-AI4Photonics/spacemap. This work was completed as part of the author's doctoral studies, the author is grateful to the SUNLAB research group, to the University of Ottawa, to the Government of Ontario, and to the NSERC CREATE program for funding and support. The aiirmap logo was created with ChatGPT.

References

[1] Synopsys Inc. *Synopsys Sentaurus TCAD*. 2025. URL: https://www.synopsys.com/manufacturing/tcad.html.

[2] Karl Pearson. "LIII. On lines and planes of closest fit to systems of points in space". In: *The London, Edinburgh, and Dublin Philosophical Magazine and Journal of Science* 2.11 (Nov. 1901), pp. 559–572. DOI: 10.1080/14786440109462720. (Visited on 04/21/2024).

[3] Ian T. Jolliffe and Jorge Cadima. "Principal component analysis: a review and recent developments". In: *Philosophical Transactions of the Royal Society A: Mathematical, Physical and Engineering Sciences* 374.2065 (Apr. 13, 2016), p. 20150202. DOI: 10.1098/rsta.2015.0202. (Visited on 04/21/2024).

[4] Wes McKinney. "Data Structures for Statistical Computing in Python". In: *Proceedings of the 9th Python in Science Conference*. Ed. by Stéfan van der Walt and Jarrod Millman. 2010. DOI: 10.25080/Majora-92bf1922-00a.

[5] The pandas development team. *pandas-dev/pandas: Pandas, version 2.2.2*. Version latest. Apr. 2024. DOI: 10.5281/zenodo.3509134.

[6] F. Pedregosa et al. "Scikit-learn: Machine Learning in Python". In: *Journal of Machine Learning Research* 12 (2011), pp. 2825–2830. DOI: 10.5555/1953048.2078195.

[7] Martín Abadi et al. *TensorFlow: Large-Scale Machine Learning on Heterogeneous Systems*. Software available from tensorflow.org. 2015. URL: https://www.tensorflow.org/.

[8] Pauli Virtanen et al. "SciPy 1.0: Fundamental Algorithms for Scientific Computing in Python". In: *Nature Methods* 17 (2020), pp. 261–272. DOI: 10.1038/s41592-019-0686-2.

[9] Charles R. Harris et al. "Array programming with NumPy". In: *Nature* 585.7825 (Sept. 2020), pp. 357–362. DOI: 10.1038/s41586-020-2649-2. URL: https://doi.org/10.1038/s41586-020-2649-2.

[10] J. D. Hunter. "Matplotlib: A 2D graphics environment". In: *Computing in Science & Engineering* 9.3 (2007), pp. 90–95. DOI: 10.1109/MCSE.2007.55.

[11] Muhammad Al-Digeil et al. "PCA-enhanced autoencoders for nonlinear dimensionality reduction in low data regimes". In: *Proceedings of the 36th Canadian Conference on Artificial Intelligence*. The 36th Canadian Conference on Artificial Intelligence. Montreal, Quebec: Canadian Artificial Intelligence Association, 2023. DOI: 10.21428/594757db.05a13011. (Visited on 06/05/2023).

[12] Martin Ester et al. "A density-based algorithm for discovering clusters in large spatial databases with noise". In: *Proceedings of the Second International Conference on Knowledge Discovery and Data Mining*. KDD'96. Portland, Oregon: AAAI Press, 1996, pp. 226–231.

[13] Leland McInnes, John Healy, and Steve Astels. "hdbscan: Hierarchical density based clustering". In: *Journal of Open Source Software* 2.11 (2017), p. 205. DOI: 10.21105/joss.00205.

[14] Stuart P. Lloyd. "Least squares quantization in PCM". In: *IEEE Transactions on Information Theory* 28.2 (1982), pp. 129–137.

[15] J. H. Ward. "Hierarchical Grouping to Optimize an Objective Function". In: *Journal of the American Statistical Association* 58.301 (1963), pp. 236–244. DOI: 10.1080/01621459.1963.10500845.

[16] Robert F. H. Hunter et al. "Machine learning enhanced design and knowledge discovery for multi-junction photonic power converters". In: *Scientific Reports* (Aug 2025). DOI: https://doi.org/10.1038/s41598-025-16408-4.

[17] National Research Council of Canada. *Supporting collaborative projects between Canada and Germany in artificial intelligence and value-added manufacturing*. 2021. URL: https://nrc.canada.ca/en/stories/supporting-collaborative-projects-between-canada-germany-artificial-intelligence-value-added.

[18] Fraunhofer Institute for Solar Energy Research. *AI-assisted design and fabrication of photonic infrared power converters for energy and telecommunication*. 2021. URL: https://www.ise.fraunhofer.de/en/research-projects/aiir-power.html.